HAL
open science

Performances of the 3” PMT front-end electronics in the JUNO experiment and study of its impact on charge and time measurements.

Clément Bordereau

To cite this version:

Clément Bordereau. Performances of the 3” PMT front-end electronics in the JUNO experiment and study of its impact on charge and time measurements.. Astrophysics [astro-ph]. Université de Bordeaux, 2022. English. NNT : 2022BORD0462 . tel-03994431

HAL Id: tel-03994431

https://theses.hal.science/tel-03994431v1

Submitted on 17 Feb 2023

HAL is a multi-disciplinary open access archive for the deposit and dissemination of scientific research documents, whether they are published or not. The documents may come from teaching and research institutions in France or abroad, or from public or private research centers.

L’archive ouverte pluridisciplinaire **HAL**, est destinée au dépôt et à la diffusion de documents scientifiques de niveau recherche, publiés ou non, émanant des établissements d’enseignement et de recherche français ou étrangers, des laboratoires publics ou privés.

THESIS PRESENTED

TO OBTAIN THE ACADEMIC RANK OF

DOCTOR
OF THE UNIVERSITY OF BORDEAUX

ÉCOLE DOCTORALE SCIENCES PHYSIQUES ET DE L'INGÉNIEUR

ASTROPHYSIQUE, PLASMA, NUCLÉAIRE

By **Clément BORDEREAU**

Performances of the 3" PMT front-end electronics in the JUNO experiment and study of its impact on charge and time measurements.

Performances de l'électronique front-end du système des PMTs 3" dans l'expérience JUNO et étude de son impact sur les mesures de charge et de temps.

Under the supervision of : **Fréderic PERROT**
Co-supervisor : **Yee HSIUNG**

Defended on December 5th 2022

Jury members :

Mr. Pao-Ti CHANG	Professor	National Taiwan University	Examiner
Ms. Selma CONFORTI	Ingénieure de Recherche	CNRS	Examiner
Mr. Olivier DRAPIER	Directeur de Recherche	CNRS	Rapporteur
Mr. Denis DUMORA	Professeur des Universités	CNRS	President of the jury
Mr. Yee HSIUNG	Professor	National Taiwan University	PhD co-supervisor
Mr. Frédéric PERROT	Maître de Conférences	CNRS	PhD co-supervisor
Mr. Laurent SIMARD	Maître de Conférences	CNRS	Rapporteur

Abstract : The observation of neutrino oscillations has led to questioning the Standard Model of particle physics, and precisely measuring the neutrino oscillation parameters and answering the question about the ordering of the neutrino mass states could provide the key to understanding other unsolved puzzles in both cosmology and particle physics. This is the objective of the Jiangmen Underground Neutrino Observatory (JUNO), a multi-purpose neutrino experiment expected to start taking data in 2024, which will detect reactor anti-neutrinos from two nearby nuclear power plants using a central detector containing 20 kton of liquid scintillator. The emitted photons will be observed by two large arrays of 20-inch (LPMTs) and 3-inch (SPMTs) photomultiplier tubes, the SPMT system having been designed to serve as a complementary array of photodetectors to the LPMT system. By mostly operating in a photon-counting mode, it will help calibrate the energy response of the LPMTs as well as help better understand the systematics of the system. Located underwater, its readout electronics consists in 128 SPMTs being connected to a single ABC front-end board hosting 8 16-channels CATIROC ASICs. Precise studies on the performances of this ABC board are presented in this thesis, including studies on pedestal measurements (0.05 photoelectron pedestal widths), charge linearity and calibration (0.05% deviation to linear model), time resolution (about 0.25 ns), crosstalk (below 0.15%), as well as on test-benches combining all the SPMT electronics to date. The boards' ability to asynchronously auto-trigger on random SPE events with thresholds as low as 1/3 photoelectron is also demonstrated, and the processing of a PMT signal within the ABC board is studied with precise parametrizations of certain CATIROC ASIC features such as the trigger time and time walk, the deadtimes and the charge acceptance. This intricate knowledge of the SPMT electronics was additionally implemented in the JUNO simulation, and simulated events showed that the impact of the response of the SPMT system on physical studies involving the charge and time information was negligible before the response of the PMTs. This work has furthermore led to the qualification of the performances of the 25,600 SPMTs and of the 220 ABC front-end boards, which will pave the way for the exploitation of the JUNO physics data starting from 2024.

Résumé : L'observation du phénomène d'oscillation des neutrinos a conduit à la remise en question du Modèle Standard de la physique des particules. Effectuer une mesure précise de leurs paramètres d'oscillation, ainsi que répondre à la question de la hiérarchie de leurs états de masse, pourrait bien fournir des éléments de réponse quant à d'autres énigmes non résolues en cosmologie et en physique des particules. C'est l'objectif de l'observatoire souterrain de neutrinos de Jiangmen (JUNO), une expérience polyvalente sur les neutrinos devant commencer à prendre des données en 2024, qui détectera les anti-neutrinos de réacteurs de deux centrales nucléaires voisines à l'aide d'un détecteur central contenant 20000 tonnes de scintillateur liquide. Les photons émis seront observés par deux grands réseaux de tubes photomultiplicateurs de 20 pouces (LPMTs) et de 3 pouces (SPMTs), le système SPMT ayant été conçu pour servir de réseau complémentaire au système LPMT. Fonctionnant principalement dans un mode de comptage de photons, il permettra d'étalonner la réponse en énergie des LPMTs et de mieux comprendre les erreurs systématiques du système. Entreposée dans de l'eau, son électronique de lecture consiste en 128 SPMTs connectés à une même carte frontale ABC, hébergeant 8 ASICs CATIROC de 16 voies. Des études précises menées sur les performances de cette carte ABC sont présentées dans cette thèse, comprenant des études sur les mesures de piédestaux (largeurs inférieures à 0,05 photoélectron), la linéarité et l'étalonnage en charge (déviation de 0,05% par rapport à un modèle linéaire), la résolution temporelle (environ 0,25 ns), la diaphonie (inférieure à 0,15%), ainsi que sur des bancs de tests combinant toute l'électronique du système SPMT à ce jour. La bonne capacité des cartes ABC à déclencher de manière asynchrone et aléatoire sur des photoélectrons avec des seuils à 1/3 de photoélectron est également démontrée, et le traitement d'un signal PM dans la carte ABC est étudié avec le paramétrage précis de certaines caractéristiques des ASICs CATIROC telles que le temps de déclenchement et le time walk, les temps morts et l'acceptance en charge. Cette connaissance approfondie de l'électronique SPMT a également été implémentée dans la simulation JUNO et les événements simulés ont montré que l'impact de la réponse du système SPMT sur des études physiques impliquant les informations de charge et de temps est négligeable devant la réponse des PMs. Ces travaux ont en outre abouti à la qualification des performances des 25600 SPMTs et des 220 cartes frontales ABC, ce qui ouvre la voie à l'exploitation des données de physique de JUNO à partir de 2024.

Acknowledgments

I would first like to thank all members of my jury, particularly Olivier Drapier and Laurent Simard, the two rapporteurs. Thank you for having accepted the task of reading my manuscript and reporting on it, I enjoyed your feedback and answering your questions on the day of the defense. I am also grateful to Denis Dumora for having presided that jury, as well as to Selma Conforti and Pao-Ti Chang for having accepted to act as examiners.

The most important person to acknowledge, though, is of course Frédéric Perrot, my thesis supervisor at LP2i Bordeaux. There is so much to say that I am not quite sure where to begin ... Let's start with the purely academic side of things, first. Thank you for these years of working together, it was a pleasure to work alongside you on the many different aspects of the JUNO SPMT system. I learned much more than I thought I would, expecting to only work in data analysis, and, in my opinion, this is largely due to your broader knowledge of the experiment as a whole and to your efforts in getting that knowledge through to me. Your insight was especially invaluable in writing about the detector and its large physics program, but citing only one example undermines the countless directions you gave me and contributions you made to my work. On a more personal note, I am really glad that we met. From the common interest in the 80s music, that made many people ask if you had selected me for the PhD program for that particular reason, to the general affinity we had, I tremendously enjoyed spending time with you and will always remember the years I spent in Bordeaux. But most importantly, I cannot thank you enough for just how much you went out of your way to help and support me through darker times. I had my moments when I was very difficult, and yet you stuck by me through thick and thin. This thesis would not have been completed without you, and to be honest, I doubt my health would have improved. I have no words to express just how profoundly grateful I am for your kindness, patience and understanding during these years of working with you. You went above and beyond what can be expected of a supervisor, thank you for always looking out for me and for my best interests, I owe you a lot.

I would also like to address special thanks to Yee "Bob" Hsiung, my co-supervisor in NTU. You welcomed me with open arms in a completely foreign country, and I will always look very fondly on the time that I spent in Taiwan. Thank you for your guidance when I was working with you and Bei-Zhen, as well as for introducing me to many aspects of Taiwanese culture that particularly enjoyed and miss a lot.

I am now extending my thanks and gratitude to the members of the Neutrino group at LP2i Bordeaux, alongside whom I have worked very closely.
Cédric Cerna, thank you for your very impressive expertise in all technical matters and for your willingness and availability to discuss them with me. You were invaluable in both driving our work efforts as a team and in helping me study and write about the SPMT electronics.
Cécile Jollet, thank you for your expertise in all theoretical matters and in data analysis. I very much respect your insight and your work, and I was very lucky to be able to have your help on both the theoretical chapter of my thesis as well as on the analysis of simulation files.
Anselmo Meregaglia, thank you for the occasional answers you gave me on very precise aspects of theoretical physics, as well as sometimes looking at my reconstruction algorithms and providing valuable input.
Christine Marquet, it was always a pleasure to walk by your office, see you were in there, and have little chats. I was really glad you could attend my defense.
Emmanuel Chauveau, I didn't see you all that much considering you were always in Modane, but thank you for solving some hair-pulling issues Axel and I sometimes faced with our codes.

Fabrice Piquemal, now director of the LP2i, thank you for always looking out for the PhD students. Special thanks to Axel Pin, alongside whom I started my PhD, and who was, by some miracle, my complete opposite in terms of skills. While you were gifted in anything experimental but had room for improvement in data analysis, I was completely useless as long as it didn't involve writing code, and so we complemented each other quite nicely. Thanks for the help, buddy, it was a pleasure learning with you !

I would also like to warmly thank the electronics engineers at LP2i, for their invaluable involvement in the project as well as for having taught me most of what I know in this field. In particular, Frédéric Druillole, who taught me that there is nothing magical in electronics, and Abdel Rebii, who spent many hours explaining to me how the firmware was supposed to be operating. I learned so much more about electronics than I ever thought I would or even would want to. Thanks to you both, I was able to sit for countless hours plugging, unplugging, performing measurements and pulling my hair out just to finally realize that the slow control hadn't gone through correctly. So, yeah, thanks for that ...

In addition to my colleagues at LP2i, I also have to extend my gratitude to close JUNO collaborators from outside the lab, in particular Mariangela Settimo and Selma Conforti.
Mariangela, thank you for being one half of the CATIROC team that I bothered so often with questions. Thank you also for the involvement you had in my PhD work, from us working together on encoding CATIROC's performances in algorithms in order to replicate its behavior and study muons, to the oh so cold winter days we spent in Nanning setting up the test benches. Thanks, Babushka !
Selma, thank you for being the second half of that CATIROC team. I don't even remember how many times I called you for explanations on how this or that feature of CATIROC worked, and often for the same explanation as the previous time ... Thank you for always taking the time to make sure everything was clear with me, for proof-reading my thesis chapter on CATIROC, as well as for having been a part of my jury.

Finally, I would like to thank my friends and family for their constant support. Special thanks to Hichem Tedjditi, alongside whom I got my Master's degree, who was always available to help motivate me when I was feeling down or was being unproductive and always willing to go over some of my work to give me his opinion, as well as to Anastasja Bietta, a close childhood friend of mine, for putting up with me all these years and for being my Burger King and Cap Ferret partner on top of a model of dedication to her own PhD work and a source of inspiration. And I am of course closing these acknowledgements by thanking my parents for their unconditional love and support. I would not be where I am if it hadn't been for them, and I apologize for having been such a source of worry these last years. Thanks, Mom and Dad !

Contents

Introduction **1**

1 Neutrino physics and oscillations **3**
1.1 Neutrino physics . . . 3
1.1.1 Introduction . . . 3
1.1.2 The neutrino in the Standard Model of particle physics . . . 4
1.1.3 Physics beyond the Standard Model . . . 7
1.1.3.1 Neutrino mass and Majorana nature of the neutrino . . . 8
1.1.3.2 Probing the nature of the neutrino with double beta decays . . . 10
1.2 Neutrino oscillations . . . 13
1.2.1 Introduction : concept of neutrino oscillations . . . 13
1.2.2 Evidence for oscillations . . . 15
1.2.3 Theory of neutrino oscillations . . . 19
1.2.4 Neutrino Mass Ordering . . . 23
1.2.5 Matter effects . . . 24
1.2.6 CP violation and Dirac phase δ_{CP} . . . 26
1.2.7 Current values of oscillation parameters . . . 27
1.3 Neutrino Mass Ordering determination . . . 27
1.3.1 Motivations for physics / Consequences of measuring the Mass Ordering . . . 27
1.3.2 Current experiments and status . . . 29
1.3.3 Future experiments using matter-modified oscillations . . . 32
1.3.3.1 Using atmospheric neutrinos - Hyper-K / ORCA . . . 32
1.3.3.2 Using accelerator neutrinos - DUNE . . . 35
1.3.4 Investigating the NMO using vacuum oscillations with JUNO . . . 36

2 JUNO physics and detector **43**
2.1 JUNO requirements : location and detector design . . . 43
2.2 Central Detector . . . 45
2.3 Veto Detector . . . 46
2.3.1 Water Cherenkov Detector . . . 46
2.3.2 Top Tracker . . . 47
2.4 Liquid Scintillator . . . 48
2.5 PMT systems . . . 50
2.5.1 LPMT system . . . 50
2.5.2 Electronics and signal acquisition . . . 53
2.5.3 SPMT system . . . 55
2.6 CD calibration system . . . 59
2.6.1 Calibration system design . . . 59
2.6.2 Radioactive sources . . . 62

2.6.3 Calibration program . . . 62
2.7 Low background strategy . . . 63
2.8 TAO . . . 65
2.9 Additional physics with JUNO . . . 67
2.9.1 Neutrino oscillation parameters precision measurements . . . 67
2.9.2 Supernova neutrinos . . . 68
2.9.3 Diffuse supernova neutrino background . . . 69
2.9.4 Solar neutrinos . . . 71
2.9.5 Geo-neutrinos . . . 73
2.9.6 Other physics . . . 75
2.10 Conclusion . . . 76

3 SPMT system and its front-end electronics 77
3.1 Motivation . . . 77
3.2 Description of the system . . . 81
3.3 PMT instrumentation . . . 83
3.3.1 3-inch PMTs . . . 83
3.3.2 High voltage divider and PMT base potting . . . 84
3.3.3 Cables and UWB connectors . . . 86
3.4 High Voltage Splitter board . . . 87
3.5 Front-end ABC board . . . 89
3.5.1 CATIROC ASICs . . . 90
3.5.2 Data and Firmware . . . 97
3.6 Global Control Unit board . . . 99
3.7 Underwater Box design and thermal studies . . . 100
3.7.1 Design . . . 100
3.7.2 Thermal studies . . . 101
3.8 Radiopurity of the SPMT system . . . 102
3.9 Conclusion . . . 104

4 Fine responses of the front-end ABC board 105
4.1 Introduction . . . 105
4.2 Data-taking tools . . . 106
4.2.1 Versions of ABC board . . . 106
4.2.2 Firmware and data-taking software . . . 106
4.2.3 Trigger modes and user parameters . . . 109
4.3 Standalone performances of the ABC board . . . 110
4.3.1 Pedestals . . . 110
4.3.2 Charge linearity and charge calibration . . . 111
4.3.3 Time resolution . . . 115
4.3.4 Crosstalk . . . 117
4.3.5 S-curves . . . 121
4.3.5.1 50% trigger efficiency threshold identification . . . 122
4.3.5.2 Trigger threshold linearity . . . 123
4.4 Combined tests . . . 123
4.4.1 V0 test benches . . . 124
4.4.1.1 Description of the V0 test benches . . . 124
4.4.1.2 32 PMT performances at LP2i . . . 125
4.4.1.3 SPMT mass testing at GXU . . . 128
4.4.2 16-channels NTU test bench for fine measurements . . . 131

4.4.3 128 PMT performances at LP2i . . . 131
4.4.3.1 Experimental setup . . . 132
4.4.3.2 Measurements and PMT performances . . . 133
4.5 PMT signal and processing . . . 137
4.5.1 PE collection and PMT waveform . . . 137
4.5.2 LED test bench for PMT waveform behavior . . . 141
4.5.3 Trigger time and time walk . . . 146
4.5.4 Processing consecutive PMT signals with CATIROC . . . 149
4.5.4.1 CATIROC dead times . . . 149
4.5.4.2 Charge acceptance . . . 151
4.6 Conclusion . . . 152

5 Implementation of the performances of the SPMT system in the JUNO simulation - Study of impacts on the charge and time measurements 155
5.1 Introduction . . . 155
5.2 SPMT simulation . . . 156
5.2.1 Electromagnetic interactions and optical properties . . . 156
5.2.2 SPMT electronics in SNiPER . . . 158
5.3 Impact of SPMT electronics on the reconstructed charge . . . 162
5.3.1 Introduction and discussion : Muon studies with trigger deadtime, charge acceptance and charge digitization deadtime . . . 162
5.3.2 Reconstructed charge using ^{12}B events . . . 165
5.4 Impact of SPMT electronics on the measured time . . . 169
5.4.1 Introduction : CATIROC trigger time spread vs PMT TTS . . . 169
5.4.2 Vertex reconstruction with the SPMT system . . . 171
5.4.2.1 Vertex reconstruction method . . . 171
5.4.2.2 Toy Monte Carlo for statistical limitation with SPMTs, first results 176
5.4.2.3 Impact of the electronics on the reconstruction . . . 178
5.5 Conclusion . . . 181

Conclusion and Prospects 183

Bibliography 185

List of Figures

1.1 Z^0 width for neutrino families . . . 5
1.2 Feynman diagram for $2\nu\beta\beta$ . . . 11
1.3 Neutrinoless double beta decay . . . 12
1.4 Neutrino mass ordering with $0\nu\beta\beta$ . . . 13
1.5 Standard Solar Model prediction of the solar neutrino flux . . . 15
1.6 SNO events . . . 17
1.7 Possible Neutrino Mass Orderings . . . 24
1.8 NOνA results . . . 30
1.9 T2K results . . . 31
1.10 NOνA / T2K comparison . . . 32
1.11 Hyper-K detector . . . 33
1.12 Hyper-K projected results . . . 34
1.13 KM3NeT/ORCA detector . . . 34
1.14 KM3NeT/ORCA projected results . . . 35
1.15 DUNE detector . . . 36
1.16 DUNE projected results . . . 37
1.17 Observable electronic antineutrino energy spectrum . . . 37
1.18 Daya Bay measurement of θ_{13} . . . 38
1.19 Electronic antineutrino survival probability . . . 39
1.20 Reactor antineutrino energy spectrum . . . 40
1.21 JUNO spectral analysis and projected results . . . 41

2.1 JUNO location and site infrastructure . . . 44
2.2 JUNO detector . . . 44
2.3 Assembling the acrylic sphere . . . 46
2.4 Top Tracker system . . . 48
2.5 LS processing system . . . 49
2.6 Different PMTs in JUNO . . . 50
2.7 PMT PDE . . . 52
2.8 PMT DCR . . . 52
2.9 PMT Resolution . . . 53
2.10 LPMT scanning for photocathode uniformity . . . 54
2.11 LPMT electronics . . . 54
2.12 PMT positioning . . . 55
2.13 PMT test stations . . . 56
2.14 Class A sampling test results comparison to vendor data . . . 58
2.15 Class B sampling . . . 59
2.16 Gamma non-linearity . . . 60
2.17 Calibration system design . . . 61

2.18 Detector non-uniformity . . . 61
2.19 Antineutrino signal and main backgrounds . . . 64
2.20 Schematic view of the TAO detector . . . 66
2.21 Precision on oscillation parameters with luminosity . . . 67
2.22 SN neutrino spectra . . . 69
2.23 Multi-flavor supernova neutrino luminosity spectra . . . 69
2.24 DNSB signal and background . . . 70
2.25 DNSB sensitivity . . . 71
2.26 Solar neutrino signal and backgrounds . . . 72
2.27 ^{8}B electron spectrum from CC, NC, and ES channels, with backgrounds . . . 73
2.28 Geo-neutrinos expected energy spectrum . . . 74
2.29 Proton decay hit time spectrum . . . 76

3.1 PMT multiplicity for 20 MeV e^{+} . . . 78
3.2 Reactor antineutrino energy spectrum for solar oscillation parameters measurement 79
3.3 Muon track reconstruction in the CD . . . 80
3.4 SPMT system overview . . . 81
3.5 SPMT electronic system schematic for 1 underwater box . . . 82
3.6 Scattered view of SPMT electronic system inside underwater box . . . 83
3.7 Batch of 16 PMTs after potting and cabling . . . 84
3.8 Principle circuit schematic of the SPMT base HV divider . . . 84
3.9 High Voltage Divider PCB . . . 85
3.10 PMT potting design schematic . . . 85
3.11 AXON connector . . . 86
3.12 High Voltage Splitter outline . . . 87
3.13 HV / signal decoupling schematics . . . 88
3.14 High Voltage Splitter board V0.3 . . . 88
3.15 High Voltage Splitter SPE waveforms . . . 89
3.16 ABC V1.2 board . . . 90
3.17 CATIROC ASIC architecture . . . 91
3.18 Preamplifier and slow shaper waveforms . . . 91
3.19 Fast shaper waveform . . . 92
3.20 DAC trigger linearity . . . 93
3.21 Digital timing diagram of PMT pulse processing chain for charge measurement . . 94
3.22 CATIROC trigger efficiency vs threshold . . . 95
3.23 CATIROC charge linearity . . . 96
3.24 CATIROC time resolution . . . 96
3.25 SPE spectrum measurement with CATIROC . . . 97
3.26 CATIROC data capture . . . 98
3.27 CATIROC first frame . . . 98
3.28 CATIROC second frame . . . 99
3.29 CATIROC data capture by the FPGA . . . 99
3.30 GCU board . . . 100
3.31 UWB prototypes . . . 101
3.32 SPMT system thermal study . . . 102
3.33 Positioning of the thermal probes on ABC V1.0 . . . 102
3.34 Radioactivity measurements . . . 104

4.1 Versions of the ABC board . . . 106
4.2 Test firmware architecture in USB mode . . . 107

4.3 CATIROC data capture in USB mode . . . 108
4.4 Firmware data format . . . 109
4.5 Pedestal distribution for ABC V0 . . . 110
4.6 Pedestal measurements comparison : single ASIC data and ABC V0 board . . . 111
4.7 Pedestal RMS comparison ABC V0 vs ABC V1.2 . . . 112
4.8 Charge linearity . . . 112
4.9 Charge calibration process . . . 113
4.10 Saturation of the charge multiplication factor of the preamplifier with its gain . . . 114
4.11 Intercept parameters obtained with the calibration of the PMT test benches . . . 115
4.12 Impact of fixed or free intercept parameter on the slope parameter . . . 116
4.13 Time differences for simultaneous events in several locations of the board . . . 117
4.14 RMS distribution of Δt values . . . 117
4.15 The two types of crosstalk in electronics . . . 118
4.16 Slow shaper curve . . . 119
4.18 Crosstalk matrix . . . 120
4.19 Example of crosstalk estimation . . . 121
4.20 Trigger threshold S-curve for signal injection . . . 122
4.21 Linearity of the trigger threshold . . . 123
4.22 Complete assembled test bench . . . 124
4.23 20 MΩ resistance in the HV Splitter boards . . . 125
4.24 SPE spectrum and fit example for one of the PMTs . . . 126
4.25 Gain measurements for both sets of 16 PMTs . . . 127
4.26 SPE resolution measurements for both sets of 16 PMTs . . . 127
4.27 Mean SPE resolution from the 32 PMTs compared to HZC values . . . 128
4.28 Dark Counting Rate measurements at $\frac{1}{4}$ PE for both sets of 16 PMTs . . . 128
4.29 128 PMTs in a dark room in GXU . . . 129
4.30 PMT High Voltage required for PMT nominal gain for 128 PMTs in GXU . . . 130
4.31 PMT SPE resolution measured for 128 PMTs in GXU . . . 130
4.32 16-channels test bench in NTU . . . 131
4.33 NTU LED test bench schematics . . . 132
4.34 128-channels test bench at LP2i . . . 132
4.35 Pedestal charge measurements on 128 channels . . . 133
4.36 Example of S-curves for one ASIC of the 128-channels test bench . . . 134
4.37 PMT Gain curves . . . 135
4.38 Measured nominal HV comparison with HZC values . . . 136
4.39 Charge spectra for 128 channels . . . 136
4.40 PMT Gain and DCR for 128 channels . . . 137
4.41 SPE charge resolution for 128 channels . . . 137
4.42 PMT signal . . . 138
4.43 Distribution of the SPE resolutions of 26,000 3" PMT . . . 138
4.44 Electron bench setup . . . 139
4.45 Pulse study from the WaveCatcher module . . . 140
4.46 Charge measurements from recorded waveforms . . . 140
4.47 WaveCatcher vs ABC comparison . . . 141
4.48 Recorded waveform with a 3" PMT . . . 142
4.49 Bellamy fits of charge distributions . . . 144
4.50 Gaussian fit of PMT waveform . . . 145
4.51 Rise time as a function of the Gaussian charge . . . 145
4.52 Charge-to-amplitude conversion . . . 146

4.53 Time walk illustration 147
4.54 Signal injection for trigger time measurements 147
4.55 Impact of trigger threshold on the trigger time 148
4.56 Behavior of the trigger time in different channels 148
4.57 Parametrization of the trigger time as a function of the signal amplitude 149
4.58 CATIROC ping pong system 150
4.59 CATIROC DDS system 150
4.60 CATIROC trigger dead time 151
4.61 CATIROC charge acceptance and correction 152

5.1 JUNO software diagram 157
5.2 JUNO optical simulation 157
5.3 Application of CATIROC features on clustered simulation hits - Input 160
5.4 Application of CATIROC features on clustered simulation hits - Output 161
5.5 Summary of the SPMT simulation status 162
5.6 Muon events in the CD 163
5.7 Muon bundle reconstruction 164
5.8 CATIROC response applied to muon events 164
5.9 Collected and reconstructed PEs for ^{12}B events 166
5.10 Impact of electronics on charge reconstruction 167
5.11 N_{PE} per PMT for different vertex positions 168
5.12 Impact of event position on charge reconstruction 168
5.13 CATIROC trigger time distributions 170
5.14 Time spread study 170
5.15 Schematic view of the vertex reconstruction process in the JUNO detector 172
5.16 Optical model accounting for the process of refraction 173
5.17 Reference PDF from 3 MeV electrons 174
5.18 Volume-dependent reference PDFs from 3 MeV electrons 175
5.19 Toy Monte Carlo 176
5.20 Reconstruction distances for 20 MeV positrons at center 177
5.21 Reconstruction distances for 20 MeV positrons at varying positions 178
5.22 Reconstruction distances for 20 MeV positrons for different electronics configurations 180
5.23 Reconstruction distance vs distance-to-center 181

List of Tables

1.1 Fermion properties. 5
1.2 Measurements of the double ratio for various atmospheric neutrino experiments. . 18
1.3 Three-flavor oscillation parameters 28

2.1 Performance requirements for the JUNO 20-inch PMTs. 51
2.2 SPMT acceptance criteria 57
2.3 Calibration sources 62
2.4 Calibration program 63
2.5 Final background budget for the main materials used in the JUNO detector 65
2.6 Efficiencies of antineutrino selection cuts 65
2.7 Neutrino oscillation parameters precision measurements 68

3.1 Global thermal study results with 10 mm aluminum heat sinks 103
3.2 Radioactivity of SPMT components 103
3.3 Contribution of SPMT components to the counting rate 104

4.1 Investigation of the SPE charge and amplitude 144
4.2 Cross-checking investigations of the SPE amplitude 144

5.1 Electronics taken into account in the JUNO simulation of 20 MeV positron events 179

Introduction

Of all the particles described in the current Standard Model of particle physics, the neutrino is the least well-known. In 1907, when the first measured beta decay revealed a continuity in the energetic distribution of electrons, it led physicists to question the otherwise fundamental principle of energy conservation. In 1930, W. Pauli "invented" the neutrino in order to preserve this fundamental principle of physics, which was followed by E. Fermi establishing the theoretical framework of radioactivity in 1934 by including this new particle. It was only two decades later, in 1956, that the first detection of a neutrino was made possible by the experiment of C. Cowan and F. Reines in Savannah-River. A series of discoveries then followed, notably proving the existence of three neutrino flavors (e, μ, τ) and demonstrating their property of oscillation from one flavor state to another. Neutrino physics is still currently one of the main fields of particle physics research.

The Standard Model of particle physics, a robust theoretical model developed in the second half of the twentieth century and repeatedly validated by many different experiments, describes the neutrino as a decaying lepton with three flavor states (ν_e, ν_μ and ν_τ), electrically neutral and interacting only by weak interaction. The observation of neutrino oscillations has led to questioning this model, with the revelation of the non-null mass of neutrinos. An extension to the Standard Model is therefore necessary to understand the origin of this mass. Determining the nature of the neutrinos, Dirac ($\nu \neq \overline{\nu}$) or Majorana ($\nu = \overline{\nu}$), could lead to insight into the mass generation mechanisms of the neutrinos and the associated new physics. To date, neutrino oscillations are the only established evidence for the existence of new physical states that have been found in laboratories. The recent years have seen immense progress in the determination of the neutrino mixing angles and mass splittings. There are several important remaining questions about the properties of neutrinos, including the absolute mass scale, the nature of their mass term (Dirac vs Majorana) and the presence of CP-violation in the lepton sector. The ultimate goal, however, remains to unveil the mechanism of neutrino mass generation, and to identify the new physical states that are involved in it. These could provide the key to understanding other unsolved puzzles in both cosmology and particle physics. Investigating these two topics (mass and nature) can have important consequences on both on the intrinsic understanding of the fundamental properties of the neutrino as well as on a much larger scale, potentially explaining the matter-antimatter asymmetry of the universe during leptogenesis.

Precisely measuring the neutrino oscillation parameters and answering the question about the ordering of the neutrino mass states is the objective of the Jiangmen Underground Neutrino Observatory (JUNO) experiment, a multi-purpose reactor neutrino experiment formed in 2013. It will be located in Jiangmen, China, at a baseline of 53 km from the Taishan and Yangjiang reactor complexes (26.6 GW_{th} total thermal power), and made up of a spherical 20 kton liquid scintillator-based detector. Reactor antineutrinos will be detected by the $\overline{\nu}_e + p \rightarrow e^+ + n$ Inverse Beta Decay (IBD) reaction, creating a prompt and delayed signal, and about 60 IBD events are planned to be detected by JUNO, per day, for the duration of its run. Two systems of photodetection have

been developed to achieve the highest coverage possible of the 35 m diameter spherical detector. A system of ∼17500 20-inch PMTs called the Large PMT (LPMT) system will collect about 1350 photoelectrons per MeV of deposited energy and will allow for a 3% energy resolution at 1 MeV, while a second system of ∼25600 3-inch PMTs, called the Small PMT (SPMT) system, was designed to serve as a complementary array of photodetectors to the LPMT system. The work presented in this thesis will focus on the SPMT system of the JUNO experiment, from its many components and electronics to the impact of its electronic performances on physical measurements. The manuscript will be structured as follows.

The first chapter delves into the theoretical aspects of neutrino physics, presenting the neutrino in and outside the framework of the Standard Model, exposing the properties of the neutrino that still need investigating, discussing the theory behind neutrino oscillations as well as the experimental observations of this phenomenon, giving the current status on the precision measurements of neutrino oscillation parameters, presenting the future experiments in neutrino physics and their potential and, finally, discussing JUNO's approach to identifying the Neutrino Mass Ordering.

The second chapter details the JUNO detector in all its systems, subsystems and components, for a global view of the experiment, as well as expands on the broader physics program of JUNO.

The third chapter delves into the SPMT system of the JUNO experiment, presenting the motivations for the development of this system, and giving a detailed description of the entire system from the PMTs to the digitization of the signals, with a focus on the electronics and the technical developments.

The fourth chapter addresses the precise studies conducted on the performances of the ABC front-end board, including studies on pedestal measurements, charge linearity and calibration, time resolution, crosstalk, test-benches combining all the SPMT electronics to date, or the processing of a PMT signal within the ABC board with precise parametrizations of CATIROC features such as the trigger time and time walk, the deadtimes and the charge acceptance.

Finally, the fifth chapter addresses the implementation of these parameters in the JUNO simulation as well as the impact of the response of the SPMT system on physical studies involving the charge and time information of simulated events, by investigating the degradation of charge and vertex reconstruction methods with the addition of the electronics during event simulations.

Chapter 1

Neutrino physics and oscillations

Contents

1.1 Neutrino physics **3**
1.1.1 Introduction 3
1.1.2 The neutrino in the Standard Model of particle physics 4
1.1.3 Physics beyond the Standard Model 7
1.1.3.1 Neutrino mass and Majorana nature of the neutrino 8
1.1.3.2 Probing the nature of the neutrino with double beta decays . . . 10
1.2 Neutrino oscillations **13**
1.2.1 Introduction : concept of neutrino oscillations 13
1.2.2 Evidence for oscillations 15
1.2.3 Theory of neutrino oscillations 19
1.2.4 Neutrino Mass Ordering 23
1.2.5 Matter effects 24
1.2.6 CP violation and Dirac phase δ_{CP} 26
1.2.7 Current values of oscillation parameters 27
1.3 Neutrino Mass Ordering determination **27**
1.3.1 Motivations for physics / Consequences of measuring the Mass Ordering . 27
1.3.2 Current experiments and status 29
1.3.3 Future experiments using matter-modified oscillations 32
1.3.3.1 Using atmospheric neutrinos - Hyper-K / ORCA 32
1.3.3.2 Using accelerator neutrinos - DUNE 35
1.3.4 Investigating the NMO using vacuum oscillations with JUNO 36

1.1 Neutrino physics

1.1.1 Introduction

Historically, neutrino physics has been closely related to radioactivity. In 1896, Henry Becquerel accidentally discovered the phenomenon of radioactivity when conducting research on the fluorescence of uranium salts. Two years later, Marie Curie confirmed the phenomenon and discovered two new radioactive chemical elements, Polonium and Radium. From these studies, three types of radioactivity were identified : alpha, beta and gamma decays, with various measurements carried out on the alpha and gamma decays showing a discrete energy spectrum. In 1914, J. Chadwick measured the energy spectrum of the β decay and showed its continuity [1], implying that, contrarily to the γ and α radiations, the energy of the β particles produced in β decays was not constant. In the case of a two-body decay, with the electron being the only particle emitted, this observed continuous spectrum would contradict the conservation of energy, one of the fundamental

principles of physics. W. Pauli, in 1930, proposed the existence of a never-before-detected particle emitted with the electron in order to try to keep this principle as a fundamental of physics, naming it "neutron" at first. He made the assumption that this particle must have a very low cross section, a very low mass, have a neutral charge and have a half-integer spin. From this postulate, and after the discovery of the neutron by Chadwick [2] (baryon composite particle) in 1933, E. Fermi formalized the theory around β radioactivity and laid the groundwork for the theory of weak interaction. β decay is thus written as :

$$ {}^{A}_{Z}X \rightarrow {}^{A}_{Z-1}Y + e^{-} + \overline{\nu}_e \tag{1.1} $$

where ν is the Pauli neutron, renamed "neutrino" to remove any confusion with the baryon. This new theory made the reproduction of the measured β emission spectrum possible, at the cost of raising a substantial challenge in the form of the detection of the neutrino.
In 1934, H. Bethe and R. Peierls [3] computed the cross-section of the neutrino and concluded that, with such a small cross-section, it would never be detected. It was not until 1956 that C. Cowan and F. Reines [4] discovered it experimentally through the inverse β^+ decay reaction $\overline{\nu}_e + p \rightarrow e^+ + n$ using reactor neutrinos. In this reaction, an antineutrino is captured by a proton, leading to the emission of a positron and a neutron. The annihilation of the positron with an electron will provide a prompt signal by detecting the two coincident 511 keV gamma rays. The neutron, after a short delay of a few tens of microseconds, will be captured (in this case by Cadmium) and cause the emission of several delayed coincidental gamma rays. The detection of the positron and of these gamma rays allowed C. Cowan and F. Reines to publish their discovery of the neutrino in 1956, by comparing the data recorded with the reactor ON and OFF.
In 1936, the discovery within cosmic rays of the muon particle [5], a negatively charged fermion heavier than the electron and with similar properties, suggests the existence of a second family of neutrinos. In 1961, Lederman, Schwartz and Steinberger confirmed the existence of the muon neutrino [6]. Tau, the third particle of the lepton family, was discovered in 1975 at the Stanford Linear Accelerator Center (SLAC). As expected, a new neutrino is subsequently discovered, the tau neutrino, observed in 2000 in the Direct Observation of the NeUtrino Tau (DONUT) experiment [7]. The precise measurement of the width of the decay peak of the Z^0 boson, carried out in the former LEP collider at CERN, allowed for the confirmation of the existence of three families of neutrinos, as the experimental data lined up with the theoretical predictions for three families of neutrinos. This measurement, performed with ALEPH, DELPHI, L3 and OPAL [8], is illustrated in Figure 1.1, and gave a number of neutrinos $N_\nu = 2.92 \ \pm 0.05$ in 2010. In 2018, this number was estimated at $N_\nu = 2.9840 \ \pm 0.0082$ [9].

1.1.2 The neutrino in the Standard Model of particle physics

Developed in the 1970s, the Standard Model of particle physics is a theoretical formalism seeking to describe the elementary constituents and fundamental interactions of the Universe. It is based on group theory and gauge symmetry. In this model, matter is made up of fermions and the interactions are conveyed by gauge bosons. The symmetry group $SU(3)_C \times SU(2)_L \times U(1)_Y$ describes the strong, weak and electromagnetic interactions.

Fermions

Fermions are half-integer spin particles obeying the Fermi-Dirac statistics and the Pauli exclusion principle, and are the elementary constituents of matter. There are 12 fermions, divided into two categories detailed in Table 1.1 :

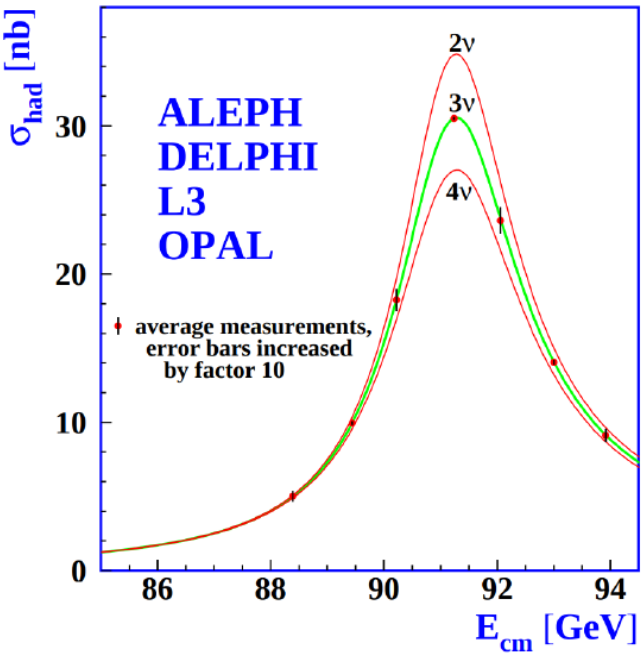

Figure 1.1: Comparison of the measured Z^0 width with the ALEPH, DELPHI, L3 and OPAL experiments and of the theoretical predictions for 2, 3 and 4 families of light neutrinos.

- Quarks : 6 quarks, sensitive to the four fundamental interactions. They have a fractional electric charge worth either $+\frac{2}{3}$ or $-\frac{1}{3}$ and exist only in pairs or trios. An anti-quark/quark pair forms a meson, while three associated quarks form a baryon. All mesons and baryons form the hadron family.

- Leptons : 6 leptons, sensitive to the weak interaction and to the electromagnetic interaction for the charged leptons. Three are electrically charged (e, μ, τ) and have a charge of -1, while three are electrically neutral $(\nu_e, \nu_\mu, \nu_\tau)$.

Fermions are classified into three generations defined by an increasing mass towards the higher generations. The first generation is the lightest and constitutes the stable matter of the Universe. The second and third generation are unstable and tend to disintegrate towards the lower generations. Each fermion has a corresponding antiparticle obtained by charge conjugation and parity symmetry (CP). Antiparticles are of equal mass and spin, but of opposite electric charge, flavor, lepton or baryon number.

Generation	Leptons			Quarks		
	Name	Mass $[MeV/c^2]$	Charge	Name	Mass $[MeV/c^2]$	Charge
1st	e^-	0.511	-1	up	2.2	$+2/3$
	ν_e	$< 1.1 \times 10^{-6}$	0	down	4.7	$-1/3$
2nd	μ	105.7	-1	charm	1.275	$+2/3$
	ν_μ	< 0.19	0	strange	95	$-1/3$
3rd	τ	1777	-1	top	173	$+2/3$
	ν_τ	< 18.2	0	bottom	4.18	$-1/3$

Table 1.1: Fermion properties. [10]

Fundamental interactions and bosons

Bosons are particles of integer spin obeying the Bose-Einstein statistics. Not being subject to Pauli's exclusion principle, several bosons can simultaneously occupy the same quantum state. Each boson is the mediator of one of the four fundamental interactions :

- **The strong interaction**: Based on the SU (3) group, it is an attractive force which only acts on quarks and allows the formation and cohesion of hadrons. It is conveyed by the exchange of 8 gluons coupling to the color charge of the quarks (red, green and blue). The gluon has a null mass and carries a color charge. The range of this interaction is of the order of 10^{-15} m.

- **The weak interaction**: Based on the SU (2) group, this is the interaction responsible for the change in flavor of quarks and leptons and thus for β radioactivity. This interaction applies to all particles. It is carried by the $W^{\pm}$ bosons (80.4 GeV) for the weak interaction involving charged currents, and by the Z^0 boson (91.2 GeV) for the weak interaction by neutral current. Due to the high mass of the $W^{\pm}$ and Z^0 bosons, the range of this interaction is of the order of 10^{-17} m.

- **The electromagnetic interaction**: Based on the U (1) group, it can be attractive or repulsive and applies to charged particles. Its mediator is the photon, which is electrically neutral and has a null mass. The range of this interaction is infinite.

- **The gravitational interaction**: This is an attractive force of extremely low intensity at the particle scale compared to the other three interactions. Gravitation is described by general relativity, but no quantum description is present in the Standard Model. Theories such as string theory, or loop quantum gravity [11] attempt to describe it on the scale of particle physics.

Electroweak theory and Higgs mechanism

During the 60s, the Glashow-Salam-Weinberg model made it possible to unify the weak interaction and the electromagnetic interaction in a single interaction: the electroweak interaction [12–14]. This model is built on a local gauge invariant theory in the gauge symmetry group SU(2)$\bigotimes$U(1), invariant under weak isospin transformation I^W and weak hypercharge $Y = 2(Q - I^W)$, with Q the electric charge. In this model, the vector bosons of the weak interaction have null masses. This hypothesis is contradicted by experimentation. In order to explain the mass of the $W^{\pm}$ and Z^0 bosons, the Higgs mechanism was introduced to allow the spontaneous breaking of the electroweak symmetry. This mechanism consists in introducing a particular scalar field in order to shift the ground state with an expected mean value of the non-zero vacuum. Globally, this process is at the origin of the mass of all fermions. In 2012, the Higgs boson ($\sim$125 GeV) was discovered at the LHC [15], thus confirming the Higgs mechanism which had been theorized independently in three articles in 1964 by Brout and Englert, Hagen Guralnik and Kibble, and Higgs [16–18].

Dirac equation

The Dirac equation describes free particles of spin $\frac{1}{2}$, such as fermions, and is based on the Dirac quadri-spinor ψ :

$$(i\gamma_\mu \delta^\mu - m)\psi = 0 \tag{1.2}$$

with m the mass of the particle at rest, δ^μ the quadrivector :

$$\delta^\mu = \begin{pmatrix} \frac{\delta}{\delta t} \\ \frac{\delta}{\delta x} \\ \frac{\delta}{\delta y} \\ \frac{\delta}{\delta z} \end{pmatrix}$$

and γ_μ the Dirac matrices defined by :

$$\gamma_0 = \begin{pmatrix} I & 0 \\ 0 & -I \end{pmatrix} \; and \; \gamma_i = \begin{pmatrix} 0 & \sigma_i \\ -\sigma_i & 0 \end{pmatrix} \tag{1.3}$$

$$\text{with } \sigma_1 = \begin{pmatrix} 0 & 1 \\ 1 & 0 \end{pmatrix}, \sigma_2 = \begin{pmatrix} 0 & -i \\ i & 0 \end{pmatrix} \text{ and } \sigma_3 = \begin{pmatrix} 1 & 0 \\ 0 & -1 \end{pmatrix}$$

Two projectors, P_L and P_R, allow the extraction of the left and right components of the Dirac bispinor :

$$P_L = \frac{1}{2}(1 - \gamma_5) \; and \; P_R = \frac{1}{2}(1 + \gamma_5) \tag{1.4}$$

$$\text{with } P_L.P_R = 0 \text{ and } \gamma_5 = \begin{pmatrix} 0 & I \\ I & 0 \end{pmatrix}$$

ψ can thus be written as $\psi = \psi_L + \psi_R = P_L\psi + P_R\psi$.
A chiral field is then the superposition of left and right helicities, which can be written as in Equation 1.5, with $\psi_{-1/2}$ the left helicity, $\psi_{+1/2}$ the right helicity, θ a term evolving in $(\frac{m}{E})$, m the mass of the particle at rest and E its energy. This equation shows that the helicity and chirality are equivalent when the mass of the particle is zero.

$$\psi_L = \psi_{-1/2} + \theta(\frac{m}{E})\psi_{+1/2} \; and \; \psi_R = \psi_{+1/2} + \theta(\frac{m}{E})\psi_{-1/2} \tag{1.5}$$

Dirac's equation (Equation 1.2) admits four solutions, corresponding to four independent states : two of positive energy and two of negative energy. They are defined by the two possible spin states (+1/2 and -1/2) and their symmetry by charge conjugation, generating particles (positive energy) and anti-particles (negative energy).

The neutrino in the Standard Model

In 1956, T.D. Lee and C.N. Yang proposed the non-conservation of parity in weak interaction to explain the "Theta Tau puzzle" [19]. The following year, this is verified in C.S. Wu's experiment [20], based on the angular distribution of the electrons emitted by the β decay of the ^{60}Co. This parity violation is maximal through the weak interaction and results in only neutrinos of left helicity (projection of the spin in the direction opposite to the movement) and antineutrinos of right helicity (projection of the spin in the same direction as motion) being able to interact, implying that the neutrino has a null mass.
In the minimal Standard Model, the neutrino is therefore a Dirac particle of zero mass, giving only two solutions to the Dirac equation : the neutrino of left chirality and the antineutrino of right chirality. The neutrino and the antineutrino are two separate particles and there is no possible transition between the two. Thus, the lepton number L is conserved, as electrically charged leptons cannot make a transition due to the conservation of charge.

1.1.3 Physics beyond the Standard Model

The Standard Model, detailed in section 1.1.2, has been demonstrated to be robust and predictive, as it has anticipated the discovery of particles or the values of experimental measurements. Devi-

ations from the Standard Model are extremely small and its predicted discoveries such as the Z or W bosons, the tau neutrino or even the Higgs boson (the last missing part of the Standard Model) make it a solid model for describing the interactions and fundamental constituents of matter. However, this model is not perfect, and does not include all observations from physics. It has at least 25 free parameters, not predicted by the model but measured by experiments, which is often considered as a degree of freedom that is too high for a "fundamental" model. The Standard Model is also unable to answer some fundamental question in Physics, such as why there are precisely three generations of fermions, how to explain the matter-antimatter asymmetry in the Universe, how to explain the baryogenesis and leptogenesis, how to explain the conservation of the quantum numbers B, L and B-L, how to explain symmetry violations such as CP violation (which could explain the matter-antimatter asymmetry), or what the origins and nature of dark matter and dark energy are.

1.1.3.1 Neutrino mass and Majorana nature of the neutrino

The null mass of neutrinos in the minimal Standard Model results from the maximum parity violation by the weak interaction. However, as will be described in section 1.2, experiments have highlighted oscillation phenomena between the flavors of neutrinos, implying a mixture of several mass states, and therefore a non-zero mass of the neutrinos. To allow for massive neutrinos while maintaining the parity violation, two mechanisms have been proposed, consisting respectively of the addition of straight neutrinos and sterile antineutrinos to the Weyl spinor and of the hypothesis of a Majorana neutrino.

Dirac mass term The Standard Model defines the neutrino by a Weyl spinor including two fields corresponding to a left chirality neutrino (ψ_L) and a right chirality antineutrino ($\overline{\psi_R}$). To allow for a massive neutrino, it is necessary to reintroduce a field corresponding to a right neutrino (ψ_R) and a left antineutrino ($\overline{\psi_L}$). In order to respect the experimental observations, these neutrinos must not interact with matter by weak interaction, and are thus considered "sterile". To allow for such characteristics, the spinor is defined as :

$$\overline{\psi_L}\psi_L = \psi_L^\dagger\gamma^0\psi_L = \psi P_L\gamma^0 P_L\psi = \psi\gamma^0 P_R P_L\psi = 0 \tag{1.6}$$

$$\overline{\psi_R}\psi_R = \psi\gamma^0 P_L P_R\psi = 0 \tag{1.7}$$

The Lagrangian can then be written as :

$$L^D_{mass} = \overline{\psi}m_D\psi = m_D\overline{(\psi_L + \psi_R)}(\psi_L + \psi_R) = m_D(\overline{\psi_L}\psi_R + \overline{\psi_R}\psi_L) \tag{1.8}$$

where m_D is defined as the Dirac mass term. This solution, while simple and minimal in terms of the modifications brought to the Standard Model, nevertheless has no intrinsic reason for being favored. It does not contribute any new explanations on the properties of the neutrino or new predictions.

Majorana mass term This mechanism helps explain the mass of neutrinos and their potential Majorana nature. A Majorana particle is a particle identical to its own antiparticle [21]. The neutrino being the only fermion with a neutral charge, it is the only candidate for being a Majorana particle. This hypothesis was formalized by Ettore Majorana and offers a representation with two degrees of freedom for the particle: ψ_L and its charge conjugate $\psi_L \xrightarrow{C} (\psi_L)^c = \psi_R^c$. Its right field is also defined by $\psi_R \xrightarrow{C} (\psi_R)^c = \psi_L^c$ and, although it does not interact experimentally, it will

generate the expression of the mass by straight current.
In this theoretical model, the charge conjugate of the left neutrino is a right antineutrino and the charge conjugate of the right antineutrino is the left neutrino. In a more general manner, the left and right fields of Majorana can be written :

$$\psi^M = \psi_{L/R} + (\psi_{L/R})^c \tag{1.9}$$

This field is a solution of the Dirac equation and is an eigenstate of the operator C with an eigenvalue of $+1$. This field is used to generate two Majorana mass terms:

$$\begin{aligned} -L^M_{mass_{L/R}} &= \overline{\psi^M} m_{L/R} \psi^M && (1.10)\\ &= m_{L/R}\overline{(\psi_{L/R} + (\psi_{L/R})^c)}(\psi_{L/R} + (\psi_{L/R})^c) && (1.11)\\ &= m_{L/R}(\overline{(\psi_{L/R})^c}\psi_{L/R} + \overline{\psi_{L/R}}(\psi_{L/R})^c) && (1.12)\\ &= m_{L/R}\overline{(\psi_{L/R})^c}\psi_{L/R} + hc && (1.13) \end{aligned}$$

where hc is the Hermitian conjugate. Unlike the Dirac mass term m_D, the Majorana mass terms $m_{L/R}$ are no longer invariant under the U (1) gauge symmetry, which implies that the lepton number is no longer preserved.

Majorana-Dirac general mass term Knowing that the neutrino can be a Dirac particle, that the right neutrino and the left antineutrino can exist without interacting, and that the Majorana fields are also a possible solution of the Dirac equations, none of the previously presented mass terms can be definitely excluded from the Lagrangian. A more general mass term corresponding to the sum of the various terms in the Lagrangian therefore needs to defined. It can be written as :

$$-L^{D+M}_{mass} = m_D\overline{\psi_R}\psi_L + \frac{1}{2}(m_L\overline{\psi^c_L}\psi_L + m_R\overline{\psi^c_R}\psi_R) + hc \tag{1.14}$$

where $\frac{1}{2}$ is a normalization factor taking into account the fact that ψ^c_L and $\overline{\psi_L}$ are not independent. The general mass term can be rearranged as :

$$-L^{D+M}_{mass} = \frac{1}{2}\overline{\Psi_L}\begin{pmatrix} m_L & m_D \\ m_D & m_R \end{pmatrix}\Psi_R + hc \tag{1.15}$$

with $\Psi_L = \begin{pmatrix} \psi_L \\ \psi^c_L \end{pmatrix}$ and $\Psi_R = \begin{pmatrix} \psi_R \\ \psi^c_R \end{pmatrix}$.
The eigenvalues of the Dirac and Majorana masses matrix allow for the determination of two mass states m_- and m_+ :

$$m_\pm = \frac{1}{2}(m_L + m_R \pm \sqrt{(m_L - m_R)^2 + 4m_D^2}) \tag{1.16}$$

$m_{L/R} = 0$ results in a pure Dirac particle, with $m_\pm = m_D$. By analogy, $m_D = 0$ results in a pure Majorana particle, with $m_\pm = m_{L/R}$.

See-Saw mechanism Although a pure Majorana particle can, like a pure Dirac neutrino, give a particle of non-zero mass violating parity (with $m_+ \neq 0$ and $m_- = 0$), such a solution is not particularly favored, and does not make it possible to explain the mass scale of the neutrino with respect to the other fundamental particles (~6 orders of magnitude separate the mass of the

electron neutrino from the electron). The See-Saw mechanism was theorized and implemented in order to explain this observation in a more natural way. It is based on two assumptions, the first being that the experiment does not allow us to demonstrate the right neutrino interaction because m_R is very large compared to m_L and m_D, and the second being that there is no left field (the Standard Model does not allow it), which implies $m_L = 0$. These postulates give a neutrino mass ordering $m_R \gg m_D \gg m_L$, resulting in new values and mass eigenstates from Equation 1.16 [22] :

$$m_+ \approx m_R \; and \; m_- = \frac{m_D^2}{m_R} \tag{1.17}$$

This entails associated eigenstates :

$$\Psi_+ = (\psi_R + \psi_R^c) + \frac{m_D}{m_R}(\psi_L + \psi_L^c) \tag{1.18}$$

$$\Psi_- = (\psi_L + \psi_L^c) - \frac{m_D}{m_R}(\psi_R + \psi_R^c) \tag{1.19}$$

This yields a neutrino defined by the field Ψ_+ mainly composed of a state of right chirality and having a very high mass (rare interaction), and a neutrino defined by the field Ψ_- mainly composed of a state of left chirality and having a very low mass. The mass of the light neutrino is especially small when the mass of the heavy neutrino is especially large, since $m_- \propto \frac{1}{m_+}$. Hence the name of the See-Saw mechanism.
This mechanism makes it possible to obtain a very low mass of the neutrino while keeping a reasonable Dirac mass (on the scale of the other fermions), because this one is counterbalanced by the high mass of the right neutrino. If the right neutrino has a high mass of the order of 10^{15} GeV, this makes it possible to provide an elegant solution to the asymmetry between matter and antimatter in the appearance of Majorana neutrinos during leptogenesis [23].

1.1.3.2 Probing the nature of the neutrino with double beta decays

Double beta decay with emission of neutrinos is a weak second order decay process corresponding to a simple double beta decay in the same nucleus. When there is conservation of the lepton number, the two electrons emitted are accompanied by the emission of two antineutrinos. This is the double beta decay with neutrino emission, $2\nu\beta\beta$, and is allowed in the Standard Model. The half-life of $2\nu\beta\beta$ ranges from 10^{18} to 10^{22} years and even today is one of the rarest decay processes observed experimentally (the rarest decay process having been observed experimentally being the 2νECEC two-neutrino double electron capture in ^{124}Xe with XENON1T at 1.8×10^{22} years [24]).
When considering that the conservation of the lepton number can be violated, the scenario of a double beta decay without neutrino emission, $0\nu\beta\beta$, becomes possible. In this case, the two electrons are emitted alone, without any neutrinos. The observation of the $0\nu\beta\beta$ would make it possible to remove the ambiguity on the nature of the neutrino (Majorana or Dirac) as well as to determine the effective mass scale of the Majorana neutrino. Neutrino emission-free double beta decay is another measurement technique for accessing the absolute mass of neutrinos, as this decay can only exist if the neutrino is massive and of Majorana.

Double beta decay with neutrino emission ($2\nu\beta\beta$) In 1935, Goeppert-Mayer [25] first formulates double beta decay as a second order process. This was observed indirectly by Till Kirsten and Oliver Schaeffer in 1968 thanks to isotopic measurements of Xenon contained in meteorites [26]. In 1987, Michael Moe, using a drift chamber (TPC: Time Projection Chamber), directly

demonstrates the $2\nu\beta\beta$ decay of the ^{82}Se. This decay involves the transformation of two neutrons into two protons with emission of two electrons and two electronic antineutrinos (Figure 1.2) :

$$^{A}_{Z}X \rightarrow^{A}_{Z+2} Y + 2e^{-} + 2\overline{\nu}_{e} \tag{1.20}$$

Neutrinos weakly interact with matter. Thus, only the two electrons are detected, giving a continuous energy spectrum with a maximum at the transition energy $Q_{\beta\beta}$. This is illustrated in green in Figure 1.3b. This decay is only allowed in nuclei with a pair-pair configuration, for which a simple beta decay is energetically impossible or very strongly suppressed by a too great difference in angular momentum (notably in the case of ^{48}Ca).

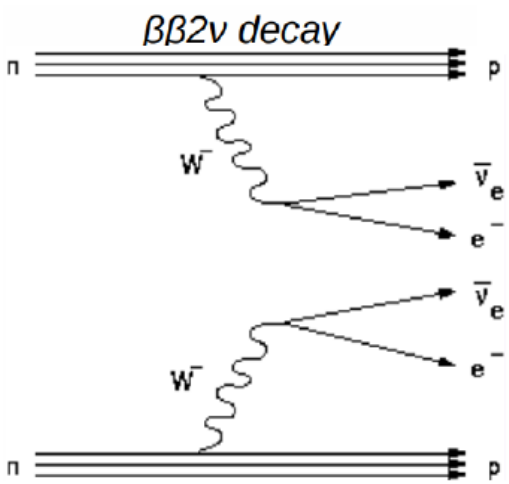

Figure 1.2: Feynman diagram for two neutrinos double beta decay processes.

The half-life of $2\nu\beta\beta$ is written as :

$$(T^{2\nu}_{1/2})^{-1} = G^{2\nu}(Q_{\beta\beta}, Z) \left| \frac{M^{2\nu}}{m_e} \right|^2 \tag{1.21}$$

with $G^{2\nu}(Q_{\beta\beta}, Z)$ the four-particle phase space factor, $M^{2\nu}$ the nuclear matrix element for the $2\nu\beta\beta$ process, and m_e the mass of the electron.
The study of the $2\nu\beta\beta$ process is very important. Electrons with energies close to $Q_{\beta\beta}$ not only constitute an irreducible background noise for the $0\nu\beta\beta$ process, detailed in the following section, studying the $2\nu\beta\beta$ decay also helps improve the constraints on the computations of the nuclear matrix elements used for the $0\nu\beta\beta$ decay.

Neutrinoless double beta decay ($0\nu\beta\beta$) The $0\nu\beta\beta$ decay process was introduced by W.H. Furry in 1939 as an application of Majorana's theory published in 1937. This decay process produces two electrons and no neutrinos, as illustrated in Figure 1.3a.

$$^{A}_{Z}X \rightarrow^{A}_{Z+2} Y + 2e^{-} \tag{1.22}$$

This process does not conserve the lepton number (ΔL=2) and it is therefore prohibited within the Standard Model, with the non-conservation of the lepton number being due to the supposed Majorana nature of the neutrino.
The $0\nu\beta\beta$ decay is thus considered to be the clearest and most direct physical phenomenon for

exploring the nature of the neutrino. Theoretically, the energy signature of the two electrons would be a monoenergetic peak at the energy $Q_{\beta\beta}$ of the transition, widened by the energy resolution of the detector. This is illustrated in red in Figure 1.3b. In the case of a Majorana neutrino, the energy distribution of the two electrons is the combination of a continuous energy spectrum due to the $2\nu\beta\beta$ decay and a monoenergetic peak due to the $0\nu\beta\beta$ decay (Figure 1.3b) centered at the energy $Q_{\beta\beta}$.

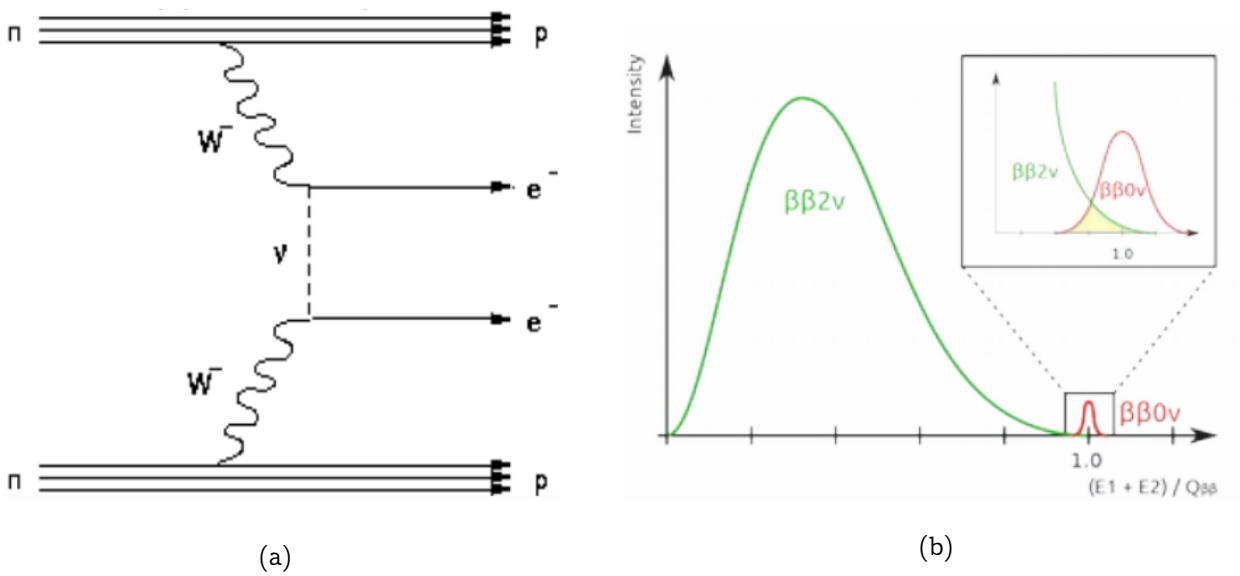

Figure 1.3: (a) Feynman diagram for neutrinoless double beta decay processes. (b) Energy spectrum of the $2\nu\beta\beta$ decay in green, and of the $0\nu\beta\beta$ in red.

Several mechanisms leading to the $0\nu\beta\beta$ decay are possible, but as demonstrated by Schlechter and Valle [27], in all cases, the observation of the $0\nu\beta\beta$ implies the presence of a Majorana and a massive neutrino. The most simple mechanism for describing the $0\nu\beta\beta$ decay, which only involves processes allowed by the Standard Model (apart from the violation of the lepton number) is the mass mechanism. The neutrino emitted at the first vertex interacts in the second after a change of reference (Lorentz transformation) allowing the reversal of helicity required for an interaction by left current of the vector-axial type (V-A). To allow this change in helicity as well as the violation of the lepton number, the neutrino must be massive and of a Majorana nature. Since the virtual neutrino is massive, its propagator introduces a mass term in the transition probability. The half-life of the process is therefore related to the effective mass of the Majorana neutrino $m_{\beta\beta}$, to the phase space factor $G_{0\nu}$ and to the nuclear matrix element $M_{0\nu}$ of the considered isotope :

$$(T^{0\nu}_{1/2})^{-1} = G^{0\nu}(Q_{\beta\beta}, Z)|M^{0\nu}|^2 \left|\frac{m_{\beta\beta}}{m_e}\right|^2 \tag{1.23}$$

with the effective mass of the neutrino $m_{\beta\beta}$ depending on the mass of each neutrino weighted by the square of the coefficients of the PMNS mixing matrix containing the Majorana phases (section 1.2.3, Equation 1.47) :

$$m_{\beta\beta} = \sum_{i=1}^{3} U_{ei}^2 m_i \tag{1.24}$$

The errors on the calculation of this matrix element, due to the approximation models used, dominate the total error on the ratio between the half-life of the decay $0\nu\beta\beta$ and the mass of the

neutrino. This results in a neutrino mass interval for the measured half-life limit.
The effective mass of the neutrino as a function of the mass of the lightest neutrino is an efficient representation, as shown in Figure 1.4, in which three different regions can be observed [28]. The region for which $m_3 < m_1 < m_2$ (blue), the region for which $m_1 < m_2 < m_3$ (red) and a completely degenerated region, when the mass of the lightest neutrino is greater than 3×10^{-2} eV, in which one can no longer distinguish the ordering of the neutrino masses (section 1.2.4).

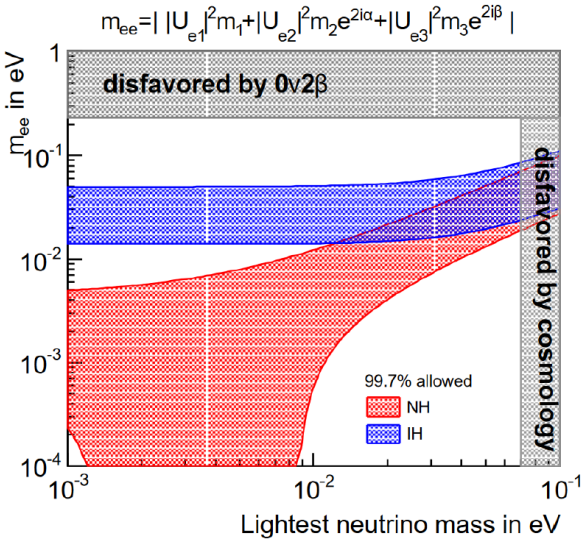

Figure 1.4: Effective mass of the Majorana light neutrino $m_{\beta\beta}$ measured with the $0\nu\beta\beta$ process as a function of the mass of the lightest neutrino. Based on the value of $m_{\beta\beta}$, it is possible to determine the spectrum corresponding to the correct ordering of the neutrino masses (section 1.2.4). The current limits on $m_{\beta\beta}$ are at $\sim$ 200 meV, and future experiments will probe the inverse ordering ($m_3 < m_1 < m_2$, blue spectrum). [28]

1.2 Neutrino oscillations

1.2.1 Introduction : concept of neutrino oscillations

It was discussed in section 1.1.2 that a neutrino is a flavour eigenstate that is either produced in a weak interaction with a charged lepton of electron, muon or tau flavour or absorbed to give such a particle. The flavour state that is generated with an electron/muon/tau is the electron/muon/tau neutrino. Alongside these different flavour eigenstates (states with definite flavour), the neutrinos also have several mass eigenstates (states which have definite mass). However, it is possible that the flavour eigenstates are not identical to these mass eigenstates.
The mass states are labelled as ν_1, ν_2 and ν_3 and have different, but close, masses. Every time an electron is created in a weak interaction, for example, one of these mass eigenstates is also created, with different probabilities. Experimentally, the neutrino masses are too small to be resolved. Not knowing which mass eigenstate was created, the resulting particle at the weak interaction vertex is considered a coherent superposition of the ν_i mass states. It is this coherent superposition that is called the electron neutrino :

$$|\nu_e >= U_{e1}|\nu_1 > +U_{e2}|\nu_2 > +U_{e3}|\nu_3 > \tag{1.25}$$

with U_{ei} elements of a unitary mixing matrix.

Considering a neutrino generated at a source and travelling in vacuum towards a detector, this neutrino will have a definite flavour, but will be produced as a linear combination of states of definite mass. These mass states will propagate out of the source towards the detector, and if they have different masses, then the phase between the mass states will change with the distance from the source (see section 1.2.3). At the detector, the mass states will have different relative phases than they had at the source, and a different neutrino flavour state could be detected. In the case of two-flavour neutrino oscillations, we will demonstrate in section 1.2.3 that the probability of detecting a flavour state ν_β at the detector while a flavour state ν_α was emitted at the source is :

$$P_{\nu_\alpha \to \nu_\beta} = sin^2(2\theta) sin^2(1.27\Delta m^2[eV^2]\frac{L[km]}{E[GeV]}) \tag{1.26}$$

This equation is called an oscillation probability, and involves several key parameters.

The mixing angle θ defines how different the flavour states are from the mass states, with $\theta = 0$ implying that the flavour states are identical to the mass states. This means that a ν_α state will propagate from the source to a detector as a ν_α with definite momentum, and never change flavours. If $\theta = \frac{\pi}{4}$, the oscillations are said to be maximal, and at some point along the path between the source and the detector, all of the ν_α states will have oscillated to ν_β states.

The mass squared difference Δm^2 is the difference of the squared masses of each of the mass states. In the case of two-flavour neutrino oscillations, $\Delta m^2 = m_2^2 - m_1^2$. For neutrino oscillations to occur, Δm^2 needs to be non-zero, and so at least one of the mass states must be non-zero. This has large implications in physics, as, for oscillations to happen, the neutrino must have a mass. The masses of the mass states must also be different. Considering the mass states as plane waves (see section 1.2.3), the masses control the relative phase of the two mass wave functions (two-flavour oscillations case). If both masses are equal, the mass states will never get out of phase and, at the detector, the same linear combination of mass states as the one generated at the source will be measured. No flavour change will have occurred. This also gives an insight into the limitations of neutrino oscillation experiments : detailed information can be gained on the difference between the mass values, but the absolute masses of the mass states cannot be probed.

The ratio L/E is the parameter that experiments can control. L is the distance between the source and the detector, and E is the energy of the neutrino. To investigate a given Δm^2 value, an experiment should be built to be maximally sensitive to the oscillation probability. This means approaching a $1.27\Delta m^2 \frac{L}{E}$ value of $\frac{\pi}{2}$. To this end, and depending on the physics scenario, either the neutrino beam energy (E) or the baseline (L) can be adjusted, or both. An ideal case would see L maximized and E minimized, but several experimental constraints must be taken into account. If the L/E ratio is fixed by nature, then experiments can only probe a certain range of (Δm^2, θ) combinations, as other choices for the values of these parameters will yield too small an oscillation probability for observation to be feasible.

In the following sections, we will address the different sources of evidence for neutrino oscillations that were experimentally collected, as well as delve into the theoretical aspect of neutrino oscillations.

1.2.2 Evidence for oscillations

Solar neutrinos

Nuclear reactions in the core of the Sun produce a pure flux of ν_e of $\sim 6 \times 10^{10}$ neutrino.cm^{-2}.s^{-1}, which is incident on earth with an energy ranging from a hundred keV to ~10 MeV. The Standard Solar Model [29] predicts that most of the flux comes from pp neutrinos with energies below 0.4 MeV. Among the experiments designed to measure this solar neutrino flux, only Gallium experiments are sensitive to this component, with the Chlorine experiment not being sensitive under the ^{7}Be line and experiments such as Super-Kamiokande or SNO only being able to view the ^{8}B and hep neutrinos as they have too high a threshold to see below ~5 MeV. The spectrum of neutrinos obtained by the latest calculations [29] is shown in Figure 1.5, together with uncertainties in the calculated fluxes and thresholds for neutrino detection by various experiments to date.

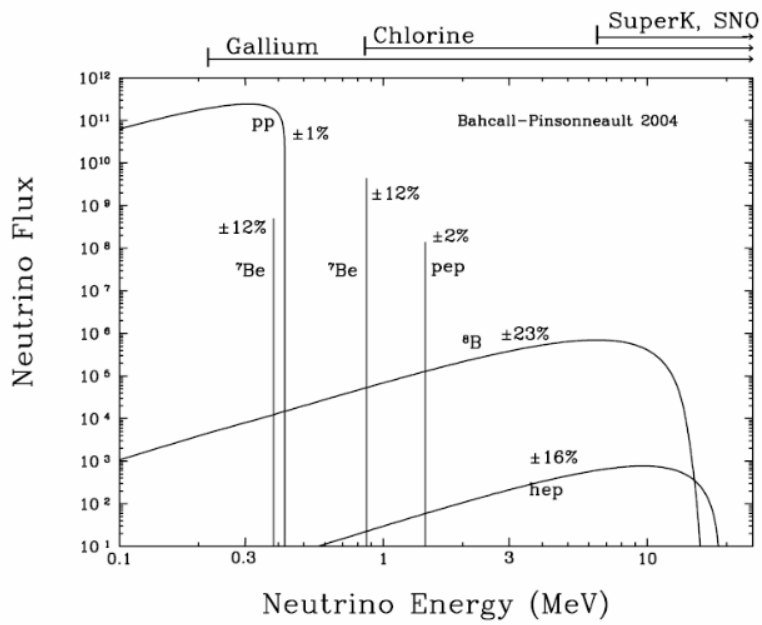

Figure 1.5: The Standard Solar Model prediction of the solar neutrino flux. Thresholds for each of the solar experiments are shown at the top. SuperK and SNO are only sensitive to Boron-8 and hep neutrinos. The Gallium experiments have the lowest threshold and can observe pp neutrinos. [29]

Historically, Ray Davis' Homestake experiment, sometimes referred to as the Davis experiment and, in original literature, called Brookhaven Solar Neutrino Experiment or Brookhaven ^{37}Cl (Chlorine) Experiment, was the first neutrino experiment designed to look for solar neutrinos. Davis' radiochemical measurements with Chlorine were sensitive primarily to ^{7}Be and ^{8}B neutrinos. It started in 1965, was operated until 2000, and, after several years of running, produced a result for the average capture rate of solar neutrinos of 2.56 $\pm$ 0.25 SNU (1 SNU = 10^{-36} neutrino interactions per target atom per second). The Standard Solar Models of the time having predicted that Homestake should have seen about 8.1 $\pm$ 1.2 SNU, over three times larger than the measured rate, this discrepancy became known as the Solar Neutrino Problem. Investigating this problem eventually led to the 2002 Nobel Prize.

The Kamiokande detector [30], with 3000 tons of light water, was operated from 1983 to 1995, and the Super-Kamiokande [31][32] detector began operation in 1996 with a 22.5 kton light wa-

ter fiducial volume. In Super-Kamiokande, the main mode of solar neutrino detection was the elastic scattering channel $\nu_e + e^- \rightarrow \nu_e + e^-$, with an energy threshold of 5 MeV due to the design of the detector. Neutrinos with energies lower than 5 MeV which elastically scattered in the target water would not generate an electron with enough momentum to be seen in the detector. This reaction is primarily sensitive to electron neutrinos, which have a cross section about six times larger than mu or tau neutrinos. With the thresholds used, the experiments were largely sensitive to solar neutrinos from ^{8}B decay, with a negligible contribution from the hep reaction. For Kamiokande, the flux of solar neutrinos from ^{8}B decay was measured [30] to be $2.8 \pm 0.19(\text{stat}) \pm 0.33(\text{syst}) \times 10^6$ cm^{-2}.s^{-1}, clearly less than the solar model prediction [29] of $5.82(1 \pm 0.23) \times 10^6$ cm^{-2}.s^{-1}. The flux measured by Super-Kamiokande in 2001 [32] was $2.35 \pm 0.02(\text{stat}) \pm 0.08(\text{syst}) \times 10^6$ cm^{-2}.s^{-1}, also significantly smaller than the prediction.

The main drawback of both the Chlorine and water experiments was that they were only sensitive to the relatively rare ^{8}B and pep neutrinos. The Gallium experiments were able to observe part of the bulk pp neutrino flux, with SAGE [33], which ran with 50 tonnes of Gallium, having observed a capture rate of 70.8 ± 5.0 SNU as opposed to the model prediction of 129 ± 9 SNU. Its counterpart, GALLEX [34], observed a rate of 77.5 ± 8 SNU. Both numbers are in excellent agreement with each other, and yet are much smaller than the predictions of the Standard Solar Model (131 SNU), by about 40%. This showed that the deficit in observed solar neutrinos was energy dependent.

In all aforementioned experiments, the model was overestimating the solar neutrino capture rate, with the discrepancy appearing to be energy dependent. From an unbiased point of view, this can either mean that the theoretical model of the Sun is wrong or that an unknown phenomenon happens to the neutrinos coming from the Sun before detection. It is however largely believed that Bahcall's Standard Solar Model (SSM) [29] describes the Sun well.
In order to show that neutrino flavour oscillations can explain the Solar Neutrino Problem, it was necessary to be able to observe the solar flux independently of neutrino flavour. All solar experiments detect solar neutrinos through charged current interactions in their detector : $\nu_e + X \rightarrow e^- + Y$. The radiochemical (Clorine, Gallium) experiments used the charged current interaction to generate unstable ions, whereas the water Cerenkov experiments needed the final state electron as a tag that a ν_e had interacted. However, with solar neutrino energies of less than $\sim$30 MeV, and a charged muon mass of 105 MeV (larger charged tau mass still), muon or tau neutrinos could not interact via the charged current, as there must be enough energy available to create the charged leptons. All experiments relying on charged current interactions to detect the neutrino were not able to see the ν_μ or ν_τ part of the flux. What was needed was a way to measure the total neutrino flux, regardless of flavour, which was finally provided by the SNO detector.

The SNO experiment [35] was primarily designed to search for a clear indication of neutrino flavor change for solar neutrinos without relying upon solar model calculations. It used a tank of heavy water as its target, consisting of D_2O, with the deuteron (nucleus of a D_2O atom) containing a proton and a neutron rather than just a proton (as in Hydrogen). The deuteron is a very fragile nucleus, taking only about 2 MeV to be broken apart into a proton and a neutron. Solar neutrinos have energies up to 30 MeV and so any of the neutrinos ν_e, ν_μ or ν_τ can break apart a deuteron in a neutral current interaction, with SNO able to detect the final state neutron. SNO was able to detect neutrinos via three different, and redundant, interactions.
The Elastic Scattering (ES) channel $\nu + e^- \rightarrow \nu + e^-$ was also used in Super–Kamiokande. Electron neutrinos can interact via both the charged and neutral currents, whereas ν_μ and ν_τ neutrinos can only interact via the neutral current at these energies due to the final lepton mass threshold. Elastic scattering probes a combination of the electron, muon and tau neutrino flux given by

$\Phi(\nu_e) + 0.15(\Phi(\nu_\mu) + \Phi(\nu_\tau))$. The Charged Current (CC) channel $\nu_e + d \rightarrow p + p + e^-$ can only be initiated by electron neutrinos and therefore only measures $\Phi(\nu_e)$. SNO used this channel to ensure the observation of the same reduction in ν_e rate as observed in previous solar neutrino experiments. The Neutral Current (NC) channel $\nu + d \rightarrow n + p + \nu$ measured the total flux $\Phi(\nu_e) + \Phi(\nu_\mu) + \Phi(\nu_\tau)$, the experimental challenge being to measure the final state neutron.
Using the measurement of these three independent reaction channels, SNO was able to disentangle the individual fluxes of neutrinos. Their measurement of the neutrino fluxes was, in units of $10^{-8}\text{cm}^2.\text{s}^{-1}$,

$$\begin{aligned}
\Phi_{CC} &= \Phi(\nu_e) &&= 1.76 \pm 0.01 \\
\Phi_{ES} &= \Phi(\nu_e) + 0.15(\Phi(\nu_\mu) + \Phi(\nu_\tau)) &&= 2.39 \pm 0.26 \\
\Phi_{NC} &= \Phi(\nu_e) + \Phi(\nu_\mu) + \Phi(\nu_\tau) &&= 5.09 \pm 0.63
\end{aligned}$$

The total flux of muon and tau neutrinos coming from the Sun, $\Phi(\nu_\mu) + \Phi(\nu_\tau)$, is $(3.33 \pm 0.63) \times 10^{-8}$ cm^{-2}.s^{-1}, about 3 times larger than the flux of ν_e. As the Sun only produces electron neutrinos, these neutrinos must have changed flavour when propagating from the Sun to the Earth. Furthermore, the SSM predicts a total flux of neutrinos with energies greater than 2 MeV (the deuteron break-up energy) of $\Phi_{SSM} = (5.05 \pm 1.01) \times 10^{-8} cm^{-2}.s^{-1}$, which is in very good agreement with the NC flux measured by SNO.
The data from SNO [36] is shown in Figure 1.6, together with the best fit to the data of the NC (8.6 MeV gamma) shape, the CC and ES reactions, and a small background component determined from independent measurements. Figure 1.6a shows the cosine of the angle between the event direction and the vector from the Sun at the time the event occurred. The peak at $cos\theta \approx 1$ in the ES distribution indicates that the events do indeed come from the Sun. Figure 1.6b shows the kinetic energy distributions for the events, with an effective electron kinetic energy threshold $T_{eff} \geq 5.5$ MeV. The observed total flux of neutrinos (dashed lines) is in excellent agreement with the flux of neutrinos obtained from solar models.

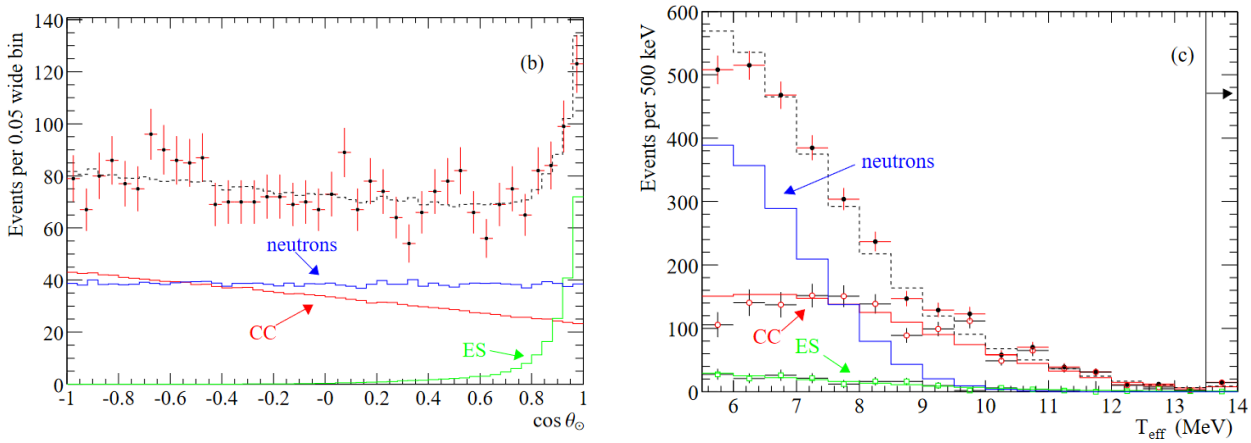

(a) (b)

Figure 1.6: Distribution of (a) cos $\theta_\odot$ and (b) kinetic energy for the selected events. The CC and ES spectra are extracted from the data using an estimator of event isotropy and cos $\theta_\odot$ distributions in each energy bin. Also shown are the Monte Carlo predictions for CC, ES, NC and internal and external-source neutron events, all scaled to the fit results. The dashed lines represent the summed components. All distributions are for events with an effective electron kinetic energy threshold $T_{eff} \geq 5.5$ MeV and a fiducial volume with radius $R_{fit} \leq 550$ cm. [36]

Atmospheric neutrinos

Earth's atmosphere is under a constant flux of cosmic rays composed of very high energy protons (95%), alpha particles (5%) and heavier nuclei and electrons (< 1%). When the primary cosmic rays hit nuclei in the atmosphere, they produce secondary particles (hadrons, mainly mesons such as pions or kaons) in a cascade called a particle shower. Atmospheric neutrinos are produced from the decay of these hadrons towards the charged leptons until they reach the electron, the lightest charged lepton. The dominant part of the decay chain is through pions :

$$\pi^+ \rightarrow \mu^+\nu_\mu \qquad \mu^+ \rightarrow e^+\nu_e\overline{\nu}_\mu \tag{1.27}$$

$$\pi^- \rightarrow \mu^-\overline{\nu}_\mu \qquad \mu^- \rightarrow e^-\overline{\nu}_e\nu_\mu \tag{1.28}$$

though, at higher energies, neutrinos are also produced from kaon decays. The total energy of such cosmic showers is very high, ranging from hundreds of MeV to several tens of TeV [37], and in general, the spectrum of the resulting neutrinos peaks at 1 GeV and extends up to a few hundreds of GeV. At moderate energies, the ratio $R = (\nu_\mu + \overline{\nu}_\mu)/(\nu_e + \overline{\nu}_e)$ is ~2 (computed models of the entire cascade process predict this ratio to be equal to 2 with a 5% uncertainty).
A detector looking at atmospheric neutrinos can be considered to be positioned on the Earth's surface. Flight distances for neutrinos detected in these experiments can thus vary from ~15 km for neutrinos coming down from an interaction above the detector to more than 13000 km for neutrinos coming from interactions in the atmosphere below the detector on the other side of the planet. Atmospheric neutrino experiments measure two quantities : the ratio of ν_μ to ν_e observed in the flux, and the zenith angle distribution of the neutrinos. To cancel systematic uncertainties, most experiments report a double ratio

$$R = \frac{(N_\mu/N_e)_{DATA}}{(N_\mu/N_e)_{SIM}} \tag{1.29}$$

where N_μ and N_e are respectively the number of ν_μ (muon-like) and ν_e (electron-like) events which interacted in the detector. The ratio of N_μ/N_e is measured both in the data and in a computational model of the experiment, which includes all known physics of atmospheric neutrino production, neutrino propagation and detector response. If the observed flavour composition agrees with expectation, R = 1.
Different R values from a number of experiments are shown in Table 1.2. With the exception of Frejus, all measurements of R are significantly less than 1, indicating that either there were fewer ν_μ in the data than in the prediction, or there were more ν_e, or both. This became known as the Atmospheric Neutrino Anomaly.

Experiment	Type of experiment	R
Super-Kamiokande	Water Cherenkov	0.675 ± 0.085
Soudan 2	Iron Tracking Calorimeter	0.69 ± 0.13
IMB	Water Cherenkov	0.54 ± 0.12
Kamiokande	Water Cherenkov	0.60 ± 0.07
Frejus	Iron Tracking Calorimeter	1.0 ± 0.15

Table 1.2: Measurements of the double ratio R for various atmospheric neutrino experiments.

In addition to low values of R, Super-Kamiokande, the most influential water Cherenkov detector in the Atmospheric Neutrino Anomaly, was able to measure the direction of the incoming neutrinos. Neutrinos are produced everywhere in the atmosphere and can reach the detector from all

directions. As such, the flux of neutrinos is expected to be isotropic. While the electron-like data of Super-Kamiokande agreed reasonably well with this expectation, the muon-like data deviated significantly. At low energies, about half of the expected ν_μ were missing over the full range of zenith angles. At high energies, the number of ν_μ coming down from above the detector seemed to agree with expectation, but half of the same ν_μ coming up from below the detector were missing. As previously mentioned, neutrinos arriving at the Super-Kamiokande detector at different zenith angles have travelled anywhere from 15 km (for neutrinos coming straight down) to 13000 km (for neutrinos coming straight up). Considering neutrino oscillations (and the oscillation probability in Equation 1.26), then for $\Delta m^2 \sim 10^{-3}$ eV^2 and neutrino energies of about 10 GeV, the oscillation probability for neutrinos coming down on the Super-Kamiokande detector ($L \sim$ 15 km) will be close to 0. On the other hand, for neutrinos coming up ($L \sim$ 13000 km), the oscillation probability will be roughly $\frac{1}{2}\sin^2(2\theta)$ (where the factor of 0.5 comes from averaging the kinematic factor $\sin^2(1.27\Delta m^2 \mathrm{L/E})$ over many oscillation periods). These oscillation probabilities explain the deficit in ν_μ coming up from below the detector observed by Super-Kamiokande and other atmospheric neutrino experiments. The reduced flux of ν_μ neutrinos coupled to the expected flux of ν_e neutrinos also indicates that the dominant oscillation mode for the atmospheric neutrinos is $\nu_\mu \rightarrow \nu_\tau$.

1.2.3 Theory of neutrino oscillations

As introduced in section 1.2.1, neutrinos are produced in weak interactions in weak flavour eigenstates of definite lepton number ($|\nu_e>$, $|\nu_\mu>$ or $|\nu_\tau>$). These flavour eigenstates are not the energy (mass) eigenstates. Each flavour eigenstate, created at the weak interaction vertex, is a coherent superposition of the energy (mass) states, and both sets of states are related to each other by a unitary matrix.

Two flavour neutrino oscillation theory

In the two-flavour case, the energy (mass) eigenstates of the Hamiltonian are $|\nu_1>$ and $|\nu_2>$, with eigenvalues m_1 and m_2 for neutrinos at rest. The unitary mixing matrix can be written as :

$$U = \begin{pmatrix} U_{\alpha 1} & U_{\alpha 2} \\ U_{\beta 1} & U_{\beta 2} \end{pmatrix} \tag{1.30}$$

As such, we can write the flavour state $|\nu_\alpha>$ as the linear combination of the mass states $|\nu_k>$:

$$|\nu_\alpha> = \sum_{k=1,2} U_{\alpha k} |\nu_k> \tag{1.31}$$

In the case of a neutrino beam containing a flavour state $|\nu_\alpha(0,0)>$, which describes a neutrino generated with a definite flavour α at space-time point (x,t) = (0,0), and aimed along the x-axis towards a detector, the mass states $|\nu_k>_{k=1,2}$ will propagate according to the time-dependent Schrödinger equation with no potential, the solution of which is a plane wave :

$$|\nu_k(x,t)> = e^{-i(E_k t - p_k x)} |\nu_k(0,0)> = e^{-i\Phi_k} |\nu_k(0,0)> \tag{1.32}$$

where the energy E_k is the eigenvalue of the propagating neutrino mass state $|\nu_k>$, $p_k = (E, \mathbf{p})$ is the 4-momentum of $|\nu_k>$ and $x = (t, \mathbf{x})$ is the 4-space vector.
At any given space-time point (x,t), the generated flavour state $|\nu_\alpha>$ will be :

$$|\nu_\alpha(x,t)>=\sum_{k=1,2} U_{\alpha k}|\nu_k(x,t)>=\sum_{k=1,2} U_{\alpha k}e^{-i\Phi_k}|\nu_k(0,0)> \tag{1.33}$$

By inverting the mixing matrix U (using its complex conjugate), it is possible to write the generated mass states as the linear combination of the generated flavour states :

$$|\nu_k(0,0)>=\sum_\gamma U^*_{\gamma k}|\nu_\gamma(0,0)> \tag{1.34}$$

By substitution, the flavour state $|\nu_\alpha>$ at the space-time point (x,t) can be written in terms of the flavour states at the generation point :

$$|\nu_\alpha(x,t)>=\sum_{k=1,2} U_{\alpha k}e^{-i\Phi_k}\sum_\gamma U^*_{\gamma k}|\nu_\gamma(0,0)>=\sum_\gamma\sum_k U^*_{\gamma k}e^{-i\Phi_k}U_{\alpha k}|\nu_\gamma(0,0)> \tag{1.35}$$

As such, the transition amplitude for detecting a neutrino of flavour β at a space-time point (x,t), given that a neutrino of flavour α was generated at the space-time point (0,0), is :

$$\begin{aligned} A(\nu_\alpha(0,0)\rightarrow\nu_\beta(x,t)) &=<\nu_\beta(x,t)|\nu_\alpha(0,0)> \\ &=\sum_\gamma\sum_k U_{\gamma k}e^{i\Phi_k}U^*_{\beta k}<\nu_\gamma(0,0)|\nu_\alpha(0,0)> \\ &=\sum_k U_{\alpha k}e^{i\Phi_k}U^*_{\beta k} \end{aligned} \tag{1.36}$$

The last step comes from the orthogonality of the flavour states : $<\nu_\gamma(0,0)|\nu_\alpha(0,0)>=\delta_{\gamma\alpha}$.
The oscillation probability from the flavour α to the flavour β as the neutrino propagates is the coherent sum :

$$\begin{aligned} P(\nu_\alpha\rightarrow\nu_\beta)=|A(\nu_\alpha(0,0)\rightarrow\nu_\beta(x,t))|^2 &=|\sum_k U_{\alpha k}e^{i\Phi_k}U^*_{\beta k}|^2 \\ &=\sum_k U_{\alpha k}e^{i\Phi_k}U^*_{\beta k}\sum_j U^*_{\alpha j}e^{-i\Phi_j}U_{\beta j} \\ &=\sum_j\sum_k U_{\alpha k}U^*_{\beta k}U^*_{\alpha j}U_{\beta j}e^{-i(\Phi_j-\Phi_k)} \end{aligned} \tag{1.37}$$

This oscillation probability formula can be developed and simplified using the values of the unitary mixing matrix U. In the case of two-flavour neutrino oscillations, the unitary matrix is the 2×2 rotation matrix, with the parameter θ known as the mixing angle :

$$U=\begin{pmatrix} cos\theta & sin\theta \\ -sin\theta & cos\theta \end{pmatrix} \tag{1.38}$$

The sum over 4 elements of Equation 1.37 can be broken down to its components :

$$\begin{aligned} &(k=1,j=1): U_{\alpha1}U^*_{\beta1}U^*_{\alpha1}U_{\beta1}e^{-i(\Phi_1-\Phi_1)}=|U_{\beta1}|^2|U_{\alpha1}|^2 \\ &(k=1,j=2): U_{\alpha1}U^*_{\beta1}U^*_{\alpha2}U_{\beta2}e^{-i(\Phi_2-\Phi_1)} \\ &(k=2,j=1): U_{\alpha2}U^*_{\beta2}U^*_{\alpha1}U_{\beta1}e^{-i(\Phi_1-\Phi_2)} \\ &(k=2,j=2): U_{\alpha2}U^*_{\beta2}U^*_{\alpha2}U_{\beta2}e^{-i(\Phi_2-\Phi_2)}=|U_{\beta2}|^2|U_{\alpha2}|^2 \end{aligned}$$

This gives an oscillation probability from the flavour α to the flavour β :

$$\begin{aligned} P(\nu_\alpha \to \nu_\beta) &= (|U_{\beta 1}|^2|U_{\alpha 1}|^2 + |U_{\beta 2}|^2|U_{\alpha 2}|^2) + U_{\alpha 1}U^*_{\beta 1}U_{\alpha 2}U^*_{\beta 2}(e^{i(\Phi_2-\Phi_1)} + e^{-i(\Phi_2-\Phi_1)}) \\ &= (|U_{\beta 1}|^2|U_{\alpha 1}|^2 + |U_{\beta 2}|^2|U_{\alpha 2}|^2) + 2U_{\alpha 1}U^*_{\beta 1}U_{\alpha 2}U^*_{\beta 2}cos(\Phi_2 - \Phi_1) \\ &= (sin^2\theta cos^2\theta + cos^2\theta sin^2\theta) + 2(cos\theta)(-sin\theta)(sin\theta)(cos\theta)cos(\Phi_2 - \Phi_1) \\ &= 2cos^2\theta sin^2\theta(1 - cos(\Phi_2 - \Phi_1)) \\ &= sin^2(2\theta)sin^2(\frac{\Phi_2 - \Phi_1}{2}) \end{aligned} \tag{1.39}$$

With $\Phi_i = E_i t - p_i x$ (Equation 1.32), the phase difference can be written as :

$$\Phi_2 - \Phi_1 = (E_2 - E_1)t - (p_2 - p_1)x \tag{1.40}$$

Assuming that the neutrinos are relativistic, and taking L to be the distance between the neutrino emission source and the detector :

$$\begin{aligned} &t = x = L \\ &E_i = \sqrt{p_i^2 + m_i^2} \Leftrightarrow p_i = \sqrt{E_i^2 - m_i^2} = E_i\sqrt{1 - \frac{m_i^2}{E_i^2}} \approx E_i(1 - \frac{m_i^2}{2E_i^2}) \end{aligned}$$

Having modelled the mass eigenstates as plane waves, instead of the more complete model of wave packets, assuming that they are created with the same energy becomes necessary (for some applications, the plane wave treatment of neutrino oscillations is wrong, but the same analysis assuming that the mass states were wave packets would yield the same results). With this assumption, and the expression of p_i, the phase difference can be written as :

$$\Phi_2 - \Phi_1 = (\frac{m_2^2}{2E_2} - \frac{m_1^2}{2E_1})L = \frac{\Delta m^2 L}{2E_\nu} \tag{1.41}$$

where $\Delta m^2 = m_2^2 - m_1^2$ and $E_\nu = E_1 = E_2$.
This gives an oscillation probability between the α and β flavours of :

$$P(\nu_\alpha \to \nu_\beta) = sin^2(2\theta)sin^2(\frac{\Delta m^2 L}{4E_\nu}) \tag{1.42}$$

which can be re-written to include Δm^2 in eV^2, L in km and E_ν in GeV :

$$P(\nu_\alpha \to \nu_\beta) = sin^2(2\theta)sin^2(1.27\Delta m^2 \frac{L}{E_\nu}) \tag{1.43}$$

A corresponding survival probability, amounting to the probability of measuring a flavour state $|\nu_\alpha >$ after having generated a $|\nu_\alpha >$ state, can be written as :

$$P(\nu_\alpha \to \nu_\alpha) = 1 - P(\nu_\alpha \to \nu_\beta) \tag{1.44}$$

Three flavour neutrino oscillation theory

In the three-flavour case, the mixing matrix can be 3×3, complex, and unitary. It is known as the Pontecorvo-Maki-Nakagawa-Sakata (PMNS) matrix [38][39] and has an equivalent role to the complex unitary matrix of Cabibbo-Kobayashi-Maskawa [40][41] in the case of quarks.

It is defined as follows :

$$U = \begin{bmatrix} U_{e1} & U_{e2} & U_{e3} \\ U_{\mu 1} & U_{\mu 2} & U_{\mu 3} \\ U_{\tau 1} & U_{\tau 2} & U_{\tau 3} \end{bmatrix} \tag{1.45}$$

$$= \begin{bmatrix} 1 & 0 & 0 \\ 0 & c_{23} & s_{23} \\ 0 & -s_{23} & c_{23} \end{bmatrix} \begin{bmatrix} c_{13} & 0 & s_{13}e^{-i\delta} \\ 0 & 1 & 0 \\ -s_{13}e^{i\delta} & 0 & c_{13} \end{bmatrix} \begin{bmatrix} c_{12} & s_{12} & 0 \\ -s_{12} & c_{12} & 0 \\ 0 & 0 & 1 \end{bmatrix} \begin{bmatrix} e^{i\alpha_1/2} & 0 & 0 \\ 0 & e^{i\alpha_2/2} & 0 \\ 0 & 0 & 1 \end{bmatrix} \tag{1.46}$$

$$= \begin{bmatrix} c_{12}c_{13} & s_{12}c_{13} & s_{13}e^{-i\delta} \\ -s_{12}c_{23} - c_{12}s_{23}s_{13}e^{i\delta} & c_{12}c_{23} - s_{12}s_{23}s_{13}e^{i\delta} & s_{23}c_{13} \\ s_{12}s_{23} - c_{12}c_{23}s_{13}e^{i\delta} & -c_{12}s_{23} - s_{12}c_{23}s_{13}e^{i\delta} & c_{23}c_{13} \end{bmatrix} \begin{bmatrix} e^{i\alpha_1/2} & 0 & 0 \\ 0 & e^{i\alpha_2/2} & 0 \\ 0 & 0 & 1 \end{bmatrix} \tag{1.47}$$

where $c_{ij} = cos(\theta_{ij})$ and $s_{ij} = sin(\theta_{ij})$ (i, j = 1,2,3), δ is a non-null Dirac phase term in the case of a CP symmetry violation (referred to as δ_{CP} from here on out and expanded upon in section 1.2.6), and α_i is the Majorana phase associated with the neutrino mass eigenstate ν_i (i = 1,2). In the case of the neutrino being a Majorana particle, $\alpha_i \neq 0$. The diagonal matrix including these phases does not influence neutrino oscillations, but does influence electroweak properties involved in processes such as neutrinoless double beta decay. The first matrix in Equation 1.46 is called the "12-sector", the second matrix is the "13-sector", and the third is the "23-sector".
The oscillation probabilities between the flavor states are calculated as in the two-flavour case, and involve the mixing angles θ_{ij} and the squared mass differences Δm^2_{ij} (i, j = 1,2,3). Assuming $\delta_{CP} = 0$ and $\Delta m^2_{13} \approx \Delta m^2_{23}$, and after some algebra, they can be written as :

$$P(\nu_e \to \nu_\mu) = sin^2(2\theta_{13})sin^2(\theta_{23})sin^2(1.27\Delta m^2_{23}\frac{L}{E}) \tag{1.48}$$

$$P(\nu_\mu \to \nu_\tau) = cos^4(\theta_{13})sin^2(2\theta_{23})sin^2(1.27\Delta m^2_{23}\frac{L}{E}) \tag{1.49}$$

$$P(\nu_e \to \nu_\tau) = sin^2(2\theta_{13})cos^2(\theta_{23})sin^2(1.27\Delta m^2_{23}\frac{L}{E}) \tag{1.50}$$

for small $\frac{L}{E}$ ratios, typical of atmospheric (mostly $\nu_\mu \to \nu_{e,\tau}$) and reactor or accelerator neutrinos ($\nu_\mu \to \nu_{e,\tau}$ or $\nu_e \to \nu_{\mu,\tau}$). For large $\frac{L}{E}$ ratios, typical of solar neutrinos (mostly ν_e), the oscillation probability can be written as :

$$P(\nu_e \to \nu_{\mu,\tau}) = cos^2(\theta_{13})sin^2(2\theta_{12})sin^2(1.27\Delta m^2_{12}\frac{L}{E}) + \frac{1}{2}sin^2(2\theta_{13}) \tag{1.51}$$

For small values of θ_{13}, $cos^2(\theta_{13}) \to 1$ and $sin^2(\theta_{13}) \to 0$. This reduces the previous equations to :

$$P(\nu_e \to \nu_\mu) = 0 \tag{1.52}$$

$$P(\nu_\mu \to \nu_\tau) = sin^2(2\theta_{23})sin^2(1.27\Delta m^2_{23}\frac{L}{E}) \tag{1.53}$$

$$P(\nu_e \to \nu_\tau) = 0 \tag{1.54}$$

for small $\frac{L}{E}$ ratios, and for large $\frac{L}{E}$ ratios :

$$P(\nu_e \to \nu_{\mu,\tau}) = sin^2(2\theta_{12})sin^2(1.27\Delta m^2_{12}\frac{L}{E}) \tag{1.55}$$

The 23-sector is thus associated with atmospheric neutrinos, and the 12-sector with solar neutrinos.

It can be seen in Equation 1.53 that the oscillation probability for ν_μ into ν_τ depends on $sin^2\theta_{23}$. As such, so does the ν_μ survival probability, which is also symmetrical around $\theta_{23} = \frac{\pi}{4}$. To first order, the ν_μ disappearance (oscillation into other flavors) is thus not sensitive to the octant of the mixing angle θ_{23}, defined as whether θ_{23} lies in the first octant $\theta_{23} < \frac{\pi}{4}$ or in the second octant $\theta_{23} > \frac{\pi}{4}$. Best fit solutions of θ_{23} appear in each octant, and determining this octant value is one of the main focuses of neutrino oscillation experiments.
In the previous oscillation probability computations, θ_{13} was considered small. This assumption was made with the knowledge that $P(\nu_\mu \to \nu_e)$ is small for atmospheric neutrinos, which suggests that θ_{13} is indeed small. In order to determine θ_{13} without having to include the other mixing angles, for a better precision on the θ_{13} measurement, the survival probability for an electron neutrino can be written to be :

$$\begin{aligned} P(\nu_e \to \nu_e) = 1 - cos^4(\theta_{13})sin^2(2\theta_{12})sin^2(1.27\Delta m^2_{12}\frac{L}{E}) \\ - sin^2(2\theta_{13})\left[cos^2(\theta_{12})sin^2(1.27\Delta m^2_{31}\frac{L}{E}) + sin^2(\theta_{12})sin^2(1.27\Delta m^2_{32}\frac{L}{E})\right] \end{aligned} \tag{1.56}$$

in which $\Delta m^2_{32} = \Delta m^2_{31} - \Delta m^2_{12}$.
If $\theta_{13} \neq 0$, this survival probability depends on a second term, driven by the atmospheric parameters (Δm^2_{31}, Δm^2_{32} and θ_{13}). The impact of this second term on the ν_e survival probability will be detailed in section 1.3.4.
Taking $\Delta m^2_{31} \approx \Delta m^2_{32}$, this survival probability can be re-written as :

$$P(\nu_e \to \nu_e) = 1 - cos^4(\theta_{13})sin^2(2\theta_{12})sin^2(1.27\Delta m^2_{12}\frac{L}{E}) - sin^2(2\theta_{13})sin^2(1.27\Delta m^2_{32}\frac{L}{E}) \tag{1.57}$$

The oscillation terms driven by Δm^2_{12} and $\Delta m^2_{31} \approx \Delta m^2_{32}$ can therefore be used to determine θ_{12} and θ_{13}, respectively. Close to the source, this probability is only sensitive to the atmospheric-scale oscillation term (involving Δm^2_{32}), and can be reduced to :

$$P(\nu_e \to \nu_e) \approx 1 - sin^2(2\theta_{13})sin^2(1.27\Delta m^2_{32}\frac{L}{E}) \tag{1.58}$$

which eliminates all the other mixing angles. The precise measurement of this parameter was performed by reactor neutrino experiments Daya Bay, Double Chooz and RENO, and will be addressed in section 1.3.4.

1.2.4 Neutrino Mass Ordering

As detailed in sections 1.2.1 and 1.2.3, the neutrino mass states, labelled as ν_1, ν_2 and ν_3, have different masses, with mass squared differences Δm^2_{ij} defined as $\Delta m^2_{ij} = m^2_j - m^2_i$ (i, j = 1,2,3). While experimental observations and measurements have concluded that $\Delta m^2_{12} > 0$ (which implies $m_1 < m_2$) and $\Delta m^2_{23} >> \Delta m^2_{12}$, the sign of Δm^2_{23} is still unknown. As such, two orderings are possible for the mass states. If $m_1 < m_2 << m_3$, the ordering is said to be normal (NO), while if $m_3 << m_1 < m_2$, the ordering is said to be inverse (IO). The term "Neutrino Mass Ordering" (NMO) is usually preferred but is sometimes also referred to as "Neutrino Mass Hierarchy". The two possible mass orderings for neutrinos are illustrated in Figure 1.7, in which the mass squared differences are referred to as the "solar" ($\Delta m^2_{12} = \Delta m^2_{sol}$) and "atmospheric" ($\Delta m^2_{23} = \Delta m^2_{atm}$) mass squared differences.

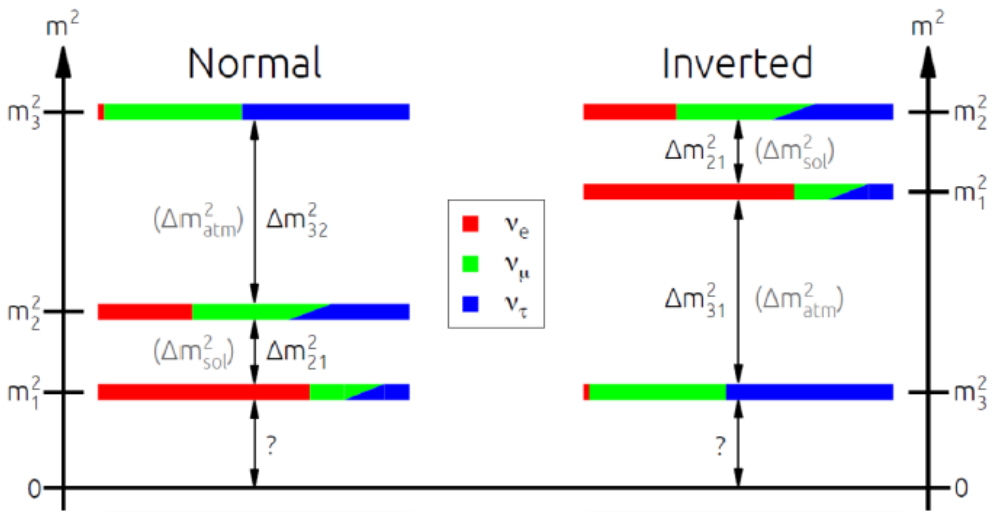

Figure 1.7: The two possible Neutrino Mass Orderings (NMO). Each mass state is additionally color-coded to represent the relative contribution of each flavour component to that state.

1.2.5 Matter effects

Section 1.2.3 introduced the concept of the neutrino mass eigenstates propagating in vacuum as plane waves, from their source to a detector. It also introduced the notion that the mass eigenstates can be better described by wave packets, produced at the same instant at the weak interaction vertex and arriving at the detector at separate times, depending on their individual velocities. Neutrino oscillations indeed occur because of a difference in phase between the wave packets of each of the mass eigenstates, with this phase difference arising from the different velocities of the wavepackets due to their mass differences.
In matter, however, the phase difference is determined by the total energy of the mass eigenstates, and if the emitted neutrino is propagating in a potential V, then the total energy of a state is $E+V$. The Hamiltonian of the system will thus be modified in matter. If the potential that the neutrino is propagating through varies for different neutrino flavours, which could occur if neutrino flavours interact differently in the considered matter, then an additional phase difference can be introduced through the interaction potential, and the neutrinos will further oscillate through "matter effects". As previously stated, the interaction of the neutrino with the environment it is crossing changes the mass eigenstates, giving them a heavier effective mass. In a vacuum (state considered for section 1.2.3), the neutrino mass eigenstates $|\nu_i>$ (i = 1,2,3) obey the equation :

$$E^2 - p^2 = m_i^2 \tag{1.59}$$

In a potential V, they obey :

$$(E+V)^2 - p^2 \approx m_i^2 + 2EV \tag{1.60}$$

The effective mass of the neutrino mass eigenstates is now $m_i^{'} = \sqrt{m_i^2 + 2EV}$, and the oscillation probabilities now need to be expressed in terms of mass eigenstates with mass eigenvalues equivalent to the effective masses, not the vacuum masses.

Electron neutrinos produced in the solar core can interact with the surrounding matter (large e^- density) through both the neutral current, process involving a Z^0 boson, and the charged current,

process involving a W^- boson and creating the associated charged lepton e^-. Muon neutrinos travelling in the solar core, however, can only interact with the surrounding matter through the neutral current, as they do not have enough energy to create the much heavier charged muon μ^- in the charged current process. Similarly, only the ν_e component of the atmospheric neutrino flux can undergo charged-current forward scattering with the electrons in matter (Earth matter). Electron neutrinos can thus interact with matter differently from the other neutrino flavour states, and these charged-current interactions introduce an additional potential V that the neutrinos propagate through, characterized by the interaction potential energy V_W :

$$V_W = \pm\sqrt{2}G_F N_e \tag{1.61}$$

where G_F is the Fermi constant, and N_e is the electron density in matter. This effective potential is positive for neutrinos and negative for antineutrinos. In matter, the electron density is however not constant, meaning that the potential V evolves as the neutrino propagates and that the Hamiltonian should be recalculated as a function of the neutrino's path length. The assumption that the electron density in matter is constant is usually made. If electron neutrinos participate in oscillations, matter effects will thus modify the oscillation probabilities with respect to the vacuum case. This perturbation to the vacuum oscillation probabilities is called the Mikheyev-Smirnov-Wolfenstein (MSW) effect [42, 43].

In the two flavour neutrino oscillation case, with neutrino flavour states $|\nu_\alpha>$ and $|\nu_\beta>$ and neutrino mass states $|\nu_1>$ and $|\nu_2>$, the impact of the matter effects on the oscillation probabilities can be expressed in reasonably simple terms and formulas. As illustrated with the solar and atmospheric neutrinos, the interaction potential V_α that $|\nu_\alpha>$ experiences is different than the interaction potential V_β which $|\nu_\beta>$ experiences.
As previously stated, the mass eigenstates in vacuum are not eigenstates of the new Hamiltonian in matter. The mass splitting in matter can thus be expressed in terms of the new mass eigenstates and eigenvalues :

$$\Delta m_m^2 = m_{1m}^2 - m_{2m}^2 = \Delta m^2 \sqrt{\left[\frac{\Delta V}{\Delta m^2} - cos(2\theta)\right]^2 + sin^2(2\theta)} \tag{1.62}$$

where Δm_m^2 is the mass splitting in matter, m_{1m} and m_{2m} are the modified mass eigenvalues in matter, $\Delta V = V_\alpha - V_\beta$, and Δm^2 and θ are the mass splitting and mixing angle in vacuum.
From the standard oscillation analysis (two-flavour oscillation case in section 1.2.3), the mixing angle in matter, linking the new mass eigenstates with the flavour states, can be expressed as :

$$sin(2\theta_m) = \frac{sin(2\theta)}{\sqrt{\left[\frac{\Delta V}{\Delta m^2} - cos(2\theta)\right]^2 + sin^2(2\theta)}} \tag{1.63}$$

The oscillation probabilities have the same form as the two-flavour mixing in vacuum, but are now expressed in terms of the mass eigenstates in matter and of the matter modified mixing angle :

$$P_m(\nu_\alpha \to \nu_\beta) = sin^2(2\theta_m) sin^2(1.27\Delta m_m^2 \frac{L}{E_\nu}) \tag{1.64}$$

The values of Δm_m^2 and $sin(2\theta_m)$ can have very interesting consequences in physics. If $\Delta V = 0$, the matter modified parameters reduce to the vacuum parameters, and $\Delta m_m^2 = \Delta m^2$ and $sin(2\theta_m) = sin(2\theta)$. If $sin(2\theta) = 0$, then $sin(2\theta_m) = 0$, regardless of any additional potential introduced by interactions with matter, which means that oscillations in matter can only occur if oscillations can

already occur in vacuum. In very dense matter, with $\Delta V \rightarrow \infty$, then $sin(2\theta_m) \rightarrow 0$, allowing no oscillations whatsoever. For a specific set of parameters giving $\frac{\Delta V}{\Delta m^2} = cos(2\theta)$, then $sin(2\theta_m) = 1$, regardless of the value of the vacuum mixing angle, which means that even if oscillations are very unlikely to happen in vacuum, there is an electron density N_e for which the oscillation probability in matter is maximal. This is called the MSW resonance.
Finally, the most interesting aspect of matter modified neutrino oscillations is their sensibility to the sign of the mass splitting, and thus to the NMO (section 1.2.4). If $\Delta m^2 \rightarrow -\Delta m^2$, $\frac{\Delta V}{\Delta m^2} - cos(2\theta)$ will have a different value, which will give different Δm^2_m and $sin(2\theta_m)$ values, and a different oscillation probability. In vacuum, $\Delta m^2 \rightarrow -\Delta m^2$ would only yield the same $sin^2(1.27\Delta m^2 \frac{L}{E_\nu})$ value.
The effective potential V being positive for neutrinos and negative for antineutrinos, it raises the effective mass of ν_e and lowers that of $\overline{\nu}_e$. Consequently, ν_e appearance is enhanced for the Normal Ordering, while $\overline{\nu}_e$ is suppressed. This is reversed under the Inverted Ordering, and this asymmetry is investigated by oscillation experiments using the matter effect to probe the NMO.

1.2.6 CP violation and Dirac phase δ_{CP}

Section 1.2.3 introduced the parameter δ_{CP} as the non-null Dirac phase term appearing in the PMNS matrix in the case of a CP symmetry violation.
There are three discrete symmetries that are used in particle physics : Charge conjugation $\widehat{C}$, which replaces particles with their antiparticles, Parity transformation $\widehat{P}$, which reverses the spatial components of wave-functions (it flips the direction of the particles, but not their spin), and Time reversal $\widehat{T}$, which reverses the interaction by running time backwards (T-symmetry is counterintuitive but explained by the fact that the Standard Model describes local properties, not global ones like entropy).
The weak interaction, at the vertex of which neutrinos are generated, violates $\widehat{P}$ and $\widehat{C}$, as do neutrinos. They violate P-symmetry as no right-handed neutrinos have ever been observed while left-handed neutrinos are plentiful, and they violate C-symmetry as no left-handed antineutrinos have ever been observed either. However, right-handed antineutrinos have been observed, and so neutrinos are thought to be symmetrical under $\widehat{CP}$.
Invariance under a symmetry implies that the probability of a particular interaction occurring is identical to the probability of the symmetrically transformed interaction occurring. In the case of neutrino oscillations from a flavour state $|\nu_\alpha >$ to a flavour state $|\nu_\beta >$, invariance under $\widehat{T}$ implies that $P(\nu_\alpha \rightarrow \nu_\beta) = P(\nu_\beta \rightarrow \nu_\alpha)$, invariance under $\widehat{CP}$ implies that $P(\nu_\alpha \rightarrow \nu_\beta) = P(\overline{\nu}_\alpha \rightarrow \overline{\nu}_\beta)$, and invariance under $\widehat{CPT}$ implies that $P(\nu_\alpha \rightarrow \nu_\beta) = P(\overline{\nu}_\beta \rightarrow \overline{\nu}_\alpha)$.
CP violation in neutrino oscillations would thus lead to an asymmetry in the oscillation probabilities for neutrinos and antineutrinos, which would highlight a difference in physics for matter and antimatter. Determining if there is indeed CP violation in the lepton sector is one of the major goals of neutrino oscillation experiments. The parameter that describes CP violation in neutrino oscillations is the phase δ_{CP}, with its value signifying how much $\widehat{CP}$ is violated.
Since δ_{CP} only appears as a complex parameter in the PMNS matrix, it can only be accessed by measurements sensitive to the complex nature of the matrix. The main issue faced when attempting measurements of parameters such as δ_{CP} or the NMO is the fact that the oscillation probabilities are multi-variable functions. They are a function of several mixing angles and mass splittings, as well as matter effects, δ_{CP} and the NMO. Typically, any single measurement and its uncertainties, giving only one value for the measured oscillation probability, encompasses a set of different possible combinations of parameter values which might be a good fit, afflicting this measurement with degeneracies. Usually, more than one experiment is needed to unravel these degeneracies, at different $\frac{L}{E}$ ratios and ideally differently sensitive to δ_{CP} and to the NMO, with

some exceptions of future experiments like DUNE (section 1.3.3.2) able to be self-sufficient in their measurements. Once the NMO is determined, measurements of δ_{CP} will become much more straight-forward.
There currently are two methods to measure δ_{CP}. The first is to measure the oscillation probabilities $P(\nu_\mu \to \nu_e)$ and $P(\overline{\nu}_\mu \to \overline{\nu}_e)$, as a violation in CP symmetry would result in a measurable asymmetry. Experiments using this method are also often probing the NMO using matter effects. As described in section 1.2.5, matter effects enhance ν_e appearance and suppress $\overline{\nu}_e$ appearance for the Normal Ordering, while this effect is reversed for the Inverted Ordering. This effect contributes to an asymmetry in the neutrino and antineutrino oscillation probabilities, a "fake CP violation" that has to be taken into account when searching for genuine CP violation.
The second method involves measuring the appearance probability $P(\nu_\mu \to \nu_e)$ as a function of the neutrino energy, for different assumed values of δ_{CP}. In the oscillated spectrum, consecutive oscillation peaks have different width and amplitude ratios depending on the value of δ_{CP}. If the experiment is able to precisely resolve these peaks in the oscillated spectrum, δ_{CP} can be measured without requiring antineutrinos.

1.2.7 Current values of oscillation parameters

The mixing angles θ and the squared mass differences Δm^2 have to be experimentally measured. Table 1.3 shows recent three-flavor oscillation parameters obtained from fits to global data [44, 45].

1.3 Neutrino Mass Ordering determination

1.3.1 Motivations for physics / Consequences of measuring the Mass Ordering

Introduced in section 1.2.4, the Neutrino Mass Ordering (NMO) remains one of the fundamental parameters of neutrino oscillations that has not yet been predicted nor measured. Determining whether the NMO is normal or inverted is one of the main goals of future neutrino oscillation experiments, and has important consequences in particle and neutrino physics.
As mentioned in section 1.1.3.1, neutrinos can have a Dirac mass, in which case neutrinos and antineutrinos are distinct particles, or a Majorana mass in which case a neutrino is its own antiparticle, distinguished only by its chirality. Determining the nature of neutrino mass by searching for neutrinoless double beta decay, as described in section 1.1.3.2, is only feasible in the case of an Inverse Ordering with expected experimental sensitivities in the next decade. The NMO thus has an impact on the time scale of searches for neutrinoless double beta decay. Determining the NMO also has consequences for neutrino astrophysics, particularly in the light curves of supernovae and for measurements of CP violation, which is necessary for leptogenesis [46], a possible explanation for the matter-antimatter symmetry in the universe.

Supernova neutrinos The NMO also has consequences for the flavour composition of neutrinos produced by nuclear processes in supernovae. Supernova neutrinos undergo the MSW effect with ordinary matter within the star itself, as well as interactions with other neutrinos [47]. In numerical simulations, the most dramatic consequence of changing the NMO is a flip in the expected energy spectrum between ν_es and ν_μs [48]. The consequence of this for a terrestrial neutrino detector, sensitive to supernova $\overline{\nu}_e$ via inverse beta decay, is a change in the shape of the supernova light curve over time [49]. This has been proposed as a method of measuring the NMO but, given the rarity of galactic supernovae, such a measurement would likely come after the NMO has already been determined by other means. It would also be very model dependent. Instead, an independent

		Normal Ordering (best fit)		Inverted Ordering ($\Delta\chi^2 = 2.7$)	
		bfp $\pm$ 1σ	3σ range	bfp $\pm$ 1σ	3σ range
Without SK atmospheric data	$\sin^2\theta_{12}$	$0.304^{+0.013}_{-0.012}$	$0.269 \to 0.343$	$0.304^{+0.013}_{-0.012}$	$0.269 \to 0.343$
	$\theta_{12}/^\circ$	$33.44^{+0.78}_{-0.75}$	$31.27 \to 35.86$	$33.45^{+0.78}_{-0.75}$	$31.27 \to 35.87$
	$\sin^2\theta_{23}$	$0.570^{+0.018}_{-0.024}$	$0.407 \to 0.618$	$0.575^{+0.017}_{-0.021}$	$0.411 \to 0.621$
	$\theta_{23}/^\circ$	$49.0^{+1.1}_{-1.4}$	$39.6 \to 51.8$	$49.3^{+1.0}_{-1.2}$	$39.9 \to 52.0$
	$\sin^2\theta_{13}$	$0.02221^{+0.00068}_{-0.00062}$	$0.02034 \to 0.02430$	$0.02240^{+0.00062}_{-0.00062}$	$0.02053 \to 0.02436$
	$\theta_{13}/^\circ$	$8.57^{+0.13}_{-0.12}$	$8.20 \to 8.97$	$8.61^{+0.12}_{-0.12}$	$8.24 \to 8.98$
	$\delta_{CP}/^\circ$	195^{+51}_{-25}	$107 \to 403$	286^{+27}_{-32}	$192 \to 360$
	$\frac{\Delta m^2_{21}}{10^{-5}eV^2}$	$7.42^{+0.21}_{-0.20}$	$6.82 \to 8.04$	$7.42^{+0.21}_{-0.20}$	$6.82 \to 8.04$
	$\frac{\Delta m^2_{3l}}{10^{-3}eV^2}$	$+2.514^{+0.028}_{-0.027}$	$+2.431 \to +2.598$	$-2.497^{+0.028}_{-0.028}$	$-2.583 \to -2.412$
		Normal Ordering (best fit)		Inverted Ordering ($\Delta\chi^2 = 7.1$)	
		bfp $\pm$ 1σ	3σ range	bfp $\pm$ 1σ	3σ range
With SK atmospheric data	$\sin^2\theta_{12}$	$0.304^{+0.012}_{-0.012}$	$0.269 \to 0.343$	$0.304^{+0.013}_{-0.012}$	$0.269 \to 0.343$
	$\theta_{12}/^\circ$	$33.44^{+0.77}_{-0.74}$	$31.27 \to 35.86$	$33.45^{+0.78}_{-0.75}$	$31.27 \to 35.87$
	$\sin^2\theta_{23}$	$0.573^{+0.016}_{-0.020}$	$0.415 \to 0.616$	$0.575^{+0.016}_{-0.019}$	$0.419 \to 0.617$
	$\theta_{23}/^\circ$	$49.2^{+0.9}_{-1.2}$	$40.1 \to 51.7$	$49.3^{+0.9}_{-1.1}$	$40.3 \to 51.8$
	$\sin^2\theta_{13}$	$0.02219^{+0.00062}_{-0.00063}$	$0.02032 \to 0.02410$	$0.02238^{+0.00063}_{-0.00062}$	$0.02052 \to 0.02428$
	$\theta_{13}/^\circ$	$8.57^{+0.12}_{-0.12}$	$8.20 \to 8.93$	$8.60^{+0.12}_{-0.12}$	$8.24 \to 8.96$
	$\delta_{CP}/^\circ$	197^{+27}_{-24}	$120 \to 369$	282^{+26}_{-30}	$193 \to 352$
	$\frac{\Delta m^2_{21}}{10^{-5}eV^2}$	$7.42^{+0.21}_{-0.20}$	$6.82 \to 8.04$	$7.42^{+0.21}_{-0.20}$	$6.82 \to 8.04$
	$\frac{\Delta m^2_{3l}}{10^{-3}eV^2}$	$+2.517^{+0.026}_{-0.028}$	$+2.435 \to +2.598$	$-2.498^{+0.028}_{-0.028}$	$-2.581 \to -2.414$

Table 1.3: Three-flavor oscillation parameters from fit to global data as of July 2020. The results shown in the upper (lower) section are obtained without (with) the inclusion of the tabulated χ^2 data on atmospheric neutrinos provided by the Super-Kamiokande collaboration (SK-atm). The numbers in the 1st (2nd) column are obtained assuming Normal Ordering NO (Inverse Ordering IO), i.e., relative to the respective local minimum. Minimization with respect to the ordering provides the same results as Normal Ordering, except for the 3σ range of Δm^2_{3l} in the analysis without SK-atm. Note that $\Delta m^2_{3l} = \Delta m^2_{31} > 0$ for NO and $\Delta m^2_{3l} = \Delta m^2_{32} < 0$ for IO. [44, 45]

measurement of the NMO will allow for tighter constraints on supernova neutrino emission models, having removed one source of uncertainty.

CP phase measurements As will be detailed in section 1.3.2 with the most recent constraints on δ_{CP} from NOνA and T2K, changing the fitted NMO hypothesis introduces a degeneracy in δ_{CP} (concept introduced in section 1.2.6), where its best fit value assuming NO is not equal to its best fit value assuming IO. While these experiments do have some sensitivity to the NMO on their own, an independent rejection of one NMO hypothesis over the other would reduce the uncertainty on δ_{CP}.

1.3.2 Current experiments and status

As described in section 1.2.5, long-baseline experiments can be sensitive to the NMO due to the interaction of neutrinos with matter as they pass through the Earth, with the baseline itself being a critical factor in the sensitivity. Due to electron neutrinos interacting with matter differently than other neutrino flavours states, ν_e appearance is enhanced for the normal ordering but suppressed for the inverted ordering, with this effect being reversed for ν_e and $\overline{\nu}_e$. The NMO can thus be estimated by measuring $\nu_\mu \rightarrow \nu_e$ and $\overline{\nu}_\mu \rightarrow \overline{\nu}_e$ appearance, with an expected asymmetry in the oscillation probabilities due to the matter effects. This can be performed with atmospheric or accelerator neutrinos. However, CP violation in the lepton sector would also contribute to such an asymmetry, which is why a combination of several experiments at different baselines can disentangle the competing effects of CP violation and matter-induced neutrino-antineutrino differences, and thus improve the sensitivity to the NMO significantly. The T2K (Japan) and NOνA (US) accelerator experiments are currently performing this measurement.

T2K uses an intense beam of muon neutrinos sent from Tokai (east coast of Japan) to Kamioka, at a baseline of 295 km ($\frac{L}{E} = \frac{295}{0.6}\frac{km}{GeV}$), while NO$\nu$A is an off-axis experiment using an upgraded NuMI beam ν_μ from Fermilab, directed at a detector in Ash River, Northern Minnesota, about 810 km away ($\frac{L}{E} = \frac{810}{2.3}\frac{km}{GeV}$). While T2K has a reduced sensitivity to the NMO when compared to NOνA, due to its shorter baseline, NOνA was projected to have the potential to make a measurement of the NMO at the 2-3 σ level, depending on the value of the CP phase parameter, δ_{CP}. The statistical separation power of NOνA showed that the separation is easiest when $\delta_{CP} \approx \frac{3\pi}{2}$. For about a third of the range of δ_{CP}, centered around $\delta_{CP} \approx \frac{3\pi}{2}$, NO$\nu$A can determine the ordering with a confidence of 2-3 σ. A combination of NOνA and T2K has the ability to resolve the ordering at 1-3 σ significance for all values of δ_{CP} : as T2K is primarily sensitive to the CP asymmetry between neutrinos and antineutrinos (effect of δ_{CP}), its results can be subtracted from the NOνA asymmetries to extract the matter-induced ordering signal.

The $P(\nu_\mu \rightarrow \nu_e)$ vs $P(\overline{\nu}_\mu \rightarrow \overline{\nu}_e)$ method is illustrated in Figure 1.8a. The X-axis represents the total number of electron-like candidates measured in the neutrino beam, another representation of the $P(\nu_\mu \rightarrow \nu_e)$ oscillation probability. The Y-axis represents the total number of electron-like candidates measured in the anti-neutrino beam, another representation of the $P(\overline{\nu}_\mu \rightarrow \overline{\nu}_e)$ oscillation probability. The theoretical values of these probabilities (or event counts) depend on the value of δ_{CP}, and so their 2D representation is shown as an elliptic distribution with 4 theoretically computed points for 4 key values of δ_{CP}. $P(\nu_\mu \rightarrow \nu_e)$ vs $P(\overline{\nu}_\mu \rightarrow \overline{\nu}_e)$ for $\delta_{CP} = 0$ is represented as an empty circle, for $\delta_{CP} = \frac{\pi}{2}$ as a full circle, for $\delta_{CP} = \pi$ as an empty square and for $\delta_{CP} = \frac{3\pi}{2}$ as a full square. This theoretical distribution is also computed and represented according to different models, in blue assuming the Normal Ordering (Hierarchy) and in red assuming the

Inverse Ordering, as well as for different scenario of θ_{23} : belonging to the lower ($< \frac{\pi}{2}$) or upper octant ($> \frac{\pi}{2}$).

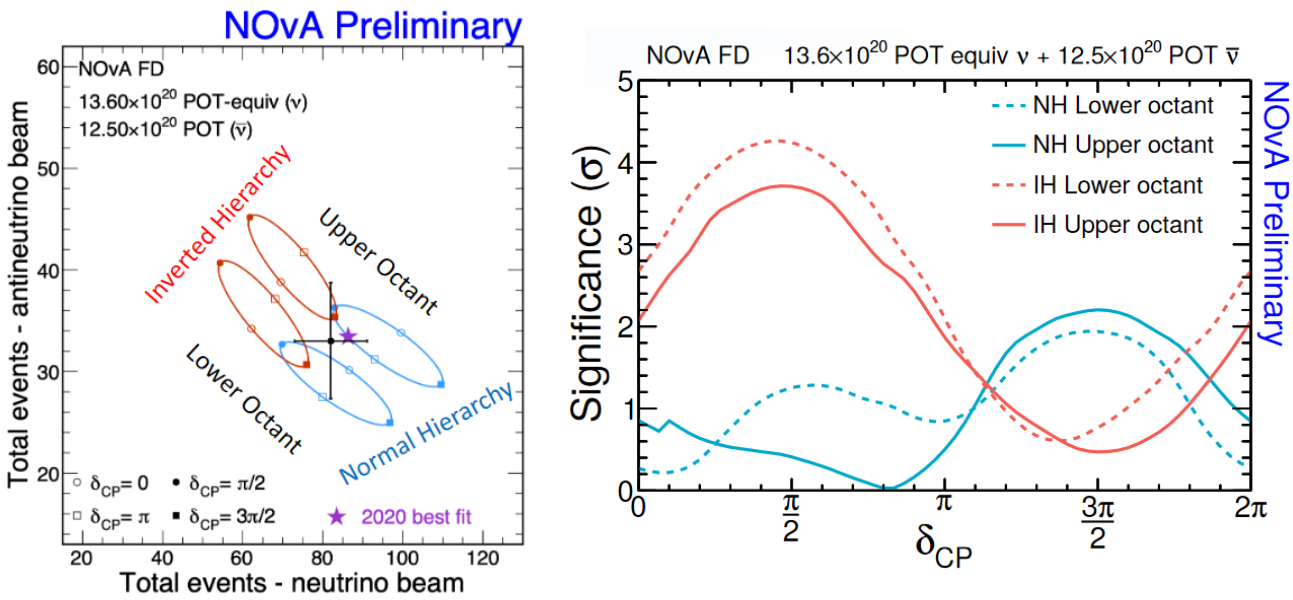

(a) (b)

Figure 1.8: (a) $P(\nu_\mu \to \nu_e)$ vs $P(\overline{\nu}_\mu \to \overline{\nu}_e)$ for the NOνA experiment, represented as the total number of electron-like candidates measured in the neutrino beam vs in the anti-neutrino beam. The latest measurement as of 2020, as well as the best fit, are superimposed on the theoretical values computed for the NO and IO models and varying values of δ_{CP} and θ_{23}. (b) Significance of the NOνA measurement in favoring a NMO model for the full range of δ_{CP} values. [50]

NOνA's measurement is shown as the black dot with error bars, and was performed with a data volume of 13.60×10^{20} POT-equiv in the neutrino beam ("Protons on Target", typical performance indicator for the data volume of accelerator-based neutrino experiments) and a data volume of 12.50×10^{20} POT-equiv in the anti-neutrino beam. NOνA's best fit to a theoretical model is represented as the purple star in Figure 1.8a.

This measurement and this best fit show no strong asymmetry in the rates of appearance of ν_e and $\overline{\nu}_e$ (when considering oscillation probabilities). Notably, the models corresponding to {NO, $\delta_{CP} = \frac{\pi}{2}$} (blue, full circles) and {IO, $\delta_{CP} = \frac{3\pi}{2}$} (red, full squares) are compatible with NOνA's results within 1 σ, both for the lower and upper octants of θ_{23}. NOνA's results, however, disfavor hierarchy-δ_{CP} combinations which would produce a strong asymmetry in the rates of appearance of ν_e and $\overline{\nu}_e$. They exclude the {IO, $\delta_{CP} = \frac{\pi}{2}$} model (red, full circles) at $> 3\ \sigma$ (for both octants), and disfavor the {NO, $\delta_{CP} = \frac{3\pi}{2}$} (blue, full squares) model at $\sim$2 σ (for both octants as well).

In Figure 1.8b, which represents the significance of the NOνA measurement in favoring a given model for the full range of δ_{CP} values, this translates as rejecting the IO around $\delta_{CP} = \frac{\pi}{2}$ for both octants (red peak, full and dashed lines) and the NO around $\delta_{CP} = \frac{3\pi}{2}$ for both octants (blue peak, full and dashed lines), as well as favoring the IO around $\delta_{CP} = \frac{3\pi}{2}$ for both octants (red valley, full and dashed lines) and the NO around $\delta_{CP} = \frac{\pi}{2}$ for both octants (blue valley, full and dashed lines). NOνA's measurement only has $\sim$1 σ significance for the favored models, showing no strong preferences. The values of the best fit are $\Delta m^2_{32} = (2.41 \pm 0.07) \times 10^{-3}\text{eV}^2$, $sin^2\theta_{23} = 0.57^{+0.04}_{-0.03}$ and $\delta_{CP} = 0.82\pi$, with NOνA's conclusions, as of 2020, being a preference for the Normal Ordering at 1.0 σ and for the upper octant at 1.2 σ.

Shown in Figure 1.9a, the $P(\nu_\mu \to \nu_e)$ vs $P(\overline{\nu}_\mu \to \overline{\nu}_e)$ measurement for T2K is illustrated as it was for NOνA (Figure 1.8a), with a few different representations. Instead of different colors, full lines and dashed lines represent the Normal and the Inverse Orderings, respectively. Colors instead represent the value of $sin^2 2\theta_{23}$ and, as such, θ_{23}'s octant position: green and blue for upper octant ($> \frac{\pi}{4}$), black for $\frac{\pi}{4}$, red for lower octant ($< \frac{\pi}{4}$). The markers for the different values of δ_{CP} also vary from NOνA's representation : $\delta_{CP} = 0$ is represented as empty squares, $\delta_{CP} = \frac{\pi}{2}$ as full squares, $\delta_{CP} = \pi$ as empty circles and $\delta_{CP} = \frac{-\pi}{2} (= \frac{3\pi}{2})$ as full circles.

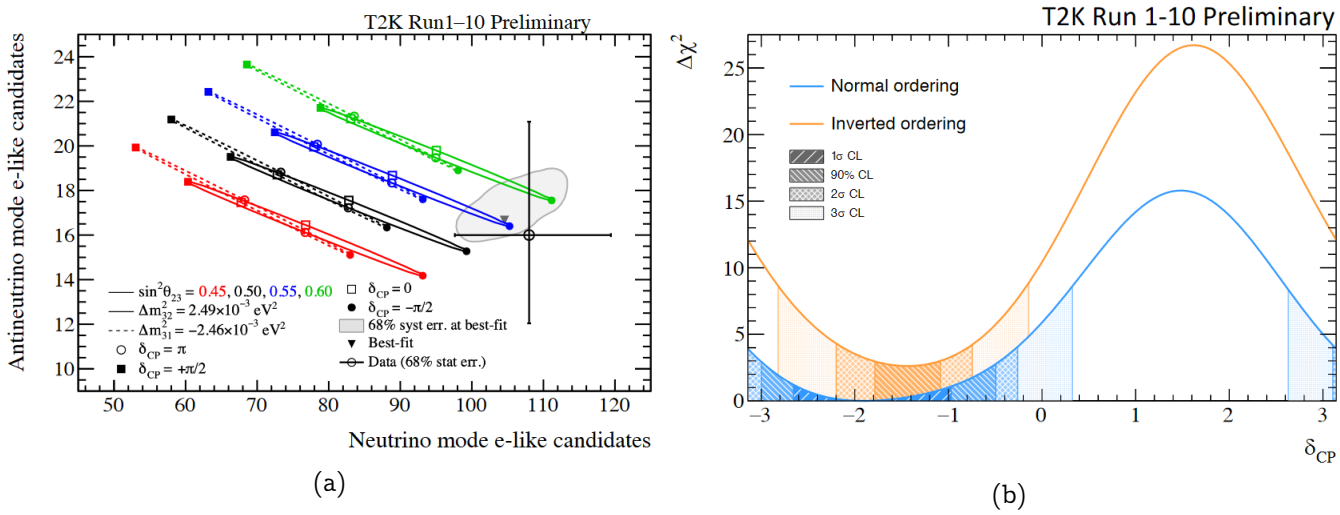

(a) (b)

Figure 1.9: $P(\nu_\mu \to \nu_e)$ vs $P(\overline{\nu}_\mu \to \overline{\nu}_e)$ for the T2K experiment. The latest measurement as of 2020, as well as the best fit, are superimposed on the theoretical values computed for the NO and IO models and varying values of δ_{CP} and θ_{23}. (b) Significance of the T2K measurement in favoring a NMO model for the full range of δ_{CP} values. [51]

T2K's measurement is shown as the black empty circle with error bars, the best fit as the full downwards triangle, and the 68% systematic error at best fit as the grey area. This measurement and this best fit are significantly different from NOνA's. They favor the model corresponding to {NO, $\delta_{CP} = \frac{-\pi}{2} (= \frac{3\pi}{2})$} for the upper octant (blue and green, full circles, full lines), which is on opposition with NOνA's measurement which disfavored it at $\sim$2 σ, and they strongly disfavor the {NO, $\delta_{CP} = \frac{\pi}{2}$} model for both octants (full squares, full lines), which NOνA slightly favored ($\sim$1 σ). On the other hand, they tend to favor the {IO, $\delta_{CP} = \frac{-\pi}{2} (= \frac{3\pi}{2})$} model for the upper octant (blue and green, full circles, dashed lines), while they disfavor the {IO, $\delta_{CP} = \frac{\pi}{2}$} model for both octants (full squares, dashed lines), as did NOνA.

Figure 1.9b also slightly differs from NOνA in its representation. The X-axis shows δ_{CP} in radians, as opposed to degrees in NOνA, and spans a range equivalent to $[-\pi, \pi]$ instead of $[0, 2\pi]$. The Y-axis shows the $\Delta\chi^2$ of the measurement, which represents the discriminating power of the analysis method between NO and IO, and the square root of which must be taken to obtain the significance in σ values. The measurement from T2K translates in this figure as rejecting the IO and the NO around $\delta_{CP} \sim 1.5 (= \frac{\pi}{2})$ (orange and blue peaks) and favoring the IO and the NO around $\delta_{CP} \sim -1.5 (= \frac{-\pi}{2} = \frac{3\pi}{2})$ (orange and blue valleys). As with NOνA's measurement, the significance values for the favored regions are low, with < 1 σ for the NO and $\sim$2 σ for the IO.

This discrepancy between NOνA's and T2K's results is illustrated in Figure 1.10, which shows the best fit from both experiments on a ($sin^2\theta_{23}$, δ_{CP}) scale. θ_{23}'s octant position is represented by the value of $sin^2\theta_{23}$, with $sin^2\theta_{23} = 0.5$ corresponding to $\theta_{23} = \frac{\pi}{4}$ (maximal mixing). Larger and lower values of $sin^2\theta_{23}$ correspond to the upper and lower octants of θ_{23}, respectively. In this figure, NOνA's result is excluded by T2K, and while the Confidence Levels (CL) of 90% and 68%

for both fits are also represented, they illustrate that there is no coverage between the 68% CL of the two experiments, with only very few areas covered by both fits at the 90% CL.

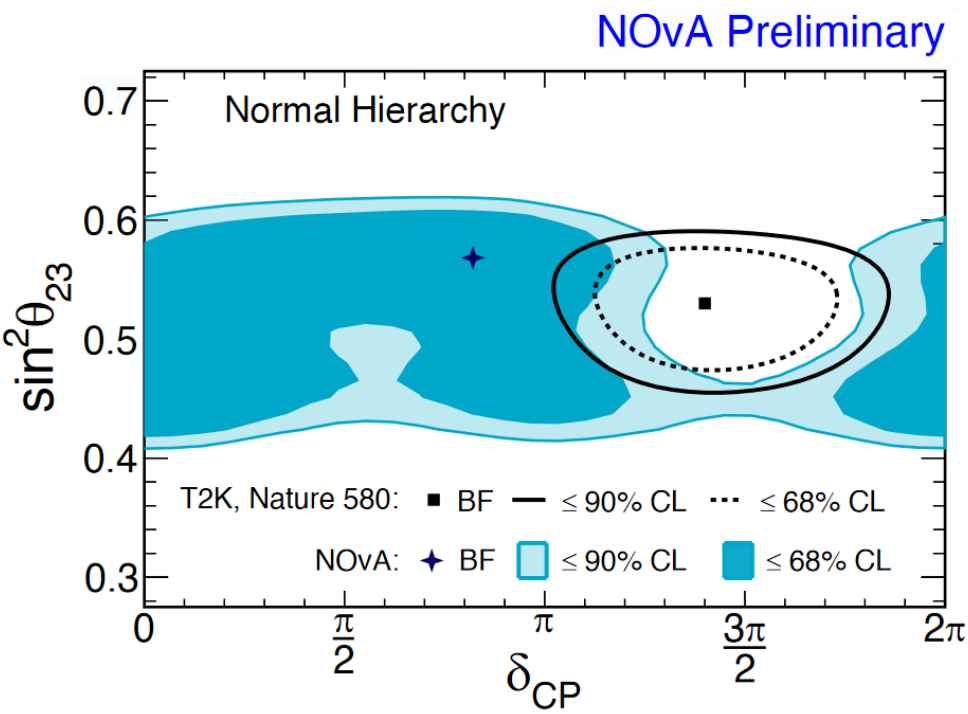

Figure 1.10: Best fits of NOνA's and T2K's measurement on a $(sin^2\theta_{23}, \delta_{CP})$ scale. NOνA's result is excluded by T2K, with no coverage between the 68% CL of the two experiments, and only very few areas covered by both fits at the 90% CL. [50]

1.3.3 Future experiments using matter-modified oscillations

As described in section 1.2.5 and illustrated in section 1.3.2 with the T2K and NOνA experiments, the oscillation probability in the $\nu_\mu \rightarrow \nu_e$ appearance channel tends to be enhanced (suppressed) if the mass ordering is normal (inverted) due to the MSW effect. For the antineutrino channel, $\overline{\nu}_\mu \rightarrow \overline{\nu}_e$, the effect is reversed. Therefore, the mass ordering can be determined by measuring these oscillation probabilities, using either atmospheric neutrinos having propagated through Earth matter or accelerator neutrinos over a long baseline.

1.3.3.1 Using atmospheric neutrinos - Hyper-K / ORCA

Hyper-K Hyper-Kamiokande [52] is the successor to Super-Kamiokande, and is a next-generation, large-scale neutrino detector designed to employ the same technique as Super-K of using a ring-imaging water Cherenkov detector to detect rare interactions of neutrinos and the possible spontaneous decay of protons and bound neutrons. It will look into the NMO using matter modified atmospheric neutrino oscillations, but will also measure neutrinos generated in the J-PARC accelerator facility (Tokai, Japan) using the same detector as the T2K experiment (295 km baseline, upgraded J-PARC beam power of 750 kW in the near future with 1300 kW long-term projection).
The optimized configuration of the detector determined by the Hyper-K collaboration is a cylindrical vertical tank with a 40% PMT photo-coverage ($\sim$ 40,000 PMTs), as shown in Figure 1.11.

This array of 20-inch PMTs (with single-photon sensitivity as the Cherenkov effect produces few photons) will enable a reconstruction of the spatial and timing distributions of the Cherenkov photons which are emitted by secondary particles from neutrino interactions and nucleon decays. A target mass of at least $\mathcal{O}(10^2)$ kton is needed in order to accumulate $\mathcal{O}(10^3)$ electron neutrino signal events and to measure the CP violation effect (δ_{CP}) with an accuracy of a few %, which is why the cylindrical detector was designed to be 60 m high and 74 m wide. With the project having been officially approved in 2020, data-taking operations are expected to begin in 2027.

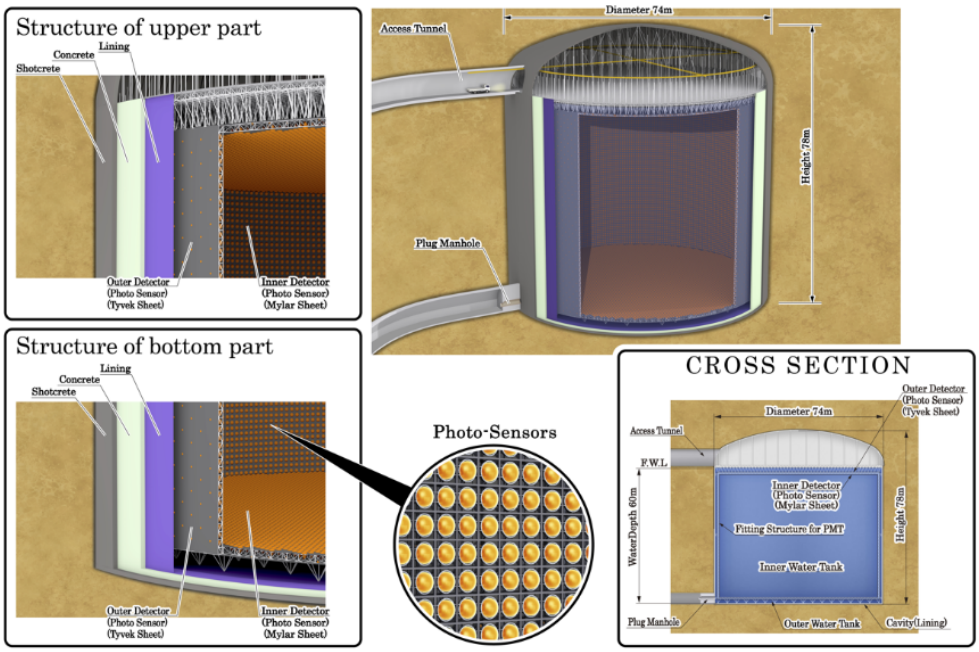

Figure 1.11: Schematic view of the cylindrical tank of Hyper-K, instrumented with high density (40% photocoverage) PMTs [52].

With a great discrimination power between charged current ν_e and ν_μ interactions, Hyper-K will have improved access to the oscillation modes with the cleanest mass ordering signature, $\nu_\mu \rightarrow \nu_e$ and $\overline{\nu}_\mu \rightarrow \overline{\nu}_e$. Hyper-Kamiokande will also make combined beam and atmospheric neutrino oscillation measurements for an increased sensitivity, With a reconstruction performance expected to meet or exceed that of its predecessor, Super-Kamiokande, as the size and configuration of the two detectors are similar enough that event selections and systematic errors are not expected to differ largely, the larger event statistics granted by Hyper-K are expected to result in improved detector systematic uncertainties.

Hyper-K's expected sensitivity when resolving the neutrino mass hierarchy and the octant of θ_{23} is shown in Figure 1.12, assuming a single cylindrical detector and 10 years of data-taking. Both panels of the figure are shown as a function of the true value of $sin^2\theta_{23}$ for the range of values allowed by recent measurements from the T2K experiment, and the width of the bands in the figures illustrates the uncertainty from δ_{CP}. In each panel, the sensitivity is defined as $\sqrt{\Delta\chi^2}$, with $\Delta\chi^2 = \Delta\chi^2_{NO} - \Delta\chi^2_{IO}$. After 10 years (a 1.9 Mton.year exposure), Hyper-K is expected to resolve the mass ordering at $\sqrt{\Delta\chi^2} > 3$ for both ordering assumptions and when $sin^2\theta_{23} > 0.53$. Similarly, the atmospheric neutrino data alone can be used to determine the θ_{23} octant at $\sqrt{\Delta\chi^2} > 3$ when $|\theta_{23} - 45| > 4°$.

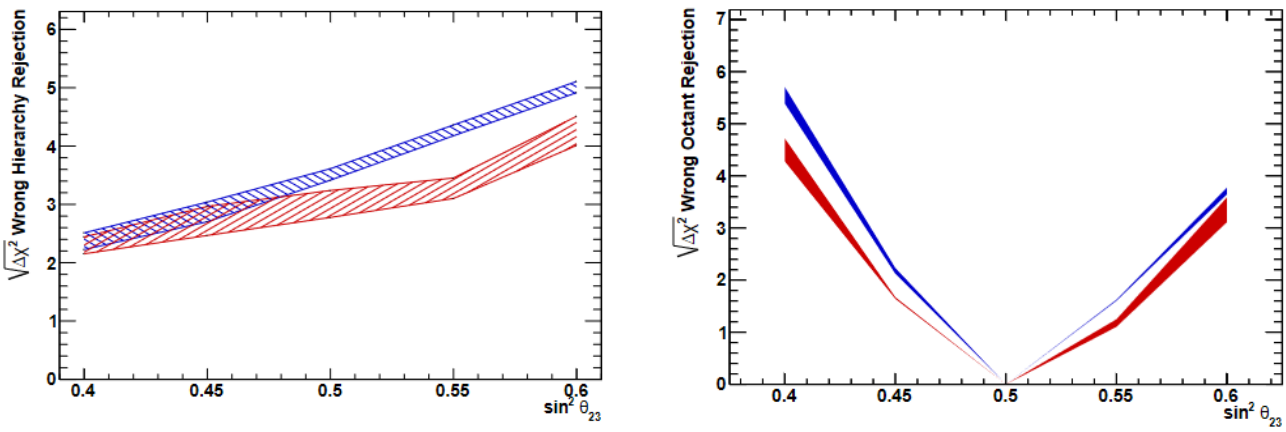

(a) (b)

Figure 1.12: (a) Neutrino mass hierarchy sensitivity as a function of the true value of $sin^2\theta_{23}$ for a single detector after 10 years (1.9 Mton.year exposure). The blue (red) band denotes the Normal (Inverted) Ordering and the uncertainty from δ_{CP} is shown by the width of the band. (b) θ_{23} octant sensitivity as a function of the true value of $sin^2\theta_{23}$, in the same configuration. [52]

ORCA ORCA (Oscillation Research with Cosmics in the Abyss) [53] is a megaton-scale Cherenkov neutrino detector currently under construction by the KM3NeT collaboration, at a depth of 2450 m in the Mediterranean Sea. Drawing on the experience of the ANTARES collaboration, ORCA will consist of an array of 115 vertical detection units, deployed with an average horizontal separation of 20 m, forming a cylinder on the seafloor. An artistic view of the detector is shown in Figure 1.13.

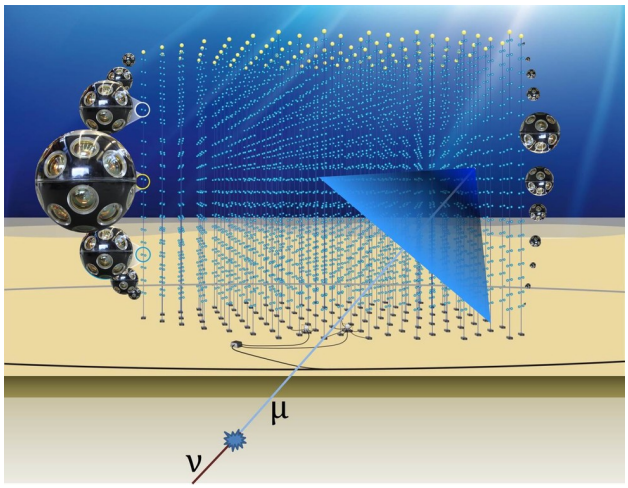

Figure 1.13: Artist view of the KM3NeT - ORCA detector.

Each line consists of 18 Digital Optical Modules (DOMs), pressure-resistant glass spheres housing 31 3-inch PMTs and their related electronics, with each DOM along a line vertically spaced at an average of 9.3 m and the first DOM at a distance of about 30 m from the seafloor. In total, a volume of about 6.7×10^6 m^3 (equivalent to 7.0 Mt of sea water) will be instrumented to detect Cherenkov radiation emitted by atmospheric neutrino interactions in the seawater and exploit the excellent optical properties of deep seawater to reconstruct both cascade events (mostly ν_e) and track events (mostly ν_μ) of atmospheric neutrinos down to a few GeV. ORCA, in its finalized state,

is expected to measure the NMO with a median significance greater than 3 σ after a few years of operation.
ORCA's sensitivity to the NMO after three years of data taking, assuming the full deployment of 115 lines, is shown as a function of θ_{23} for both NMO in Figure 1.14b. Assuming the current best estimates for θ_{23}, the NMO sensitivity is projected to be 4.4 σ for the NO and 2.3 σ for the IO. Figure 1.14b shows the sensitivity for both NMO as a function of data taking time. The NMO can be determined at the 3 σ level after 1.3 years if the true NMO is the NO. In the case of the IO, however, it may take up to 5 years even with the full deployment of 115 lines to reach the 3 σ significance. This estimation of the required data-taking time was performed assuming the deployment of 115 lines. Contrarily to other future experiments, ORCA already has a few lines installed, and as such will be able to take and analyze data progressively. A project for the deployment of 50 lines was recently approved and funded, but the deployment of all planned 115 lines will be spread on the scale of about a decade.

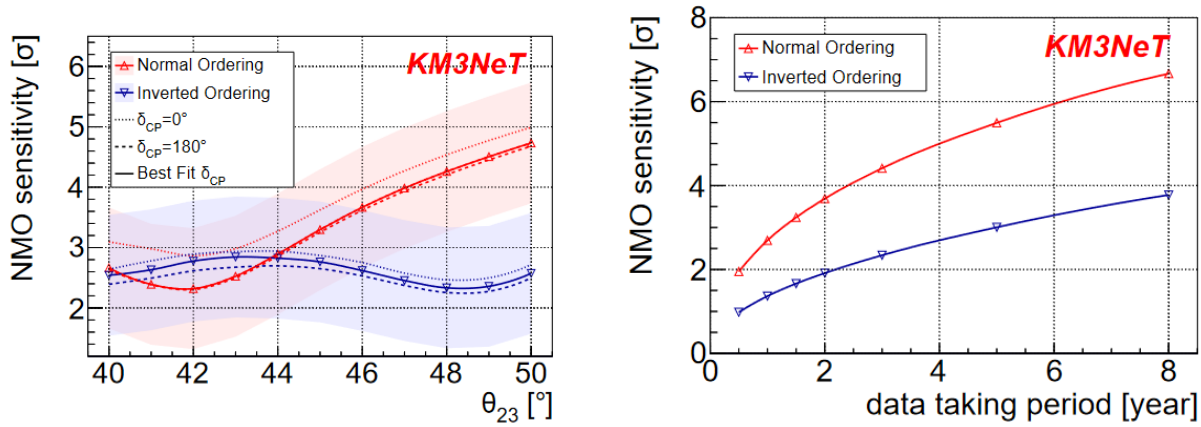

(a) (b)

Figure 1.14: (a) Sensitivity to the NMO after three years of data taking, as a function of the true θ_{23} value, for both the NO (red upwards triangles) and the IO (blue downward triangles) and under three assumptions for the value of δ_{CP}: 0° (dotted line), 180°(dashed line) and the best fitted δ_{CP} value for the NO and IO (plain line, from NuFIT [44, 45]). The coloured shaded areas represent the sensitivity that 68% of the experiment realisation would yield. (b) Sensitivity to the NMO as a function of data-taking time for both the NO (red upwards triangles) and the IO (blue downwards triangles), for the latest oscillation parameter values (NuFIT [44, 45]). [54]

1.3.3.2 Using accelerator neutrinos - DUNE

DUNE [55–57] is an experiment directly following in the footsteps of T2K and NOνA (section 1.3.2), aiming to determine the NMO using the same method of measuring ν_e and $\overline{\nu}_e$ appearance in ν_μ and $\overline{\nu}_\mu$ beams, and an even greater baseline for a significantly increased sensitivity to the NMO through the matter effects. It will consist of two neutrino detectors placed along the path of the world's most powerful neutrino beam, located at the Fermi National Accelerator Laboratory (Fermilab) in the US. The proton beam power is expected to be 1.2 MW at start-up, and increasing after some years of operation to 2.4 MW. One detector will record particle interactions near the source of the beam, while a second, much larger, detector will be located underground at the Sanford Underground Research Laboratory in Lead, South Dakota, at a 1300 km baseline from the source. This far detector will have a fiducial mass of 40 kt and will be composed of four similar modules, each instrumented as a liquid argon time-projection chamber (LArTPC). The

concept of the LArTPC provides excellent tracking and calorimetry performance, and is thus ideal for massive neutrino detectors which require a high signal efficiency and an effective background discrimination. This results in an excellent capability to identify and precisely measure neutrino events over a wide range of energies, and an excellent reconstruction of the kinematic properties with a high resolution.

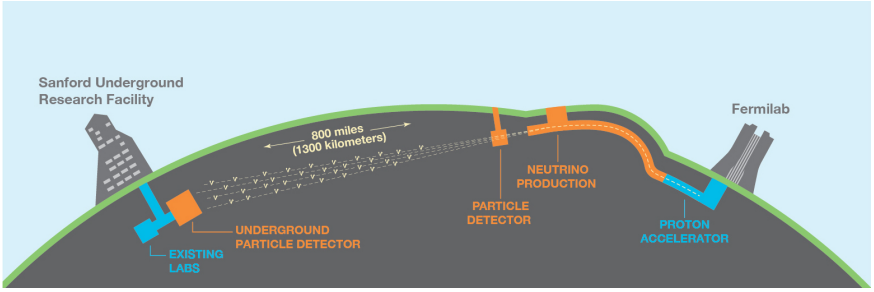

Figure 1.15: Schematic view of the DUNE detector.

At a baseline of 1300 km, the large asymmetry in the $\nu_\mu \to \nu_e$ versus $\overline{\nu}_\mu \to \overline{\nu}_e$ oscillation probabilities, the sign of which depends on the NMO, is approximately $\pm 40\%$ in the region of the peak flux. This is larger than the maximal possible CP-violating asymmetry associated with δ_{CP}, meaning that both the NMO and δ_{CP} can be determined unambiguously by DUNE with high confidence levels. DUNE's goal is to determine the NMO with a significance of at least $\sqrt{\Delta\chi^2} = 5$ for all δ_{CP} values. Figures 1.16a and 1.16b show the significance with which the NMO can be determined assuming respectively the NO and the IO as a function of the true value of δ_{CP}, for 7 and 10 years of data-taking (half in neutrino mode and the other half in antineutrino mode). The characteristic shape of the distributions is due to the near degeneracy between matter and CP-violation effects that occurs near $\delta_{CP} = \frac{\pi}{2}$ ($\delta_{CP} = \frac{-\pi}{2}$) for the true NO (IO). For such event statistics and a time scale optimistically starting around 2026, the NMO is projected to be determined with a minimum significance of $\sqrt{\Delta\chi^2} = 5$ for all δ_{CP} values.

1.3.4 Investigating the NMO using vacuum oscillations with JUNO

The Jiangmen Underground Neutrino Observatory (JUNO) is a multipurpose reactor neutrino experiment with the primary goal of determining the Neutrino Mass Ordering using vacuum oscillations instead of matter modified oscillations like other future experiments (section 1.3.3). It will be located in Jiangmen, China, at a baseline of 53 km from the Taishan and Yangjiang reactor complexes (26.6 GW_{th} total thermal power), and made up of a spherical 20 kton liquid scintillator-based detector under a rock overburden of about 700 m.

Reactor antineutrinos will be detected by the $\overline{\nu}_e + p \to e^+ + n$ Inverse Beta Decay (IBD) reaction in which the reactor antineutrino $\overline{\nu}_e$ interacts with a proton p from the liquid scintillator, creating a positron e^+ and a neutron n. The positron quickly deposits its energy and annihilates into two 511 keV γ particles, which gives a prompt signal. The neutron then scatters in the detector, undergoing thermalization until it is captured by a proton $\sim$200 μs later and releases a 2.2 MeV γ. Considering how the reactor flux decreases with the energy of the $\overline{\nu}_e$, and how the cross-section of the inverse beta decay reaction increases with this same energy, the energy at which the $\overline{\nu}_e$ are detected is distributed in a bell curve around 4 MeV, as is illustrated in the observable neutrino spectrum shown in Figure 1.17.

The oscillated neutrino spectrum, derived from this observable spectrum after oscillation of the $\overline{\nu}_e$ into other flavour states, is expected to be different for the normal and inverted mass orderings, and the small differences in the neutrino spectrum depending on the considered NMO will be

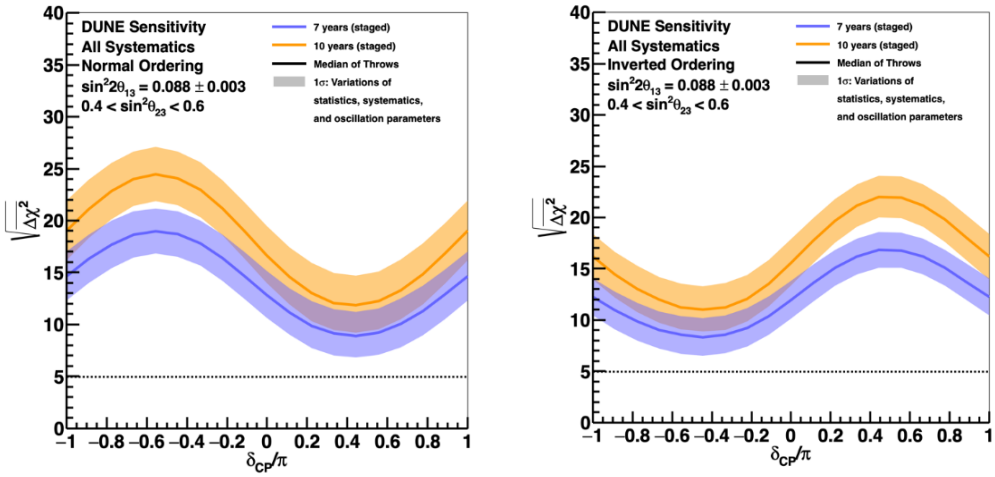

(a) (b)

Figure 1.16: (a) Significance of the DUNE determination of the neutrino mass ordering, as a function of the true value of δ_{CP}, for seven (blue) and ten (orange) years of exposure and assuming the NO. The widths of the transparent bands cover 68% of fits in which random throws are used to simulate statistical variations and select true values of the oscillation and systematic uncertainty parameters, constrained by pre-fit uncertainties. The solid lines show the median sensitivity. (b) Significance of the DUNE determination of the neutrino mass ordering, as a function of the true value of δ_{CP}, for seven (blue) and ten (orange) years of exposure and assuming the IO. [58]

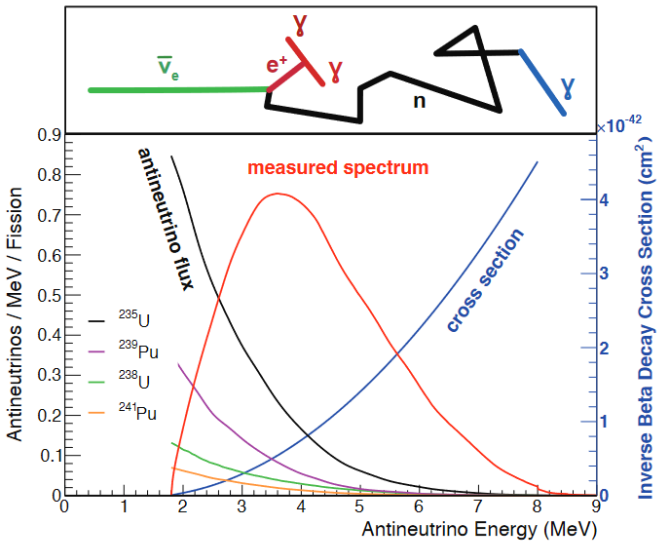

Figure 1.17: The observable $\overline{\nu}_e$ spectrum (red), represented as a function of the antineutrino energy, is a product of the antineutrino flux from reactor (black) and the cross section of inverse beta decay (blue). The contributions of four fission isotopes to the antineutrino flux are shown for a typical pressurized water reactor. The inverse beta decay reaction is drawn schematically on top of the spectrum. [59]

measurable in the oscillation patterns caused by the non-negligible value of θ_{13}. Section 1.2.3 introduced the concept of measuring θ_{13} by measuring the ν_e survival probability in the 3-flavour

case (Equation 1.56, rewritten for clarity) :

$$P(\nu_e \to \nu_e) = 1 - sin^2(2\theta_{13}) \left[cos^2(\theta_{12})sin^2(\Delta_{31}) + sin^2(\theta_{12})sin^2(\Delta_{32})\right] \\ - sin^2(2\theta_{12})cos^4(\theta_{13})sin^2(\Delta_{12}) \tag{1.65}$$

where $\Delta_{ij} = 1.27\Delta m^2_{ij}\frac{L}{E}$. This survival probability involves the solar (θ_{12}) and atmospheric (θ_{13}) mixing angles as well as the solar (Δm^2_{12}) and atmospheric (Δm^2_{31} and Δm^2_{32}) mass splittings and, at a short baseline from the source, is only sensitive to the atmospheric driven term (Equation 1.58). One of the ways to measure this probability is to use the $\overline{\nu}_e$ generated in vast quantities in nuclear reactors ($\sim 10^{20}$ neutrinos/GW), with invariance under $\widehat{CPT}$ implying that $P(\overline{\nu}_e \to \overline{\nu}_e) = P(\nu_e \to \nu_e)$. This was the method used by reactor neutrino experiments Daya Bay, Double Chooz and RENO for a precise measurement of θ_{13}.
Daya Bay, located in Southern China, is made up of eight 20-ton liquid scintillator-based detectors observing $\overline{\nu}_e$ from 6 nuclear reactor cores, with baselines of 360 m, 500 m and 1700 m. It reported in 2012 a positive measurement of $sin^2(2\theta_{13})$, comparing the measured energy spectrum of $\overline{\nu}_e$ from the reactors to the model spectrum in the absence of oscillations and finding a clear deficit in the observed data. Figure 1.18 shows results from Daya Bay published in 2018, which gave a $sin^2(2\theta_{13})$ value of 0.0856 ± 0.0029 [60] and thus a non-negligible value of θ_{13} of $\sim 8.5°$. This result was validated by measurements from RENO and Double Chooz who reported mixing angle measurements of $sin^2(2\theta_{13}) = 0.0896 \pm 0.0048$ [61] and $sin^2(2\theta_{13}) = 0.105 \pm 0.014$ [62].

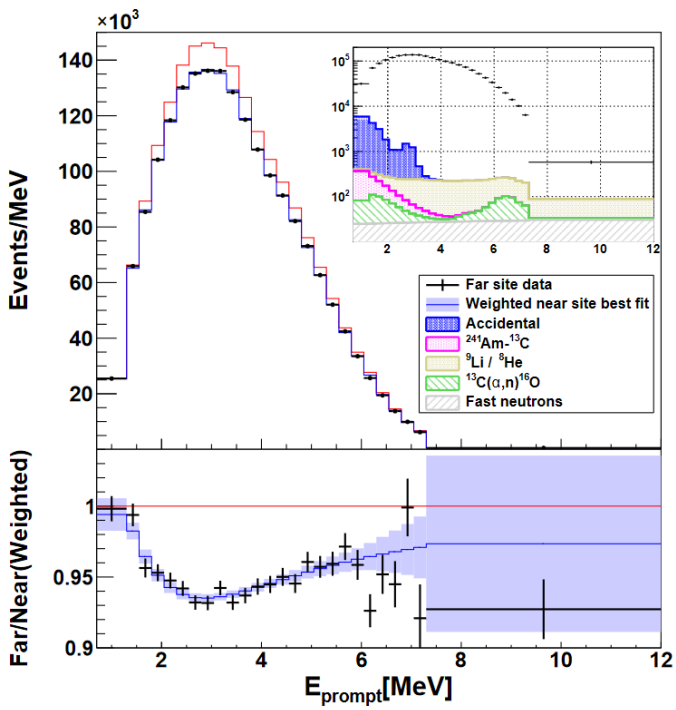

Figure 1.18: Daya Bay's 2018 reported results, showing the background-subtracted energy spectrum at the far site (black dots) compared to the expected spectrum (derived from near-site measurements) excluding (red line) or including (blue line) the best-fit oscillation. The ratios of the data points to the expected non-oscillated spectrum are shown in the bottom panel. [60]

As $\theta_{13} \neq 0$, the atmospheric driven term in Equation 1.65 has an impact on the survival probability, and as its value depends on the mass ordering (Δm^2_{32} and Δm^2_{31} have different values depending

on the NMO), this measurement can be used to probe the NMO using vacuum oscillations.
The values taken by this probability, as a function of the baseline L, are represented in Figure 1.19, with several components highlighted : a main, slow oscillation driven by the solar parameters (Δm^2_{12} and θ_{12}) and corresponding to the second term of Equation 1.65, and a faster and finer oscillation driven by the atmospheric parameters (Δm^2_{31}, Δm^2_{32} and θ_{13}) and corresponding to the first term of Equation 1.65. In the total spectrum, the fast atmospheric oscillations are observed on top of the slow solar ones.

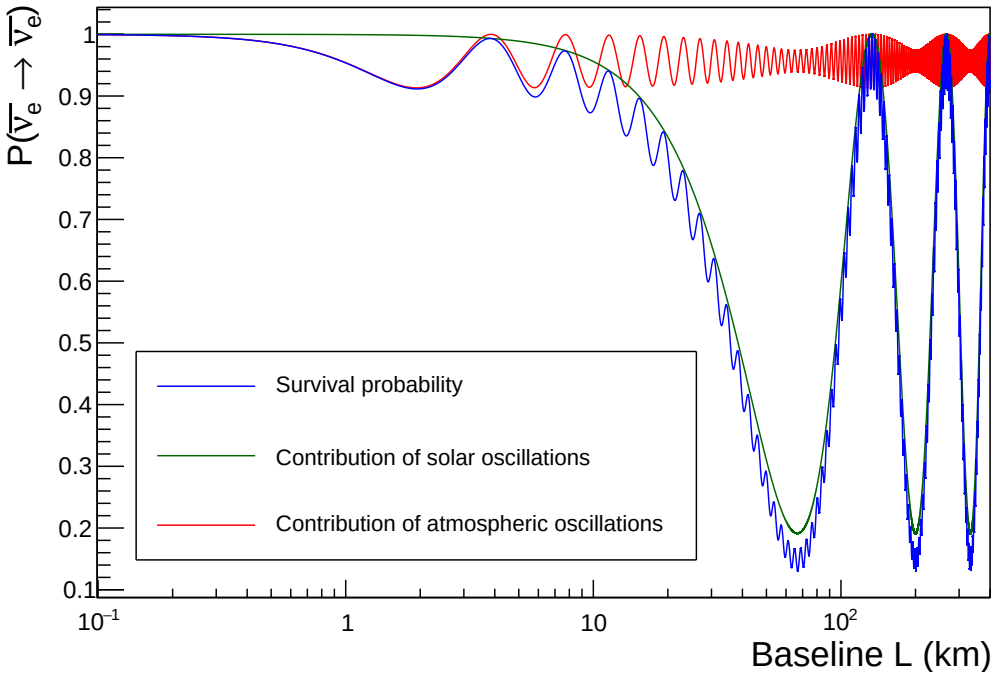

Figure 1.19: Electronic antineutrino survival probability (blue) as a function of the baseline, computed for a $\overline{\nu}_e$ energy of 4 MeV. The solar (green) and atmospheric (red) components of the oscillations are also represented.

In order to perform the most precise measurement of θ_{12}, the experiment must be maximally sensitive to the solar component of the oscillations, which means that $sin^2(1.27\Delta m^2_{12}\frac{L}{E})$ needs to be maximal and which requires $1.27\Delta m^2_{12}\frac{L}{E} = \frac{\pi}{2}$. For antineutrino energies around 4 MeV, and for a Δm^2_{12} value of $7.42^{+0.21}_{-0.20}$ (from Table 1.3), this gives an optimal baseline $L \sim 40 - 70$ km. In Figure 1.19, the first maximal oscillation can indeed be observed around these baseline values.
The atmospheric component of the $\overline{\nu}_e$ survival probability, illustrated by the fast oscillations in Figure 1.19, is responsible for the fine structure of the oscillated antineutrino energy spectrum, which contains the NMO information. The spectrum is shown in Figure 1.20, in which the solid grey line represents the non-oscillated spectrum, the dashed grey line corresponds to the spectrum after the solar-driven oscillations, and the blue and red solid lines take into account the fast atmospheric-driven oscillations for the NO and the IO, respectively. As can be observed, the oscillation pattern is slightly different depending on the NMO.
The precise measurement of the oscillated antineutrino spectrum is thus crucial in JUNO for the determination the NMO. Since the fine structure of the neutrino oscillations can only be resolved with an energy resolution better than δm^2_{21} / $|\delta m^2_{31}|$, this requires an unprecedented relative energy resolution of $\frac{\sigma_E}{E} = 3\%/\sqrt{E_{vis}}$, E_{vis} being the visible energy in the detector in MeV. This method

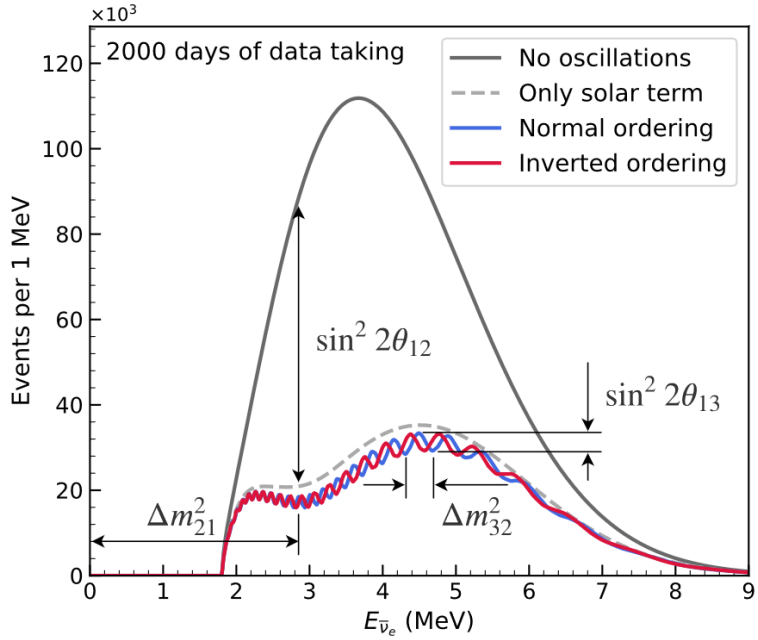

Figure 1.20: Expected antineutrino energy spectrum for the JUNO experiment, weighted by IBD cross-section and assuming 2000 days of data-taking, with and without oscillation for the NO and IO. The dependence on the solar and atmospheric oscillation parameters is also shown. [59]

of identification of the NMO, by using the oscillation interplay between Δm^2_{31} and Δm^2_{32}, has no dependence on the CP-violating phase δ_{CP} or the octant of θ_{23}, playing a key role when combined with other neutrino experiments.

From the measured oscillated antineutrino spectrum, the sensitivity to the NMO can be evaluated by performing different spectral analyses. One of the proposed analyses is employing a least-squares method and constructing a χ^2 function [63]. Because only two of the three mass-squared differences are independent, Δm^2_{12} is taken as one of the working parameters for this method, with a second working parameter defined as :

$$\Delta m^2_{ee} = cos^2(\theta_{12})\Delta m^2_{31} + sin^2(\theta_{12})\Delta m^2_{32} \tag{1.66}$$

to precisely and optimally determine the shape of the disappearance probability around the first oscillation minimum.

The χ^2 function is constructed as :

$$\chi^2_{REA} = \sum_{i=1}^{N_{bin}} \frac{[M_i - T_i(1 + \sum_k \alpha_{ik}\epsilon_k)]^2}{M_i} + \sum_k \frac{\epsilon_k^2}{\sigma_k^2} \tag{1.67}$$

where M_i is the number of measured neutrino events in the i-th energy bin, T_i is the predicted number of neutrino events with oscillations, σ_k is a systematic uncertainty, ϵ_k is the corresponding pull parameter and α_{ik} is the fraction of neutrino event contribution of the k-th pull parameter to the i-th energy bin. The considered systematic uncertainties include the correlated (absolute) reactor uncertainty (2%), the uncorrelated (relative) reactor uncertainty (0.8%), the background uncertainties, the spectral shape uncertainty (1%) and the non-linearity uncertainty [63].

With the χ^2 function constructed, a scan of the values of Δm^2_{ee} is conducted, the value of the other working parameter Δm^2_{12} being known. For each Δm^2_{ee} value, a different theoretical antineutrino spectrum is computed for the NO and IO models, and the measured spectrum is fit to both theoretical spectra using the chi-squared method. A χ^2 distribution as a function of the values of Δm^2_{ee} is obtained for each NMO model, and the difference between the minimum of each distribution is taken as a measure of the median NMO sensitivity. The discriminator of the NMO can be defined as :

$$\Delta\chi^2_{MO} = |\chi^2_{min}(NO) - \chi^2_{min}(IO)| \tag{1.68}$$

with $\chi^2_{min}(NO)$ and $\chi^2_{min}(IO)$ possibly located at different Δm^2_{ee} values. It is the discriminating power between the NO and the IO. If the $\Delta\chi^2_{MO}$ value is low, then the best fit of the measured spectrum to the NO theoretical spectrum, calculated for a given Δm^2_{ee} value, gave a similar χ^2 value to the best fit of the measured spectrum to the IO theoretical spectrum, calculated for (possibly) a different Δm^2_{ee} value, and no NMO model can be favoured.
This is illustrated in Figure 1.21a, which represents the χ^2 distributions for the NO and IO as a function of Δm^2_{ee}, with the absolute minimum χ^2 subtracted from all χ^2 values. The $\Delta\chi^2_{MO}$ value can be read on the Y-axis by taking the difference between the minimum of the NO function and the minimum of the IO function. Figure 1.21a additionally compares the NMO sensitivity for the ideal and real distributions of the reactor cores (distances of a few tens of m instead of 0 m), with the real distribution inducing a degradation of $\Delta\chi^2_{MO}$ of ~5 (the σ significance can be obtained by taking $\sqrt{\Delta\chi^2_{MO}}$).

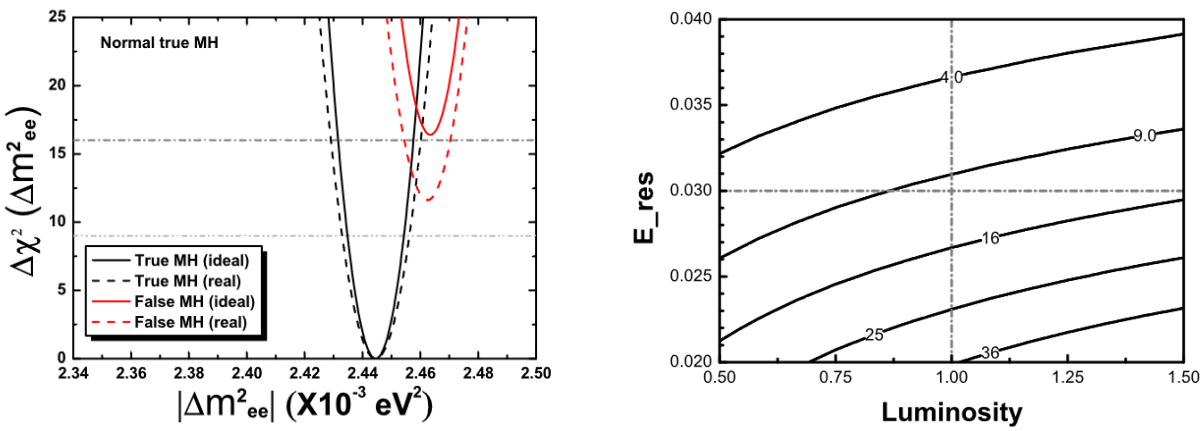

(a) (b)

Figure 1.21: (a) Comparison of the NMO sensitivity in the NO (black) or IO model, for the ideal (solid) and actual (dashed) distributions of the reactor cores. The real distribution gives a degradation of $\Delta\chi^2 \approx 5$. [63] (b) The iso-$\Delta\chi^2_{MO}$ contour plot as the function of the energy resolution of the detector and of the event statistics (luminosity) normalized to 10^5 events. The vertical dash-dotted line stands for the nominal running of six years with 80% signal efficiency. [59]

To highlight the impact of the energy resolution on the NMO sensitivity, iso-$\Delta\chi^2_{MO}$ contours are shown in Figure 1.21b as a function of both the energy resolution as well as the event statistics. The event statistics are represented as the luminosity, normalised to 10^5 IBD events expected in 6 years of data-taking. With 10^5 measured IBD events and an energy resolution of $3\%/\sqrt{E_{vis}}$, the JUNO experiment will reach a $\Delta\chi^2_{MO} > 9$ ($> 3\ \sigma$). However, for even a slight degradation of

the energy resolution, such as a degradation from the projected $3\%/\sqrt{E_{vis}}$ to $\sim 3.5\%/\sqrt{E_{vis}}$, the $\Delta\chi^2_{MO}$ measurement will be severely impacted with many more years of data-taking required to reach a 3 σ NMO determination, even beyond the scope of 9 years (1.5 on the luminosity scale).

As mentioned, other spectral analyses have been proposed during the conception of the JUNO experiment, including a method applying Fourier cosine and sine transforms to the L/E spectrum [64]. Once data has been collected, different analyses will be performed and their results compared. In the framework of the determination of the NMO using vacuum oscillations with JUNO, the following chapter will describe the detector itself and its requirements for this measurement, as well as JUNO's additional physics program.

Chapter 2

JUNO physics and detector

Contents

2.1 JUNO requirements : location and detector design **43**
2.2 Central Detector **45**
2.3 Veto Detector **46**
2.3.1 Water Cherenkov Detector 46
2.3.2 Top Tracker 47
2.4 Liquid Scintillator **48**
2.5 PMT systems **50**
2.5.1 LPMT system 50
2.5.2 Electronics and signal acquisition 53
2.5.3 SPMT system 55
2.6 CD calibration system **59**
2.6.1 Calibration system design 59
2.6.2 Radioactive sources 62
2.6.3 Calibration program 62
2.7 Low background strategy **63**
2.8 TAO **65**
2.9 Additional physics with JUNO **67**
2.9.1 Neutrino oscillation parameters precision measurements 67
2.9.2 Supernova neutrinos 68
2.9.3 Diffuse supernova neutrino background 69
2.9.4 Solar neutrinos 71
2.9.5 Geo-neutrinos 73
2.9.6 Other physics 75
2.10 Conclusion **76**

2.1 JUNO requirements : location and detector design

The Jiangmen Underground Neutrino Observatory (JUNO) is a multi-purpose neutrino experiment formed in 2013, with the objective of determining the neutrino mass ordering (MO). This is planned to be achieved by detecting reactor anti-neutrinos from two nuclear power plants, with the site location optimized to have the best sensitivity for mass hierarchy determination, at ∼53 km from both the Yangjiang and Taishan nuclear power plants. The detector will be deployed in a laboratory 700 meters underground. A map of the geographical area in which the detector is currently being built is shown in Figure 2.1a and a scheme of the above-ground laboratory is illustrated in Figure 2.1b.

The JUNO experiment consists in a central detector, a water Cherenkov detector and a muon

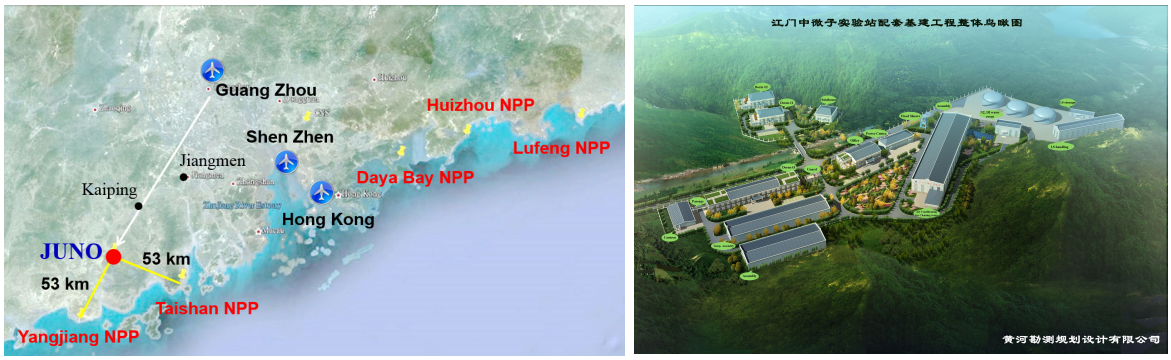

(a) (b)

Figure 2.1: (a) Location of the JUNO detector site, located 53 km away from the Yangjiang and Taishan nuclear power plants. (b) Envisioned above-ground site infrastructure. The central detector will be located 700 m underground.

tracker, which are its main components. The central detector is a liquid scintillator detector of 20 kton target mass and $3\%/\sqrt{E(\mathrm{MeV})}$ energy resolution. The central detector is submerged in a water pool for muon detection and protection against the natural radioactivity of the surrounding rock. On top of the water pool, there is another muon detector called Top Tracker (TT) to accurately measure the muon track. A schematic view of the JUNO detector is shown in Figure 2.2a.

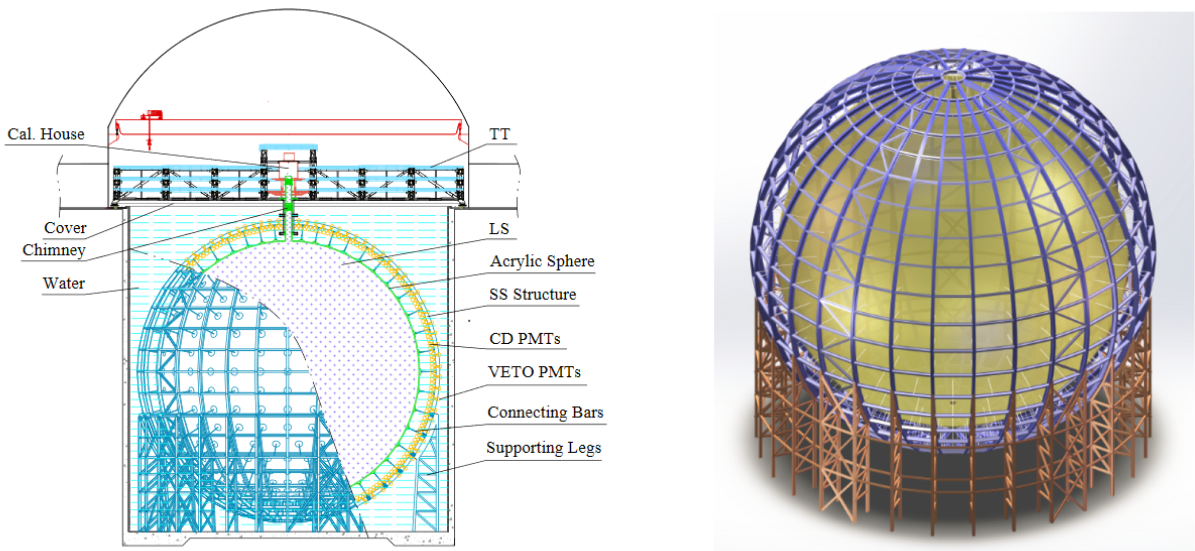

(b)

(a)

Figure 2.2: (a) Schematic view of the JUNO detector. (b) Schematic view of the acrylic sphere within the stainless-steel double layer structure.

Reactor antineutrinos are the major neutrino source for the JUNO experiment, The electron antineutrinos from the 26.6 GW_{th} power plants are to be detected via the $\overline{\nu}_e + p \rightarrow e^+ + n$ inverse beta decay (IBD) reaction, in which the positron quickly deposits its kinetic energy and annihilates into two 0.511 MeV photons. This gives what is called a prompt signal, which contains

the visible energy from the neutrino, typically from 0 to 10 MeV. The created neutron is mainly captured by a proton after a scattering of approximately 200 μs in the detector, and releases a 2.2 MeV photon, which gives a delayed signal. The IBD reaction shows a peculiar correlation in energy, time and space between the prompt and delayed signals. Therefore, the identification of anti-neutrino events is performed by applying, among others, a basic set of preliminary selection cuts [59] :

- prompt signal energy : 0.7 MeV $< E_p <$ 12 MeV
- delayed signal energy : 1.9 MeV $< E_d <$ 2.5 MeV
- time difference between prompt and delayed signal : $\Delta t_{p-d} <$ 1.0 ms
- distance between prompt and delayed signal : $D_{p-d} <$ 1.5 m

JUNO is planning on detecting about 60 IBD events from nuclear power plants, per day, for the duration of its run [65]. Aside from the signal, different sources of background are expected in JUNO, the major sources being contributed to by the natural radioactivity and the products of cosmic muons (see section 2.7).

It is crucial to achieve a $3\%/\sqrt{E(\mathrm{MeV})}$ energy resolution for the determination of the MO. This will be mainly achieved through the strict requirements on the liquid scintillator (LS) (transparency and light yield), which will be detailed in section 2.4, and with an unprecedented PMT coverage detailed in section 2.5. Section 2.2, about the Central Detector, will precede these two sections and introduce the main components of the detector. The JUNO detector also requires an energy linearity better than 1%. A calibration strategy, consisting in various calibration sources covering most of the IBD energy ranges being deployed regularly to calibrate the energy scale to a sub-percent level has thus been developed and will be detailed in section 2.6. In order to provide a precise reference antineutrino spectrum, the JUNO-TAO experiment was also proposed as a satellite experiment of JUNO to measure the near reactor antineutrino spectrum with sub-percent energy resolution, and will be detailed in section 2.8.

2.2 Central Detector

The objective of the central detector (CD) of JUNO is to measure the neutrino energy spectrum using 20 kt of liquid scintillator (LS) and a large array of photo-multipliers, with the LS contained within an acrylic spherical vessel with an inner diameter of 35.4 m and a thickness of 120 mm. The acrylic vessel is transparent for scintillation light to pass through and later be detected by the PMTs. It will be supported by a stainless steel structure with an inner diameter of 40.1 m, called the main structure, which is designed with a lattice shell structure of 30 longitudinal beams and 23 latitudinal beams, both in H shape. Five in-plane supports are uniformly arranged along the longitudinal direction to improve the torsional stiffness and stability of the structure. The shell structure is supported by 30 pairs of support legs and 60 base plates fixed on the concrete floor of the water pool. A total of 590 connecting rods are arranged to connect the main structure to the acrylic vessel. Figure 2.2b shows the acrylic sphere and the double layer stainless-steel truss of the central detector.

The acrylic spherical vessel will be made by bulk polymerization of 265 pieces of acrylic spherical panels. A specialized recipe for the JUNO CD acrylic panel was designed and produced to significantly increase the light transparency and improve the anti-aging. The radiopurity of this acrylic reaches a level of less than 0.5 ppt for Uranium and Thorium (1 ppt = 10^{-12} g/g), with the process of unmolding and thermoforming during production having been optimized to increase the transparency of the acrylic panels to over 96% in water. Figure 2.3a shows a schematic view of one of the acrylic panels, initially straight, being bent to allow for the simultaneous bonding of all the acrylic panels in one layer of the sphere. Connection nodes are present on the panels to link them

to the stainless steel main structure ans support the acrylic vessel. This new bonding method was developed to reduce the on-site construction time of the acrylic vessel, and is illustrated in Figure 2.3b. All rows of acrylic panels will then be mounted using a lifting platform to assemble the full acrylic sphere, a schematic view of which is shown in Figure 2.3c. A chimney of about 80 cm in diameter is designed on top of the acrylic sphere, which will be used as the filling port and interface to the calibration system, and an outlet may be designed on the bottom of the sphere for the cleaning of the sphere and the recycling of LS during the run of the detector. The whole structure of the CD must be stable and reliable for 30 years of JUNO designed lifetime.

(a) (b) (c)

Figure 2.3: (a) Bending of one of the acrylic panels, with its connecting nodes. (b) Assembly of a row of acrylic panels. The sphere will be constructed by mounting these rows using a lifting platform. (c) Acrylic sphere after assembly of all the panels. The connecting nodes will allow for the support of the panels by the stainless steel structure.

2.3 Veto Detector

In order to shield the fast neutrons and the natural radioactivities from the surrounding rocks, at least 4 meters of water surrounding the central detector are needed. In addition, when being instrumented with PMTs, the water pool will also serve as a Water Cherenkov Detector to tag muons. In addition to the 20” PMTs of the CD, approximately 2000 20” PMTs (MCP-PMTs, section 2.5) are thus added in the water pool for cosmic ray muon veto by detecting Cherenkov light generated by cosmic muons. These PMTs will be mounted on the outside surface of the stainless steel structure that supports the liquid scintillator vessel. A tracking detector, called Top Tracker (TT), is also placed on top of the water Cherenkov detector to help muon tagging as well as track reconstruction.

2.3.1 Water Cherenkov Detector

As shown in Figure 2.2a, the Water Cherenkov Detector (WCD) consists of a cylinder with a 43.5 meter diameter and a 44 meter height, filled with 35 ktons of ultrapure water. The Cherenkov light produced by the muons passing through the volume is read by 2400 20” MCP-PMTs installed on the stainless steel latticed shell surface surrounding the central detector. Tyvek reflector film is coated on the pool wall surface and on the stainless steel latticed shell surface to increase the light collection efficiency.

The water system includes two plants, the ground and underground ones for water production and circulation. The ground part produces the first stage water with production rate 100 tons/hour and then the water will be transported by a stainless steel pipes in the 1300 m long slope tunnel to

the underground plant for purification and circulation in the WCD. The experiment uses several materials with different mechanical behaviour with respect to the temperature, in particular the acrylic sphere as the LS container. In order to keep the mechanical stability, the water temperature around the acrylic sphere has to be stabilized at 21 $\pm$ 1°C.
The concentration of radon in tap water is about 20 Bq/m^3. It should be reduced by a factor of 100 ($\sim$0.2 Bq/m^3) to reach the radiopurity requirements. A radon removal system is combined with the underground water system to reduce radon concentration. Using a multiple stages degassing membrane system, the radon concentration can be controlled to lower than 0.05 Bq/m^3. In addition, a HDPE (High Density PolyEthylen) film will be used as a liner to cover the pool and will prevent radon diffusion from the external rocks. The activity of the rock is indeed very high, and will thus contain a high level of radon.
The 20-inch PMTs in both the central detector and the water Cherenkov detector are easily affected by the geo-magnetic field. The detection efficiency of the PMTs decreases by $\sim$50% under the intensity of the geomagnetic field (0.5 G) and a shielding system is necessary to compensate the geomagnetic field. One set of 32 circular coils was designed to shield the detector from the geomagnetic field and maintain PMT performances.
Finally, the muon flux in the experimental hall is 0.036 Hz/m^2, with 209 GeV average muon energy under 700 meter overburden mountain. Based on the JUNO detector simulation study, the average track length of muons going through the pool is about 13 meters. With this system, the average number of fired PMTs can reach $\sim$370 and the muon tagging efficiency can reach 99.5%. Most of the un-tagged muons have short tracks ($<$ 0.5 meter) and are far from the central detector, and thus do not pose a problem, as the fast neutron background from these un-tagged muon is very small.

2.3.2 Top Tracker

The Top Tracker (TT) implemented in JUNO was dismounted from the OPERA detector, and will be placed on top of the JUNO water Cherenkov detector to be used as a cosmic muon tracker. As shown in Figure 2.4a, 'walls' of plastic scintillator, called TT walls, will be placed in horizontal layers on top of the JUNO central detector, rather than vertically as it was done in OPERA. The TT will be composed of 62 walls each with a data sensitive area of 6.7$\times$6.7 m^2. Each wall is formed by four vertical (x) and four horizontal (y) modules, and each module is composed of 64 scintillating strips. Each strip is read on both sides by a Hamamatsu 64-channel multi-anode PMT. The total surface which could be covered by the 62 x-y walls is 2783 m^2. The TT walls will be distributed on 3 horizontal layers, separated by 1.5 m, on a 3$\times$7 horizontal grid, as shown in Figure 2.4b. There is a 15 cm overlap between adjacent walls of the same layer to avoid dead zones in the detector. The 3 walls in the center of the TT are moved up to leave enough space for the calibration house and the Central Detector chimney.
Identifying the entry point of the muon tracks is extremely important in properly tracing them. The total surface that the TT could cover depends on the number of superimposed $x - y$ layers (composed by consecutive TT walls), but it will never be able to cover the entire surface of the detector. With this geometry, about 1/3 of all atmospheric muons passing through the CD will also cross the 3 layers of the TT, and can be well-tracked, as illustrated in Figure 2.4b. In these cases, the TT can be used as a veto, but for the remaining muons crossing the CD, the veto strategy will depend only on the WCD and the CD. One notable region where the TT veto is particularly effective is for atmospheric muons entering the detector through the chimney region, which is well covered by the TT and might present difficulties for the other subsystems.
Due to the small granularity of the TT, of 2.6 $\times$ 2.6 cm^2, using the TT reconstruction and its associated trigger logic will yield a reconstruction efficiency for atmospheric muons of about 93%,

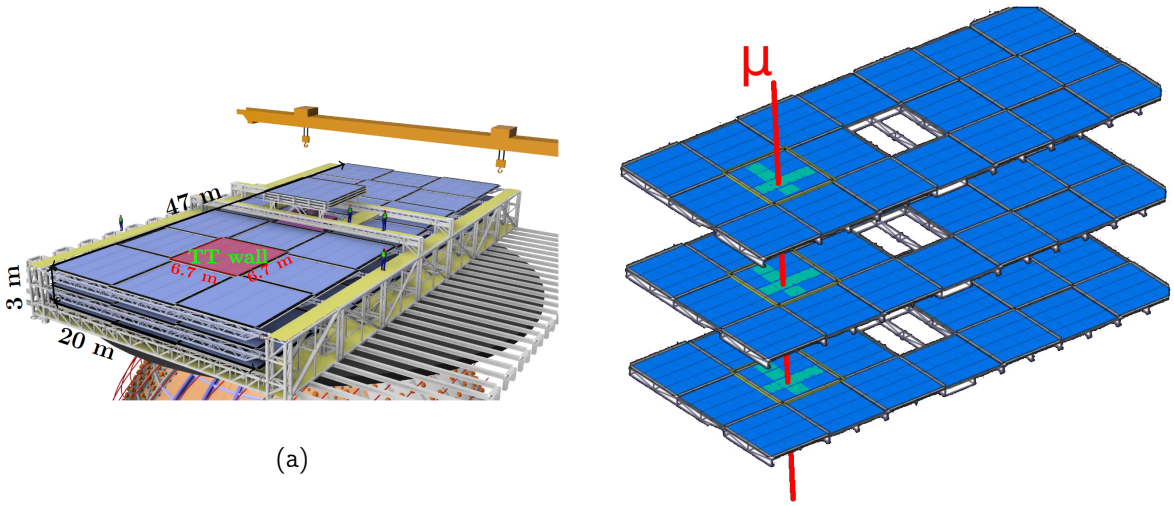

(a) (b)

Figure 2.4: (a) Top Tracker. (b) Drawing of the TT (without chimney walls) with a muon passing through vertically. In green are shown which modules would have seen the light from this muon to illustrate the possible trigger configurations.

with a median angular resolution of 0.20°. By also requiring a corresponding signal to be seen in the CD or WCD, the TT provides a well reconstructed muon sample, with a purity > 99%, that can be used to calibrate and to tune reconstruction algorithms in the CD and WCD. Well reconstructed muons from the TT will also be used to measure the distribution of the distance between the muon and the cosmogenic isotopes produced in the CD, a key component in deciding the size of the muon veto cylinder used in the analysis.

2.4 Liquid Scintillator

As described in section 2.2, 20,000 tons of Liquid Scintillator (LS) are contained inside an acrylic vessel of 35.4 m diameter, the LS serving as the target medium for the detection of neutrinos. There are three components to the JUNO LS recipe : Linear Alkyl Benzene (LAB), forming the bulk of the target material, 2,5-diphenyloxazole (PPO) and 1,4-bis(2-methylstyryl)benzene (bis-MSB). The optimal LS composition to maximize the light yield was determined, using one of the Daya Bay detectors, to be purified solvent LAB with 2.5 g/L PPO, and 3 mg/L bis-MSB [66]. This composition gives an attenuation length of 25 m at 430 nm, with a dominating decay time of about 5 ns, allowing the photons generated by a reaction at the very center of the target volume to reach the PMTs.

To improve the optical and radio-purity properties of the LS, a combined system of purification was designed by the JUNO collaboration according to a strategy optimized with good success with the Daya Bay experiment. The flowchart of the LS processing system is shown in Figure 2.5, according to which the raw LAB will pass through an alumina column and a distillation plant, before being mixed with the PPO and the bis-MSB to form the LS master solution. After these first stages are performed in the above-ground laboratory, the LS will then undergo two purification stages, going through the underground water extraction system and stripping system. A final quality check will be performed in the OSIRIS detector.

In the alumina column system, the LAB will be purified to improve its transparency. This system consists of 8 60 cm-wide, 2.6 m-tall filtration columns, 2 alumina filling tanks and 3 buffer tanks,

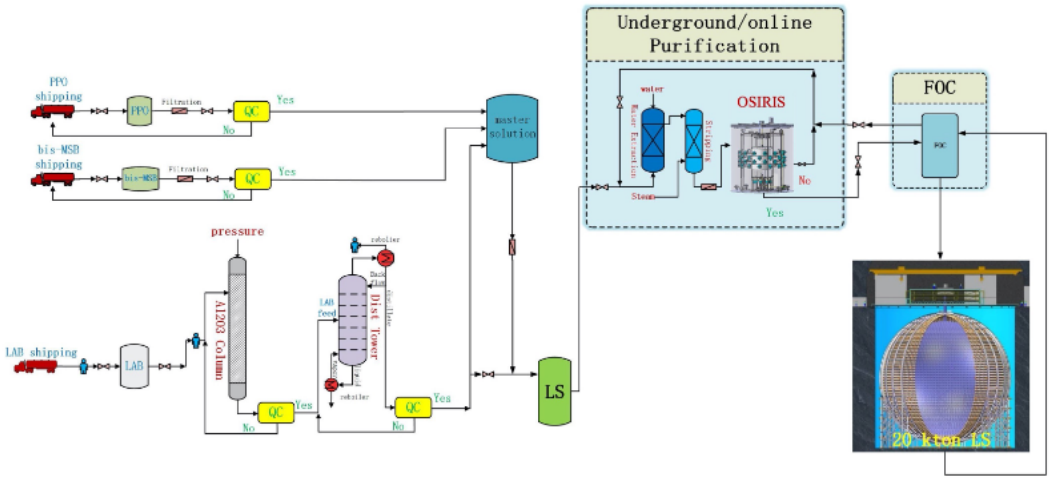

Figure 2.5: Flowchart of the liquid scintillator processing system.

and was shown to be able to increase the attenuation length of LAB. Special care is paid to reduce the radon and U and Th radiation background in the LAB.

The second stage of the purification process, the distillation system, uses distillation in partial vacuum (5 mbar) to remove the heaviest radio-impurities (^{238}U,^{232}Th and ^{40}K) from LAB as well as to further improve its optical properties in terms of absorbance spectrum and attenuation length. The LAB distillation technique was tested in one of the Daya Bay detector using a distillation pilot plant, and was proved effective in terms of radio-purity and optical transparency [67].

Following the distillation process, the mixing system is located in the liquid scintillator (LS) hall, above ground. It is responsible for dissolving PPO and bis-MSB into LAB to form the LS master solution batch by batch. The PPO and bis-MSB are purified using an acid/water washing method.

First of the last two purification stages, the water extraction system is used to remove U and Th radiation in the LS. In this system, the water and LS are fully mixed by turbine stirring, with a LS flow rate of 7 m^3/h and a water flow rate of 1.4–2.3 m^3/h. The water with ultra low U/Th and Rn will be provided by an ultrapure water (UPW) system with a U/Th concentration of less than 10^{-15} g/g. The aim of this method is to guarantee that the concentrations of ^{238}U and^{232}Th in the LS do not exceed the given limits of 10^{-15} g/g or 10^{-17} g/g for the neutrino mass ordering or solar neutrino measurements, respectively.

The stripping plant is the final stage of the purification process, its main purpose being the removal of radioactive gases and gaseous impurities from the liquid scintillator, using a gaseous stream of nitrogen and/or super-heated steam in counter current flow mode. The purification process is performed inside a 9-meters-high stripping column, in partial vacuum (about 250 mbar), using ultra-pure nitrogen and ultra-pure water (UPW) steam. During the tests carried out at the Daya Bay laboratory in 2018, this system allowed for a 95% purification efficiency in Rn removal [67]. As the full-size plant has since been improved with a 50% higher stripping column, an even better efficiency is expected.

Following this purification process, the LS is sent to the OSIRIS detector for a final quality check. The Online Scintillator Internal Radioactivity Investigation System (OSIRIS) [68] is a stand-alone detector to monitor the radiopurity of the LS while the JUNO CD is filled, and to confirm the proper operation of the aforedescribed purification plants. Its main purpose is to ensure that the concentrations of ^{238}U and ^{232}Th in the LS do not exceed the requirements. This will be achieved by observing the easy-to-identify fast coincidence decays of ^{214}Bi-^{214}Po (τ ~237 μs) and ^{212}Bi-

^{212}Po (τ ~0.43 μs) in ~20 m^3 of LS (about 17 tons). These decays indicate the presence of ^{238}U and ^{232}Th, respectively. The OSIRIS detector has a JUNO-like design. It is composed of a 3 m wide and tall cylindrical acrylic vessel to contain the LS to be tested, which is mounted inside a water-filled steel tank for shielding against external radiation. The detector is located in a bypass to the main LS line, allowing for a sampling of a relevant fraction (~1/6) of the LS processed in the purification plants. During the LS filling of the JUNO detector, a continuous flow mode in OSIRIS is foreseen, where new LS is constantly added at the top of its acrylic vessel while the already-monitored LS is drained from below. The sensitivity of the ^{238}U and ^{232}Th measurement in this continuous mode will be better than 10^{-15} g/g, which is the requirement in JUNO for the determination of the neutrino mass ordering.
After validation of the purity of the LS by OSIRIS, the Filling, Overflow and Circulation (FOC) system will be used to fill the CD. It will simultaneously fill pure water into the acrylic vessel and the water pool, and then replaces the water in the acrylic vessel with LS.

2.5 PMT systems

Once the acrylic sphere and stainless-steel truss are completely built, two different systems of PMTs will be installed on the truss, facing inwards to collect the light emitted by the LS. About 18,000 20-inch LPMTs and 25,600 3-inch SPMTs will make up these systems, with these PMTs arranged as close to each other as possible to provide a 77% optical coverage to meet the energy resolution requirements. The following sections will detail both the LPMT and the SPMT systems.

2.5.1 LPMT system

For the LPMT system, an extensive R&D was conducted with the NNVT company in China to produce a new PMT design without dynodes in order to maximize the photoelectron detection efficiency and thus the energy resolution, and so 15000 Micro Channel Plate (MCP) PMTs (N6201) were produced and delivered by NNVT. 5000 additional dynode PMTs (R12860-50 HQE) have also been delivered by the Hamamatsu company. These latter PMTs have a mature technology, a good reliability, and a very good TTS, with the downside of being more expensive, not having any possible R&D conducted to improve their design, and having a low radiopurity (up to one order of magnitude from the NNVT PMTs depending on the isotope). Figures 2.6a and 2.6b respectively show a PMT from the Hamamatsu and NNVT productions.

(a) (b)

Figure 2.6: PMTs in JUNO (a) 5k 20-inch Hamamatsu PMTs. The model presented in this figure has had its photocathode removed. (b) 15k 20-inch NNVT MCP-PMTs.

The performance of these PMTs crucially contributes to the final energy resolution of the whole detector system, mainly their photon detection efficiency (PDE) and dark count rate (DCR). More parameters such as timing and pulse shape parameters are also relevant for event reconstruction and background reduction. This lead to a set of requirements for the performance of the 20-inch PMTs being defined. It is shown in Table 2.1 [69].

Parameter	Unit	Tube type	Min.	Typical	Max.
PDE@420 nm	%	both	24.0	27.0	-
P/V ratio of SPE	-	Hamamatsu	2.5	3.0	-
		NNVT	2.5	3.5	-
DCR@0.25 PE	kHz	Hamamatsu	-	20	50
		NNVT	-	-	100
Rise Time	ns	Hamamatsu	-	-	8.5
Fall Time	ns	Hamamatsu	-	-	12
Supply HV (@G = 10^7	V	Hamamatsu	-	2000	2350
		NNVT	-	2000	2800
TTS (FWHM)	ns	Hamamatsu	-	2.7	3.5
		NNVT	-	12.0	15.0
Pre-pulse ratio	%	Hamamatsu	-	0.8	1.5
After-pulse ratio	%	Hamamatsu	-	10	15
		NNVT	-	1	2

Table 2.1: Performance requirements for the JUNO 20-inch PMTs.

All 20000 PMTs must be tested at least once to make sure that all these requirements are met. A dedicated multi-channel system was thus designed and built for the testing of the 20-inch PMTs. After a first visual verification of the state of the PMTs, checking for potential damages or impurities in the photocathode, all bare PMTs are tested in the container system. The explicit purpose of this container system is the testing and characterization of all 20-inch PMTs of JUNO for the PDE, Transit Time Spread (TTS), DCR, gain, Peak-to-Valley (P/V) ratio, fall time, rise time and pre-pulse and after-pulse ratio parameters. The PMT measurement system is made up of two containers, inside which is a shelf structure housing 36 drawer boxes acting as individual measurement stations for the mass testing of the PMTs. In each drawer box are two different light sources : a self-stabilized LED illuminating the whole photocathode of the PMT, and a fibre connected to a picosecond laser used for the TTS measurement. 5 reference PMTs per container, in arbitrary drawer boxes, are used to monitor the measurement system [70].

One of the most critical requirements for JUNO PMTs is a high photon detection efficiency (PDE), corresponding to the photocathode quantum efficiency (QE) multiplied by the efficiency of photoelectron collection efficiency (PCE) in the PMT vacuum. All the bare PMTs received from the vendors were thus checked in detail to measure their performances for this parameter. Figures 2.7a and 2.7b show the distributions for the PDE of all the PMTs and of all the MCP-PMTs, respectively.

As seen in Figure 2.7a, the MCP-PMTs from NNVT have on average a slightly better PDE than the Hamamatsu PMTs, with an average of respectively 28.9% and 28.1%. The total mean value for all the PMTs is 28.7%. It should be noted, as seen in Figure 2.7b, that the quality of the NNVT production increased with the R&D, as 2 types of PMTs can be identified, the High QE and the Low QE PMTs. The mean value for the PDE of these PMTs increased from 26.8% to 29.9%. All these values fulfill the requirements. 1,350 photoelectrons (PE) are expected to be generated per MeV of deposited energy at the center of the CD, an unprecedented number of PEs collected at

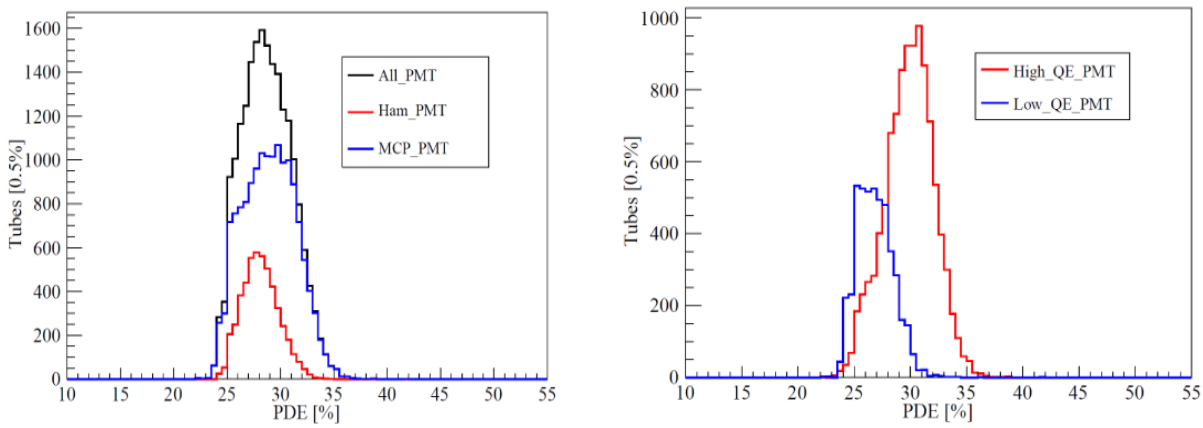

(a) (b)

Figure 2.7: Measured PDE of bare PMTs. (a) For both types of tubes. (b) For NNVT MCP-PMTs.

this energy.
Equally as important as the PDE, the dark count rate (DCR) is also a key parameter of the PMTs to be measured. Figures 2.8a and 2.8b show the distributions for the DCR of all the PMTs and of all the MCP-PMTs, respectively. As seen in Figure 2.8a, the MCP-PMTs from NNVT tend to have a much larger DCR than the Hamamatsu PMTs, with an average of respectively 49 kHz and 15.3 kHz. The total mean value for all the PMTs is 40.5 kHz. As seen in Figure 2.7b, the increase in the quality of the NNVT production as for the PDE parameter had no impact on the DCR of the PMTs. These values do not exceed the requirements.

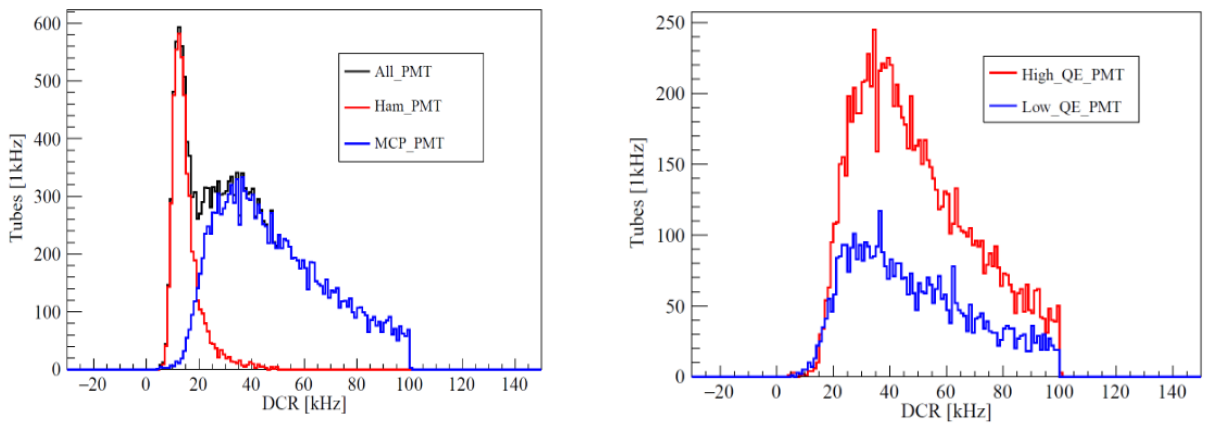

(a) (b)

Figure 2.8: Measured DCR of bare PMTs. (a) For both types of tubes. (b) For NNVT MCP-PMTs.

Figures 2.9a and 2.9b show the distributions for the charge resolution of the single photoelectron peak of all the PMTs and of all the MCP-PMTs, respectively. As seen in Figure 2.9a, the MCP-PMTs from NNVT tend to have a worse resolution than the Hamamatsu PMTs, with an average of respectively 33.2% and 27.9%. The total mean value for all the PMTs is 31.9%. As seen in Figure 2.9b, the increase in the quality of the NNVT production as for the PDE parameter also had a negligible impact on the resolution of the PMTs.
For TTS measurement, about ∼1000 Hamamatsu PMTs were tested, with the PMTs considered as having passed the requirements for TTS $\leq$ 1.5 ns (σ), and being double checked for

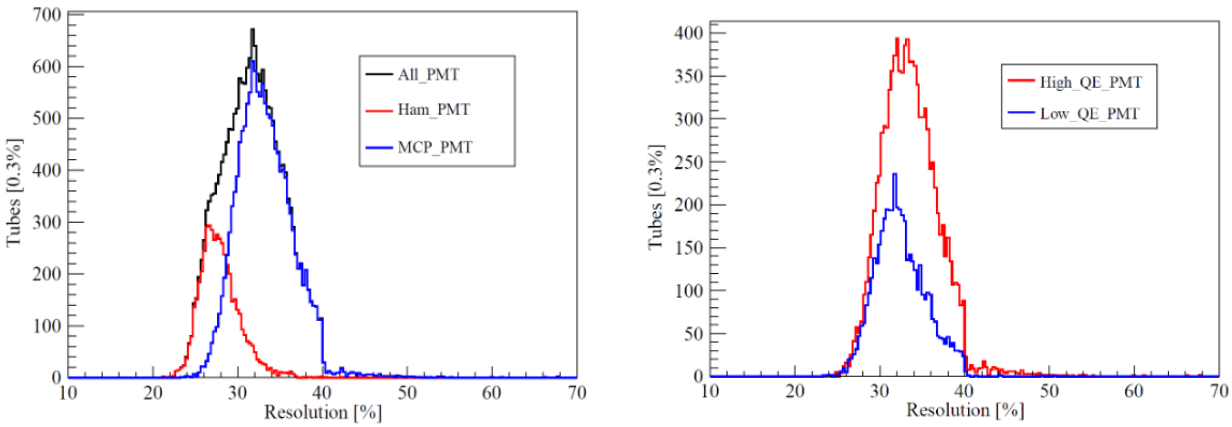

(a) (b)

Figure 2.9: Measured Resolution of bare PMTs. (a) For both types of tubes. (b) For NNVT MCP-PMTs.

1.5 ns $<$ TTS $\leq$ 2.0 ns. Over the full sample, the mean TTS value is 1.39 $\pm$ 0.26 ns when excluding PMTs with TTS $>$ 3 ns, considered as having failed the requirements. When considering the estimated systematic effects, the mean TTS value is $\sim$1.13 ns, consistent with the typical value for Hamamatsu PMTs. In comparison, MCP-PMTs have a much larger TTS ($\lesssim$ 5.1 ns, σ), but they were selected for the SPMT array on purpose in order to maximise the PDE parameter.
There are additional measurements for after-pulse ratio or photocathode uniformity performed on a randomly selected sub-sample. These sample tests are performed at the scanning station, independently from the tests in the containers. The scanning station is a complex system for the zonal testing and characterization of the large photocathode of the 20-inch PMTs. Its main purpose is to estimate the PDE non-uniformity along the photocathode, but it can also help provide complementary information to reveal potential issues with the PMTs tested in the container system. The scanning station is made up of a rotating base supporting a rotating frame, with 7 self-stabilized light sources (LEDs) installed on a rotating arc, and is enclosed in a dark room. There are 168 points tested along the photocathode surface. At each point, charge spectra are obtained, from which the PDE and the Gain are extracted. The LEDs are individually calibrated by a reference small PMT on a regular basis. Figure 2.10a shows the scanning station, while Figure 2.10b shows the scanning map of the photocathode uniformity for one of the Hamamatsu PMTs.

2.5.2 Electronics and signal acquisition

The initial design of the large PMT electronics [71] and the following R&D program have been driven by the main requirements of reconstructing the deposited energy in the LS with high resolution and a good linearity response over a wide dynamic range : from 1 PE for low energy events to 1000 PEs for showering muons and muon bundles. In addition, a precise measurement of the photons arrival times is required [71].
The current design of the large PMT electronics, a scheme of which is shown in Figure 2.11, is an optimization of previous developments where the large PMT electronics was split into two parts, one being the 'wet' electronics (located at few meters from the PMTs inside a custom stainless steel box) and the other being the 'dry' electronics in the electronics rooms. Output signals from 3 PMTs are fed to the front-end and read-out electronics located inside the UWB, and the PMT high voltage is provided for each individual PMT by a custom High Voltage module located inside. The analog signal is amplified and converted to digital with a 12 bit, 1 GS/s, custom Analog-to-Digital

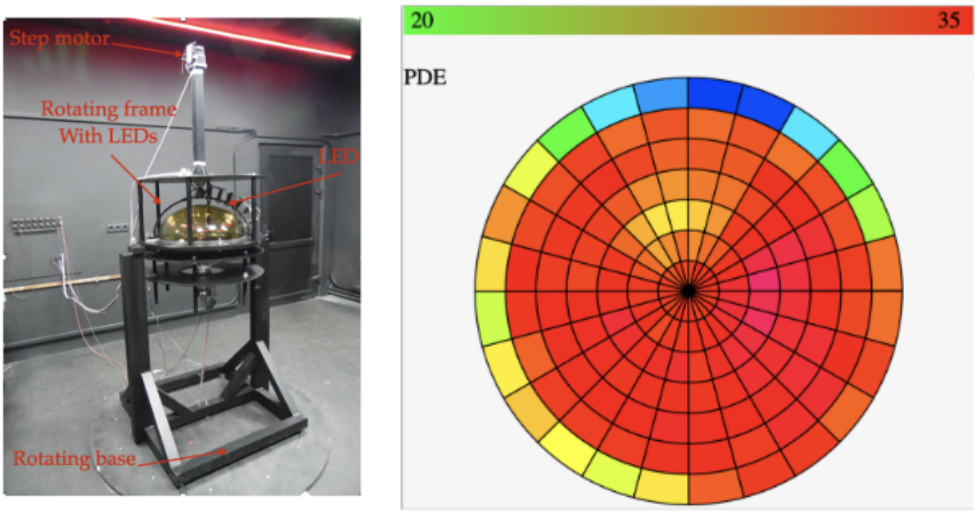

(a) (b)

Figure 2.10: (a) Scanning station for the 20-inch PMTs. (b) Scanning map of the photocathode uniformity for an arbitrary Hamamatsu PMT. The green areas correspond to a PDE value of 20% and the dark red areas to 35%. The PDE value tends to be much lower at the edge of the photocathode.

Converter (ADC). The signal is further processed (local trigger generation, charge reconstruction and timestamp tagging) and stored temporary in a local memory before being sent to the data acquisition (DAQ), once validated by the global trigger electronics.
The large PMT electronics can work with a centralized 'global trigger' mode, in which the information of the single 'fired' PMTs is collected and processed in a Central Trigger Unit (CTU). The CTU then validates the trigger based on a simple PMT multiplicity condition or a more refined topological distribution of the fired PMTs. With a typical energy threshold in JUNO of 0.2 MeV, the CTU would validate the trigger for ∼300 fired LPMTs. Upon such a trigger request, validated waveforms are sent to the DAQ event builder through the Gigabit Ethernet asynchronous link.

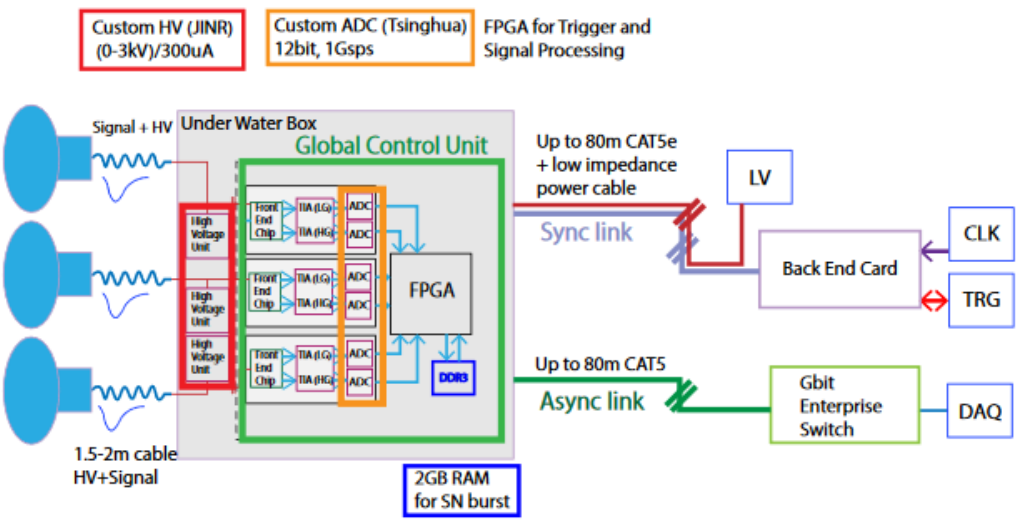

Figure 2.11: LPMT electronics.

2.5.3 SPMT system

The small PMT system of the JUNO experiment was proposed to the collaboration in 2014 in order to install up to 36,000 3-inch PMTs (SPMTs) in the gaps between the 20-inch PMTs LPMT system, 3 inches being the maximum size allowed by the positioning of the LPMTs. Formally approved of early 2017, this sub-system thus became a part of JUNO very late in the experiment's development, and is not featured in the JUNO Conceptual Design Report (CDR) but in a separate SPMT CDR [72]. One of the main objectives was to keep the R&D aspect of its components to a minimum. The current PMT model used in the SPMT system is the HZC XP72B22, an upgrade on the HZC XP72B20 model used in KM3NeT. The main improvement was the shape of the glass bulb on the B22 model to improve the TTS from a mean value of 1.9 ns to 1.5 ns (σ). To this end, the resistor ratios of the first 3 dynodes of the PMT were set as 3:2:1. Due to the limited number of possible positions for the SPMTs due to the stainless steel structure supporting the acrylic sphere of the central detector, the number of predicted installed SPMTs was reduced to $\sim$ 26,000, and so an international bidding for the production of 26,000 3-inch PMTs (including 1000 spares) was organized in May 2017. The Chinese company Hainan Zhanchuang (HZC) Photonics was chosen to be the supplier. As with the LPMT system, the SPMT readout electronics will be located underwater, both to avoid transmission losses in the long distance to the surface and to reduce the costs associated with the required cabling.
An illustration of the positioning of the SPMTs with respect to the LPMTs is shown in Figure 2.12.

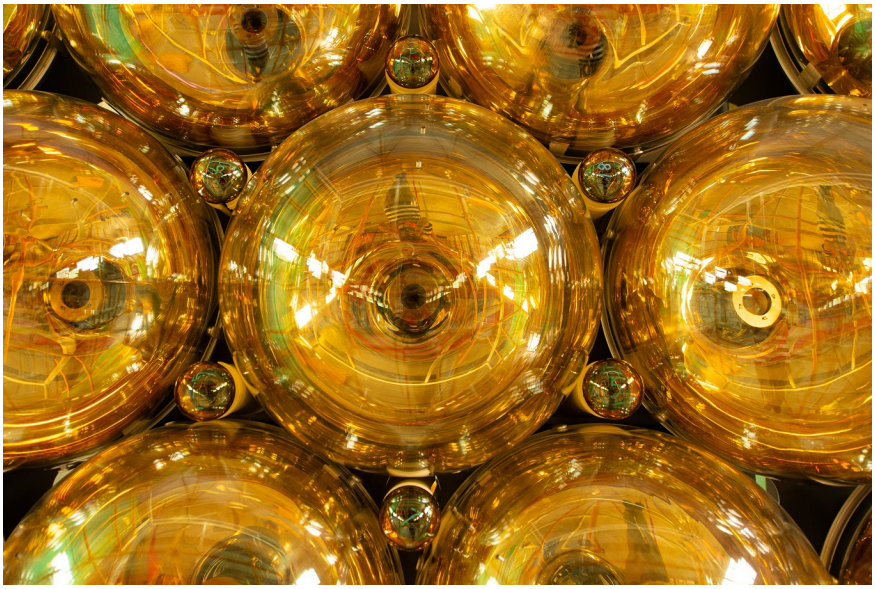

Figure 2.12: LPMT and SPMT positioning.

The SPMT system will work in parallel with the LPMT system to observe the same set of events. Of course, the SPMTs will collect less light than the LPMTs, with an expected light yield of $\sim$40 PEs per MeV, as opposed to the expected 1350 PEs per MeV from the LPMT system. As a consequence of lower photo-electron statistics, the SPMT system will have a worse energy resolution in comparison with the LPMTs. However, the solar mode of the IBD spectrum generates oscillations which remain distinguishable even with the energy resolution of the SPMT system. This means that the SPMT system can serve as an independent photo-detection system to determine the oscillation parameters Δm^2_{21} and θ_{12}, respectively defining the frequency of the oscillations, and their amplitude.
The positioning of these PMTs in the experiment remains a complicated matter. Factors like

impossible positions for the PMTs due to the stainless steel structure, cabling based on position, and shading from and on the LPMTs have to be taken into consideration. Shading being the major concern, for efficiency and sensitivity purposes, a 5 cm forward offset of the SPMTs with respect to the LPMT equator has been agreed upon by the collaboration. 128 SPMTs will be connected to a single UnderWater Box (UWB), in a similar design to the LPMT system albeit with a much larger multiplicity. In the case of the SPMT system, however, the output signals will be digitized and only the charge and time information will be stored and used, as opposed to the full waveforms being registered in the LPMT system. The SPMT electronic boards and their connection to one UWB are under optimization. Chapter 3 will give more details about the electronics.
The produced PMTs were measured in four main test stations, shown in Figure 2.13, the performances of which were reviewed and monitored throughout the entire PMT production period.

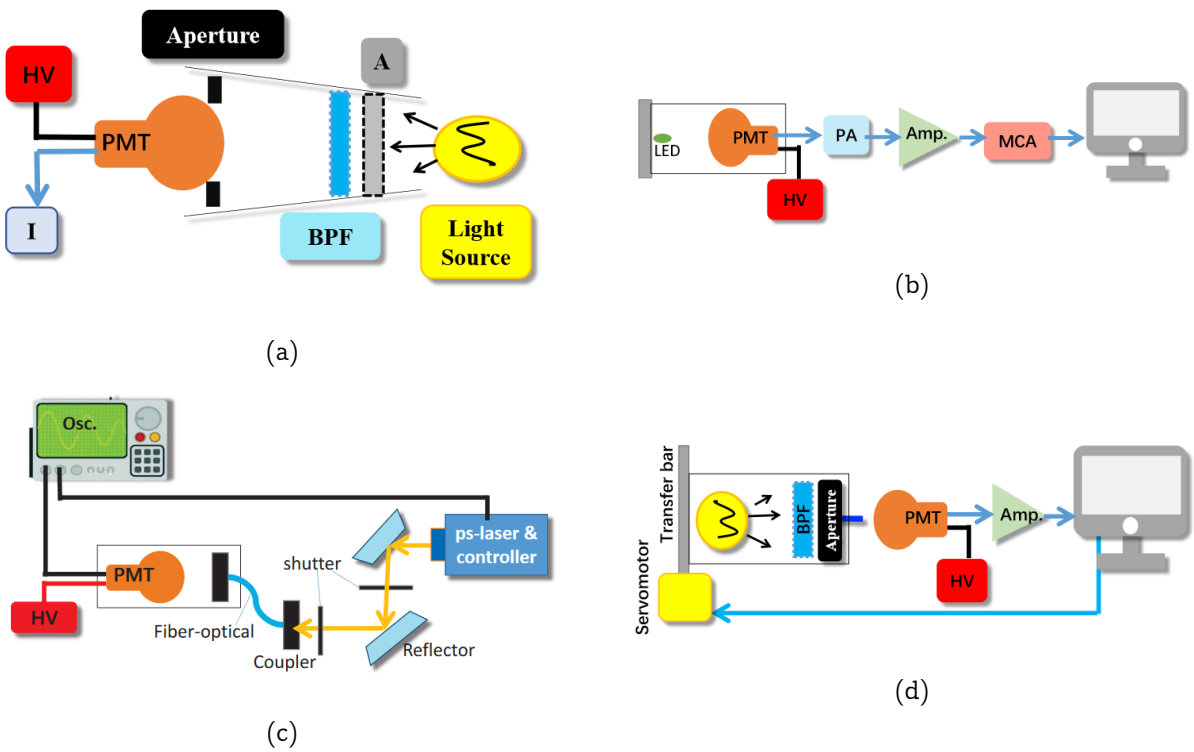

Figure 2.13: (a) Diagram of the static station to measure QE and HV. (b) Diagram of SPE station to measure SPE resolution, PV ratio and DCR. (c) Diagram of the TTS station. (d) Diagram of the scanning station.

A static station (Figure 2.13a) tested the Quantum Efficiency (QE) and the High Voltage (HV) required to obtain the PMT nominal Gain of 3×10^6. In a dark room, a quartz tungsten lamp provides a light source passing through a 400 nm wavelength band pass filter (BPF) and 70 mm diameter aperture before hitting the photo-cathode.
A second station, the SPE station (Figure 2.13b), was designed to illuminate a PMT with a LED and measure the SPE spectrum related parameters : the SPE resolution, the Peak-to-Valley (PV) ratio, and the Dark Counting Rate (DCR) at 0.25 PE and 3 PE thresholds. A LED provides single 420 nm photons, with a distance to the PMT of about 15 cm, fully covering the PMT cathode. The PMT signal is amplified sequentially by two amplifiers and fed into a multi-channel analyzer to get the SPE spectrum. The LED light was turned off when measuring the DCR, and the PMTs were put into the dark box for at least 4 hours before measurement.
A timing station (Figure 2.13c) measured the TTS of the PMTs, as well as the pre-pulse and

after-pulse ratios. A picosecond laser (405 nm) was used as a light source, with a laser controller providing two synchronized signals, one to drive the laser pulse and the other to trigger the oscilloscope. The light from the laser was reflected, went through a shutter, into a short plastic fiber carrying the light to the PMT cathode.
A scanning station (Figure 2.13d) was required by JUNO to measure the non-uniformity of the QE and the effective diameter of the PMT photo-cathode. A quartz tungsten lamp provided a $\sim$2 mm light spot on the photo-cathode through a small circular window with a 420 nm film. The light source, together with the window, could be moved in a 100×100 mm^2 square with a 2 mm step length, and thus realized a QE scanning for the photo-cathode in 2,500 pixels.
The first two stations were used by HZC as a standard procedure to test the basic parameters (QE, HV, SPE resolution, PV ratio, DCR) for all PMTs, while all four stations were used by JUNO for the sampling test.
Due to the high number of produced PMTs, not every PMT could be extensively tested by the JUNO collaboration during production, and as such, a sampling test was designed by IHEP. The different PMT parameters were given different sampling tests and criteria based on their importance. There were 15 parameters specified by JUNO for the acceptance test, as shown in Table 2.2, and requirements were put not only on the performance of any individual PMT, but also on the average performance of a batch of tested PMTs. The parameters were divided in four different classes according to the test time demands, products quality variation, and importance to JUNO. The class A parameters were all tested by HZC during production, and by JUNO with a 10% sampling. The class B and C parameters where only measured by JUNO, and respectively selected randomly with a 3% and 1% sampling. The class D parameter required destructive measurements, and was only performed for 3 PMTs. All of the samplings were done by JUNO shifters. Table 2.2 shows the summary of the 3" PMTs acceptance criteria and test results for all parameters.

Parameters	Class	Requirement		Test fraction		Tolerance	Results
		(limit)	(mean)	HZC	JUNO	of diff.	(mean)
Φ (glass bulb)	A	(78,82) mm	-	100%	10%	-	OK
QE@420 nm	A	>22%	>24%	100%	10%	<5%	24.9%
High Voltage	A	(900,1300) V	-	100%	10%	<3%	1113 V
SPE Resolution	A	<45%	<35%	100%	10%	<15%	33.2%
PV Ratio	A	>2	>3	100%	10%	-	3.2
DCR@0.25 PE	A	<1.8 kHz	<1.0 kHz	100%	10%	-	512 Hz
DCR@3.0 PE	A	<30 Hz	-	100%	10%	-	7.2 Hz
TTS (σ)	B	<2.1 ns	-	-	3%	-	1.6 ns
Pre-pulse	B	<5%	<4.5%	-	3%	-	0.5%
After-pulse	B	<15%	<10%	-	3%	-	3.9%
QE non-uniformity	B	<11%	-	-	3%	-	5%
Φ (eff. cathode)	B	>74 mm	-	-	3%	-	77.2 mm
QE@320 nm	C	>5%	-	-	1%	-	10.2%
QE@550 nm	C	>5%	-	-	1%	-	8.6%
Aging	D	>200 nA $\cdot$ years	-	-	3 PMTs	-	OK

Table 2.2: Summary of the 3" PMTs acceptance criteria and test results for different parameters. The results for class A parameters are obtained with the mean value of the total vendor data, after JUNO modified its acceptance measurement modification. The other results were from the JUNO acceptance test.

There were 6 main parameters defined as belonging in class A of the acceptance test : the QE,

the HV for nominal gain, the SPE resolution, the PV ratio, and the DCRs at 0.25 PE and 3.0 PE thresholds. The sampling test results for these parameters are shown in Figure 2.14 and compared with the vendor data, after rescaling the distributions. A good agreement between the sampling test results and the vendor data is apparent, and the results respect the requirements defined in Table 2.2.

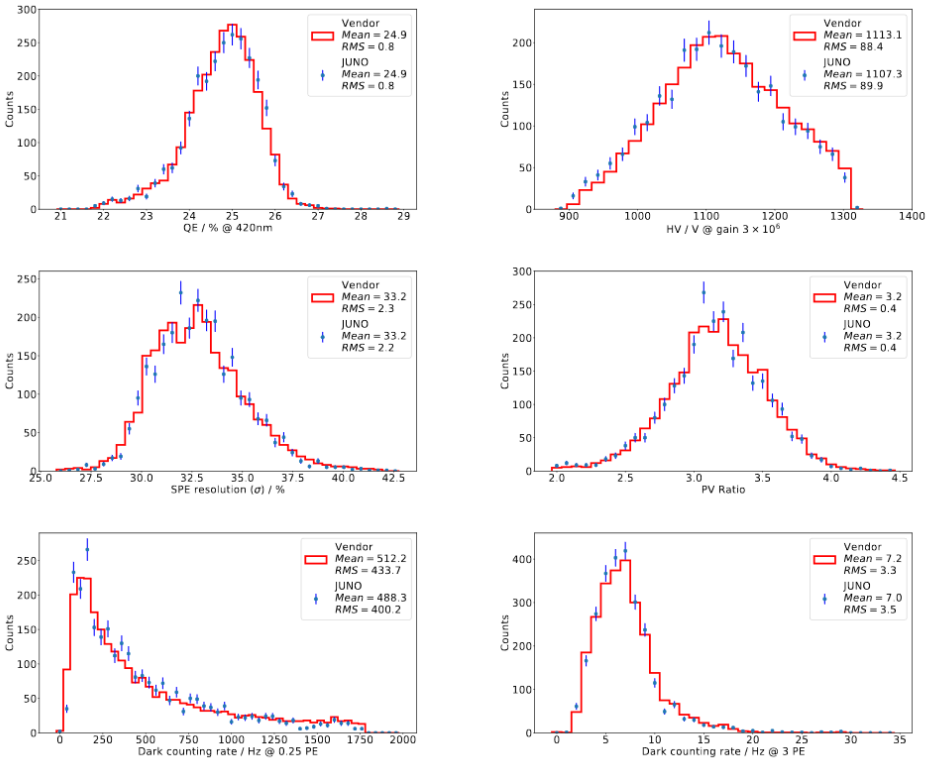

Figure 2.14: The PMT sampling test results (2,600 PMTs) for class A parameters and comparison with vendor data (26,000 PMTs), after normalization.

For the QE at 420 nm, the HV at gain 3×10^6 and the SPE resolution, 3 important parameters of class A, the difference between the sampling test result and the vendor data was required to be smaller than a tolerance, respectively defined as 5%, 3% and 15% for any single PMT. These tolerances correspond to a 4-6 σ margin, to allow the normal fluctuation to be accepted. The fractions of PMTs out of the tolerance ranges, among 2600 tested PMTs, are respectively 1.6%, 2.7% and 2.4%, and a majority of the PMTs were in agreement with the vendor data after being re-tested.

The ratio of PMTs tested for parameters in classes B and C was respectively 3% and 1%, both classes sampled by the JUNO shifters from a sub-batch of 150 PMTs that had passed the class A acceptance test. The class C sample was fully contained in the class B sample. In the TTS station, the TTS, pre-pulse and after-pulse parameters were measured, and the results are shown in Figure 2.15. With an average of 1.6 ns (σ) at the HV ratio 3:2:1 and a relative standard deviation of 10.5%, the TTS distribution was determined to be very stable.

In the scanning station, the non-uniformity of the QE and the effective photo-cathode diameter were measured. With a mean QE non-uniformity of 5% and a mean effective photo-cathode diameter of 77.21 mm for the 790 tested PMTs, the measurements were in accordance with the requirements and no PMT was rejected. The mass of the PMTs was also measured during the acceptance test procedure, with the goal of identifying the more massive PMTs to position at the

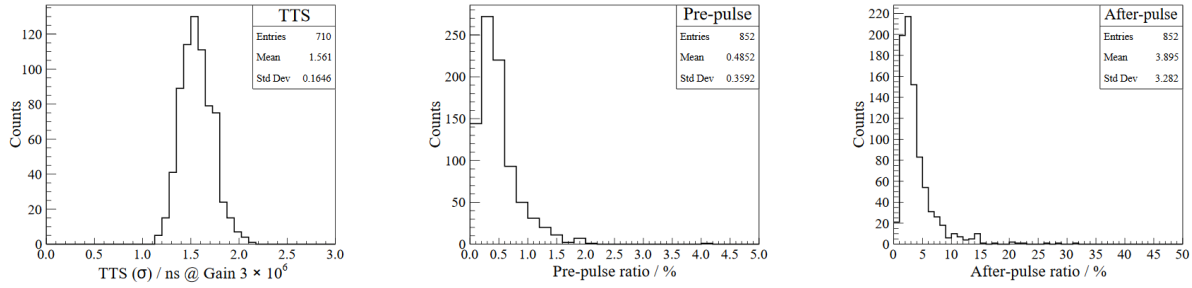

Figure 2.15: Distribution of TTS, Pre-Pulse and After-Pulse from the sampling test. The TTS distribution has fewer entries as the first tens of PMTs were measured at a HV ratio of 3:1:1, and these data were not taken into account in the distribution. the upper requirements for these parameters were respectively 2.1 ns, 5%, 15%.

bottom of the water pool, and the less massive ones at the top. An unusually low mass could also indicate a thinner glass bulb, which could present risks of shattering under the water pressure.
Conforming to JUNO's requirements on the production, the average good rate of the mass production was about 80.5%, with the quality of the production increasing every year. In the last year of production, the rate of good produced PMTs reached 87.8%.

2.6 CD calibration system

Particle interactions in the LS will produce scintillating and Cherenkov ($\leq$10%) photons, in numbers mostly proportional to the deposited energy, which will then be converted to photoelectrons by the PMTs. However, there is an intrinsic non-linearity in the scintillation mechanism, due to the quenching effect on the scintillation photons, depending on the energy and type of the particle [9]. This effect, combined with the non-linearity on the Cherenkov light mechanism to give the "physics non-linearity", can be calibrated by the combination of radioactive sources and natural radioactivity background. Figure 2.16 shows the non-linearity of gamma particles by representing the ratio between the visible energy E_{vis}, defined as the energy estimated based on the detected number of PEs, and the true energy E_{true} as a function of the true energy. At different energies, the quenching effect does not have the same impact on the eventual visible energy of the particles, and this phenomenon needs to be taken into account in the physics measurement of the JUNO experiment.
In order to correct this energy non-linearity, the collaboration developed a calibration program involving multiple calibration sources and scan systems of multiple dimensions. This calibration is necessary to fulfill the requirements of the JUNO central detector of a 3% effective energy resolution parameter at 1 MeV and of a better than 1% energy linearity, in order to precisely determine the neutrino mass ordering. The multiple scan systems will also enable the calibration of the non-uniformity of the Central Detector.

2.6.1 Calibration system design

The hardware design of the calibration system was driven by the requirement to have a 3D map of the detector response. This requires being able to not only place a source along the central axis of the CD, but also on a circle at the LS-acrylic boundary as well as in the region in-between. This design consists of several independent subsystems, which allow for the possibility of having several different types of scans of the whole detector, and which are all shown in Figure 2.17a.

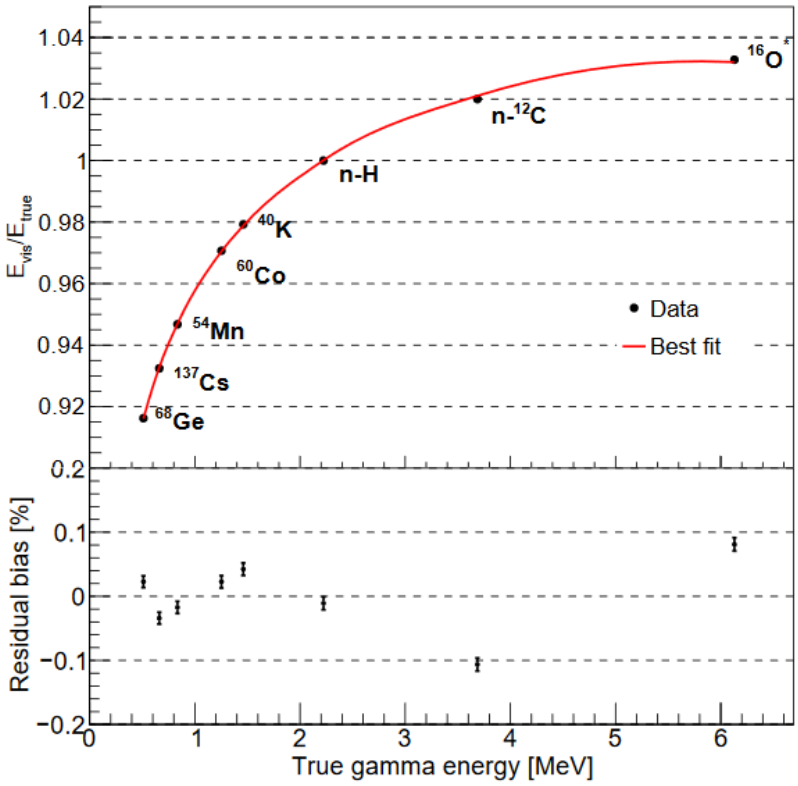

Figure 2.16: Fitted and simulated gamma non-linearity using the ratio of the visible energy to the true.

In the one-dimensional scan scenario, the Automatic Calibration Unit (ACU) is deployed through the chimney to calibrate positions along the central axis of the Central Detector, with multiple radioactive sources and pulsed laser light [65]. This is represented by the red dots in Figure 2.17b. The precision of the calibration positions can be controlled to less than 1 cm. This is crucial because, in addition to the energy non-linearity, the total number of PEs collected by the LPMT and SPMT systems is also position-dependent in JUNO, for instance due to PMT solid angles, optical attenuation effects, reflections at material interfaces, or shadowing due to opaque materials. This intrinsic position non-uniformity, mostly energy independent, has to be corrected by this multi-positional calibration to optimize the energy resolution. Figure 2.18 shows the mean number of photoelectrons collected by the PMTs per MeV, for 2.22 MeV gammas, as a function of the radius (distance of the event to the center of the detector) for a few representative polar angles θ in spherical coordinates. The number of collected PEs increases with the radius, as the photons are less attenuated due to having less LS to cross to reach the PMTs, until a decrease due to the combination of the total reflection of photons at the acrylic/water interface as well as gamma leakage at the edge of the CD. Within the same radius, there is an additional dispersion in θ due to effects such as PMT coverage, of about of 3-4%.
In the two-dimensional scan scenario, in order to calibrate the non-uniformity of the detector, a source attached to one of the Cable Loop Systems (CLS) is moved on a vertical half-plane, with tunable hanging wire lengths to reach off-center positions [73]. Two sets of CLSs will be deployed to provide a 79% effective coverage area, as is illustrated in Figure 2.17b with the green dots. The redundant coverage of these two sets will be used to cross-check the azimuthal asymmetry. A Guide Tube (GT), which longitudinally surrounds the outside of the CD, will be used to calibrate

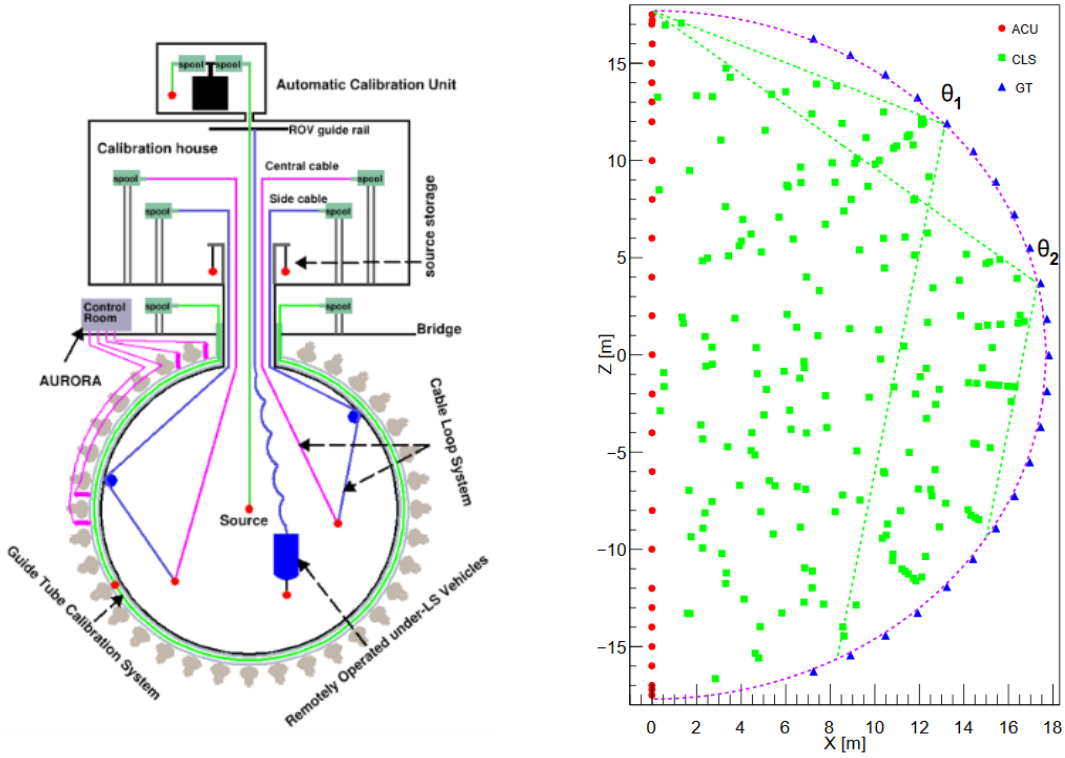

(a) (b)

Figure 2.17: (a) Overview of the calibration system, including the Automatic Calibration Unit (ACU), two Cable Loop Systems (CLSs), the Guide Tube (GT), and the Remotely Operated Vehicle (ROV). The red points represent a source assembly. (b) The optimized 250 calibration points in a half vertical plane of the JUNO CD. The purple dashed line represents the acrylic boundary. The green dashed lines are the assumed boundaries of the CLS.

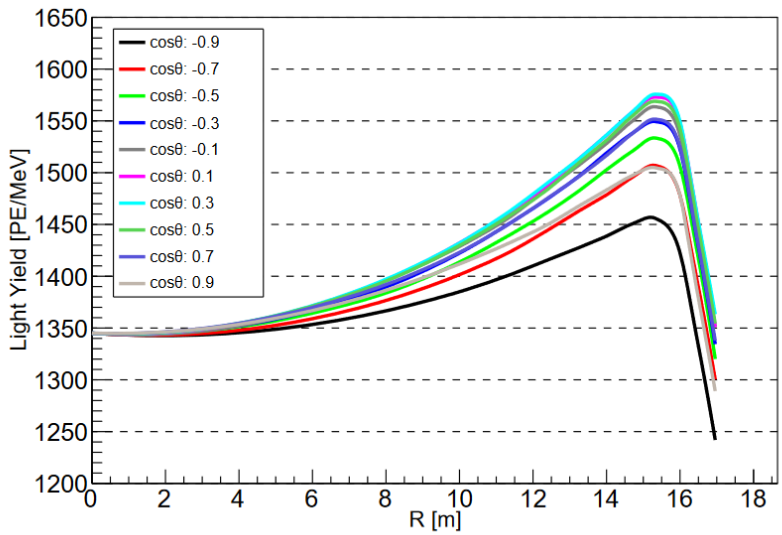

Figure 2.18: Mean number of PEs per MeV for 2.22 MeV gammas as a function of the radius, along a few representative polar angles.

the non-uniformity at the CD edge due to gamma leakage. To do so, a source will be pulled in the Teflon GT with servomotors and Teflon-coated steel cables to reach the desired locations. This is represented in Figure 2.17b by the purple dots at the acrylic boundary.
In the three-dimensional scan scenario, the Remotely Operated under-LS Vehicle (ROV) will be suspended in the LS with a radioactive source to calibrate the desired positions. The ROV motion will be controlled with multiple orientation motors and an umbilical cable, used to deliver the power and the transfer control signals, with a camera inserted in the ROV to observe the situation inside of the CD.
As the ACU, CLS and ROV systems will be inside of the CD, they will be installed and assembled in an air-tight stainless steel calibration house located on top of the detector, to avoid air-born radon diffusion into the LS. Changing the calibration sources will be done automatically through a set of designated structures. An additional unit, the Unit for Researching Online the LSc tRAnsparency (AURORA) is an auxiliary laser diode system to monitor the attenuation and scattering length of the LS.

2.6.2 Radioactive sources

Radioactive sources with gammas, positrons and neutrons will be used for calibration in order to correct the energy responses in the [1-8 MeV] energy range of the IBD events. The time responses will be corrected using a pulsed UV laser (266 nm wavelength) [74]. The radioactive sources as well as the types of emitted radiations are listed in Table 2.3. For a large LS detector such as JUNO, thin-walled electron or positron sources would pose a risk of leakage of radionuclides. Instead, γ sources ranging from a few hundred keV to a few MeV are considered, to cover the range of the prompt energy of IBDs. The ^{68}Ge sources decay to ^{68}Ga via electron capture, which then decays by β_+ to ^{68}Zn. The kinetic energy of the positrons will be absorbed by the enclosure, so only the annihilation gammas are released. In addition, (α, n) sources such as ^{241}Am-Be (AmBe) and ^{241}Am-^{13}C(AmC) can be used to provide both high energy gammas and neutrons, the latter of which also produce capture gammas on hydrogen and carbon atoms in the LS. This is done in order to mimic and calibrate the delayed signal of the IBDs.

Source	Type	Radiation
^{137}Cs	γ	0.662 MeV
^{54}Mn	γ	0.835 MeV
^{60}Co	γ	1.173 + 1.333 MeV
^{40}K	γ	1.461 MeV
^{68}Ge	e^+	annihilation 0.511 + 0.511 MeV
^{241}Am-Be	n,γ	neutron + 4.43 MeV (^{12}C*)
^{241}Am-^{13}C	n,γ	neutron + 6.13 MeV (^{16}O*)
(n,γ)p	γ	2.22 MeV
(n,γ)^{12}C	γ	4.94 MeV or 3.68 + 1.26 MeV

Table 2.3: List of radioactive sources considered in the JUNO calibration.

2.6.3 Calibration program

A calibration program has to be defined for both global, comprehensive measurements, as well as for narrower but more regular ones. For this program, the rates of the radioactive sources are set to be around a few hundreds of neutron or gamma emissions per second, so that the data rate during the calibration does not differ too much from the data rate during the neutrino data

taking. Similar to what was done for the Daya Bay calibration, the JUNO calibration program was envisioned to be separated into weekly, monthly, and comprehensive but infrequent calibrations. As a requirement, source deployments should not introduce noticeable radio-impurities such as radon. The nominal speed of the source movement is about 1 m/min.
The start of the experiment is likely to be immediately followed by a comprehensive calibration, in order to achieve a necessary basic understanding of the CD performance. This calibration will then need to be repeated a few times throughout the life time of the JUNO experiment. In such a calibration, multiple sources will be deployed to the CD center to study the non-linearity. The AmC neutron source will be deployed to the full set of 250 points using the ACU, CLS and GT. The total time of such a calibration is expected to be about 48 hours. Weekly and monthly calibrations have also been designed to track major changes in the detector properties, such as variations in the light yield of the LS, PMT gains, or electronics, with the monthly calibrations going through a more limited number of positions. These calibrations are summed up in Table 2.4, with the comprehensive calibration referred to as the special calibration.

Program	Source	Energy [MeV]	Calibration points
Weekly calibration	Neutron (Am-C)	2.22	5
	Laser	/	10
Monthly calibration	ACU - Neutron (Am-C)	/	27
	ACU - Laser	/	27
	CLS - Neutron (Am-C)	/	40
	GT - Neutron (Am-C)	/	23
Special calibration	Neutron (Am-C)	2.22	250
	Neutron (Am-Be)	4.4	1
	Laser	/	8
	^{68}Ge	0.511×2	1
	^{137}Cs	0.662	1
	^{54}Mn	0.835	1
	^{60}Co	1.17 + 1.33	1
	^{40}K	1.461	1

Table 2.4: Baseline plan of the different calibrations. For the comprehensive calibration, the Am-C will be deployed into 250 points utilizing the ACU, CLS and GT. All other sources will rely on the ACU only. More sources at other locations are also possible. The weekly calibration will be performed using the ACU, and the monthly calibrations using the ACU, CLS and GT.

2.7 Low background strategy

The main expected background sources to the antineutrino IBD process in JUNO are cosmic muons through cosmogenic isotopes induced by muon spallation in the liquid scintillator, fast neutrons, natural radioactivity, geoneutrinos and α-n reactions. The contribution of five backgrounds to the neutrino spectrum is illustrated in Figure 2.19.
Apart from the natural radioactivity, the impact of all these sources on the JUNO measured event rate is determined by the choice of the experimental site and can only be diminished by efficient tagging, careful event reconstruction, and dedicated veto strategies. The JUNO detector is located in an underground laboratory with 700 m overburden, i.e. 1800 m.w.e. At this depth, the muon flux at the JUNO site is of about 0.004 Hz/m^2 with a mean energy of 207 GeV. The rate of muons passing through the ultrapure water of the WCD is of 10 Hz, while the rate of muons passing

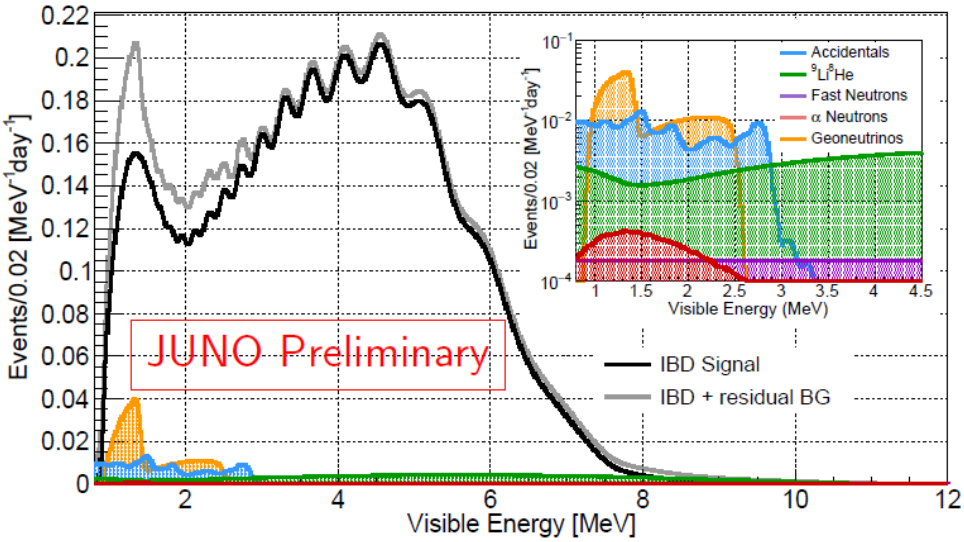

Figure 2.19: Spectra for the antineutrino signal and five kinds of main backgrounds, including the accidental, ^{9}Li/^{8}He, fast neutron, and ^{13}C$(\alpha, n)^{16}$O and geoneutrinos. [59]

through the liquid scintillator is of 3.6 Hz. Fast neutrons produced by muons passing through the rock and the detector materials may reach the liquid scintillator and mimic an IBD event: the efficient muon tagging by the WCD of JUNO will remove most of these events, leading to a low impact on the background budget of the fast neutrons. Muons and muon showers interact with ^{12}C in the LS, producing light isotopes called cosmogenics by hadronic or electromagnetic processes. The produced β–n decaying nuclides can also mimic an IBD signal : the resulting ^{9}Li/^{8}He are the most dangerous correlated ones for background. In this respect, there are various physics driven models for veto strategies to reduce the impact of the cosmogenic background in the different JUNO physics channels. For well-tracked muons in the CD, only the LS volume within a cylinder of distance to the muon track with R $<$ 3 m and within time to the preceding muon T $<$ 1.2 s will be vetoed, in order to maximize the detector live time and minimize the dead volume losses. Natural radioactivity comes from all the JUNO materials and the environment. The radioactivity from external materials, mainly ^{238}U (U) and ^{232}Th (Th) chains and ^{40}K, can be effectively removed by fiducial volume (FV) cuts and energy thresholds. The JUNO default values for neutrino mass ordering analysis are E_{th}=0.7 MeV and r_{LS}=17.2 m. It is important to distinguish the *internal background*, coming from the LS itself and the *external background*, coming from the other parts of the JUNO detector. Indeed, for the internal background, all the radionuclides especially from the U/Th chains will contribute to the deposited energy whatever the nature of the emitted particles (α, β and γ). In this case, a fiducial volume cut would be useless for removing the background events, since they are uniformly distributed in the LS. On the contrary, only a part of the radionuclides will contribute to the external background considering the very short ranges of the α and β particles in solid materials, which will exclude pure α and β emitters. Only high energy γs will be able to reach the LS and deposit energy, mainly coming from ^{214}Bi (U chain), ^{208}Tl (^{232}Th chain) and ^{40}K. In this case, the fiducial volume cut is more effective as it is illustrated in Table 2.5 for all the materials except LS. Huge efforts on material screening and convenient arrangement of the experimental apparatus were the main driving actions during JUNO planning and designing, in order to contain the single event rate below 10 Hz in the fiducial volume of JUNO. Giving this rate and the required correlation in energy, time and space between the prompt and delayed signals, the accidental background rate from the natural radioactivity is expected to be about 0.9 count per day (cpd).

Material	Mass [t]	Target impurity concentration					Singles	
		^{238}U [ppb]	^{232}Th [ppb]	^{40}K [ppb]	^{210}Pb [ppb]	^{60}Co [mBq/kg]	No FV [Hz]	FV [Hz]
LS	20000	10^{-6}	10^{-6}	10^{-7}	10^{-13}		2.5	2.2
Acrylic	610	10^{-3}	10^{-3}	10^{-3}			8.4	0.4
SS structure	65 1000	0.2 1	0.6 3	0.02 0.2		1.5 20	15.9	1.1
PMT glass	33.5 100.5 2.6	400 200 400	400 120 400	40 4 200			26.2	2.8
PMT readout	125 16.3	68 93	194 243	5 12		16 14	3.4	0.4
Other							2.5	0.3
Sum							59	7.2

Table 2.5: Final background budget for the main materials used in the JUNO detector with reconstructed energy E_{rec} larger than 0.7 MeV. The expected count rates are given in both the full detector volume (No FV, i.e. $r_{LS} = 17.7$ m) and within the default FV ($r_{LS} = 17.2$ m). The "Other" components include all materials that have relatively smaller contribution to the background such as the calibration parts, the LPMT cover, the rock, and the radon in the water.

A set of preliminary selection criteria is studied in the JUNO Yellow Book [59]. Table 2.6 summarizes the efficiencies of the selection cuts and the corresponding reductions for various backgrounds. JUNO will observe 60 IBD events per day, with about 6% (3.6 cpd) background contamination.

Selection	IBD efficiency	IBD	Geo-νs	Accidental	^{9}Li/^{8}He	Fast n	(α,n)
-	-	83	1.5	-	84	-	-
Fiducial volume	91.8%	76	1.4	410	77	0.1	0.05
Energy cut	97.8%	73	1.3		71		
Time cut	99.1 %						
Vertex cut	98.7%			1.1			
Muon veto	83%	60	1.1	0.9	1.6		
Combined	73%	60	3.55				

Table 2.6: Efficiencies of antineutrino selection cuts, signal and background rates, expressed in counts per day (cpd). [59]

2.8 TAO

The Taishan Antineutrino Observatory, abbreviated as TAO, was designed and proposed by the collaboration as a way to precisely measure the reactor anti-neutrino spectrum. With a liquid scintillator (LS) detector at ~30 m from a reactor core of the Taishan Nuclear Power Plant, it is intended to provide a reference spectrum for the determination of the neutrino mass ordering by JUNO, and is expected to start its data taking at a similar time as JUNO. With a fiducial volume of LS of about 1 ton, the IBD event rate of TAO will indeed be more than 30 times that of JUNO, providing enough statistics for the desired reactor anti-neutrino spectrum. Although a $3\%/\sqrt{E}$ energy resolution is enough for TAO to serve as the reference detector of JUNO, the energy

resolution should be as high as possible to study the fine structure of the reactor antineutrino spectrum and create a highly resolved benchmark to test nuclear databases.
Therefore, TAO will use Silicon Photomultiplier (SiPM) with a $> 50\%$ photon detection efficiency to observe the LS with an almost full coverage (10 m^2 surface). The detector will have to be operated at -50°C to lower the dark noise of these SiPMs to $\sim$100 Hz/mm^2, with the simulation predicting about 4500 photoelectrons observed per MeV. This corresponds to a $1.5\%/\sqrt{E}$ resolution. Taking into account the other detector responses, the energy resolution could reach $< 2\%/\sqrt{E}$.
The schematic drawing of the TAO detector is shown in Figure 2.20. The Central Detector (CD) detects reactor antineutrinos with 2.8 tons of Gadolinium-doped LS (GdLS) contained in a spherical acrylic vessel with an inner diameter of 1.8 m. To contain the energy deposition of gammas from positron annihilation, a 25-cm selection cut will be applied for the positron vertex from the acrylic vessel, resulting in 1 ton fiducial mass. As such, the IBD event rate in the fiducial volume will be about 2000 events per day with the detection efficiency taken into account. A spherical copper shell with an inner diameter of 1.884 m and a thickness of 12 mm frames the acrylic vessel, and provides mechanical support and thermal stability for the SiPM tiles. The resulting gap between the SiPM surface and the acrylic vessel is $\sim$2 cm. The copper shell is installed in a cylindrical stainless steel tank with an outer diameter of 2.1 m and a height of 2.2 m. This stainless steel tank is filled with Linear Alkylbenzene (LAB) as the buffer liquid used to shield from the radioactivity of the outer tank and to optically couple the acrylic vessel and the SiPM surfaces. It is insulated with 20 cm thick Polyurethane (PU) for the detector to be operated at -50°C.

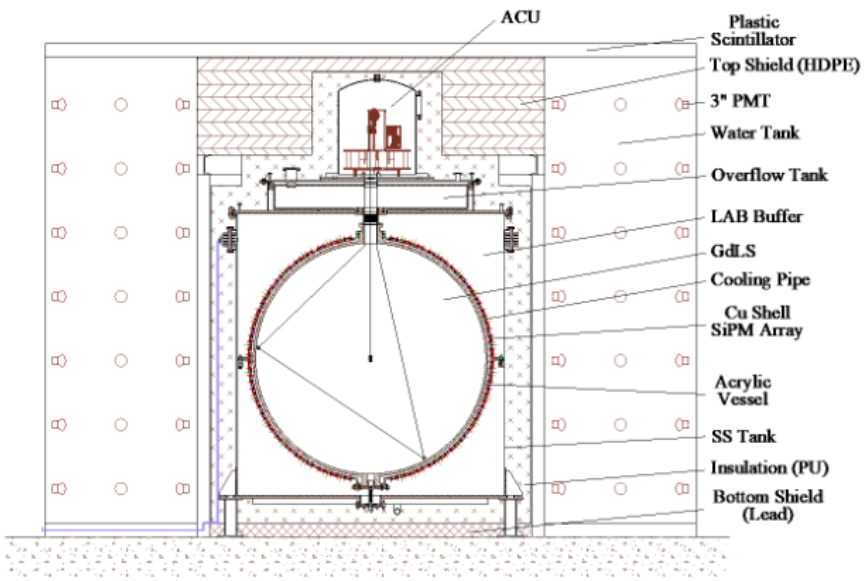

Figure 2.20: Schematic view of the TAO detector.

The CD is surrounded by 1.2 m thick water tanks on the sides, a 1 m thick High Density Polyethylene (HDPE) on the top, and 10 cm thick lead at the bottom to shield it from the ambient radioactivity and cosmogenic neutrons. Cosmic muons will be detected by the water tanks with PMTs and by Plastic Scintillator (PS) on the top.
The Taishan Nuclear Power Plant, providing the reactor anti-neutrinos for the TAO experiment, is located 53 km away from the JUNO experiment. It has two cores currently in operation, both European Pressurised Reactors (EPR) with 4.6 GW thermal power. The baseline of the TAO

CD is ∼30 m from a reactor core, with the far reactor core of the Taishan Nuclear Power Plant contributing to only about 1.5% of the total reactor antineutrino rate of TAO. This allow for a great confidence in the desired reference spectrum. The muon and cosmogenic neutron rates in the Taishan Neutrino Laboratory, 9.6 m underground, are measured to be 1/3 of those on the ground. Simulations show that the cosmogenic fast neutron background, accidental background, and cosmogenic ^{8}He/^{9}Li background can be controlled to $< 10\%$ of the signal with the shielding and muon veto designs.

2.9 Additional physics with JUNO

2.9.1 Neutrino oscillation parameters precision measurements

As described in section 1.3.4, JUNO will observe the effects of the solar and atmospheric oscillations simultaneously. The solar oscillations, driven by Δm^2_{21} and modulated by $sin(2\theta_{12})$ (Figure 1.20), cause the slow oscillation (low frequency) in the electronic antineutrino survival probability (illustrated in Figure 1.19) which is responsible for the bulk of the reactor antineutrino disappearance. The atmospheric oscillations, driven by Δm^2_{32} and modulated by $sin(2\theta_{13})$ (Figure 1.20), cause the higher frequency oscillations on top of the slower ones (illustrated in Figure 1.19). Measuring the oscillated reactor antineutrino spectrum with a resolution of 3% at 1 MeV will allow for the determination of these 4 parameters simultaneously, with 3 of these parameters measured at unprecedented precision levels, as illustrated in Figure 2.21.

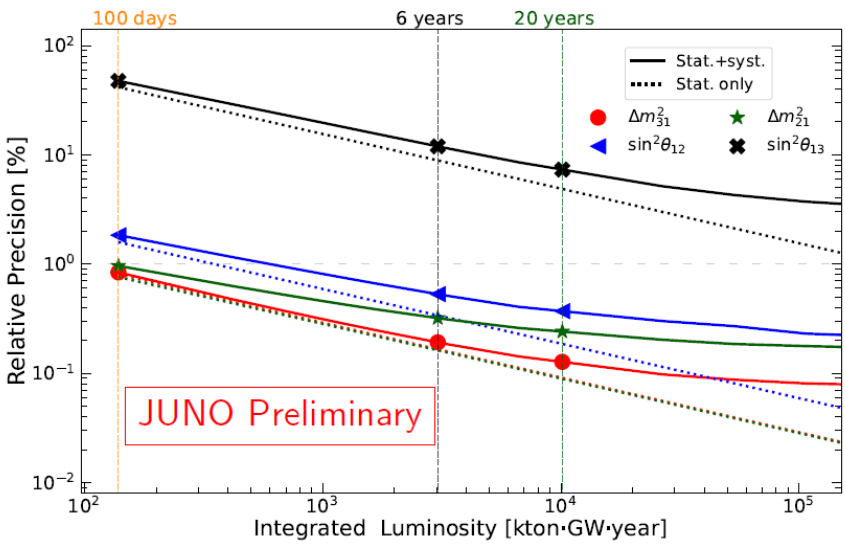

Figure 2.21: Relative precision of the measurement of different oscillation parameters as a function of the luminosity of the JUNO experiment. The markers and vertical lines stand for 100 days, 6 years and 20 years of data-taking.

This figure shows the time evolution of the precision on the oscillation parameters obtained with the JUNO experiment, from recent preliminary studies, as a function of the integrated luminosity. The markers correspond to 100 days, 6 years and 20 years of data-taking. Figure 2.21 indicates that the precision on the oscillation parameters will come to the sub-percent level after about one year of data-taking. The precision on $sin(2\theta_{12})$, Δm^2_{21} and $|\Delta m^2_{ee}|$ measurements for 100 days, 6 years and 20 years is shown in Table 2.7, with a comparison to the current precision on these parameters, respectively 4%, 2.8% and 1.1%, obtained from the combined NuFit results (Table 1.3 [45]). Within just 100 days of data-taking, JUNO will thus be able to reach a much better precision

on the neutrino oscillation parameters than all current experiments combined, and therefore, tests of the unitarity of the lepton mixing matrix will be feasible at unprecedented precision levels.

	JUNO 100 days	JUNO 6 years	JUNO 20 years	Current precision
$sin^2(\theta_{12})$	1.85%	0.52%	0.33%	4.0%
Δm^2_{21}	0.97%	0.31%	0.22%	2.8%
$\lvert\Delta m^2_{ee}\rvert$	0.81%	0.18%	0.11%	1.1%

Table 2.7: Precision on $sin(2\theta_{12})$, Δm^2_{21} and $|\Delta m^2_{ee}|$ measurements obtained for 100 days, 6 years and 20 years of data-taking with the JUNO experiment. The current precisions on these parameters shown as comparison.

2.9.2 Supernova neutrinos

Neutrinos are crucial players during all stages of stellar collapses and explosions, with the detection of two dozen neutrino events from supernova (SN) 1987A in Kamiokande-II [75], Irvine-Michigan-Brookhaven [76], and Baskan [77] having essentially confirmed the scenario of the delayed neutrino-driven explosion mechanism for core-collapse supernovae (SNe) [78–82]. Future large water-Cherenkov (Hyper-Kamiokande), liquid-scintillator (JUNO), and liquid-argon time projection chamber (DUNE) neutrino detectors will all be able to register large statistics of SN neutrinos, and thus have great potential to provide their complete flavor information.

Theoretical predictions of the SNe neutrino-emission depict three main phases, namely the shock-breakout burst phase, during which 99% of the energy is released in neutrinos and antineutrinos of all flavors, the post-bounce accretion phase and the proto-neutron star cooling phase. It is highly desired to obtain a clear observation of these discriminative phases, with crucial information carried in the total energy, luminosity evolution, spectral distribution, and the mix of different flavors of the SN neutrinos. Before a massive star collapses and forms a SN, a significant number of MeV-energy neutrinos can also be produced via the thermal processes and nuclear weak interactions. Such pre-supernova neutrinos are also useful to prove the theory of stellar evolution [83, 84].

JUNO, with its 20 kt of LS, has excellent capability for multi-channel detection of all flavors of both $\mathcal{O}$(10 MeV) post-shock neutrinos and $\mathcal{O}$(1 MeV) pre-supernova neutrinos, mainly via the inverse beta decay (IBD), the elastic neutrino-electron scattering (eES), and the elastic neutrino-proton scattering (pES). For a typical galactic distance of 10 kpc and typical SN parameters, JUNO will register ~5000 IBD events, ~300 eES events and ~2000 pES events. The charged-current and neutral-current interactions of neutrinos on ^{12}C nuclei are observable as well [85], and the neutrino event spectra with respect to the visible energy in these six main reaction channels are shown in Figure 2.22. The $\mathcal{O}$(1 MeV) pre-supernova neutrinos could provide a unique and independent early warning for the optical observations of core-collapse SNe, and will be detectable via the IBD and eES channels.

The energy spectra of $\overline{\nu}_e$, ν_e, and ν_x (ν_μ, ν_τ, and $\overline{\nu}_\mu$, $\overline{\nu}_\tau$) is of crucial importance to understand the microscopic physics of SN explosions. The pES events of all flavors in LS can be used to extract the spectral information of ν_x [86], and by combining all channels, JUNO has a unique opportunity to provide flux information and to reconstruct the multi-flavor supernova neutrino energy spectra, as demonstrated by a model-independent approach [87, 88]. Figure 2.23 shows the multi-flavor supernova neutrino luminosity spectra as a function of the timing of the event, for the 3 supernova phases aimed to be investigated.

SN bursts can be challenging on the electronics of the data acquisition systems. JUNO, for example, has the opportunity to be able to handle Betelgeuse (0.2 kpc), resulting in a challenging 10 MHz trigger rate acceptance. The JUNO front-end-electronics will be featured with real-time waveform

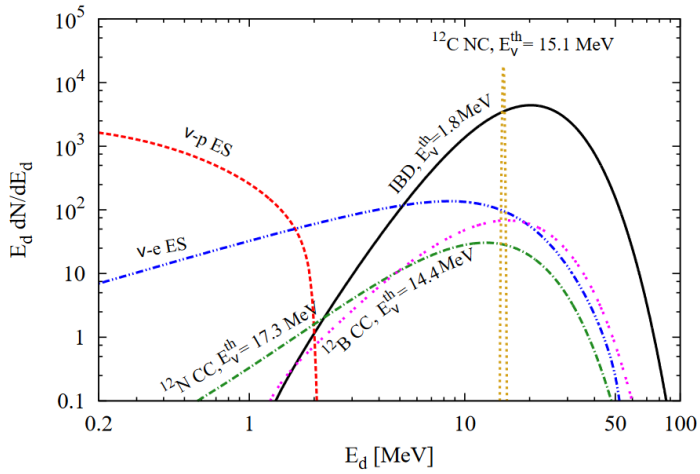

Figure 2.22: Neutrino event spectra with respect to the visible energy E_d in the JUNO detector for a typical SN at 10 kpc [59].

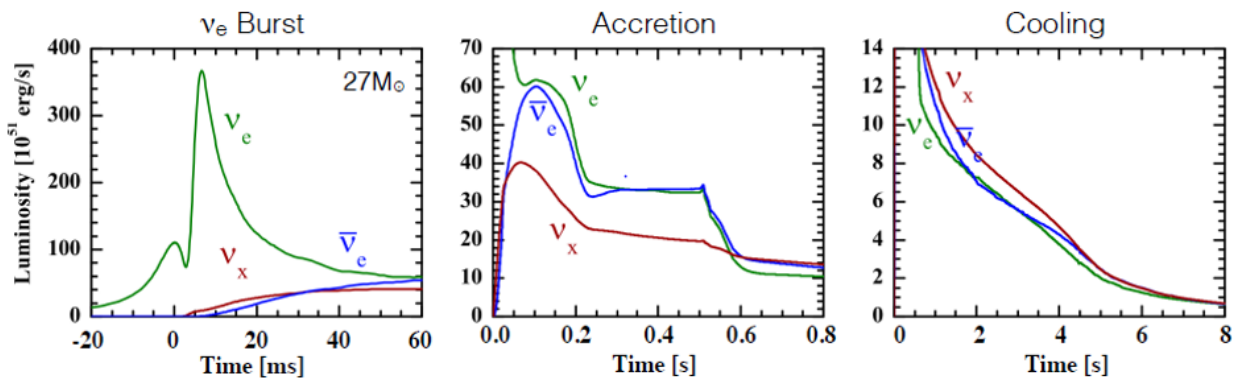

Figure 2.23: Multi-flavor supernova neutrino luminosity spectra for the 3 supernova phases : burst, accretion and cooling .

processing in the FPGA and a 2 GB DDR3 memory shared by three PMTs, maximizing JUNO's ability of real-time monitoring and data acquisition for the neutrinos from core-collapse SNe. A dedicated multi-messenger trigger system is also under design to achieve an ultra-low detection threshold of $\mathcal{O}$(10 keV), in order to position JUNO as a powerful broad-band multi-messenger observatory and connect it to the global network of multi-messenger observatories.

No SN burst neutrinos have been observed so far since SN 1987A, with an expected rate of 1.63 $\pm$ 0.46 core-collapse SN per century [89]. With large neutrino detectors like JUNO coming online in the near future, it is still promising to obtain a high-statistics measurement of the neutrinos from a galactic core-collapse SN in the next few decades, allowing for a better understanding of the explosion mechanism and for an investigation of the intrinsic properties of the neutrinos such as the absolute scale of neutrino masses [90]. The detection of the integrated signal from all past stellar core-collapse SNe, the diffuse SN neutrino background, will also improve our understanding of cosmology.

2.9.3 Diffuse supernova neutrino background

Core-collapse Supernovae (SNe) in our own galaxy, while being rare events, are continuously proceeding throughout the visible universe, sending bursts of neutrinos in the Earth's direction,

and as such are all contributing to a low background flux of low-energy neutrinos called the Diffuse Supernova Neutrino Background (DSNB). This background is on the level of $\sim$10 ν.cm^{-2}.s^{-1}. Information on the red-shift dependent Supernova rate, average SN neutrino energy spectrum and fraction of black hole formation in core-collapse SNe is contained in the exact flux and spectrum of the DNSB. JUNO is in an excellent position to detect the $\overline{\nu}_e$ component of the DSNB flux, with about 2-4 expected IBD events per year in the energy range above the reactor $\overline{\nu}_e$ signal, depending on the DSNB model.

However, many sources of background interfere with the DSNB signal, one of them being the terrestrial flux of $\overline{\nu}_e$ from reactors and atmospheric neutrinos, which causes an irreducible background of real IBD coincidences and reduces the detection window of the DNSB to the range of about 8 to 30 MeV. Cosmic muons are also penetrating the detector and, though spallation processes, generate βn-emitting isotopes in the LS, like ^{9}Li, as well as fast neutrons when passing through the rock surrounding the detector. Both types of particles can mimic IBD coincidence signals and, respectively, can be effectively reduced by a coincidence veto in the wake of a through-going muon or a fiducial volume cut.

The most critical background is created by neutral-current (NC) interactions of atmospheric neutrinos with ^{12}C [91, 92], for which the emission of one neutron together with a prompt energy deposit may be able to mimic the IBD coincidence signal of DSNB. As depicted in Figure 2.24a, which displays an exemplary event spectrum for DNSB expected mean energy $\langle E_\nu \rangle = 15$ MeV, this background rate surpasses the DSNB signal by more than an order of magnitude, greatly compromising the measurement. However, the intrinsic pulse-shape discrimination (PSD) capabilities of liquid scintillators can be used to suppress the NC background to an acceptable level, assuming PSD efficiencies for which 50% of the DSNB signal and 1.1% of the NC background survive after the PSD selection [93]. The spectra post-PSD are shown in Figure 2.24b, with the DSNB signal now dominating all backgrounds in the range from 11 to $\sim$22 MeV.

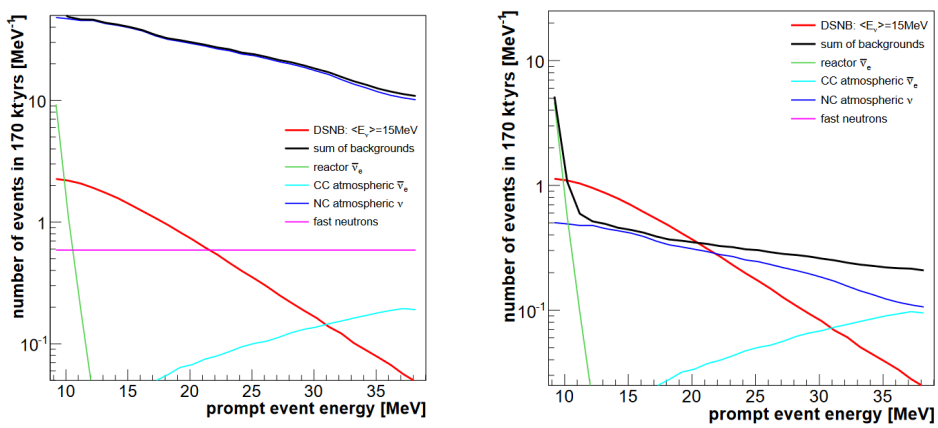

Figure 2.24: (a) DSNB signal and background spectra. The background by atmospheric-neutrino NC reactions dominates over the whole range of the observation window from 11 to 30 MeV. (b) DSNB and background spectra after application of pulse shape discrimination. The DSNB signal is dominating all backgrounds in the spectral range from 11 to $\sim$22 MeV.

Due to the irreducible backgrounds from reactor $\overline{\nu}_e$ in the low-energy range and atmospheric $\overline{\nu}_e$ at high energies, the DSNB observation window is narrow, with the visible energy E_{vis} constrained by 11 MeV $\leq E_{vis} \leq$ 30 MeV. When determining the sensitivity of JUNO for a positive PSD detection, based on a rate analysis in the observation window, this result depends on the mean

energy $\langle E_{\overline{\nu}_e} \rangle$ underlying the DSNB signal. As illustrated in Figure 2.25, JUNO can be expected to provide 3σ evidence of the DSNB signal after 10 years of data taking for $\langle E_{\overline{\nu}_e} \rangle \geq 15$ MeV.

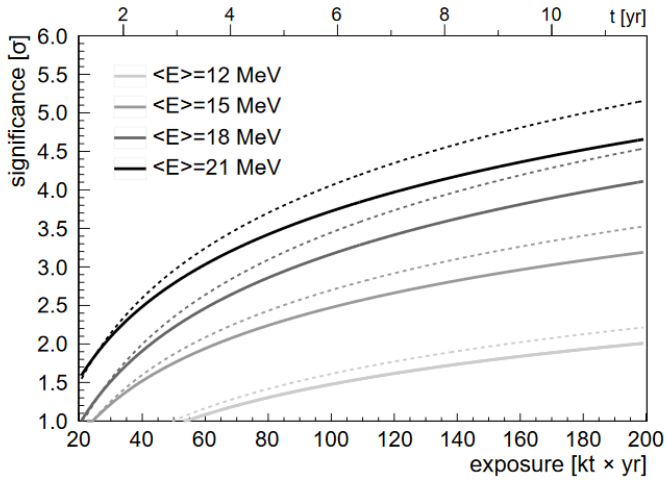

Figure 2.25: Sensitivity to the DSNB signal vs. exposure, depending on mean spectral energy and background uncertainty for which 20% (10%) is assumed for solid (dashed) lines.

2.9.4 Solar neutrinos

Solar neutrinos, produced in the thermonuclear fusion reactions in the solar core, represent a natural source of neutrinos with an energy spectrum extending up to about 16 MeV, and have played a significant role in the development of neutrino physics and astrophysics as they can reveal direct information about the solar core and can be exploited to study the fundamental neutrino properties and their interaction with matter.

In the last decade, a substantial experimental progress has been made by Borexino (LS detector) and Super-Kamiokande (WCD detector), via the high precision real-time spectroscopy of solar neutrinos based on their elastic scattering (ES) off electrons, with Borexino having performed a comprehensive measurement of pp-chain solar neutrinos [94] and having observed solar neutrinos from the Carbon-Nitrogen-Oxygen (CNO) fusion cycle [95], and Super-K having collected the world's largest sample of ^{8}B solar neutrinos, making it possible to study in detail the spectral distortion in the transition region of the electron neutrino survival probability P_{ee} to constrain the neutrino oscillation parameters (mixing angle θ_{12}, mass-squared difference Δm^2_{21}) [96, 97].

Several open questions in solar neutrinos still remain, and could potentially be answered with significant efforts on detector design, construction, and data analysis, especially for any improvements on the flux measurement. In neutrino oscillation physics, the transition region of P_{ee} has not been fully explored, since the analysis threshold of the ES electrons is difficult to reach below 3 MeV and 3.5 MeV, in Borexino and Super-K respectively, with its shape being sensitive to Δm^2_{21} values and able to be used to test new physics, such as non-standard interactions or the existence of sterile neutrinos [98]. Future, more precise measurements of $sin^2\theta_{12}$ and Δm^2_{21}, using solar neutrinos, will also contribute to testing the consistency of the standard three neutrinos framework and to probing new physics beyond the Standard Model. Solar physics, such as the metallicity problem, will also profit from more precise flux measurements of all neutrino components [99].

The JUNO experiment, with a Borexino-type liquid scintillator detector but a much larger target mass, comparable to that of the Super-K water Cherenkov detector, has the potential to make significant contributions to the solar neutrino measurements, with a Δm^2_{21} precision measurement

using electron signals of the ES channel and a new ^{8}B neutrino flux measurement via the ν_e ^{13}C charge current (CC) and the ν_x ^{13}C neutral current (NC) reactions.
As a LS-based detector, the primary detection channel of solar neutrinos in JUNO is the elastic scattering (ES) with electrons. The background to this detection consists of the intrinsic natural radioactivity in LS, the natural radioactivity from external detector materials, and unstable isotopes produced by cosmic ray muons passing through the detector. The external background, with energies larger than 2 MeV, can be suppressed to a negligible level with a shielding consisting of the $\sim$ 1.7 m water and 4.7 m of LS, making the reduction of the analysis threshold to 2 MeV possible in a spherical fiducial volume with a reduced radius of 13 m. This threshold can not be reduced any further due to the presence of more than 10,000 cosmogenic ^{11}C isotopes per day in the LS. At higher energies, the fiducial volume can be enlarged to radii of 15 m and 16.5 m for visible energy ranges of 3-5 MeV and 5-16 MeV, respectively. Finally, the muon-induced background can be well-suppressed by a cylindrical volume veto along the muon track, and a spherical volume veto around a spallation neutron candidate. Assuming a 10^{-17} g/g level for the intrinsic ^{238}U and ^{232}Th contamination in the LS, and ten years of data taking, about 60,000 signal events and 30,000 background events are expected in the energy range above 2 MeV after all cuts applied [100], with the signal and background spectra shown in Figure 2.26.

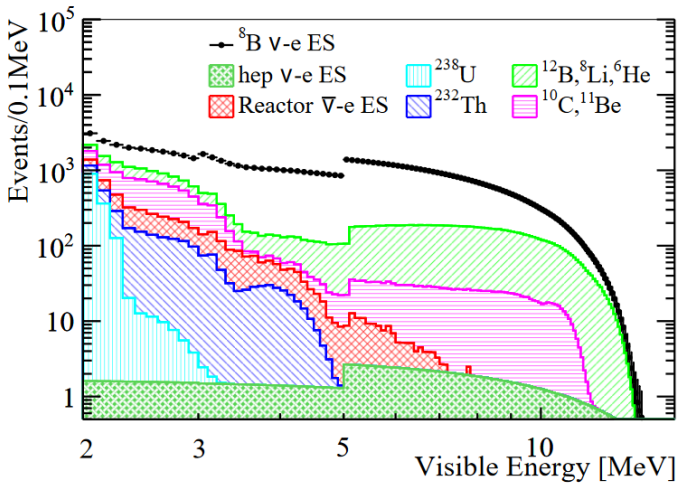

Figure 2.26: Signal and background spectra above 2 MeV of singles expected in JUNO in 10 years after the selection cuts, including different fiducial volumes in different energy intervals ([2-3] MeV, [3-5] MeV and [5-16] MeV).

Neutrino oscillation physics would benefit from a large and low-threshold ES electron sample of ^{8}B neutrinos as, in the standard neutrino oscillation framework, a joint fit of the ES reaction rate, the spectral distortion and the day-night asymmetry of the ^{8}B neutrino interaction rate yields a simultaneous determination of $sin^2\theta_{12}$ and Δm^2_{21}. The precision on $sin^2\theta_{12}$ is however limited by the arrival neutrino flux uncertainty, and so a more precise $sin^2\theta_{12}$ measurement requires a new ^{8}B neutrino flux measurement via the NC or CC channel.
In addition to the ES channel, the 1.1% natural abundance of ^{13}C makes it possible to measure the ^{8}B neutrino flux via both the CC and NC channels [101, 102], with the main reactions being the $\nu_e + ^{13}\text{C} \rightarrow e^- + ^{13}\text{N}$ CC reaction and the $\nu + ^{13}\text{C} \rightarrow \nu + ^{13}\text{C}^* \left(\frac{3}{2}^-\right)$ NC reaction. With 9×10^{30} ^{13}C nuclei in the 20 ktons of LS, about 6,000 CC signals and 3,000 NC signals are expected in 10 years of data-taking [102]. For the $\nu + ^{13}\text{C} \rightarrow \nu + ^{13}\text{C}^* \left(\frac{3}{2}^-\right)$ NC reaction, the 3.685 MeV γ's from the deexcitation of ^{13}C* form a small peak on the ES electron spectrum, as is shown in

Figure 2.27. With the excellent energy resolution of JUNO, the area of the γ peak can be obtained from a joint fitting with the continuous spectrum of ES electrons. Since the ES electrons dominate the background in the CC and NC detection, a joint fitting among the three channels needs to be performed, with the statistical limits of the CC and NC reaction rates expected to reach 7% within 10 years of data taking.

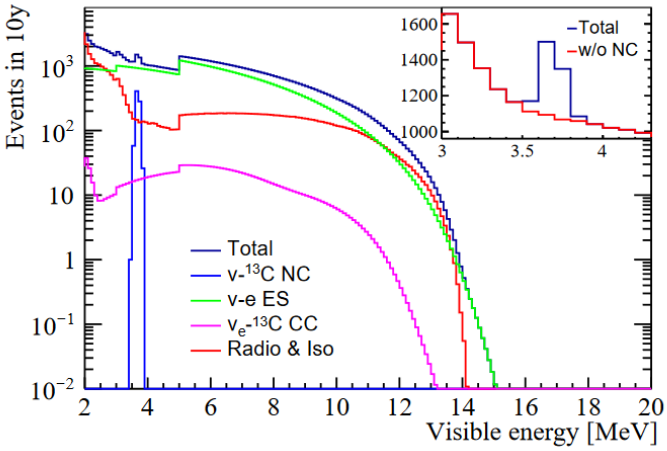

Figure 2.27: Electron spectrum from CC, NC, ES, and backgrounds. The 3.685 MeV γ's from the deexcitation of $^{13}C^*$ in the NC channel form a small peak on the ES electron spectrum.

The unprecedented energy resolution of JUNO should make it possible to detect ^{7}Be solar neutrinos, as well as solar neutrinos from *pp* cycles. However, due to constraining irreducible backgrounds, exceeding the respective 2.7% and 10% precisions of their flux measurements set by Borexino will be challenging.

2.9.5 Geo-neutrinos

Geoneutrinos are antineutrinos from the decays of long-lived radioactive elements inside the Earth, and are a unique tool to study our planet, in particular its radiogenic power, and to bring valuable insight on its formation and chemical composition. The inverse beta decay on protons with 1.8 MeV threshold makes it possible to measure geoneutrinos from the ^{238}U and ^{232}Th decay chains. Only two experiments have measured geoneutrinos so far, KamLAND and Borexino, both experiments having reached a precision of about 16-18% by detecting in total $168.8^{+26.3}_{-26.5}$ events in KamLAND [103] and $52.6^{+9.4}_{-8.6}(\text{stat})^{+2.7}_{-2.1}(\text{sys})$ events in Borexino [104]. However, neither experiment has sufficient sensitivity to determine the Th/U ratio, an important parameter for understanding the Earth's formation with a good accuracy.

Furthermore, the two experiments show a discrepancy between their results. Borexino excluded the null-hypothesis of a mantle signal at 99.0% C.L., and estimated the Earth radiogenic power from U and Th as $31.7^{+14.4}_{-9.2}$ TW, setting tight upper limits on the power of a georeactor hypothesised to be present inside the Earth [105–108]. KamLAND estimated the Earth radiogenic power from U and Th as $12.4^{+4.9}_{-4.9}$ TW, and prefers the geological models with lower concentration of heat-producing elements in the Earth. The next generation experiments like JUNO are needed to provide firm results concerning the Earth's radiogenic power and to fully exploit geoneutrinos in order to understand the natural radioactivity of our planet. With its detector volume being at least 20 times larger than the existing detectors, JUNO will allow for a high statistics measurement of geoneutrinos, and as such represents a fantastic opportunity for their study.

The expected geoneutrino signal depends on the U and Th abundance and distribution in the Earth. The published JUNO sensitivity studies [109] consider a global composition of the Earth [110], and give an expected geoneutrino signal in JUNO of $39.7^{+6.5}_{-5.2}$ TNU. One TNU (Terrestrial Neutrino Unit) corresponds to 1 event detected with a detector of 100% detection efficiency containing 10^{32} target protons (roughly 1 kton of liquid scintillator), in 1 year. This corresponds to a measurement of 400 geoneutrinos, more than the total number of geoneutrinos ever measured by all the previous experiments, per year.
The 500 km range of the crust around JUNO contributes to more than 50% of this total signal [110]. Thus, local refined geological models are needed for a precise estimation of the crustal signal and a subsequent disentanglement of the mantle signal. The main challenge for the JUNO geoneutrino measurement is the rather large reactor antineutrino background, in addition to other non-antineutrino backgrounds like cosmic muons, cosmogenic ^{9}Li-^{8}He, fast neutrons, ^{13}C(α,n)^{16}O reactions, and accidental coincidences. The expected energy spectrum for IBD events in JUNO when searching for geoneutrinos is shown in Figure 2.28. The geoneutrino signal, in red, is greatly overshadowed by the reactor antineutrino "background".

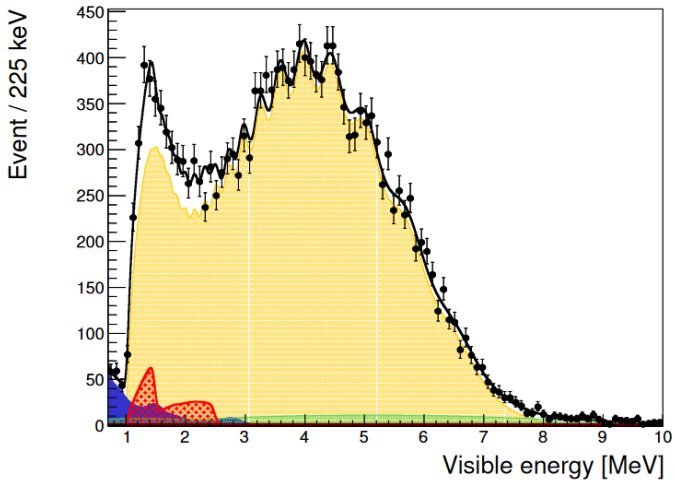

Figure 2.28: Energy spectra of prompt IBD candidates from geoneutrinos (red), reactor antineutrinos (yellow), and other non-antineutrino backgrounds (^{13}C(α,n)^{16}O in blue, ^{9}Li-^{8}He in green) for one year of data-taking in JUNO after the selection cuts.

Considering the muon veto (17% exposure loss), IBD selection (80% efficiency), and detector response (3% at 1 MeV energy resolution) of JUNO, two methods were used to assess the potential of the JUNO geoneutrino measurement. They yielded compatible results and the first (second) method estimated the precision of the geoneutrino measurement with a fixed chondritic mass Th/U = 3.9 in the fit as 17 (13)%, 10 (8)%, 8 (6)%, and 6 (5)% after 1, 3, 5, and 10 years of data taking. After several years of measurements, JUNO also has the potential to constrain the Th/U ratio in the observed geoneutrino signal [109].
To reduce the uncertainty of the geoneutrino flux prediction, local refined geological models were built. They were motivated by the measurement that geoneutrino signals produced by U and Th in the continental crust within ~100 km of the detector make up the signal from the whole mantle [110], which illustrates the importance of refined geological models around JUNO. The South China Block surrounding JUNO was thus studied and characterized in terms of density, crustal layers thickness, and chemical composition.
JULOC (JUNO Local Crust) [111], a 3-D comprehensive high resolution crustal model around JUNO, covers an area of 10°×10° around the detector and uses seismic ambient noise tomography

[112] in input to provide information about the thickness and density of the upper, middle, and lower crust around JUNO. On the basis of compiled U and Th abundances data from over 3000 rock samples, the JULOC model suggests that the local upper (middle and lower) crust has higher (lower) average U and Th abundances than the global average. The estimated crustal geoneutrino signal by JULOC is 38.3 $\pm$ 4.8 TNU, to be compared with $28.2^{+5.2}_{-4.5}$ TNU [110] based on a global crustal model [113]. This shows the potential for these locally refined geological models to provide an extraction of the mantle components.

2.9.6 Other physics

Atmospheric neutrinos

Atmospheric neutrinos are known to be a very important neutrino source to study the neutrino oscillation physics. They have a broad range in baseline ($\sim$15-13000 km) and energy ($\sim$0.1 GeV-10 TeV), and contain neutrinos and antineutrinos of all flavors. When they pass through the Earth, the resulting Mikheyev-Smirnov-Wolfenstein (MSW) matter effect [114] will play a key role in determining the neutrino mass ordering (NMO), for which the JUNO sensitivity from atmospheric neutrinos is complementary to that from the JUNO reactor neutrino results, their combined sensitivity exceeding the purely statistical combination of their stand-alone sensitivities [115, 116].
Numerical results, using atmospheric ν_μ and $\overline{\nu}_\mu$ events to evaluate their contributions to the NMO [59], have shown that JUNO's NMO sensitivity can reach 0.9 σ for a 200 kt.year exposure and $sin^2\theta_{23} = 0.5$. An optimistic sensitivity may reach up to 1.8 σ for 10 years of data taking. A combined NMO sensitivity with both atmospheric and reactor neutrinos in JUNO will be evaluated.
JUNO's performances in reconstructing the atmospheric neutrino spectrum can also be evaluated, the difference in the time evolution of the scintillation light on the PMTs allowing for the discrimination between the flavors of the primary ν_e and ν_μ neutrinos. To reconstruct the time pattern of events, the signals from the 3" PMTs will be used, because of their good time resolution.

Proton decay

One of the three basic ingredients for an initially symmetrical Universe [117], the baryon number (B) is necessarily violated in the Grand Unified Theories (GUTs) [118, 119], which can unify the strong, weak and electromagnetic interactions into a single underlying force at a scale of $M_{GUT} \simeq 2\times10^{16}$ GeV, and so searches for its violation could explain the observed cosmological matter-antimatter asymmetry. A general prediction of the GUTs, the observation of which would allow for the confirmation of the baryon number violation, is the nucleon decay. However, no experimental evidence to date for the proton decay or B-violating neutron decay has been found. With a 20 kton LS detector, JUNO is expected to have a good performance on the nucleon decay search, especially on the mode of $p \rightarrow \overline{\nu}\mathrm{K}^+$. This decay mode displays a clear three-fold coincidence feature in time : a prompt signal from the K^+ kinetic energy, a short delayed signal (τ = 12.38 ns) from its decay daughters and a long delayed signal (τ = 2.2 μs) from the final Michel electron.
Searching for this time-correlated triple coincidence, the JUNO detector can effectively identify the $p \rightarrow \overline{\nu}\mathrm{K}^+$ signals and reject the atmospheric neutrino backgrounds. A data sample containing $p \rightarrow \overline{\nu}\mathrm{K}^+$ events and background atmospheric neutrinos was generated using a Monte Carlo simulation and was used to estimate the sensitivity of the proton decay measurement.
The primary production K^+ and their decay daughters will leave two deposition signals in the hit-time spectrum obtained with the 3-inch PMT system of JUNO, after time-of-flight correction. Considering the lifetime of K^+ ($\lesssim 5\times10^{-8}$ s), both signals will pile up, and the 3-inch PMT system (TTS of 1.5 ns) of JUNO can observe this pile-up shape in the hit time spectrum, as

shown in Figure 2.29a. As such, the uprising time of $p \rightarrow \overline{\nu}K^+$ events should be larger than that of atmospheric neutrinos [120], which is a first discriminating factor. An even more powerful selection of $p \rightarrow \overline{\nu}K^+$ events can be performed with the help of a multi-pulse fitting method [121], with which it is possible to reconstruct both signals, get the correlated time difference, as well as get the energy deposition of each signal. This fitting method is illustrated in Figure 2.29b.

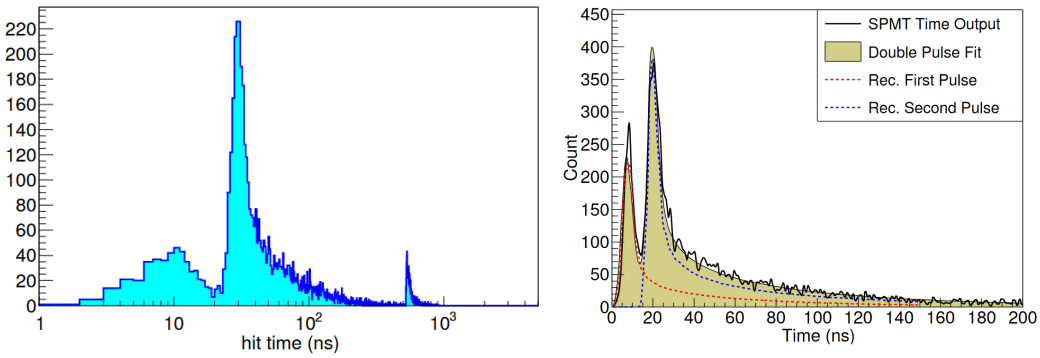

(a) (b)

Figure 2.29: (a) Hit time distribution after TOF correction. A double signal pile-up shape is observed, with the third signal in around 500 ns coming from the Michel electron. (b) Multi-pulse fitting of proton decay hit time spectrum. The time difference between the two fitted signals is 11 ns.

With additional cuts on visible energy, fiducial volume, muon veto, and Michel electron and neutron capture, and considering 10 years of data taking, about 31% of the $p \rightarrow \overline{\nu}K^+$ events of the data sample were conserved while only 0.3 background events remained. According to the Feldman-Cousins approach [122], the preliminary sensitivity on the $p \rightarrow \overline{\nu}K^+$ decay process lifetime with the JUNO detector is estimated as 8.3×10^{33} years, with a 90% C.L., for 10 years of JUNO data taking.

2.10 Conclusion

The international JUNO collaboration was established in 2014, with the publication of the Conceptual Design Report [71], followed in 2015 by the beginning of operations such as the setting-up of the PMT production line, the R&D of the Central Detector components and the start of the civil construction. By 2016, the PMT production had started as well as the production of the CD components, and the JUNO Yellow book was published [59]. Several milestones were then reached with the years : the delivery of the Top Tracker and the start of the mass PMT testing in 2017, the potting of all PMTs, the start of both the delivery of the surface facility and of the production of the acrylic sphere in 2018, and the start of the production of the electronic systems in 2019. This chapter presented all systems, subsystems and components of the JUNO detector in their state at the time of writing this thesis, as well as the broader physics program of JUNO beyond the NMO determination. In 2021, the civil construction and the preparation of the laboratory were completed, and the construction of the detector started. This construction will be on-going through 2022, and the JUNO detector is currently scheduled to be ready for data-taking in 2023.

Chapter 3

SPMT system and its front-end electronics

Contents

3.1 Motivation **77**
3.2 Description of the system **81**
3.3 PMT instrumentation **83**
3.3.1 3-inch PMTs 83
3.3.2 High voltage divider and PMT base potting 84
3.3.3 Cables and UWB connectors 86
3.4 High Voltage Splitter board **87**
3.5 Front-end ABC board **89**
3.5.1 CATIROC ASICs 90
3.5.2 Data and Firmware 97
3.6 Global Control Unit board **99**
3.7 Underwater Box design and thermal studies **100**
3.7.1 Design 100
3.7.2 Thermal studies 101
3.8 Radiopurity of the SPMT system **102**
3.9 Conclusion **104**

3.1 Motivation

The Small PMT (SPMT) system is designed to serve as a complementary array of photodetectors to the Large PMT (LPMT) system. Its 3-inch PMTs, described in section 2.5, will observe the same events as the LPMTs, and will thus have the potential to cross-check LPMT measurements. About 40 PEs per MeV of deposited energy will be collected by the SPMT system, as opposed to the ∼1350 PEs per MeV of the LPMT system. This means that in the ∼[0-10] MeV interest energy range of the IBD events coming from reactor antineutrinos, up to ∼400 PEs can be collected by the SPMT system. With 25,600 SPMTs, and considering their solid angle, almost every PMT having recorded such an event will have only been hit once by a photon. This gives a configuration in which, most of the time, the PMTs will either collect one or no PE, unlike the LPMTs. This is called the "photon-counting mode" of the SPMTs.

Figure 3.1a illustrates this photon-counting mode. It represents, for 20 MeV e^+ events uniformly distributed in the CD, the percentage of SPMTs having collected N_{PE} photoelectrons, against the distance-to-center of the event. These events have a high energy, typically IBD events of antineutrinos from supernovae, and are taken as a worst-case scenario in the illustration of the

photon-counting mode. In this configuration, and considering only the SPMTs having collected any light, more than 90% of the hit SPMTs were only hit once by a photon and subsequently produced a photoelectron. The ∼8% remaining SPMTs were hit twice, with a negligible fraction (∼1.5%) having been hit more than twice. In these cases, the event tends to be located towards the edge of the detector. Such events will typically yield a larger number of PMTs hit numerous times, with a lower overall number of hit PMTs. The concentration of the statistics in Figure 3.1a in the 12-16 m region is due to the uniformity in volume of the simulated e^+ events and to this region representing an important fraction of the detector volume. This photon-counting mode of the SPMT system is further highlighted when compared to the response of the LPMT system to the same events, shown in Figure 3.1b. Only about 45% of the LPMTs were hit once, with much greater multiplicities reached as the distance-to-center of the events increases, up to more than 100 PEs for some PMTs. For lower energy events, most importantly reactor $\overline{\nu}_e$ IBD events, ∼95% of hit SPMTs will only be hit once, ∼5% 2 to 5 times, with a negligible fraction of SPMTs having been hit more than 5 times.

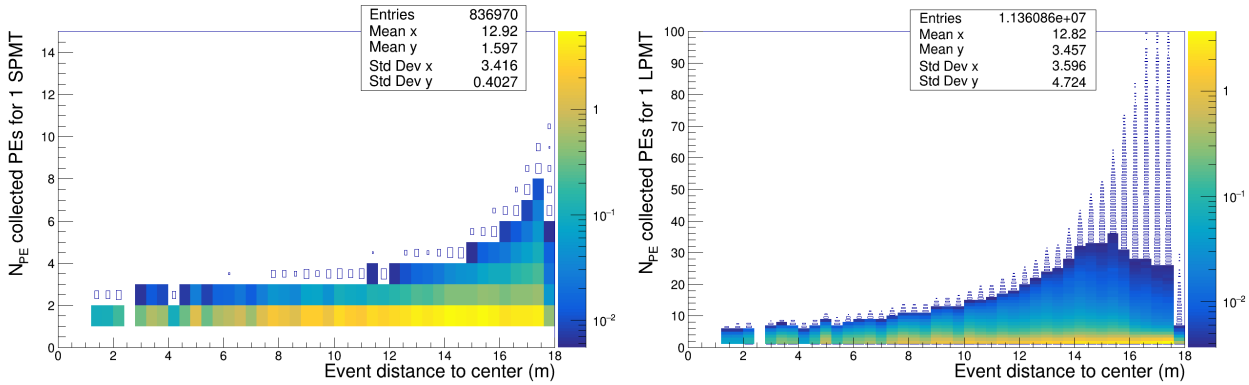

(a) (b)

Figure 3.1: Multiplicity of collected PEs by both PMT systems for 20 MeV e^+ events uniformly distributed in the JUNO detector, against the distance-to-center of the events. The percentage of PMTs having collected N_{PE} photoelectrons is represented on the coloured Z-axis, with empty boxes used for the lowest percentages outside of the colour palette. (a) Multiplicity for the SPMT system. (b) Multiplicity for the LPMT system.

This photon-counting mode has several consequences on the logistics and objectives of the SPMT system, notably the fact that it is unnecessary for the SPMT system to record the waveforms of the PMTs. In most physics cases, counting the number of hit PMTs will allow for a rather precise estimation of the total charge measurement and of the energy of the event (the general requirement for JUNO is to have a systematic uncertainty on the energy measurement lower than 1%). This has an impact on the strategy of the electronics system, detailed starting from section 3.4.
The main consequence, however, is that the SPMT system will be able to measure the charge of every event with almost no instrumental non-linearity, contrarily to the LPMT system (see Figure 3.1b for the possible multiplicities of collected PEs reached by the LPMTs). It is thus possible to use the charge response of the SPMT system to compare it to that of the LPMT system, point out any non-linearities it may show, and correct them during the calibration runs. This is envisioned to be performed with a UV laser system [74] at the center of the detector, capable of producing a uniform illumination tunable over the full range of the IBDs (0 - 100 PEs per LPMT channel). As the laser intensity varies, the response of the SPMT system is expected to be linear, and so the evolution of the ratio of the LPMT system charge to the SPMT system charge leads to the determination of the LPMT system instrumental non-linearity. This calibration

method is not affected by any physics non-linearity, as both measurement systems are exposed to the same energy deposition, nor by the non-uniformity of the detector, as the calibration source is placed at the center of the detector. This calibration can however be biased if the instrumental non-linearity of the LPMT system depends on the arrival time profile of the photons, which may be different between the laser calibration source and actual physical events. This can be controlled by the subsequent use of radioactive calibration sources [123], as described in section 2.6.2.

Despite its much lower number of PEs collected per MeV of deposited energy compared to the LPMT system, the accumulation of statistics over time will ensure that the SPMT system also has potential for the independent measurement of certain parameters, notably the solar oscillation parameters Δm^2_{21} and θ_{12}. Derived from the slow oscillations in the reactor antineutrino energy spectrum as illustrated in Figure 3.2a, these two parameters define the frequency of the neutrino oscillations and their amplitude, and are much less sensitive to a poorer energy resolution than Δm^2_{32} and θ_{13}. As shown in Figure 3.2b, a 3% energy resolution oscillated spectrum, representing the spectrum reconstructed by the LPMT system, allows for the determination of these Δm^2_{32} and θ_{13} parameters in the fast oscillations, which are lost as the energy resolution worsens. With the SPMT system and its 40 collected PEs per MeV, the energy resolution will be ~16%. The resulting energy spectrum is confined within the spectra reconstructed for a 15% and a 18% energy resolution in Figure 3.2b. While the fast oscillations necessary for the measurement of Δm^2_{32} and θ_{13} are no longer visible in such a case, the slow oscillations still allow for a precise identification of the maxima and minima of oscillations, and thus for a measurement of the solar parameters. The precision of this measurement is dominated by statistics, and not energy resolution, hence why the SPMT system will be able to perform a complementary measurement from the LPMT system.

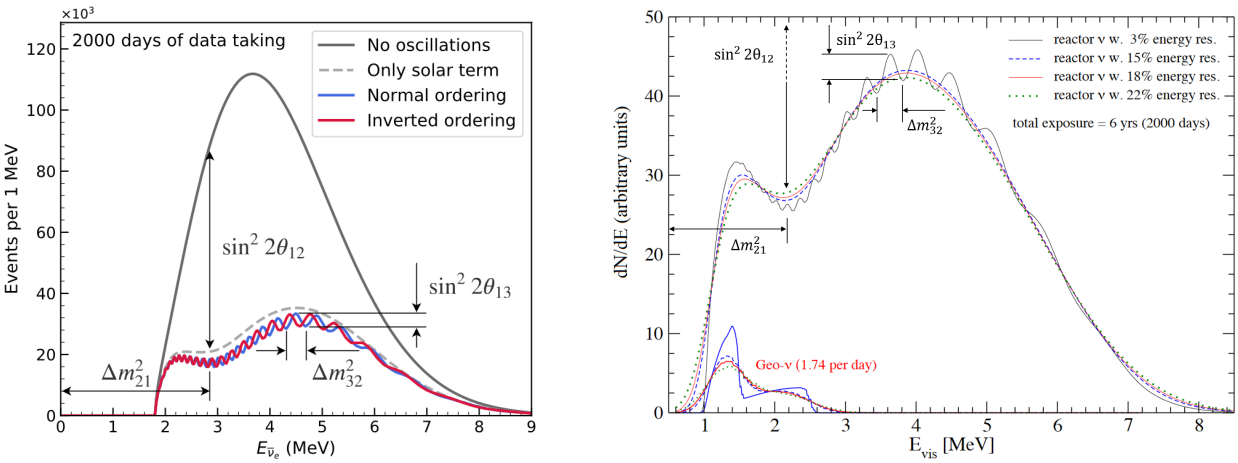

(a) (b)

Figure 3.2: (a) Expected JUNO antineutrino energy spectrum weighted by IBD cross-section, with and without oscillation. Both the normal and inverted orderings are represented, assuming 2000 days of data-taking. The spectrum is dependent on the four oscillation parameters. (b) Zoom on the oscillated spectrum in the Normal Ordering, computed for multiple energy resolutions. The spectrum reconstructed using the LPMT system is represented by the 3% energy resolution. The spectrum reconstructed using the SPMT system is confined within the 15% and 18% energy resolution configurations.

Sensitivity studies have shown an expected 0.5% sensitivity on $sin^2 2\theta_{12}$ and an expected 0.3% sensitivity on Δm^2_{12} within 6 years of data taking with the SPMT system. This is a robust

measurement when compared to the expected 0.54% and 0.24% expected sensitivities with the LPMT system [71].
In addition to their potential for cross-checking and independent measurements, the SPMTs have a very good TTS when compared to the majority of the LPMTs, with an average value of 1.5 ns (σ) while the ~12600 NNVT MCP-PMTs have TTS values around 5 ns. The 5000 Hamamatsu PMTs, making up the rest of the LPMTs, have a mean TTS value of 1.1 ns. When considering only the good PMTs for timing measurements, the SPMT system represents ~10% of the effective photocathode coverage, thus having a non-negligible impact. As mentioned in section 2.9.6, the SPMT system will be able to improve the measurement precision of atmospheric neutrinos and proton decay events in JUNO. For atmospheric neutrinos, as the difference in the time evolution of the scintillation light on the PMTs allows for the discrimination between the flavors of the primary ν_e and ν_μ neutrinos, the SPMT system will help reconstruct the time pattern of events with its good time resolution. For proton decay events, the SPMT system will be able to identify the pile-up signal of the primary production K^+ of the $p \to \overline{\nu}K^+$ events and help discriminate them from atmospheric neutrinos.
The SPMT system will also positively contribute to the reconstruction of certain events in the detector, notably muons tracks in the CD and supernova events, due to its good timing precision. Reconstruction studies on muon tracks [124] have shown a significant contribution of the SPMT system, as shown in Figures 3.3a and 3.3b, in which the performance of the reconstruction algorithm ($\Delta D = D_{sim} - D_{rec}$) is presented against the track's true distance D_{sim} from the center. Figure 3.3a shows the performance that can be achieved with only the LPMT system, with a strong increase in bias for ΔD for increasing D_{sim} values, while Figure 3.3b shows both PMT systems used in a combined fit. Both PMT systems isolated exhibiting an opposite bias in ΔD for larger D_{sim} values, the effects of the two complementary systems cancel each other out in the combined fit, resulting in a reconstruction with only a small mean bias in ΔD of less than 10 cm for most of the tracks. Improving the muon track reconstruction will allow for a refined muon veto strategy and a better rejection of cosmogenics.

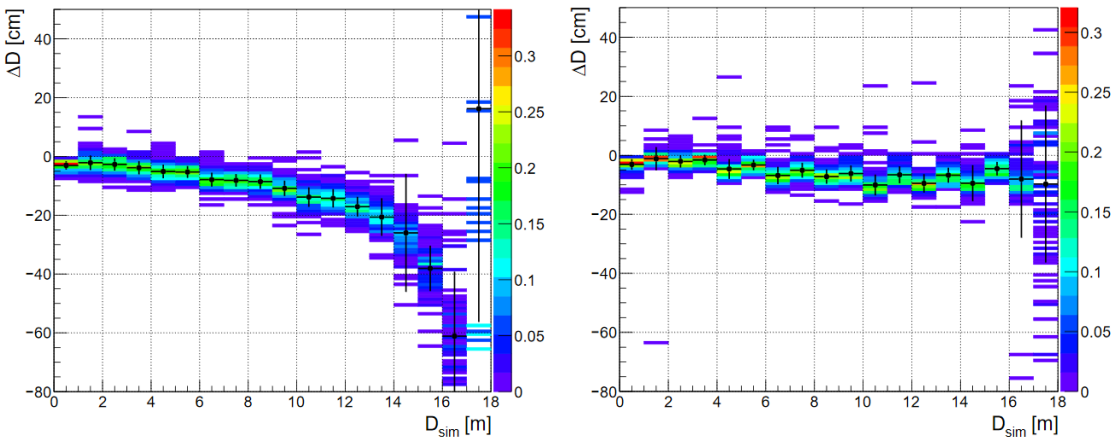

(a) (b)

Figure 3.3: Reconstruction results for a sample of 5900 simulated muon tracks with smeared hit times according to the PMT's TTS. (a) Results when using only the LPMT array. (b) Results with the combination of both PMT systems into one fit. The reconstruction distance ΔD shows a large improvement at larger distances D_{sim} from center over the LPMT system alone, with a small mean bias of less than 10 cm. On the very edge of the sphere,the reconstruction performance declines because the muon travels only a short distance through the LS.

3.2 Description of the system

The small PMT system of the JUNO experiment was introduced in the collaboration in 2016 in order to install up to 36,000 3-inch PMTs (SPMTs) in the gaps between the 20-inch PMTs making up the main LPMT system, 3 inches being the maximum size allowed by the positioning of the LPMTs, as shown in Figure 3.4. The maximum number of 36,000 SPMTs was derived from the limited number of possible positions for the SPMTs due to the stainless steel structure supporting the acrylic sphere of the central detector. Additional constraints regarding the financial cost of such a system and the limited interest for physics with too many SPMTs drove the number of scheduled SPMTs to be reduced to ∼25,600. Section 2.5 gives in-depth information about the SPMTs. As with the LPMT system, the SPMT readout electronics will be located underwater, both to avoid transmission losses in the long distance to the surface and to reduce the costs associated with the required cabling. The interrogations on PMT positioning and cabling drove the rest of the requirements for the SPMT system. A schematic view of the positioning and cabling of the SPMT is shown in Figure 3.4.

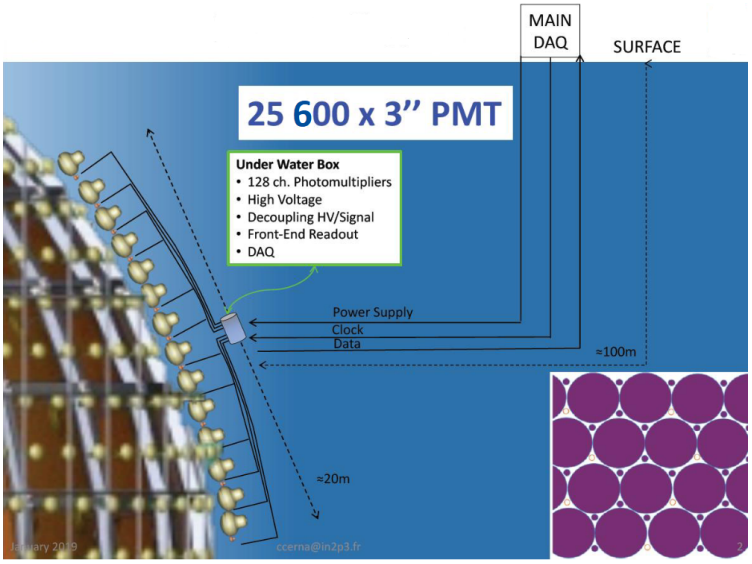

Figure 3.4: SPMT system overview. 128 3" PMTs are connected to an UnderWater Box (UWB) containing the readout electronics system. The PMT signals are then sent to the surface for storage and analysis. The 3" PMTs are positioned in the center gap of a group of 3 20" PMTs.

As explained in section 3.1, the SPMTs can consistently operate in the photon-counting mode (observation of a single photo-electron or no signal) for all events inside the Central Detector in the energy region of interest (0-10 MeV). As such, in the SPMT system, the waveforms of the PMTs will not be recorded. The signal will be digitized and the readout electronics will only deliver information about timing and charge. As the waveforms will not be recorded, the electronic readout can be designed to be more compact in order to reduce the required number of electronic boards and cables, leading to more SPMT channels handled by one set of electronics than LPMT channels in the LPMT system. The objective for the SPMT system was thus to determine the multiplicity of the SPMT readout system.

There are 2 main specifications for the cabling, first being the length of the cables for signal quality. There are ∼26,000 PMTs to cover the whole sphere, and ∼10 m cables are known to transport low amplitude signals with good quality. By defining areas of about 10 m radius for joint cabling and signal readout, this gives about 200 PMTs in these zones. So about 200 PMTs would need to be grouped to one underwater box for signal readout. The second specification is to have ∼50%

overlap in the electronics coverage in any given PMT zone. If one underwater box fails, this avoids a completely blind spot in the PMT coverage. In one PMT zone of ∼200 PMTs, only 50% of these PMTs should thus be joined for data readout. This would mean ∼100 PMTs connected to every underwater box, 128 PMTs per underwater box being a good compromise when considering channel readout. Finally, each PMT requires a High Voltage powering and a signal readout, and needing two cables for these operations to be carried out would result in a very large number of required cables, which would increase the risks of failures at cable interfaces and the total cost of the SPMT system. As transporting signals over a High Voltage power line and decoupling the signal from the HV at a distance of 10-20 m is known to be successful and reliable, it was thus decided to power the PMTs and readout their signal over the same cable. This increases the requirements on the cables, now having HV and RF specifications, but deeply decreases the number of required cables. The decoupling capacitor is thus shifted from the PMT divider to the front-end electronics.

For the electronic readout of the PMT signals, the CATIROC ASIC (designed in the OMEGA laboratory in France) [125] had already been accepted by the SPMT group of the JUNO collaboration for its efficient output of the charge and timing information [126]. This chip has 16 channels and thus can readout 16 PMT signals, meaning that the challenge for the SPMT system was to satisfyingly house 8 CATIROC ASICs on a single front-end board, named the ABC (ASIC Battery Card) board. Achieving this would allow for 128 PMT signals to be read by a single readout system contained in a single UWB. 200 underwater boxes and readout systems would then be needed to cover the 25,600 3-inch PMTs.

The output signal from any PMT is conducted through the cable at its base and delivered to the readout electronics contained in the corresponding UWB. Several electronic boards make up the system, and are involved in a complex series of signal deliveries and receptions. A schematic view of the SPMT electronics system is shown in Figure 3.5.

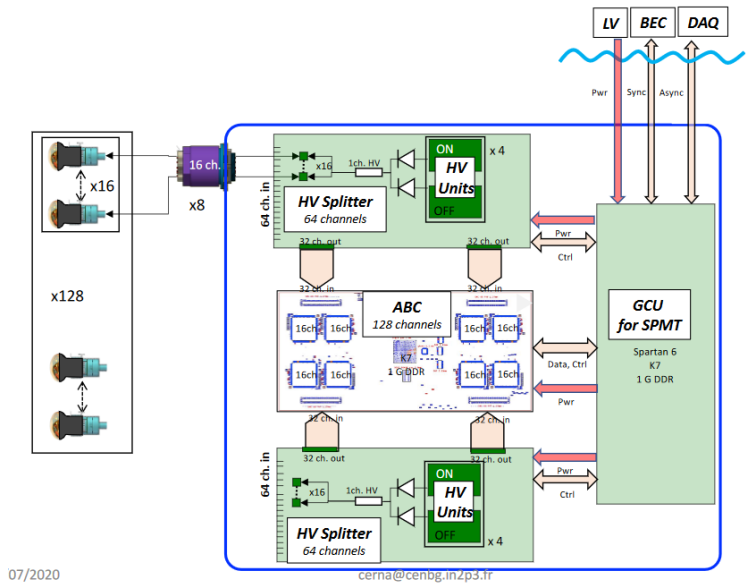

Figure 3.5: SPMT electronic system schematic for 1 underwater box. 2 High Voltage Splitter boards power the 128 PMTs and decouple their signal. The CATIROC ASICs on the ABC board process the PMT signals and the data is sent to the GCU board, which powers the whole electronic system, receives the clock signal from JUNO in a Synchronous mode (Sync) and transfers the data to the back-end electronics for Data Acquisition (DAQ) in an Asynchronous mode (Async). The Low Voltage (LV) supplies all the UWB.

The first level in the electronics for the PMT signal is a front-end board named the High Voltage Splitter board (2 64-channels splitter boards in each UWB), which sets the High Voltage to each of the connected 3" PMTs as well as decouples the physics signal from the high voltage. The physics signal goes to the front-end readout board called the ABC (ASIC Battery Card), composed primarily of 8 CATIROCs managing the physics signals and of a KINTEX 7 FPGA controlling each CATIROC and monitoring environmental parameters of the board. The goal of the ABC board is to measure both the signal's arrival time and its charge, and the information is sent by the FPGA to the Global Control Unit board (GCU). This board has two main functions : it powers both the splitter boards and the ABC board, and it receives the data from the ABC board to transfer it to the back-end electronics. The main challenge of the SPMT system will be to process signals with amplitudes around 2-3 mV.
A global schematic view of the system components connected to one of the 200 UWB is showed in Figure 3.6. In the following sections, every component of the SPMT system will be detailed.

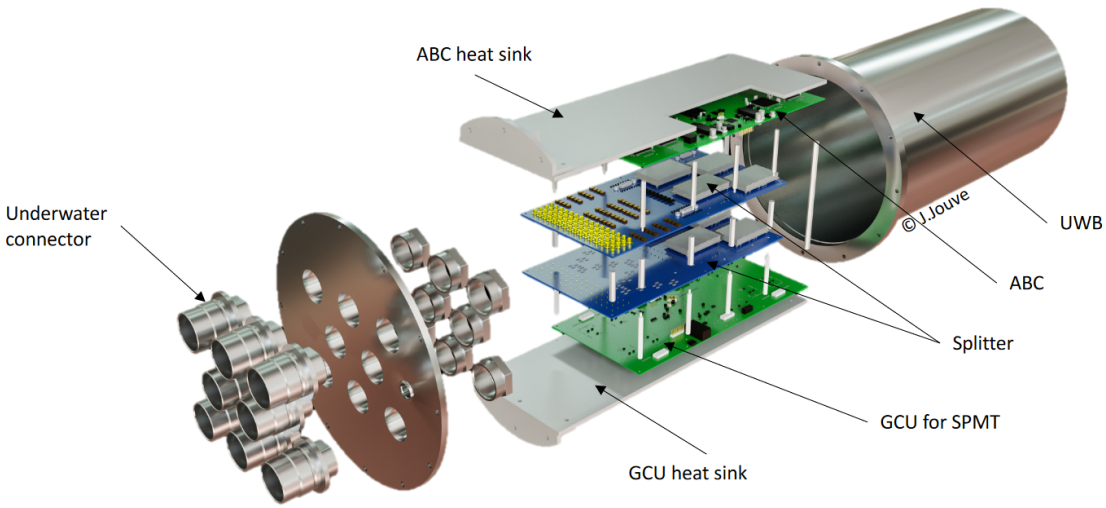

Figure 3.6: Scattered view of SPMT electronic system inside underwater box. 16 PMTs per connector make up the 128 PMTs readout by the electronic system of one UWB. 200 UWB cover the 25,600 PMTs.

3.3 PMT instrumentation

3.3.1 3-inch PMTs

The performances of the 3-inch PMTs of the SPMT system were described in section 2.5.3. As mentioned in section 3.2, the SPMTs will be grouped by 16 according to their nominal High Voltage for a gain of 3×10^6, each batch of 16 PMTs powered with the same High Voltage value and connected to the 16 channels of a CATIROC ASIC. 128 PMTs will be connected to one ABC board, housing 8 CATIROCs and contained in one underwater box. Figure 3.7 illustrates 16 PMTs, complete with their HV dividers, potting, cables and connector to the underwater box, which will all be described in the following sections.

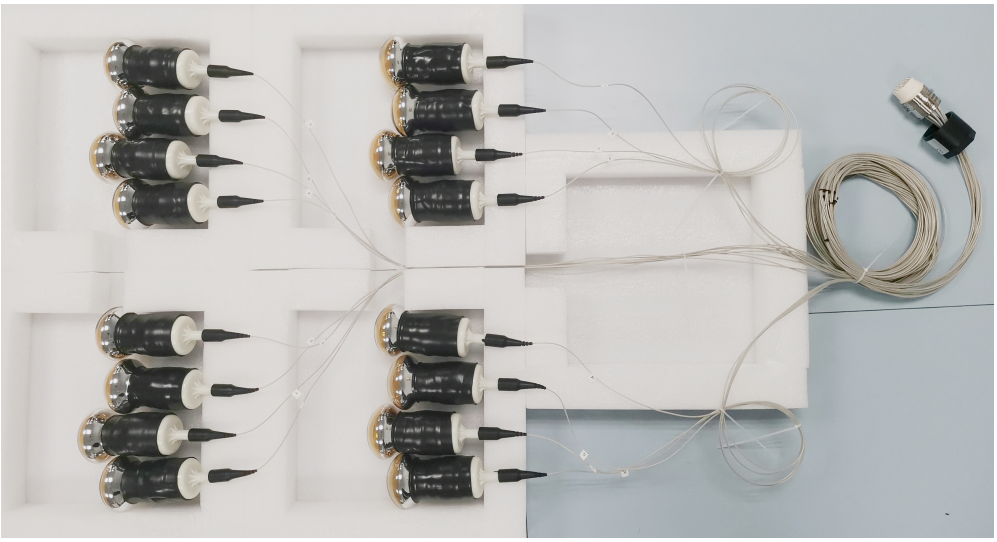

Figure 3.7: Batch of 16 PMTs after potting and cabling, showing the PMT instrumentation from PMTs to UWB connector.

3.3.2 High voltage divider and PMT base potting

In the SPMT system, the 3-inch PMT base is a HV divider, and as such, the printed circuit board (PCB) of the base will be soldered directly to the SPMT dynodes and cathodes. As mentioned in section 2.5.3, the final design of the HV divider has a HV ratio of 3:2:1 for the first 3 dynodes, and its principle circuit schematic is shown in Figure 3.8. This design is the result of a specific study by IHEP to optimize the TTS of the PMTs as well as their collection efficiency.

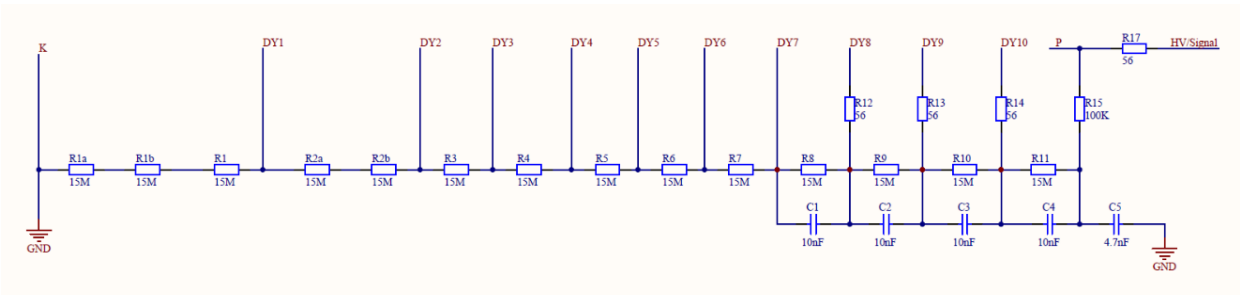

Figure 3.8: Principle circuit schematic of the SPMT base HV divider.

The single cable connecting the SPMT base to the readout electronics will be used to both supply the high voltage and deliver the signal transmission, and is soldered to the PCB of the HV divider. To meet all the general specifications, notably the power consumption in an UWB, the HV will be lower than 1.5 kV, which limits the DC current to around 10 μA, and controls the power consumption to less than 0.015 W per channel and thus less than 2 W per UWB. The target gain of the SPMTs ranges from 10^6 to 10^7, with a nominal value at 3×10^6. The PCB of a HV divider with all its components is shown in Figure 3.9.

Because the SPMTs will be underwater, a cylindrical shell needs to be bonded at the base of the PMT to guarantee that the whole component is waterproof. This base is sealed by filling it with several sealants. The selection criteria applied to the shell material includes the ability to withstand a water pressure of 0.5 MPa (equivalent to 50 m of water) and be compatible with the ultra-pure water of the water pool for more than 20 years (no damage to the shell nor pollution

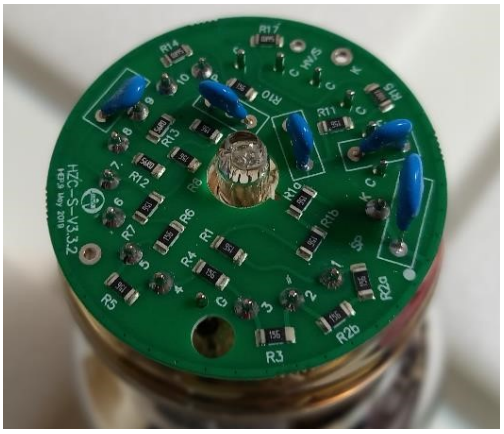

Figure 3.9: High Voltage Divider PCB.

to the water). The Acrylonitrile Butadiene Styrene (ABS) material satisfies all these criteria and is the default choice for the potting shell. For the shell interior, from the glass of the PMT base up to the soldered cable, polyurethane is the best potting sealant, guaranteeing a good insulation performance and a good ageing property. In order to properly seal the cable, the most delicate part of the potting since leakage often occurs along the cable, HDPE epoxy is used. The potting design schematic is shown in Figure 3.10.

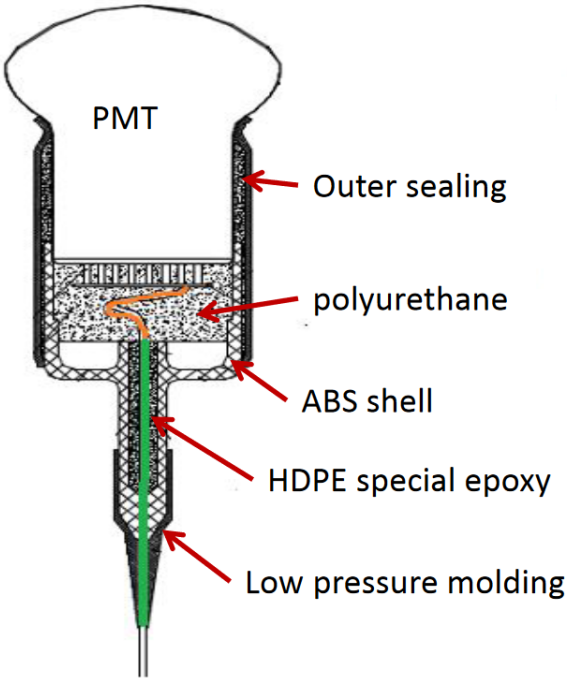

Figure 3.10: PMT potting design schematic.

A thermo-retractable sleeve is tightly wrapped around the completely potted PMT in order to add a protective layer. The cable connected to the base is lead out through the outlet, and is used for supplying both high-voltage (HV) and signal transmission.

3.3.3 Cables and UWB connectors

The cable connecting the PMT to the readout electronics carries both the high voltage and the PMT signal. As such, it needs to enter the potting of the PMT and be connected to both the HV divider at the base of the PMT and to the HV Splitter board in the UWB. It is a custom RG178 coaxial, 50 Ω-impedance cable developed by the french Axon company, with a dedicated technology designed to block the longitudinal water penetration in case of a damaged jacket underwater. It has a 2 mm diameter and is 10 m long with a maximum voltage of the DC current of 1.5 kV. It was designed to operate in an environment with a maximum water pressure of 0.8 MPa, and a temperature of 21°C. To be resistant to ultra-pure water, it is covered with an outer jacket in extruded HDPE. An attenuation of 1.71 dB/m at 1 GHz has been measured, resulting only in a ∼11% single PE charge loss for 10 m coaxial cables.
A specific connector has been developed to allow the PMT cables to safely enter the UWB. This connector is the result of a R&D work by the Axon company. To accommodate the 128 SPMTs supposed to be connected to the readout electronics, this connector is designed to be composed of 16 coaxial RF micro-connectors withstanding 1.5 kV, with the challenge of conducting 16 un-decoupled signals, as the HV and the PMT signals are only decoupled by the HV splitter board inside the UWB. As such, each connector operates with a 50 Ω impedance. Tests were conducted at up to 1.8 kV, with the connector guaranteed safe at 1.5 kV.
This connector is compatible with the RG178 coaxial cables originating from the PMTs, and guarantees that the connection is completely water-proof. This is achieved with a double, dissimilar waterproof seal at each stage of the connector. It also needs to fulfill the same requirements as the PMT coaxial cables with respect to the environment it operates in.
Figure 3.11 shows both sides of the connector : the receptacle, which is the fixed part of the connection, mounted on the UWB and connected inside to the HVS (Figure 3.11a) and the plug, attached to the PMT through the 5-10 m cables (Figure 3.11b). Both sides are made of stainless steel SS304L. The water tightness of the connection is guaranteed by a series of FKM and silicon O-rings, D-rings and interfacial seals. Over the plug, the water tightness with the 16 cables is achieved with the overmoulding of the connector body, made of polyethylene, with the HDPE of the outer jacket of the RG178.

(a) (b)

Figure 3.11: AXON connector (a) Receptacle (on UWB). (b) Plug (Linking PMTs to UWB).

The 16 cables in output of one connector, corresponding to the 16 channels delivering the PMT un-decoupled signals, are themselves connected to the readout electronics. The following section will detail the components of the readout electronics system.

3.4 High Voltage Splitter board

As introduced in section 3.2, the two 64-channels High Voltage Splitter boards in each UWB drive the HV to the 128 SPMTs as well as decouple it from the physics signal. The HVS board is a front-end board populated purely by passive components. Figure 3.12 shows the top view of the outline of the board, with the main components colour-highlighted. The current version of the HVS is V0.3, produced in small numbers and used in combined tests with the rest of the electronics (section 4.4.3). HVS V0.3 is a 350 mm × 190 mm board with 8 layers, and is 4.5 mm thick.

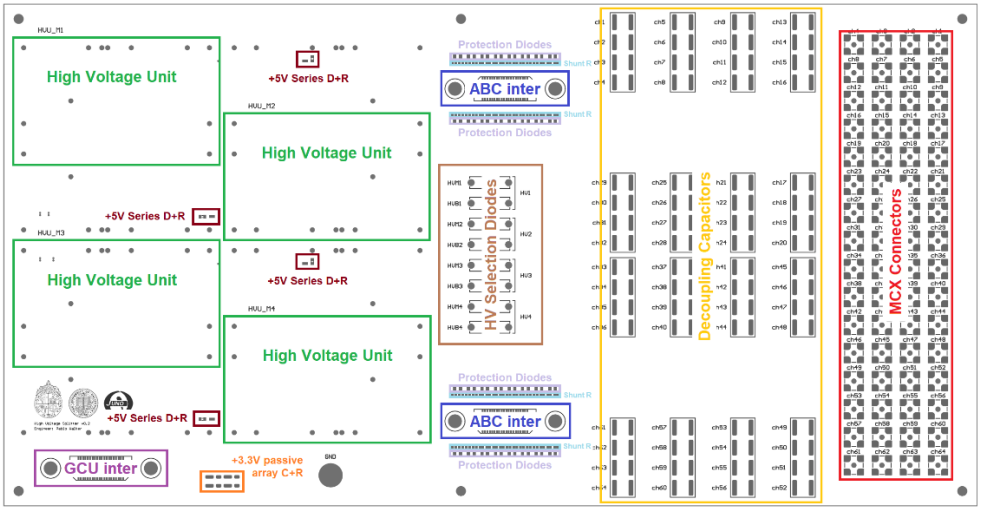

Figure 3.12: Top view of the High Voltage Splitter outline.

In order to provide the high voltage necessary to power the PMTs, 8 DC-DC converter boards, known individually as the High Voltage Unit (HVU), are mounted on top of the HVS (green components in Figure 3.12). These units, which take +24 V direct current and provide the HV output in the desired range of 800-1500 V, will be grouped in pairs for a 1:1 redundancy. For each HVU ON (operating normally), there is another HVU OFF (in idle mode) that serves as a backup in case of failure. Consequently, only 4 HVUs are operational at any given time. 4 are placed on the top layer of the board, while the other 4 are placed on the bottom layer. This serves to increase the reliability of the SPMT system, with reduced chances that a failure of a HVU will lead to the loss of active PMTs in the experiment. Following the output of the HVUs, there is a series diode (brown components in Figure 3.12), capable of withstanding the HV reverse bias. This is what allows for safe redundancy. However, the necessary presence of these protection diodes to allow a safe switch between HVUs ON and HVUs OFF adds a layer of complexity and possible failures to the board. Each HVU is powered and controlled by the GCU through a RS485 emitter/receiver interface and a "Look at Me" signal. The power supply and control of each HVS board is physically done through a single 40-pins SAMTEC connector in interface with the same connector on the GCU (purple component in Figure 3.12). The high voltage output of each operational HVU is connected to 16 individual SPMT channels through long coaxial cables plugged in the MCX connectors (red components in Figure 3.12). As such, there is a common high voltage for 16 PMTs, which implies that SPMTs should be grouped according to their Gain at a fixed HV value.

After the PMT signal is directed to the board through the coaxial cable and MCX connectors, it is decoupled from the HV by the decoupling capacitors (orange components in Figure 3.12). Figure 3.13 shows the schematics of the HV / signal decoupling for 16 PMTs connected to one CATIROC readout chip, with 2.2 nF capacitors in the HVS board acting as high-pass filters cutting

off the invariant HV. Small and brief fluctuations to this HV, due to PMT signals, are passed by the decoupling capacitors and feed the CATIROC readout.

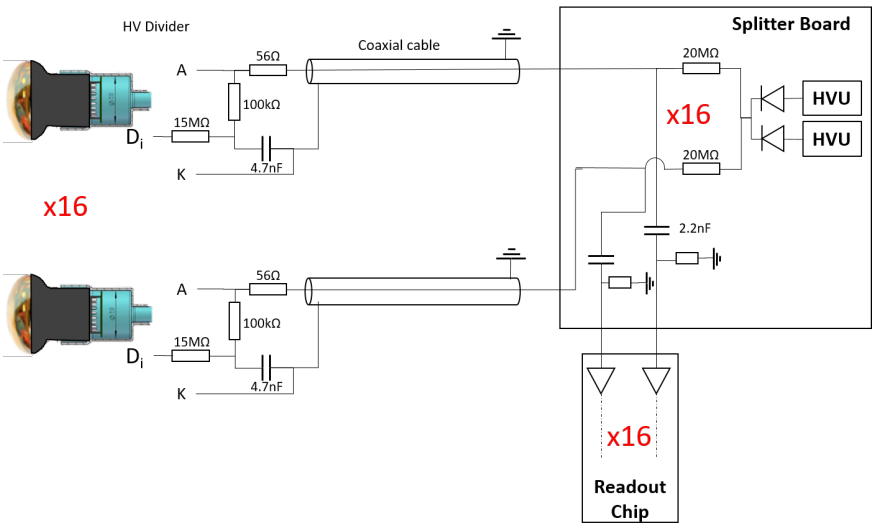

Figure 3.13: HV / signal decoupling schematics for 16 PMTs connected to one of the 8 CATIROC readout chips on an ABC board. In each channel, the PMT signal goes through the HV Divider and the coaxial cable before being decoupled by 2.2 nF capacitors acting as high-pass filters.

The decoupled signal is then sent to the ABC board though two 40-pins SAMTEC connectors (blue components in Figure 3.12). Each connector carries 32 signal channels, for a total of 64 PMTs connected between each HVS board and the ABC board. The remaining 8 pins (for each connector) are connected to analog ground. A picture of the HVS V0.3 board is shown in Figure 3.14 for illustration purposes.

Figure 3.14: High Voltage Splitter board V0.3.

As part of extensive tests performed on HVS V0.3, two different SPMTs were used to measure SPE signals using two different cable lengths. These measurements were performed at a gain slightly higher than the nominal PMT gains, and for each channel measured, 1000 independent events were stored in memory and averaged to obtained the average SPE waveform. Representative plots for the average SPE waveform are shown in Figures 3.15a and 3.15b for cable lengths of 5 m and 10 m respectively. The High Voltage was increased from 900 V to 1150 V in the 10 m cable case in order to reach the same SPE amplitude as for the 5 m cable case. No clear waveform differences are observable at the SPE range once the amplitudes have been adjusted.

These tests also included a cross-talk studies for validation of the design, according to which the worst case scenario shows a cross-talk of up to 1.6%, likely to be the limiting factor in the total cross-talk budget of the electronics.

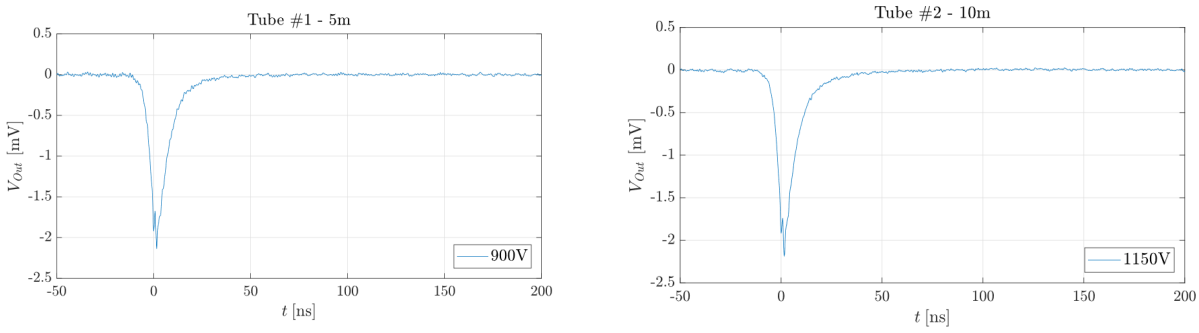

(a) (b)

Figure 3.15: SPE waveform with High Voltage Splitter V0.3. (a) 5 m cable length, 900 V. (b) 10 m cable length, 1150 V.

3.5 Front-end ABC board

The PMT signal readout, after decoupling by the HVS board, is performed with a front-end ABC (ASIC Battery Card) board, the PCB of which measures 35×17 cm and is composed of 12 layers. Eight 16-channels CATIROC (Charge And Time Integrated Read Out Chip) ASICs provide a trigger-less, digitized time and charge output. This is the main function of the ABC board, and the responsible components will be further detailed in the following section. The other key component of the ABC board is a high-performance Kintex-7 Field Programmable Gate Array (FPGA), responsible for the communication with the slow control parameters controlling the behaviour of the CATIROC ASICs, as well as the data capture, processing and further packaging of the CATIROC output. The FPGA provides two clocks to the eight CATIROC ASICs, running at 40 and 160 MHz, ensuring the local synchronisation. It also implements additional advanced features (event labelling, dead-time monitoring, etc.). A 1-GB dual data rate (DDR3) high-bandwidth memory provides additional buffering resources to hold data until data transfer to the GCU through a 40-pin SAMTEC connector.

Both sides of version V1.2 of the ABC board are shown in Figure 3.16. The CATIROC ASICs and the FPGA on the top side, with the connectors on the bottom, because the top side will be connecting with a flat surface to allow for thermal regulation, and as such will not be available for connections with the other electronic boards.

The ABC board is powered twice in 12 V, once for the analog components (ASICs) and once for the numerical components (FPGA, DDR3). Its consumption is around 15 W. Since it hosts eight CATIROCs (500 mW consumption per chip, 4 W in total) and provides them with their required power supply (3.3 V and 1.8 V) and bias voltages, the ABC board allows for the readout of 128 SPMT channels. As such, it is also connected to two HV splitter boards in order to process the pre-decoupled PMT signal. The following section details the most important components of the ABC board, the CATIROC ASICs.

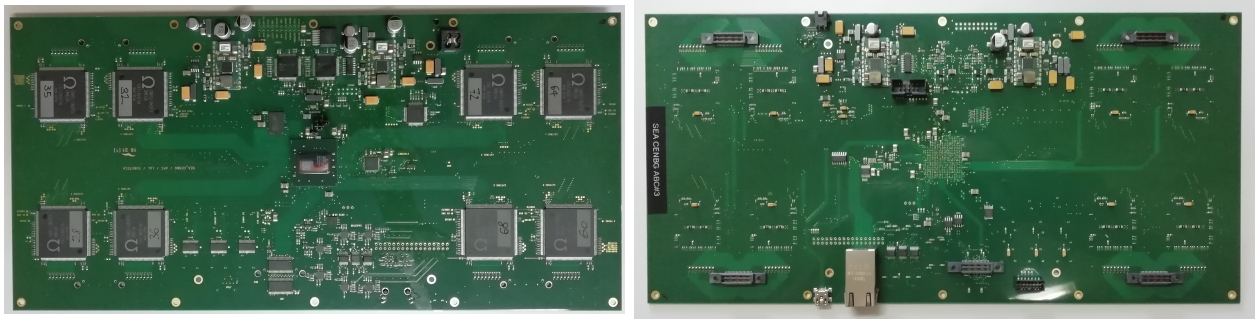

(a) (b)

Figure 3.16: ABC V1.2 board (a) Top side with main components. The 8 CATIROC ASICs are positioned on both sides of the board in a square formation and can be identified by the Ω symbol on their surface (OMEGA laboratory). The FPGA is the central piece of the board, as it collects all the data from the 8 ASICs. Other components are mainly decoupling capacitors. (b) Bottom side with connectors to the electronic system. The connectors in each corner are the SAMTEC connectors to the HV splitter boards, and central-top connector is the SAMTEC connector to the GCU.

3.5.1 CATIROC ASICs

CATIROC is a 16-channel front-end ASIC developed by the french OMEGA laboratory [125, 126], designed and customized to readout photomultiplier tubes (PMTs) in large scale applications. It is a complex SoC (System on Chip) that integrates many functions, as it needs to auto-trigger asynchronously on any single photoelectron detected in the independent 16 PMT-connected channels and provide digitized time and charge outputs. An adjustable gain is featured for each input channel to compensate for the gain variation between the PMTs. A shift register is used to send the configuration parameters (named slow control parameters) inside the chip, and is piloted by the FPGA. There are 328 Slow Control (SC) parameters, loaded serially to control the chip, impacting the configuration and the operating mode of the ASIC.

The chip architecture is shown in Figure 3.17, and will be walked through in detail to follow the processing of a PMT signal. The description will focus on 1 channel out of the 16 that are read by a single chip. There are 4 main circuits in the architecture :

- The red circuit, corresponding to the low gain and high gain preamplifiers
- The purple circuit : the fast channel, with a fast shaper, designed for the trigger signal generation
- The green circuit : the slow channel, with 2 slow shapers, for charge measurements
- The orange circuit : for the time measurements

The input of the electronic chain of CATIROC, for one channel, is the fast current signal (negative amplitude, rise time ∼few ns) coming from a PMT. A 50 Ω resistor is placed outside every ASIC channel input to terminate the PMT cable impedance, so that a voltage signal is sent to the first stage of the channel, the preamplifiers.

This PMT signal is first processed by the red block on the chip architecture, the 2 voltage preamplifiers. The low and high gain preamplifiers, working in parallel, have a fixed input capacitance of respectively 5 pF and 0.5 pF and a variable feedback capacitance (ranging from 0.008 pF to 1 pF, tunable on a 8-bits slow control parameter). By adjusting the value of the feedback capacitance, it is possible to adjust the gain of the preamplifiers, and so the total gain of the system, possibly to compensate the gain variation PMT to PMT. The low and high gain preamplifiers have a fixed gain ratio of 10. The use of HG and LG paths allows to achieve a dynamic range spanning from

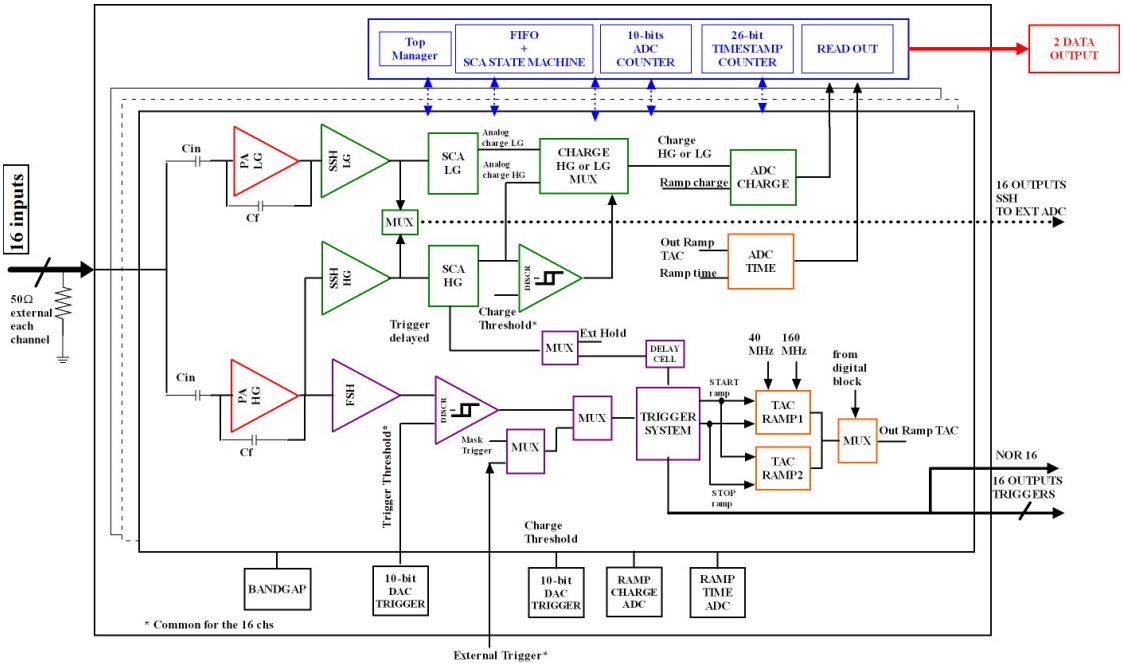

Figure 3.17: CATIROC ASIC architecture.

160 fC (0.3 PE at a PMT gain of 3×10^6) up to 70 pC (145 PEs) with a preamplifier gain of 20. The output of each of the preamplifiers is a positive voltage signal, as shown in Figure 3.18a.

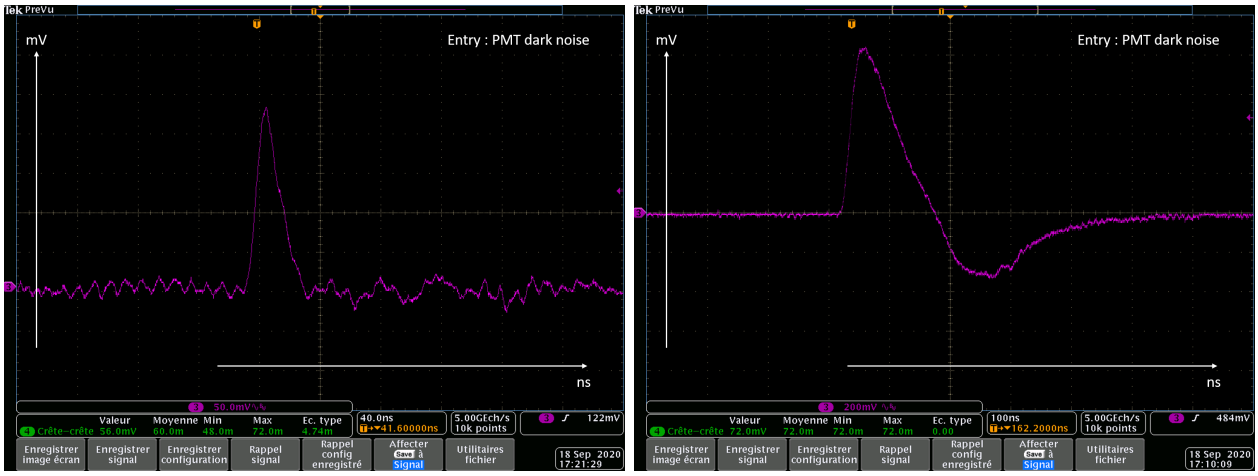

(a) (b)

Figure 3.18: (a) Preamplifier output waveform for the High Gain mode. (b) Slow shaper waveform in the High Gain mode.

These two amplified signals feed two channels, a slow channel for the charge measurements (green block on Figure 3.17) and a fast channel for the trigger production (purple and orange block on Figure 3.17). The 2 signals in output of the high and low gain preamplifiers will be processed by two slow shapers in parallel (SSH HG and SSH LG green triangle cells on Figure 3.17). They are CRRC2 filters, cutting the high and low frequencies, with variable gain and peaking time. The peaking time, common for all channels, can vary from 25 ns to 100 ns. The slow shapers reduce the signal fluctuations induced by the electronic noise, thus giving an image of the signal with an optimized signal-to-noise ratio. The output of the low and high gain slow shapers are large

positive voltage signals, an example of which is shown in Figure 3.18b. The charge measurements will be performed on these slow shaper waveforms.
In parallel of the slow shapers processing the outputs of the high and low gain preamplifiers, the high gain preamplifier waveform also feeds the fast channel and is processed by a fast shaper (FSH purple triangle cell in Figure 3.17). The fast shaper is a CRRC filter, cutting the high and low frequencies, with a time constant of 5 ns. The purpose of the fast shaper is to filter the noise and, with its high gain, to generate a high fast signal. Since the objective is to be able to trigger over very small signals (charge equivalents of 1/3rd of PE, maybe even 1/4th of PE), a maximum signal amplification is required, and so the output of the high gain preamplifier is the only one shaped by the fast shaper (as it is logically the best suited to be).
The resulting fast shaper waveform is a negative voltage signal with a baseline of ∼1.9 V. As it is not an image of the PMT signal anymore, deriving the charge from this waveform is not possible. Figure 3.19 shows an example of a fast shaper waveform.

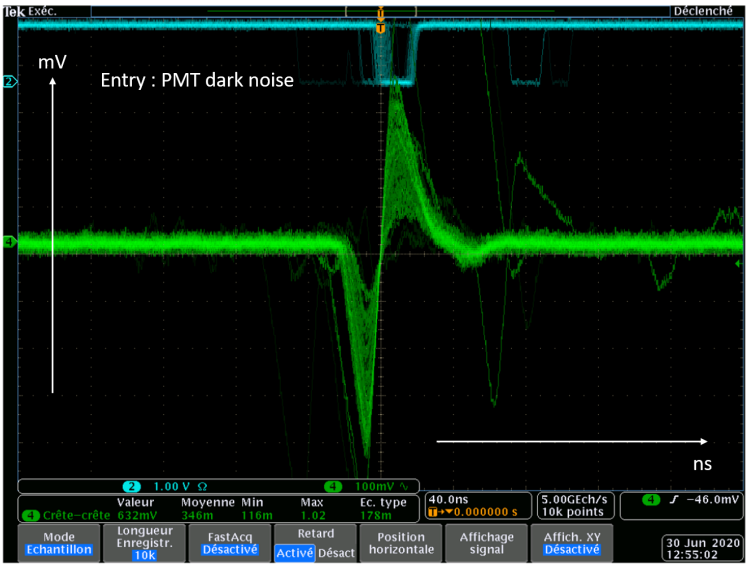

Figure 3.19: Fast shaper waveform (green) obtained with a PMT signal. In blue, resulting trigger signal.

The fast shaper is followed by a low offset discriminator, in order to continuously compare the voltage of the fast shaper waveform to a threshold value called the trigger threshold, configured as a 10-bit DAC value common to all 16 channels of the ASIC.
The trigger threshold ranges between 1 and 1.9 V, with a slope of about 0.9 mV/DACu, as shown in Figure 3.20. Since the fast shaper waveform is a negative voltage signal with a positive baseline, the trigger threshold cannot exceed this baseline of 1.9 V. When the output of the fast shaper is "higher" than the threshold of the discriminator (at a lower amplitude value due to the negative pulse), a trigger signal will be generated (TRIGGER SYSTEM purple square cell on Figure 3.17), and the rising and falling edges of this positive square signal are lined up with the two instances in which the fast shaper waveform crossed the threshold horizontal line.
The time at which the fast shaper output signal exceeds the fixed trigger threshold discriminator value depends on the PMT pulse amplitude. As the amplitude varies, the timing of the signal shifts, and as such, variations in signal amplitude can spoil the timing distribution. This phenomenon is called "time walk", and has been measured to be ∼5 ns at preamplifier gain 20.
This trigger signal will be processed by two separate blocks in the chip architecture to allow for the charge and time measurements.

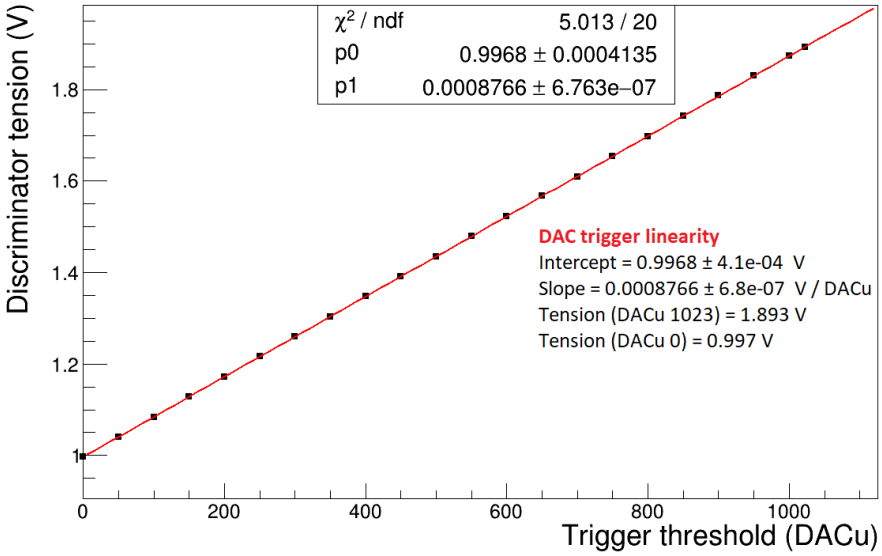

Figure 3.20: DAC trigger linearity, DACu to Voltage slope.

For the charge measurement, the trigger signal is sent to a delay cell (purple square cell in Figure 3.17), and a delayed step signal called the HOLD signal is generated. This signal is sent to two parallel analog memories (SCA HG and SCA LG green square cells in Figure 3.17), along with the outputs of the high gain and low gain slow shapers (sent to their respective SCA). SCA stands for Switched Capacitor Array. The falling edge of the HOLD signal corresponds (in time) to the maximum amplitude on the two slow shaper signals (high gain and low gain), and allows for these maximum tension values to be stored in one of the two capacitors of each analog memory. These tension values are called the analog charges. With this depth of two capacitors, the two SCA work in a "ping-pong" mode in order to minimize the dead time during digitization : while a channel is being digitized (ping), the shaper outputs can be sent to the second capacitor of each SCA (pong).
A second step signal, called the READ signal and delayed from the HOLD signal, is also generated. On the rising edge of this READ signal, the tension values stored in the capacitors of the two SCA are sent to a Multiplexer (CHARGE HG or LG MUX green square cell in Figure 3.17), where only one of the HG or LG analog charges (tension values) will be selected for conversion by a 10-bit Wilkinson Analog to Digital Converter (ADC).
This selection is performed automatically by a discriminator on the high gain analog charge before the READ signal (DISCRI green square cell in Figure 3.17), because the high gain channel is the first to saturate. When saturating, the high gain channel output in the analog memory will be a near-constant tension value. The threshold of this discriminator, common to the 16 channels and called the gain threshold, is set by an internal 10-bits DAC and is configured so that the voltage equivalent to its DACu value is a little lower than the maximum tension that the high gain channel can deliver before saturation. If the tension value stored in the high gain analog memory is higher than this gain threshold value, then the discriminator will order the selection of the tension value stored in the low gain analog memory. The output of this discriminator is sent to the same MUX as the analog charges, and the selected charge is then converted by the ADC into the final output ADCu charge measurement (ADC CHARGE green square cell in Figure 3.17).
A synthetic digital timing diagram of the electronic processing of a PMT signal for the charge measurement is presented in Figure 3.21.

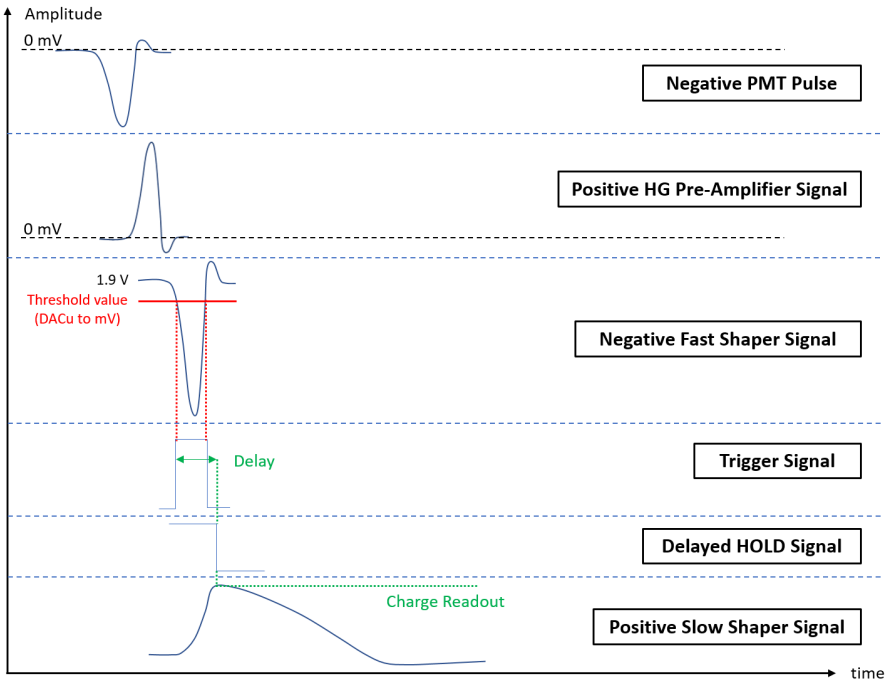

Figure 3.21: Simplified digital timing diagram of the PMT pulse processing chain for the charge measurement.

In parallel, the trigger signal is processed by the fast channel orange block in Figure 3.17 for the time measurement, achieved by the measurement of a "coarse time" and a "fine time".
The "coarse time" measurement is performed by a 26-bit Gray Counter with a resolution of 25 ns due to the 40 MHz clock, overflowing at 1.67 s. This coarse time is saved in a 26-bit register when the fast channel (purple block in Figure 3.17) has a trigger indicating a detected signal (rising edge of the generated trigger signal). This trigger, synchronized with the 40 MHz clock, allows for the measurement of a fine time in the 25 ns window of the coarse time, with a TAC (Time to Analog Converter) ramp. The maximum value of this ramp, a tension, is stored in an analog memory, and then converted into ADCu by a 10-bit ADC converter (ADC TIME orange square cell in Figure 3.17), giving the fine time measurement. The total time stamp can be computed using the coarse time and the fine time values.
In addition to the electronic processing of a PMT pulse, it is crucial to understand and measure other CATIROC features in order to justify the use of this chip in the JUNO experiment. In the following sections, several tests performed by the French teams on an evaluation board (developed by OMEGA laboratory) are summarized [126], including the characterization of the trigger efficiency as a function of the discriminator threshold, the measurement of the dead times of the chip, the charge linearity over a wide signal range, the characterization of the charge acceptance as well as the correction of possible charge biases, and the time resolution of the chip.
The tests were performed using a signal generator (Tektronix AFG3252C), injecting pulses of 10 ns width and 5 ns edge time into the readout channels to mimic a potential signal from a PMT. For the charge measurements, the amplitude was adjusted in order to scan a range of charges from a few fC up to about 60 pC. The pulse frequency was typically set at 10 kHz, and was varied up to 1 MHz for dead time studies. The default gain value of the preamplifiers is 20.

Trigger efficiency

The trigger efficiency is defined as the ratio between the number of trigger counts in the output of CATIROC ("trigger output") and the number of injected pulses for a given threshold. The efficiency as a function of the discriminator threshold (also called S-curve) is shown in Figure 3.22 for pedestal measurements as well as different input signals (0.16 pC, 0.32 pC and 0.48 pC). Each thin line making up one line distribution corresponds to one of the 16 channels. As previously mentioned, the trigger threshold is common to the 16 channels, so the optimal tuning of the threshold will have to be defined for each CATIROC during the readout boards and PMTs calibration.

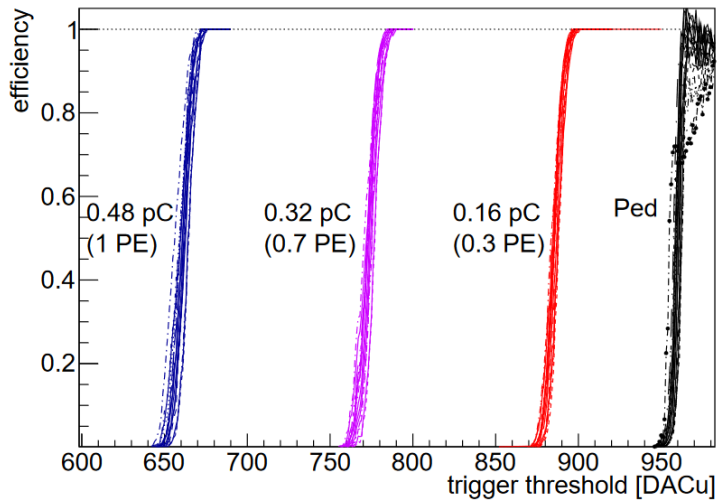

Figure 3.22: Trigger efficiency as a function of the threshold for various injected charges up to 480 fC and a PA gain of 20. The corresponding signal value in PE is also indicated, considering a gain of 3×10^6. [126]

From these S-curves, the threshold values allowing to trigger on given charge inputs can be determined, depending on the required trigger efficiency. A threshold of 0.3 photo-electron is typically considered in experiments using PMTs and is shown to be attainable with CATIROC.

Charge linearity

The linearity of the charge measurement was tested for all 16 channels, for signals ranging between 0.1 pC and 70 pC. Figure 3.23 shows the charge linearity in one channel as an example. The HG (red) and the LG (blue) ranges are shown for the charges contained in both SCA capacitors ("ping" and "pong", respectively the filled and empty markers). The PE equivalent of the injected charges (at nominal PMT gain 3×10^6) is shown as an additional scale. Repeating these measurements on a second test board (with an independent setup) provided compatible results, and the residuals with the linear model are within 4 ADCu ($\sim$0.5% to $\sim$2%).

Time resolution

In order to characterize the time resolution (σ_T) of the system, two measurements are performed. First, the time difference dT is measured between two consecutive signals injected in the same i-th channel. Then, the same signal is simultaneously injected in the channels i and j using a passive signal splitter, and the time difference dT_{ij} is measured. In the first approach, the dT distribution is expected to be centered at the signal generator period, with a spread related to

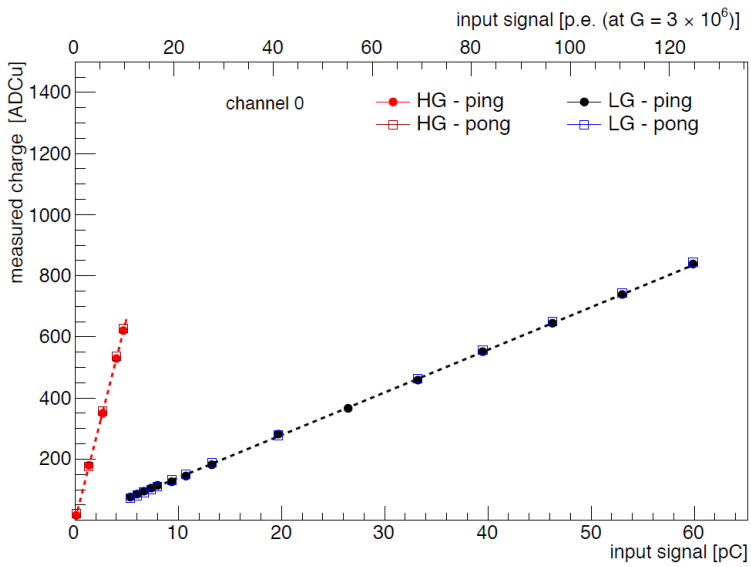

Figure 3.23: Linearity of one of the channels for the high-gain in red and the low-gain in blue. Empty and filled markers denote the two capacitors (ping/pong) in the analog memory. [126]

the time resolution convoluted with the jitter of the signal generator. An example is shown in Figure 3.24 as the thick blue distribution in the case of channel 0. The signal generator period is subtracted for intuitive plotting reasons.

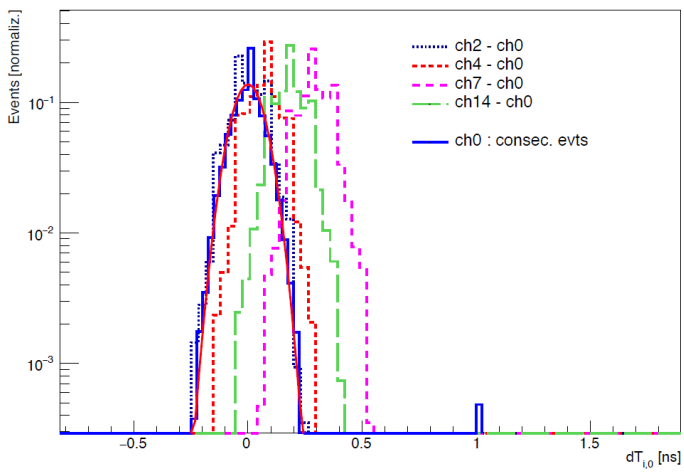

Figure 3.24: Example distributions of $dT_{i,j}$ between the i-th channel and channel $j = 0$ (thin dashed lines). The thick blue histogram is the case of dT_{00} (subtracted of the signal generator period) obtained from the time difference between consecutive signals injected in the same channel ($i = j = 0$). [126]

The second approach is performed to get rid of the systematics due to the signal generator. This method is however sensitive to potential systematics between different channels. The distributions of dT_{ij}, also shown in Figure 3.24 as dotted lines, are then expected to be centered at zero with a measured spread σ_{ij} derived from the time resolutions σ_i and σ_j of the two channels :

$$\sigma_{ij} = \sqrt{\sigma_i^2 + \sigma_j^2} \approx \sqrt{2}\sigma_T \tag{3.1}$$

This is under the assumption that $\sigma_i \approx \sigma_j = \sigma_T$. With both approaches, the value of σ_{ij} is within 150 ps.

Single photo-electron spectrum with PMTs

In order to evaluate the CATIROC performance when employed to read the signals from a 3" PMT, its single photo-electron spectrum was measured with a test-bench consisting of a light-tight box ($50\times40\times25$ cm^3) containing up to two 3" PMTs (model HZC XP72B22) powered with a negative high voltage (HV). A simple approach to measure the SPE spectrum is to look at the dark noise, which is mostly due to thermo-ionic emission from the photo-cathode, leakage current between the cathode and the dynodes and ionization from residual gases. To ensure that a steady dark current is reached, data were always acquired at least 3 hours after any manipulation requiring the PMT exposition to light. Figure 3.25 shows the SPE spectrum for ping and pong data. The SPE position, calculated after pedestal subtraction, is 39 ADCu, which corresponds to 0.3 pC with the proper calibration data, and the relative SPE resolution is 33%. As clearly visible in the figure, the spectral distributions are slightly different for ping and pong data. This difference, mostly due to the offset in the pedestal, is stable against the HV and is corrected once the proper calibration for "ping" and "pong" is applied.

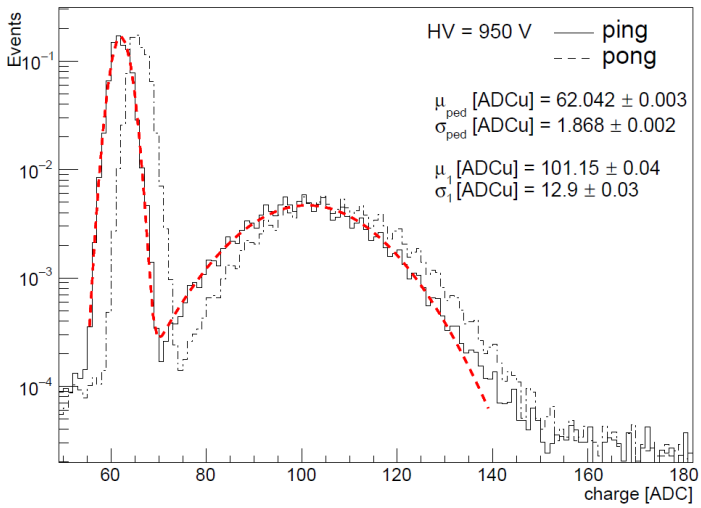

Figure 3.25: Example of the spectrum of a 3" PMT measured with CATIROC. Data acquired with the ping and pong capacitors can be reconstructed separately guaranteeing that the resolutions are not degraded. [126]

3.5.2 Data and Firmware

The digital part of the CATIROC chip, responsible for the data generation and transmission, is divided in 2 blocks, with 1 block for 8 channels. For each block, one serial link reads out the internal memories containing the data, and transmits the data within 1 strobe, at a rate of 80 MHz. Consequently, each CATIROC sends 2 strobes in order to transmit the data from its 16 channels. These strobes, and the data they contain, are completely anonymous regarding their

origin (CATIROC number, first or second half of the 16 channels), and this identification will be performed by the FPGA when receiving and organizing the data. Each strobe is composed of 2 frames, each containing specific information, and the time delay between the 2 frames varies depending on the value of the charge and fine time measurements, as it impacts their conversion time. One such strobe is shown in yellow in Figure 3.26 after capture on an oscilloscope. Each of its frames contains the CATIROC data (in blue) in 8 smaller bunches, one for each channel.

Figure 3.26: Data Capture in USB mode in the ABC board. In yellow, the 2 frames contained in the CATIROC strobe for 8 channels, each containing specific information. The delay between the first and second frames depends on the conversion time for the charge and fine time measurements. In blue, contained in each frame, CATIROC data for each of the 8 channels, with Channel Nb and CT in Frame 1 and Gain, Charge and FT in Frame 2.

The first frame, illustrated in Figure 3.27, contains the information about the channel number, coded over 3 bits (within 0 and 7 included), and about the coarse time, coded over 26 bits. As such, the first frame contains a maximum of 8 words of 29 bits, meaning that for a data transfer of 80 MHz, the first frame can take up to 2.9 μs to be transferred.

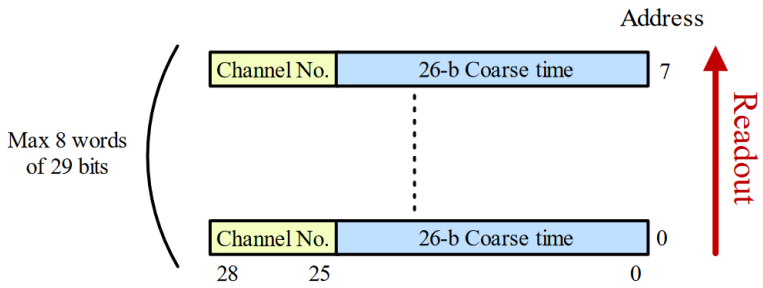

Figure 3.27: CATIROC first frame.

The second frame, illustrated in Figure 3.28, contains the information about the gain, coded over 1 bit (0 or 1), about the charge, coded over 10 bits ([0-1023]), and about the fine time, coded over

10 bits as well. As such, the second frame contains a maximum of 8 words of 21 bits, meaning that it can take up to 2.1 μs to be transferred.

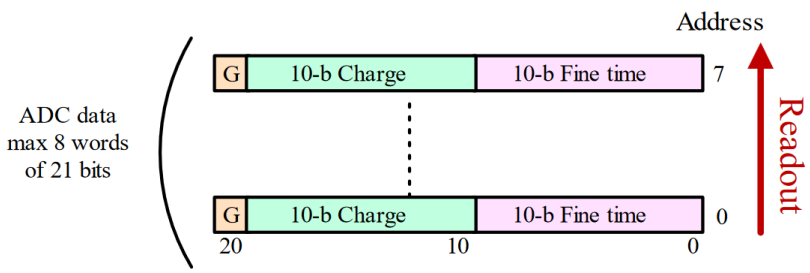

Figure 3.28: CATIROC second frame.

This data is sent to the other main component of the ABC board, the FPGA, which samples the data and organizes it before sending it to the GCU. The FPGA actions are programmed and controlled by the firmware using the Hardware Description Language (HDL). This firmware for the final state of the JUNO experiment is currently being designed and refined, with circular buffers to avoid losing any event. A schematic view of the data capture by the FPGA with transfer to the GCU is shown in Figure 3.29. This firmware envisioned for the final state of the JUNO experiment will use a circular buffer to collect the data from a triggered channel in a group of 8 without having to wait for the other channels. The event identification will be performed at the level of the Event Builder by comparing the event trigger times, and no header information will be transmitted to the GCU, which will regularly interrogate the circular buffer for data transfer.

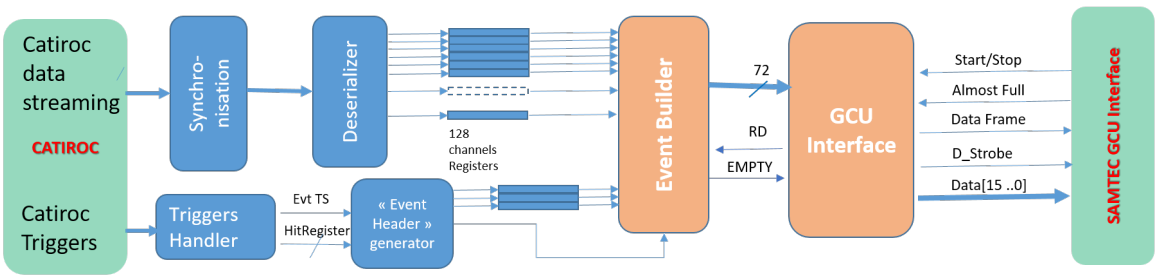

Figure 3.29: CATIROC data capture by the FPGA, with transfer to the GCU. Envisioned schematics, under discussions and optimization.

A test firmware has nevertheless been designed for data-taking in order to extensively test the SPMT electronics, and will be described in section 4.2.2 (data transfer via USB to characterize the ABC board and via USB or GCU for combined tests using 128 PMTs).

3.6 Global Control Unit board

After digitization, events are sent from the CATIROC ASICs to the FPGA, and then to the Global Control Unit (GCU) board via the 40-pins SAMTEC connector. The GCU allows a continuous data readout, which is sent to the DAQ system (in the surface facility) for storage and analysis. The GCU board is however also used to start the SPMT system, synchronous to all independent UWB, and to provide a synchronous clock.

It consists of a 35 cm × 17 cm PCB board, 2 mm thick, with 16 layers. 8 of these layers are used for signal transmission, 5 for grounding, and 3 to allow it to power the SPMT system. Its main components are a KINTEX 7 FPGA, a Spartan 6 FPGA and a 2 Gigabits DDR3. Both sides of the GCU board are shown in Figure 3.30.

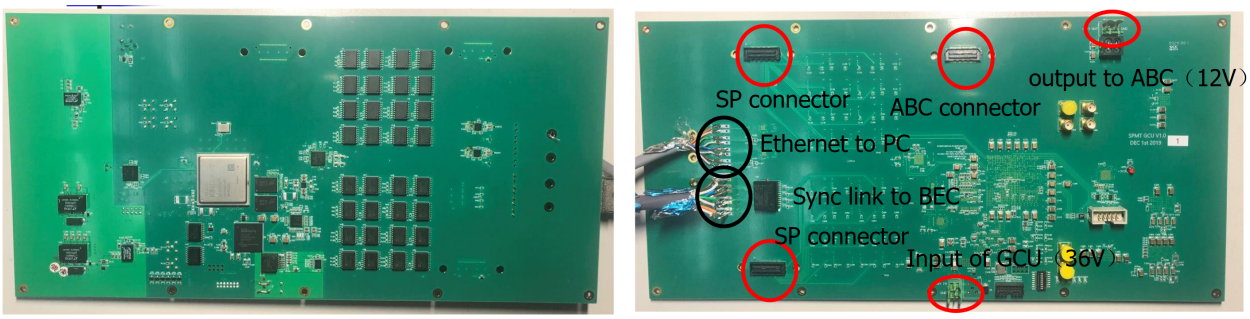

(a) (b)

Figure 3.30: GCU board (a) Bottom side with components. (b) Top side with connectors to the electronic system.

It is powered by 36 V coming from the surface, and provides the 12 V power supply to the ABC board and the ABC board communication as well as the 24 V power supply to the HV splitter boards and the high voltage units. These HV units then produce the HV necessary to power the PMTs. It is also used to allow a safe remote reprogramming support, with its dedicated Spartan 6 FPGA for remote firmware update.
As can be seen in Figure 3.30b, one GCU board connects to 2 HV splitter boards via SAMTEC connectors, to one ABC board via SAMTEC connector, to one pair of power cables, to BEC via FTP cables for clock distribution and trigger management, to an Ethernet switch via UTP cables for DAQ and slow control, and to an AC-DC power supply via low resistance power cables. In terms of production, the V1.0 of the GCU-ABC board was finalized, as well as its firmware, and it has been used in combined tests with 128 PMTs at LP2i Bordeaux (section 4.4.3).

3.7 Underwater Box design and thermal studies

3.7.1 Design

Each independent Under Water Box (UWB) is filled with all the electronic boards required to control as well as process the signals from 128 3" PMTs. 200 underwater boxes are required to complete the SPMT system, and 220 underwater boxes will be built to allow for a margin of error when validating the production.
The core of the underwater boxes is a 50 cm long (internal measurement), 10-inches wide (253 mm), 4.19 mm thick, stainless steel (SS304L) cylindrical body with one welded lid and one removable lid (20 mm) to allow the placement and the cabling of all the components of the SPMT electronic system. This removable lid is screwed shut, and is sealed with 3 "redundant" O-rings, 2 axial and a radial one (different materials), to guarantee the water tightness. Through this removable lid are connected the 128 PMTs by way of the 8 Axon underwater connectors, each handling 16 channels. A welded below (flexible metallical underwater tube) on the fixed lid contains the 2 Ethernet cables connecting to the GCU as well as the twisted pair cable powering the system. A scattered view of an underwater box, with its electronic system, was previously shown in Figure 3.6, and UWB prototypes are shown in Figure 3.31.

Figure 3.31: UWB prototypes, with a 50 cm long, 10-inches wide and 4.19 mm thick stainless steel cylindrical body equipped with one welded lid and one removable lid to allow the placement and the cabling of all the components of the SPMT electronic system. The removable lid is screwed shut on the left prototype, in order to be sealed and guarantee the water tightness.

The Final Design Review for the underwater boxes was passed in January 2020, and the manufactured prototypes have been tested extensively in France and in Chile. The production of the 220 underwater boxes is planned in China.

3.7.2 Thermal studies

In terms of thermal studies of the SPMT electronic system, the general requirements for the JUNO experiment are to guarantee a lifespan of 20 years for each system, as well as a $< 5\%$ loss over the first 6 years of running. In terms of thermal energy dissipation, 6.8 kW is the total JUNO requirement for the SPMT system, mainly to guarantee the proper temperature of the water pool, with each UWB having a budget of 34 W, 20% margins included. This translates into a thermal requirement of $< 40°$C on the surface of each component, to guarantee a proper ageing and the reliability of the system.

The hottest component of the SPMT electronic system is the ABC board, weighting $\sim$71% in the electricity and heat balance. It has a total 24 W consumption, margins included, with 15 W for the board itself and 5 W for the DDR. The GCU has a consumption of 7 W, the rest of the components being negligible in the budget (the total consumption of the HV units only amounts to about 3 W). In order to cool down the system, most of the resources had to be allocated to the ABC board and the GCU, favouring a cooling by thermal conduction using 10 mm aluminum heat sinks. The heat emitted by both boards is transmitted first to the heat sinks, and to a lesser degree to the UWB via the heat sinks, which is then cooled by the 21°C water of the water pool. The rest of the components are cooled down by convection inside the UWB.

The heat sinks are positioned inside the UWB, parallel to the electronic boards, as can be seen in Figure 3.6. Their main points of contact with the boards are directly on their hottest components, with a thermal paste to facilitate the conduction. The thermal paste is an excellent electrical insulate, commonly used in the field of micro-electronics. In the case of the ABC board, the main points of contact are the 8 CATIROC ASICs and the FPGA.

This conduction method was tested on the ABC V1.0 board inside of its UWB, submerged in 23°C

water. 6 PT100 thermal probes were positioned over the ABC surface, with 2 additional probes in the UWB (mid heat sink and on the UWB-LID). The temperature of the key components was monitored in air (21°C) and in water (23°C). Figure 3.32a shows the probes being applied to the ABC board, while Figure 3.33 shows a more precise view of the numbered position of the probes. Figure 3.32b shows the sealed UWB being submerged in water for the thermal study.

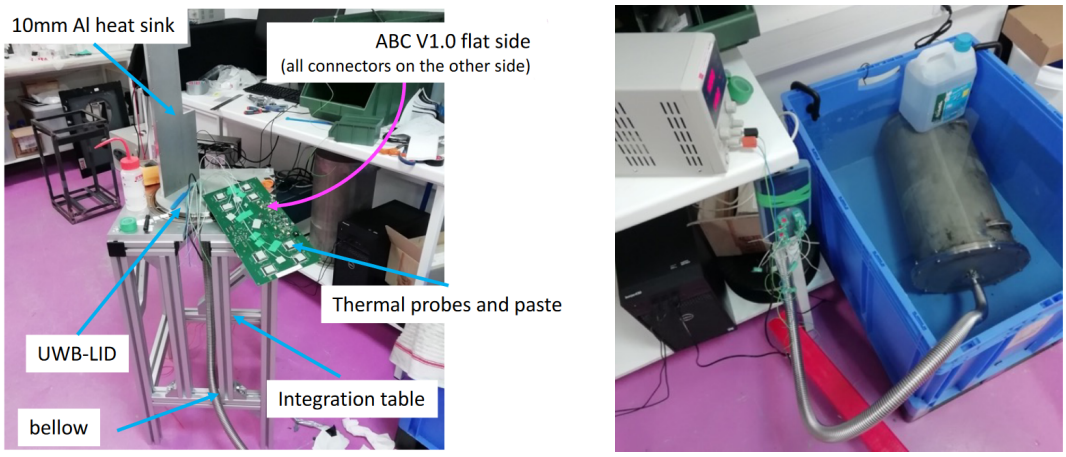

(a) (b)

Figure 3.32: SPMT system thermal study at LP2i (a) Thermal probes applied to the flat side of the ABC V1.0 board (on UWB). (b) Closed underwater box submerged in 23°C water for thermal monitoring of the electronic components.

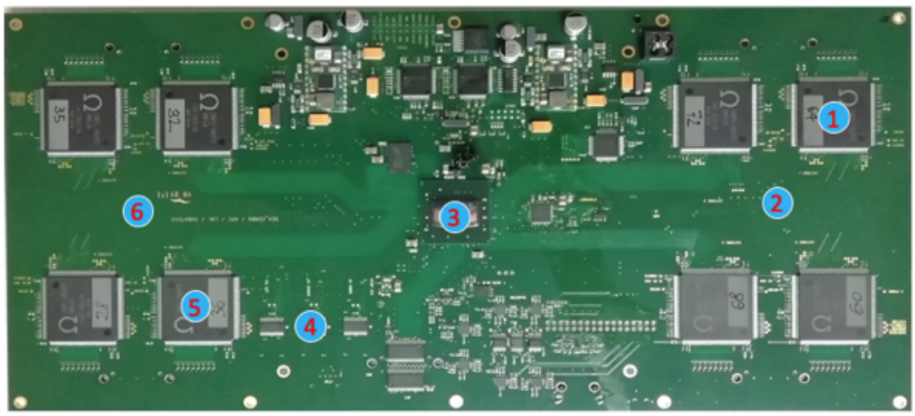

Figure 3.33: Positioning of the thermal probes on ABC V1.0.

The results are presented in Table 3.1. All components have a temperature below 40°C, yielding very satisfying results. Using thinner heat sinks would allow for a gain in UWB mass as well as in production costs, so an optimization of this design could be worth investigating.

3.8 Radiopurity of the SPMT system

As presented in section 2.7, the radioactivity of the JUNO materials – mainly U, Th and K - is one of the main backgrounds contributing to the accidental background. Thus, all materials have to be screened in order to select the less radioactive ones. The most critical component of the

#	Positioning of the probe	T in 20°C air (°C)	T in 23°C water (°C)
1	CATIROC chip	35.8	36.0
2	PCB	35.6	36.1
3	FPGA	34	34.8
4	Clock	36.7	37.4
5	CATIROC chip	31.6	32.1
6	PCB	31.3	32.5
7	Mid heat sink	30.2	30.3
8	UWB-LID	23.8	23.0

Table 3.1: Global thermal study results with 10 mm aluminum heat sinks

PMT is usually the glass itself. The components of the PMT glass have been carefully selected, especially the quartz sand, and controlled during the 2 years of production in order to fulfill the JUNO SPMT glass requirements, i.e. U $<$ 400 ppb ($<$ 5 Bq/kg), Th $<$ 400 ppb ($<$ 1.7 Bq/kg) and K $<$ 200 ppb ($<$ 53 Bq/kg) [127]. The mass of the 3" PMTs ($\sim$100 g) being much smaller than the mass of the 20" PMTs ($\sim$7 kg), the radiopurity requirements for the SPMT system are less stringent than for the LPMT system.
The other important components are the HV divider, the potting and the UWB, including mechanical structures and electronic boards. Table 3.2 gives the list of the materials, their total mass in the system as well as their radioactivity after being measured by low background gamma spectrometers in various laboratories (LSM, Bordeaux, Milano-Bicocca, IHEP and CJPL), as shown in Figures 3.34a and 3.34b.

Components	Total mass (kg)	^{238}U (Bq/kg)	^{232}Th (Bq/kg)	^{40}K (Bq/kg)
3-inch PMTs	2600	2.4	1.4	26.6
HV divider	150	25.9	24.8	23.1
Potting	5050	0.9	0.2	5.0
UWB structure and connectors	7420	$<$0.08	$<$0.07	$<$0.27
Cables	1460	0.06 $\pm$ 0.02	$<$0.042	$<$0.023
HV splitter boards	420	27.7 $\pm$ 2.0	34.2 $\pm$ 2.5	33.9 $\pm$ 2.3
ABC board	70	6.7 $\pm$ 0.5	9.3 $\pm$ 0.5	5.3 $\pm$ 1.1
GCU board	70	6.0 $\pm$ 0.3	7.1 $\pm$ 0.4	46.5 $\pm$ 6.1

Table 3.2: List of the SPMT components, their mass and their radioactivity, measured by low background gamma spectrometry. Uncertainties are only statistical uncertainties at 68% C.L. and limits are given at 95% C.L. for a single measurement. For PMTs, HV divider and potting material, the values have been measured from several samples.

The total activity of each component has been calculated from Table 3.2 according to their mass. For the UWB components, their relative contribution to the counting rate in the Fiducial Volume (FV) of JUNO (R $<$ 17.2 m) have been simulated using the SNiPER software (described in section 5.2). The main contribution is coming from the HV Splitter board whereas the ABC board contribution is about 7%. Efficiencies have been also determined by simulations for the PMT, the HV divider and the potting, depending on their location, which is closer to the JUNO sphere (R$\sim$19.3 m) when compared to the UWB (R$\sim$20 m). The main contribution is coming from the PMTs themselves and the total expected counting rate in the FV of the SPMT system with E $>$ 0.7 MeV is about 0.15 Hz, i.e. below the 0.2 Hz requirement for the SPMT system. Table 3.3 summarizes the contribution of each part of the SPMT system to the total counting rate.

(a) (b)

Figure 3.34: (a) From right to left, HV PCB divider, ABS shell for the potting, PMT, PMT+HV divider and PMT+HV divider+potting. (b) Pieces of ABC board measured by a Germanium spectrometer at Modane underground laboratory (LSM).

Components	Total mass (kg)	Counting rate (mHz)	Counting rate (%)
3-inch PMTs	2600	50	37
HV divider	150	45.8	29
Potting	5050	21.5	13
UWB components	7420	33.5	21
Total		150.8	100

Table 3.3: Contribution from each sub-part of the SPMT system to the SPMT counting rate in the fiducial volume (R $<$ 17.2 m) and with E $>$ 0.7 MeV.

This rate is negligible compared to the full counting rate from all the JUNO materials expected to be within 10 Hz in JUNO [128].

3.9 Conclusion

The SPMT system of the JUNO experiment is a complex system, with no sub-systems of its own despite the numerous varied components making it up, from the SPMTs themselves to the UWB containing all the electronics required for data acquisition and transfer. All components of the SPMT system were described in this chapter, with a focus on the electronics, in particular the ABC board and the CATIROC ASICs. The following chapter will capitalize on the knowledge of the inner workings of the CATIROC ASICs to present studies conducted on the fine responses of the ABC front-end board.

Chapter 4

Fine responses of the front-end ABC board

Contents

4.1 Introduction **105**
4.2 Data-taking tools **106**
4.2.1 Versions of ABC board 106
4.2.2 Firmware and data-taking software 106
4.2.3 Trigger modes and user parameters 109
4.3 Standalone performances of the ABC board **110**
4.3.1 Pedestals 110
4.3.2 Charge linearity and charge calibration 111
4.3.3 Time resolution 115
4.3.4 Crosstalk 117
4.3.5 S-curves 121
4.3.5.1 50% trigger efficiency threshold identification 122
4.3.5.2 Trigger threshold linearity 123
4.4 Combined tests **123**
4.4.1 V0 test benches 124
4.4.1.1 Description of the V0 test benches 124
4.4.1.2 32 PMT performances at LP2i 125
4.4.1.3 SPMT mass testing at GXU 128
4.4.2 16-channels NTU test bench for fine measurements 131
4.4.3 128 PMT performances at LP2i 131
4.4.3.1 Experimental setup 132
4.4.3.2 Measurements and PMT performances 133
4.5 PMT signal and processing **137**
4.5.1 PE collection and PMT waveform 137
4.5.2 LED test bench for PMT waveform behavior 141
4.5.3 Trigger time and time walk 146
4.5.4 Processing consecutive PMT signals with CATIROC 149
4.5.4.1 CATIROC dead times 149
4.5.4.2 Charge acceptance 151
4.6 Conclusion **152**

4.1 Introduction

Following the technical description of the SPMT system presented in the previous chapter, including the electronics, this chapter will detail the tests conducted on different versions of the ABC

board for precise measurements of its performances.
Section 4.2 will introduce the several versions of the ABC board used for the performance studies, present the firmware and software used for data-taking, as well as list the different possible configurations for the CATIROC ASICs in order to investigate specific features. Standalone performances of the ABC board will then be presented and discussed in section 4.3, including pedestal measurements, charge linearity, time resolution and crosstalk. Section 4.4 will address the development and commissioning of combined test benches at LP2i Bordeaux (LP2i) (sections 4.4.1.2 and 4.4.3) and in GXU for the mass testing of the SPMTs (section 4.4.1.3). Finally, a description of the processing of a PMT signal by the SPMT electronics will be given in section 4.5, with a focus on PMT waveform behavior and trigger time behavior in section 4.5.2 and section 4.5.3 respectively.

4.2 Data-taking tools

4.2.1 Versions of ABC board

While the current and final design of the ABC board is detailed in section 3.5, several steps and adjustments were needed to obtain this version. The ABC V0 boards were the first 3 boards manufactured and used in early tests in 2018-2019, in order to validate the schematics and the response of the SPMT electronics, and to identify potential issues to correct and optimize in subsequent versions of the board. The V0 version, shown in Figure 4.1a, has a mostly identical layout to the V1.2 version, shown in Figure 4.1b and described in section 3.5. Depending on the version of the ABC board used for performance studies, the results presented in the following sections can thus be representative of an earlier state in the development of the electronic system than the current Final Design Review (FDR)- and Production Readiness Review (PRR)-passed status and produced boards, and were instrumental in its optimization.

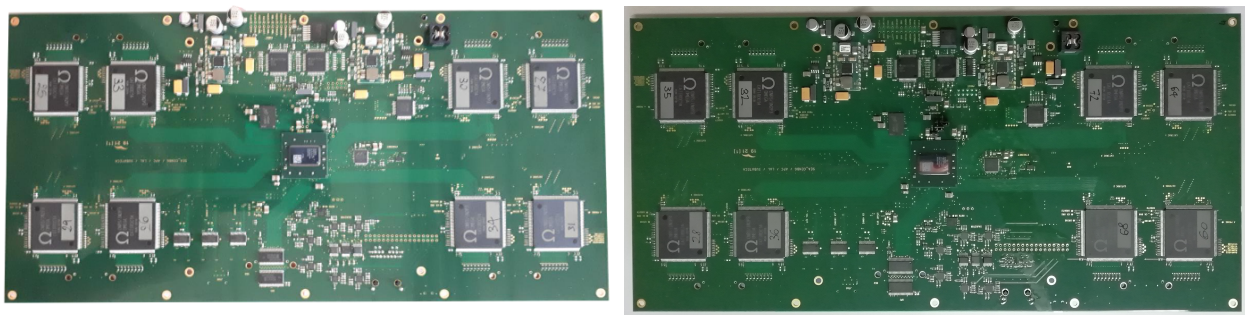

(a) (b)

Figure 4.1: (a) ABC board V0. (b) ABC board V1.2.

4.2.2 Firmware and data-taking software

As detailed in section 3.5.2, the digital part of the CATIROC chip, responsible for the data generation and transmission, is divided in two blocks, with one block for 8 channels. For each block, the data is transmitted within one strobe which contains two frames, each frame transmitting different information. As such, for each event, the firmware controlling the FPGA, which samples the data and organizes it, has to handle 16 independent blocks with variable arrival times. Contrarily to the firmware envisioned for the final state of the JUNO experiment, which will transmit data by sending it to the GCU, the firmware used in the production tests of the ABC board was developed to transfer data using the USB mode, to avoid needing the GCU in the measurement of the ABC

board's performances. A schematic view of the data capture by the FPGA in the USB mode is shown in Figure 4.2, in which the CATIROC trigger outputs are used to define an event window and construct an event header and in which the data stream (charge and time) is deserialized into 128 72-bits registers and feeds the USB readout after going through an event builder module. A secondary chain in the firmware identifies the edges of the trigger signals to count the number of triggers and construct S-curves (section 4.3.5).

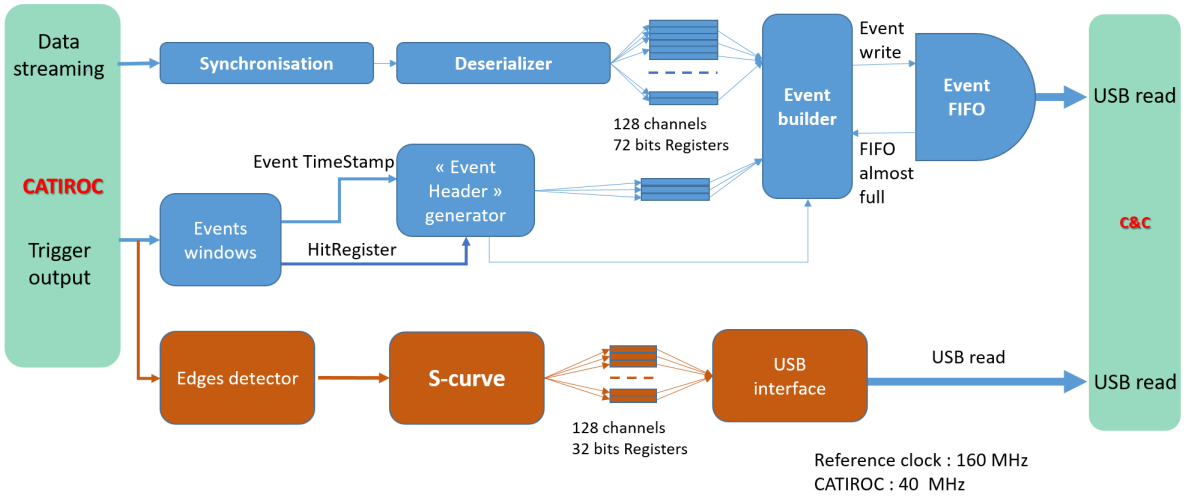

Figure 4.2: Test firmware architecture in USB mode.

The synchronization from the CATIROC data streaming is the core of the test firmware currently used. It forces the synchronization of the data readout of 8 channels in order to ensure their quality and integrity, the schematics of which are shown in Figure 4.3. During the CATIROC data streaming, the CATIROC trigger signals are monitored by the FPGA. For each block of 8 channels, as soon as a trigger signal is identified, a logical OR opens a square signal, the falling edge of which marks the opening of a frame strobe. As the two data frames are collected for this block of 8 channels, the end of the second frame marks the end of the frame strobe. For each CATIROC, two frame strobes will thus be collected, and as all 16 frame strobes are collected for the entire ABC board (8 ASICs, 2 frame strobes per ASIC), a signal indicating the end of the event is generated after the last frame strobe has ended.
Information about the recorded channels for each event is used to create an under-optimized 27-Bytes header to the event, containing the time stamp, the number of recorded channels, the nature of the hit (ping, pong, or deadtime), as well as a hit register detailing precisely which of the 128 channels have been triggered. This header is then sent to the Event Builder block in Figure 4.2. In parallel to the creation of this event header, and with the synchronization detailed in Figure 4.3, the data sent in strobes from the CATIROC ASICs is read and sent to 128 separate registers. The register number corresponding to the channel is identified with the internal knowledge of which CATIROC sent the data strobe combined with the channel number (from 0 to 7) contained in the second frame. Before the data is sent to the channel register, it is first formatted to fit a new data model :

- The gain (second frame, 1 bit) and the channel number (first frame, 3 bits) are used to code a new information about the channel number over 8 bits (1 Byte), with the gain information used as the most significant bit. In the new data format, the channels are numbered from 0 to 127 for high gain charge measurements, and from 128 to 255 for low gain charge measurements.

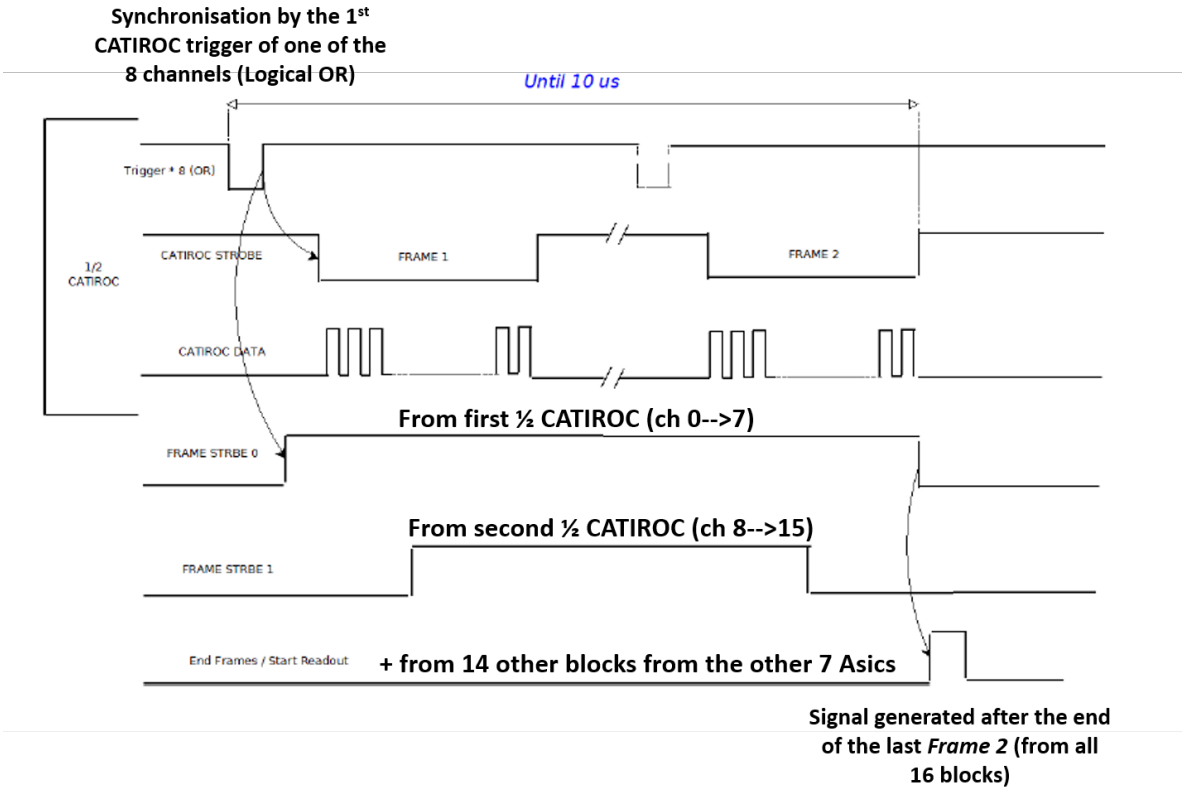

Figure 4.3: Data capture in USB mode in the ABC board. The first half of the diagram corresponds to one half-CATIROC (one of the 16 blocks), while the bottom half shows the frame strobes from both halves of the CATIROC and the last line in the diagram shows the signal generated once information from all 16 blocks has been collected.

- The coarse time (first frame, 26 bits, resolution of 25 ns due to the 40 MHz clock, overflowing at 1.67 s) is coded over 32 bits (4 Bytes), with the 6 most significant bits with a value of 0.
- The charge (second frame, 10 bits) is coded over 16 bits (2 Bytes), with the 6 most significant bits with a value of 0.
- The fine time (second frame, 10 bits) is coded over 16 bits (2 Bytes), with the 6 most significant bits with a value of 0.

The data in the new data format takes up 9 Bytes of information for each channel. Once the channel registers are filled with the formatted data, they are emptied in the Event Builder block, which feeds the USB readout. They are sent following the event header. As such, the maximum size of an event is 1179 Bytes ($27 + 128 \times 9$). The test firmware operates with a first-in, first-out system (FIFO) which empties continuously but can become saturated if the rate of data writing on the FIFO is superior to the rate at which it empties via the USB mode. This test firmware, used in the following performances studies, is not optimized with respect to the size of an event, with a 27-Byte header and 9 Bytes of information per triggered channel, or with respect to the dead-time induced by the processing of this event, as the data transfer only occurs once the signals from the 16 CATIROC blocks have been acquired and an event trigger has been determined. Figure 4.4 shows the schematics of the data format, assuming all 128 channels are triggered. For pedestal measurements, all 128 channels will indeed be triggered, while for signal injections performed for test measurements, only the injected channels will be triggered (N « 128).

The FPGA, the data acquisition and the data visualisation are controlled by DAVIS (Data Ac-

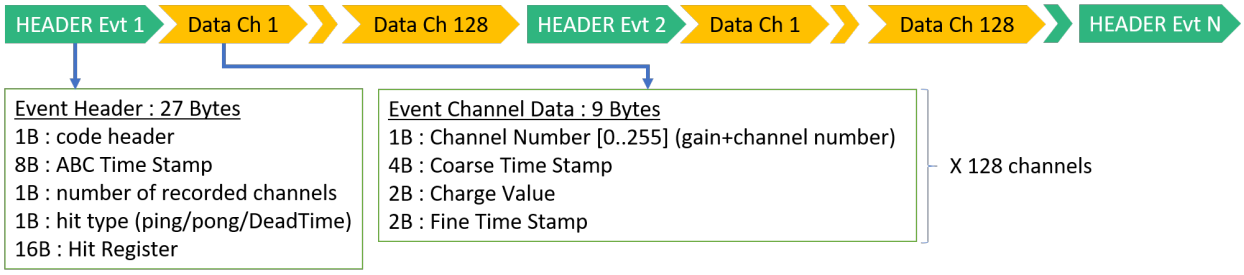

Figure 4.4: Event data format, with a 27-Byte header and 9 Bytes of information per triggered channel, leading to a maximum event size of 1179 Bytes.

quisition Verification Integration System), a software framework designed to pilot heterogeneous systems by piloting each instrument individually and allowing for an inter-instrument communication. With a clean coding structure allowing for the conservation of test scenarios in a reference space and for developments to happen in a work space, DAVIS can insure a complete separation of the back-end, front-end, and data treatment aspects of the data-taking. It will notably enable the control and configuration of a pulse generator for automatic signal injections with varying charges or amplitudes.

4.2.3 Trigger modes and user parameters

Section 4.2.2 described how CATIROC triggers are synchronized and how CATIROC data is processed by the FPGA before transmission via USB mode. However, several different trigger modes can be used to generate this data, depending on the ABC board performances investigated. The natural behaviour of the CATIROC ASICs involves an internal trigger, described extensively in section 3.5.1, which can also be referred to as the physics trigger mode. This trigger generation depends on the comparison of the voltage of the fast shaper waveform to a threshold value called the trigger threshold (10-bit DAC value) by a discriminator. Instead of using this internal trigger, the readout of every channel regardless of their measured signal can be also be forced by the FPGA, resulting in a force trigger mode which can be referred to as the pedestal trigger mode. An external trigger can be used as well, by using a trigger signal generated by a Pulse Generator and then distributed to every channel of the ABC board to force their readout. This external trigger mode is particularly useful when performing crosstalk measurements.
Once the trigger mode has been chosen by the user to investigate a given ABC board performance, the CATIROC ASICs can be configured with several key parameter values for a data acquisition in a precise configuration. Such parameters usually include :

- The preamplifier gain, which can be adjusted for each channel and can take discrete values between 5 and 640. The two main configurations typically used in the following measurements are 20 and 40, and this parameter is usually modified to observe the SPE spectrum.
- The gain mode, which can be set to forced high gain, forced low gain or to an automatic switching between the two modes. The high gain mode amplifies the signal by 10 times compared to the low gain mode, and the automatic gain mode will always be used in the following measurements.
- The charge threshold, which impacts the charge value at which the automatic choice between high gain and low gain is performed (see section 3.5.1).
- The trigger threshold, defined in section 3.5.1, which impacts the amplitude at which a signal will generate a CATIROC trigger signal. This parameter is typically modified to cut off parts or the entirety of the pedestal signal.

- The CATIROC internal delay before the charge measurement on the slow shaper (see section 3.5.1). By default, this parameter is optimized for a maximal charge measurement, usually around 30 ns.

4.3 Standalone performances of the ABC board

4.3.1 Pedestals

The first tests performed on the ABC V0 mostly consisted in pedestal measurements in the force trigger mode, which were studied with a 2D representation of the charge measurements in each ABC channel. After a few hardware modifications, all three ABC V0 boards were measured, with the following figures focusing on the pedestal measurements of the ABC V0 board located at LP2i (the other two being shared at that time with the Subatech and APC laboratories). Figure 4.5a shows the pedestal distribution in each channel, while Figure 4.5b shows the histogram of the pedestal RMS values.

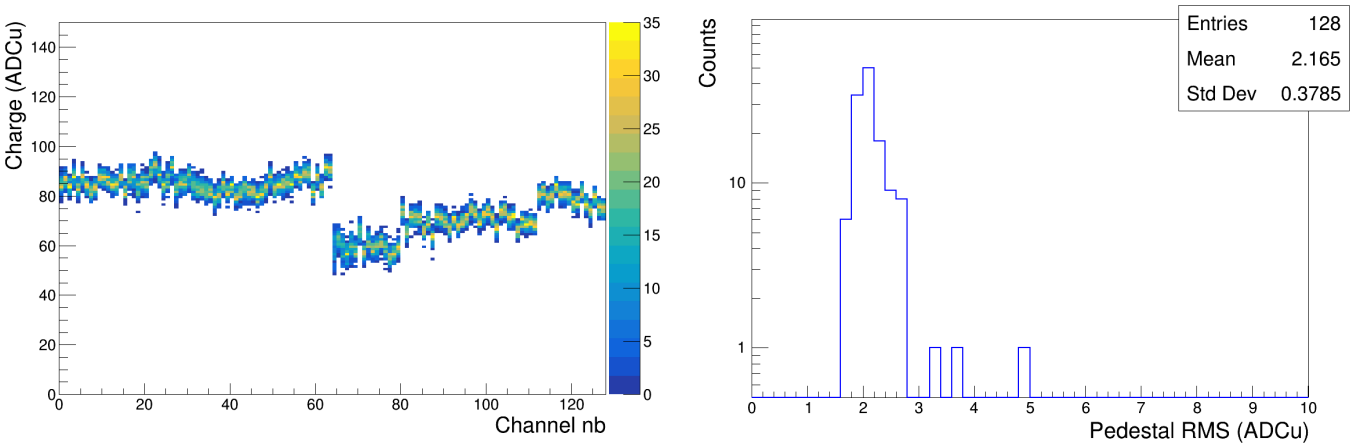

(a) (b)

Figure 4.5: (a) Pedestal distributions for one of the three ABC V0 boards. (b) Pedestal RMS for the 128 channels.

Considering a mean value of pedestal RMS of ∼2.2 ADCu, this corresponds to a charge of 0.024 pC at a preamplifier gain of 20 and a corresponding ADCu to pC slope of ∼90 ADCu/pC (Figure 4.8). This represents a 0.05 photoelectron (PE) equivalent pedestal width. In comparison, PMTs have a SPE charge resolution of ∼33%, meaning a width of ∼0.33 PE for a single PE measurement. Taking the total width of the charge measurement to be $\sigma_Q^2 = \sigma_{PMT}^2 + \sigma_{Elec}^2$, this would give $\sigma_Q \approx 0.334$ PE and would imply a lower than 2% contribution of the pedestal width on the charge measurement uncertainty.

Another method of measuring the pedestal mean values in each channel of the ABC V0 board is to perform charge linearity measurements and taking the intercept parameter of the linear fit. A precise study of the charge linearity of the board will be shown in section 4.3.2, but comparing the reference pedestal values of the bare CATIROC ASICs before they were mounted on the ABC board (obtained with charge linearity measurements performed at the OMEGA laboratory with a test board equipped with a single ASIC) to the pedestal values obtained with the intercept of the linearity fit on the much more complex ABC V0 board is an efficient method to ensure that the board itself is not introducing additional noise or perturbations to the charge measurements. Figure 4.6 shows, in the top half, the pedestal values of each channel of the ABC V0 board in

red and the reference pedestal values for the channels of the CATIROC ASICs mounted on the board in blue. In the bottom half, the differences between the two values in each channel are represented. With a mean charge value of 6.8 ADCu added to the baseline by the ABC V0 board, meaning ∼10% of the original value (equivalent to 0.2 pC), the ABC V0 board introduces an offset to the charge measurement, that will be calibrated, but barely impacts the RMS of these pedestal distributions.

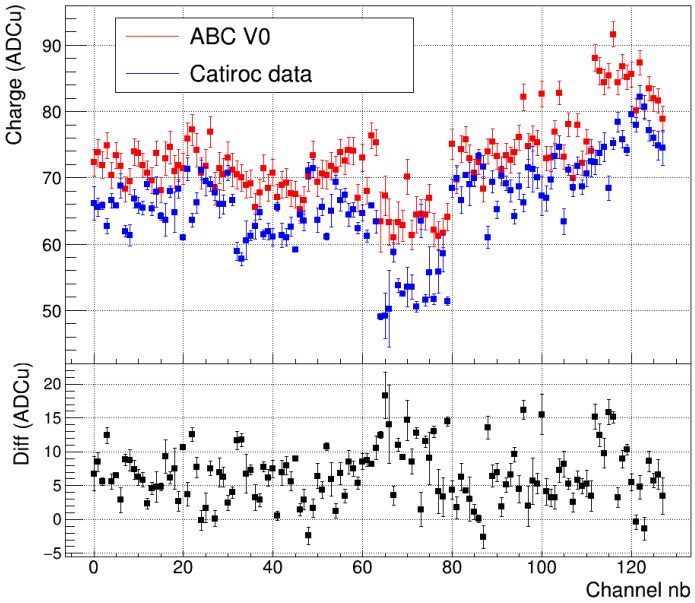

Figure 4.6: Pedestal comparison between measurements on the ABC V0 board and the data from the ASICs hosted on the board as measured during production at the OMEGA laboratory. The difference between the two values is shown in the bottom half.

The pedestal distributions were slightly impacted by the transition from the ABC V0 board to the ABC V1.2 board. Figure 4.7 shows the 1D distributions of the RMS values of the pedestal distributions for all channels of the 3 ABC V0 boards and the 5 ABC V1.2 boards, rescaled to the same number of entries for comparison. Despite a very slight increase in the RMS mean value, from ∼2.2 to ∼2.3 ADCu for the ABC V0 boards and ABC V1.2 boards respectively, the spread of the RMS values is greatly decreased in the case of the ABC V1.2 boards, from 0.36 to 0.2 ADCu, implying a better uniformity in the channels of the board in its latest version.

4.3.2 Charge linearity and charge calibration

As detailed in Section 3.5.1, the CATIROC ASIC processes signals for the charge measurement through parallel slow shapers, each with a different gain (High Gain, Low Gain, with a factor 10 amplification difference), and then selects the charge output based on a discriminator configured with a DACu value called the charge threshold. When verifying the charge linearity in a channel, two ranges are expected, one before the transition from High Gain to Low Gain and the other right after to increase the dynamic range of the readout system. Figure 4.8 shows, in its top half, the charge linearity in an arbitrary channel of the ABC V0 board, with 30 charge injections ranging from ∼1 pC to ∼70 pC and a preamplifier gain value of 20. For a DACu charge threshold value of 820, the switch to the Low Gain mode was around charges of 8.8 pC. In the bottom half of Figure 4.8 are shown the relative differences between data points and the linear model, with the High Gain range of the model showing deviations from the data points below 0.05%. Larger

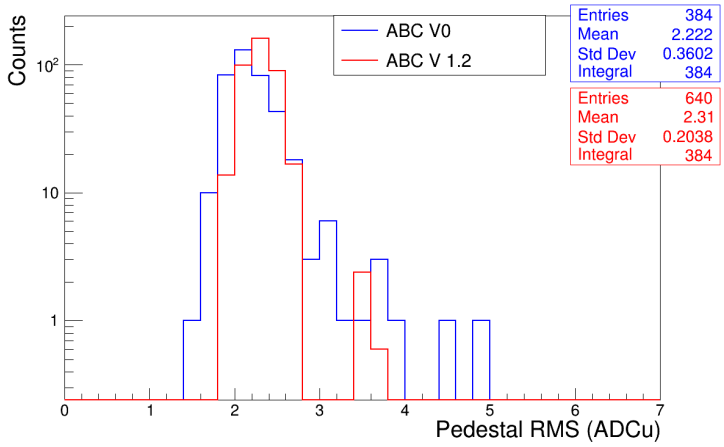

Figure 4.7: Distribution of the RMS values of the pedestal distributions for all channels of the 3 ABC V0 boards and the 5 ABC V1.2 boards, rescaled to the same number of entries for comparison.

deviations, up to 2.5%, are observed in the Low Gain range of the linear model, oscillating around 0 and thus showing no intrinsic bias. The charge linearity test in an arbitrary channel was very satisfactory. At a preamplifier gain of 20, up to 70 pC charges can be measured by CATIROC, corresponding to 140 measured PEs at a PMT gain value of 3×10^6, which will cover a wide range of physical events.

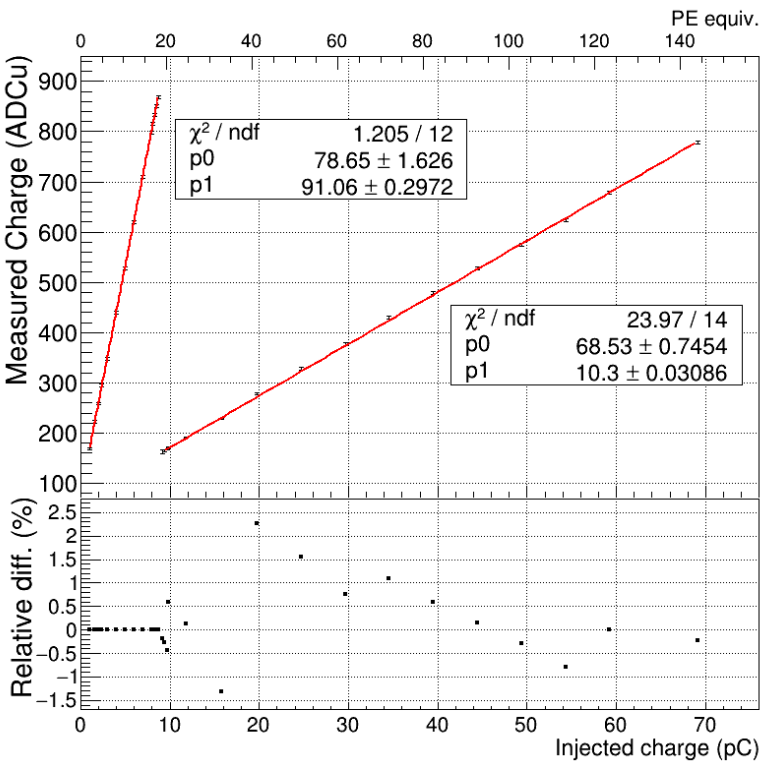

Figure 4.8: Charge linearity test in channel 103, on Ping events. High Gain fit on the left, Low Gain fit on the right. The PE equivalent of the injected charges, assuming a PMT gain of 3×10^6, is shown on the top axis. The bottom half shows the relative differences between the data points and the linear model.

The development at LP2i of two test-benches equipped with ABC V0 boards, in order to send them to Guangxi University (GXU) for the mass-testing of the SPMT production (see section 4.4.1.3) and to demonstrate the combined performances of the SPMT electronics, was an important milestone. Both of these boards were thus calibrated in charge, in order to estimate the gain of the tested PMTs for a given High Voltage. As the relation between the ADCu measurement of the SPE peak given by the CATIROC ASICs and its equivalent charge in pC needs to be known for each channel, all channels of both boards were manually calibrated for multiple preamplifier gain values. This charge calibration was performed using pulse generator signal injections in each channel, with varying amplitudes and known charge equivalents.
The signal delivered by the pulse generator was a trapezoidal signal with 5 ns for the rise time and fall time and 10 ns for the width, with an attenuation factor of 19.9 in output of the generator. In order to precisely know the value of the injected charge, indispensable for the charge calibration of the ABC boards, the injected signals were first collected by a commercial module called WaveCatcher developed at LAL [129], with the objective of obtaining an amplitude-to-charge correspondence for the generator signals. The WaveCatcher module acts as an oscilloscope, and measures the charge of the injected signal. The relation between charge and amplitude for the injected signal was measured to be $Q(pC) = C \times A(mV)$, with $C = (8.83 \pm 0.02) \times 10^{-3}$ pC/mV. With a precisely controlled injected signal, each channel of both ABC V0 boards was calibrated for multiple preamplifier gain values, as illustrated in Figure 4.9a, which shows the measured charge in ADCu as a function of the injected charge in pC for an arbitrary channel of the test benches. For each gain value, charges scanning the High Gain range and the Low Gain range were injected, with a focus on the High Gain range characterization, more relevant for the PMT mass testing and the SPE peak measurements. For each charge, many signals are injected and a histogram is filled by subtracting the pedestal reference value in this channel to each charge measured in ADCu. This distribution is fitted with a Gaussian model, and the position of the peak is taken as the mean charge value in ADCu.

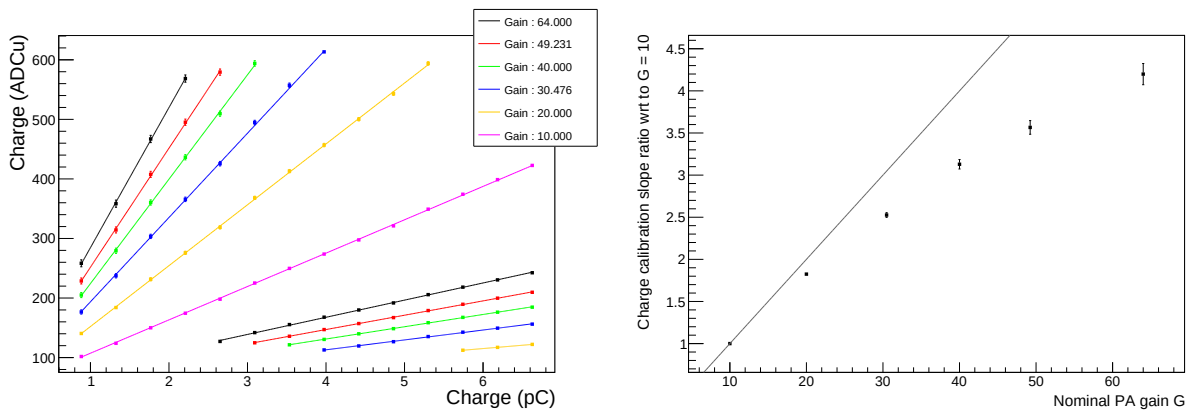

(a) (b)

Figure 4.9: (a) Calibration of the charge response of an arbitrary channel for multiple preamplifier gain values. Each ADCu/pC graph is fitted using a linear model. (b) High Gain slope ratio of gain G vs nominal gain $G = 10$. The expected $y = \frac{x}{10}$ line is shown as the grey solid line, showing the deviation from linearity due to the gain saturation.

Calibrating the ABC V0 boards for multiple preamplifier gain values highlighted a saturation in the preamplifier gain, as the ratio of the slope parameters of the calibrations for different gains tends to decrease as the gain increases, indicating a loss of amplification. This is illustrated in Figure 4.9b, in which the ratio between the slope parameter of the High Gain calibration at a

gain value G and the slope parameter of the High Gain calibration at the reference gain $G = 10$ is plotted as a function of the gain G. A saturation effect is clearly visible, with increases in gain values failing to match the expected amplification ratio. This phenomenon is a known feature of the CATIROC ASIC, and has been precisely measured [126], as shown in Figure 4.10 in which the ratio between the measured charge at a gain value G and the charge measured at the reference gain $G = 10$ for the same signal injection is plotted as a function of the gain G. Even if the preamplifier gain can extend up to 640, only the interval up to 80 looks exploitable with small saturation effects, which is sufficient for typical applications where the PMTs can be grouped to have similar gains at the nominal high voltage value and thus an adjustment of the individual gain values over a large range is not necessary. The maximum variations observed among three tested CATIROCs (gray band) and within the 16 channels of a same CATIROC (red) are also shown. In practice, the effect of this variation is negligible, as the preamplifier can be fully characterized for each ASIC separately during the production test phase of the chips or of the readout boards.

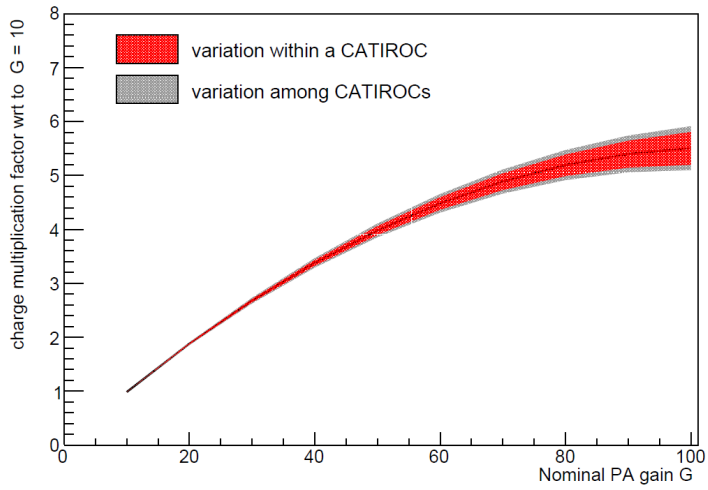

Figure 4.10: Charge multiplication factor (effective gain) vs preamplifer (PA) nominal gain G. The average gain linearity is shown as dark solid line with a gray band indicating the maximum variation between different CATIROCs and a red shaded band indicating the variation within channels of the same CATIROC. [126]

Fitting each ADCu/pC graph with a linear model, as shown in Figure 4.9a, gives a slope parameter and an intercept parameter, for both ping and pong channels and for the HG and LG modes. Having subtracted the pedestal reference values from each charge measurement, the intercept parameter is expected to be 0 for each channel. Figure 4.11a shows the distribution of the intercept parameters for all 128 channels of the first calibrated ABC V0 board (embedded in the first test bench referred to as test bench A), for a preamplifier gain of 40 and Ping and Pong events. Despite the large error bars on the measurements (small deviations on the slope parameter impact the intercept parameter on a larger scale) making every intercept value compatible with the expected 0, it appears that the intercept values are distributed within ± 8 ADCu of the expectation. Figure 4.11b shows the 1D distribution of the intercept parameters for the 128 channels, and confirms a range of about ± 8 ADCu for the intercepts with mean values close to ~ 2 ADCu, indicating a small bias in the fit.

In order to estimate if these intercept values are significantly large, the difference in the slope parameter when the intercept is taken to be 0 or is left free can be calculated, as well as the the impact of this slope difference on the measurements of PMT properties. The values of the slope parameter in each channel (gain 40) when the intercept parameter was fixed and left free are shown

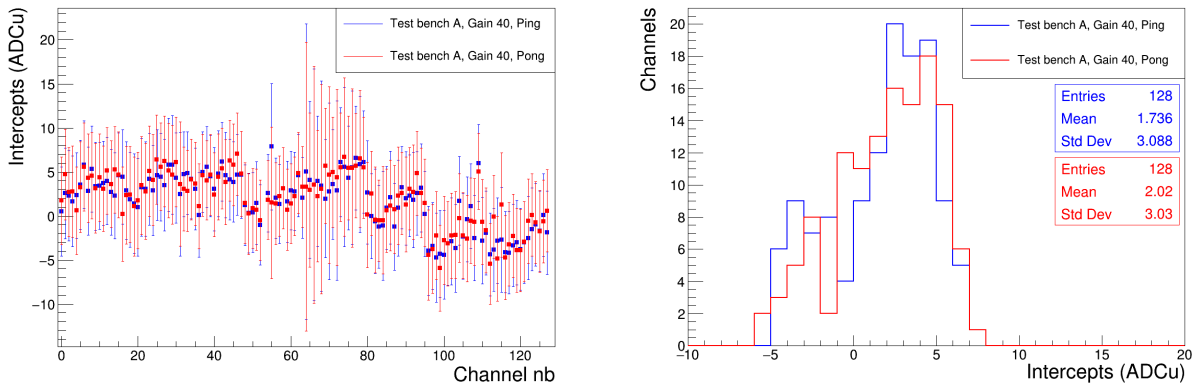

(a) (b)

Figure 4.11: (a) Intercept parameters for each channel obtained with the charge calibration of the PMT test benches. The reference pedestal values in each channel were subtracted from the charge measurements, and the intercept values are expected to 0. (b) 1D distribution of the intercept values.

in Figure 4.12. In the bottom half of each figure, the relative difference between the two cases is shown. In the worst case scenario, fixing the intercept parameter to 0 when fitting results in a ∼2% relative difference on the slope parameter. The relative difference between the values of the slope parameter depending on the fitting method can be directly correlated to the relative difference between PMT gain measurements depending on whether the calibration intercept parameter was fixed to 0 or left free, as the relation between slope parameter and PMT gain measurement is linear. Having demonstrated that there was no significant impact of fixing the intercept parameter to 0 or leaving it free, it will be fixed to 0 for PMT performance studies.

4.3.3 Time resolution

The time resolution of simultaneous events in different channels of the ABC board is a crucial parameter to investigate in order to quantify the contribution of the ABC board to the total time resolution of the measurements when compared with the TTS of the PMTs. This test was performed by injecting charges simultaneously in two different channels of the ABC V1.2 board, by splitting the signal from a pulse Generator, in order to study the time differences between two correlated events in both channels. The measurements were performed in the internal trigger mode. Equation 4.1 shows how the absolute time is computed using the Coarse Time (CT) and Fine Time (FT) information, with FT_{min} being the minimum value of the FT ramp and the FT range FT_{range} being channel dependent (see section 3.5.1).

$$T_{absolute} = CT \times 25\ ns - \frac{(FT - FT_{min}) \times 25\ ns}{FT_{range}} \tag{4.1}$$

As previously detailed, the CT is coded over 26 bits, and can thus take values ranging from 0 to $2^{26} - 1$, each unit of CT representing 25 ns because of the 40 MHz clock. The FT is coded over 10 bits, but does not necessarily take values over the whole [0,1023] range in each channel. The response is channel dependent, and the range of the FT values in each channel has to be considered and calibrated for a proper input in the absolute time computation. Signal injections in every channel to scan and identify the whole FT range were automatized.

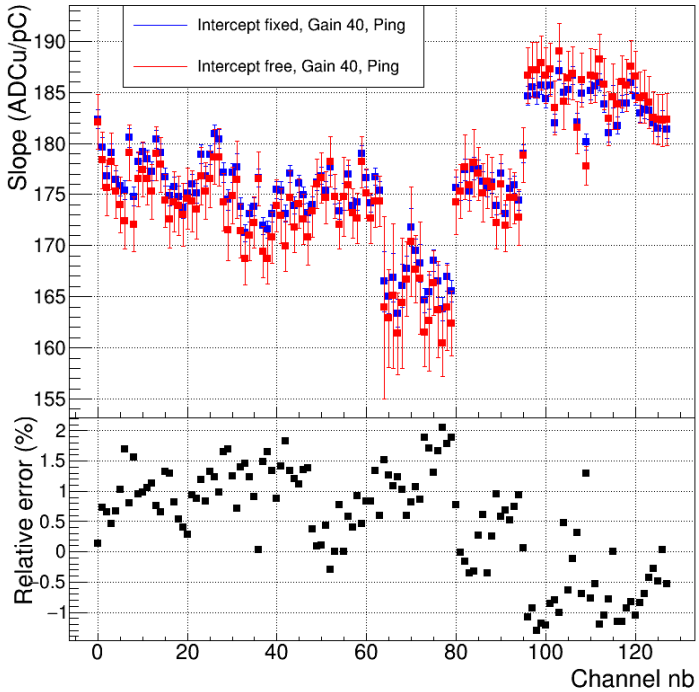

Figure 4.12: Impact of fixing or leaving the intercept parameter free on the slope parameter of the charge calibration of the PMT test benches. The bottom plot shows the relative difference between the 2 cases. With differences only up to ∼2%, the impact is negligible.

Figure 4.13 shows the time differences Δt between events in a reference channel (ASIC 5, channel 80) of the ABC V1.2 board and correlated events in other channels of the board, in order to investigate the time response in different locations. Δt is defined as :

$$\Delta t = t_{ref} - t_i \tag{4.2}$$

with i the channel number going from 0 to 127 excluding $i = ref$. One channel in each ASIC was investigated with regards to the reference channel, with the channel chosen for ASIC 5 being different from the reference channel, and RMS values ranging from ∼0.20 to ∼0.25 ns are observed. Constant Δt values will be calibrated in the final state of the experiment using a LED in the central detector. As such, the RMS of the Δt distributions are far more valuable to measure. The distribution of these RMS values for the 127 investigated channels is shown in Figure 4.14, with a mean value of ∼0.23 ns. Compared to the standalone CATIROC time resolution of 150 ps, the ABC board introduces additional time fluctuations and worsens the time resolution to 230 ps.
Considering a mean value of Δt RMS of ∼0.23 ns, the contribution of the time resolution of the ABC board to the total time resolution of the JUNO SPMT electronics is negligible before the TTS of the PMTs, with a mean value of 1.56 ns. Taking the total time resolution to be $\sigma_t^2 = \sigma_{TTS}^2 + \sigma_{\Delta t}^2$, this would give $\sigma_t \approx \sigma_{TTS} \approx 1.58$ ns, meaning a contribution of the ABC board to the total time resolution of ∼1.2% of the TTS contribution. Moreover, a 0.23 ns Δt RMS for two channels in the ABC board is negligible for the physics prospects of the JUNO experiment, notably for vertex reconstructions. As light travels 20 cm in 1 ns in the liquid scintillator, a 0.23 ns uncertainty in the time measurement would only imply a lower than 5 cm bias on the vertex position, which is very much below the scope of the current vertex reconstruction methods for the SPMT system.

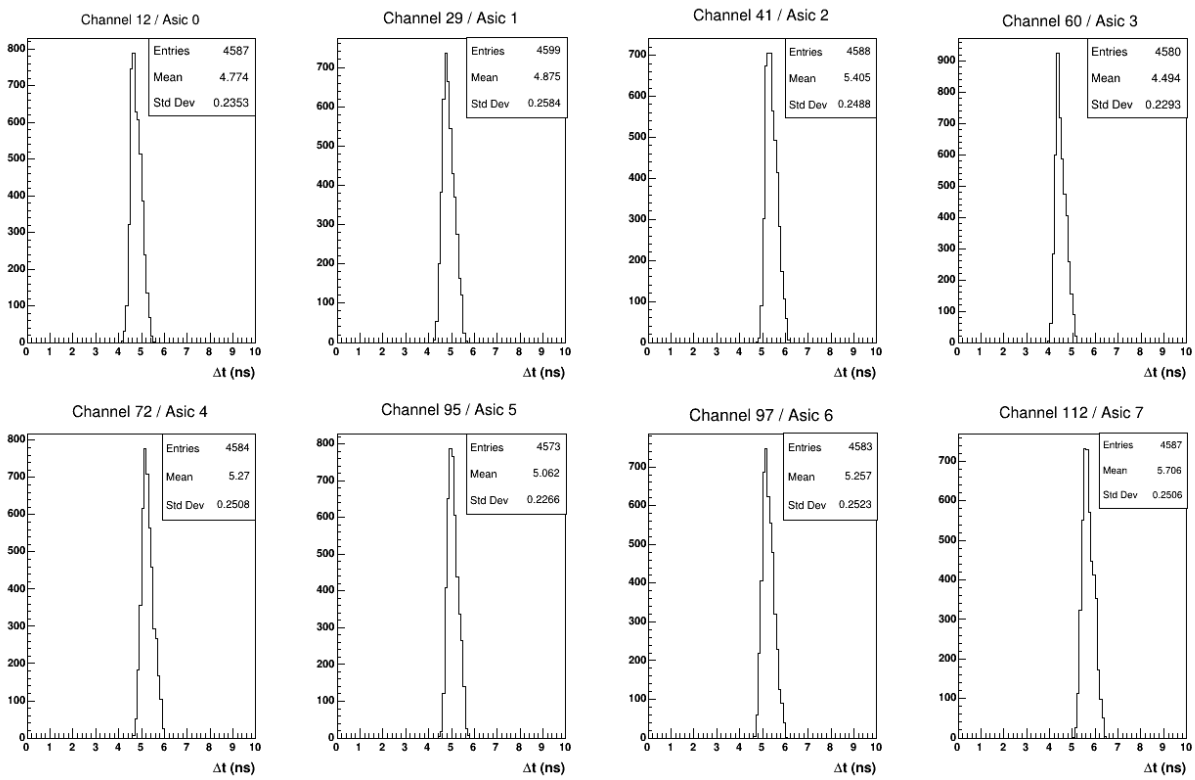

Figure 4.13: Example of time differences for correlated events after signal injections in a reference channel in ASIC 5 and several other channels over the ABC V1.2 board. The Δt distributions are illustrated for all ASICs. For ASIC 5, the investigated channel is different from the reference channel.

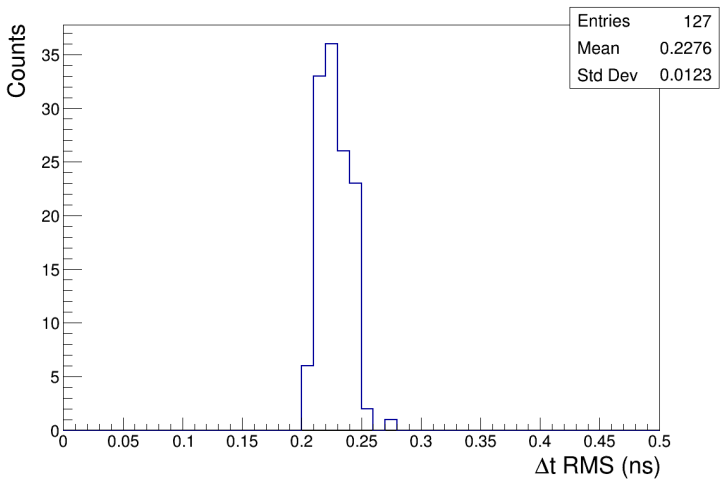

Figure 4.14: RMS distribution of Δt values for all channels of the ABC V1.2 board with respect to a reference channel.

4.3.4 Crosstalk

Determining the amount of crosstalk present in the ABC board is another crucial performance of the board to evaluate. There are two types of crosstalk : the first from parasitic capacitors, and

the second from parasitic self-inductors. The difference is actually important for the identification of the investigation method to be used. Parasitic capacitors are natural capacitors, as opposed to electronic components. Figure 4.15a shows two conductive tracks, one of which is powered by a tension V_s, with insulation between them. This naturally acts as a capacitor which sends an image of the source signal to the second track, disturbing it. Self-inductors are created in adjacent circuits when a variation in tension occurs in one of the circuits. Figure 4.15b shows this phenomenon : following Maxwell's equations, a tension variation in a first circuit induces a variable magnetic field. As such, an electrical current, which is actually an image of the first signal, will be induced in any conductor in this magnetic field. And any current going through the cables of a circuit will induce a tension, thus disturbing the signal in the second circuit. In return, the tension variation in the second circuit will likewise disturb the first circuit.

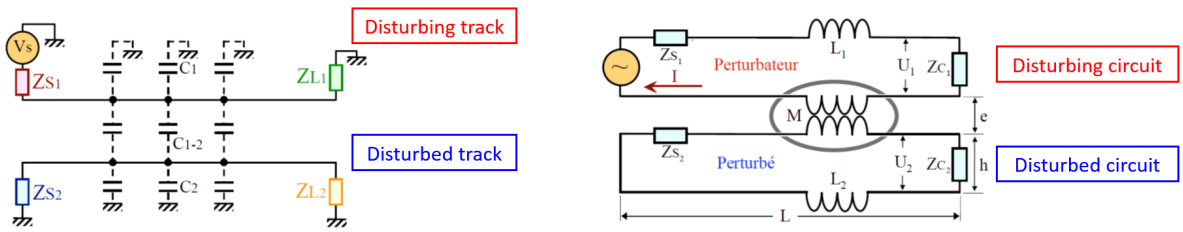

(a) (b)

Figure 4.15: (a) Crosstalk due to parasitic capacitors between two conductive tracks. (b) Crosstalk due to parasitic self-inductors in two electronic circuits.

These effects can be reduced by increasing the distance between each track and circuit (three times the width of the track is the distance typically used). This has been done in the ABC prototypes, and as such, the most important crosstalk contributions should come from the connectors, where the tracks get progressively closer. The crosstalk type investigated in this section is the case of charges in an injected channel having an effect on the baseline of other channels in the board. While some amount of crosstalk in an electronic board is to be expected, the objective of this study was to determine if that amount would be problematic for the physics prospects of the SPMT system.

As mentioned in section 4.2.3, the external trigger is a trigger signal generated by the Pulse Generator, that is distributed to each channel of the ABC V0 board and that forces the readout of every channel. It is usually used to measure baselines and pedestal values, but if handled properly in conjunction with the other functions of the board, it can be used to force a readout of every channel during a charge injection in a given channel. The aim of this study is to quantitatively measure the crosstalk and thus estimate the fraction of charge induced in the channels of the board when a charge is injected in one specific channel. In this configuration, the injected charge will be read via internal trigger, delivered by the ASIC, whereas the baselines of the other channels will be read via external trigger, induced by the Pulse Generator. The trigger signal from the Pulse Generator (external trigger) however has to be adapted through an additional level adaptor in output of the Pulse Generator. This adds a delay to the external trigger, which needs to be compensated. In order to compensate this delay and have correlated events between the different channels, the same delay has to be applied to the injected signal from the Pulse Generator. Since the external trigger is given directly by the Pulse Generator, regardless of the pulse itself, only the internal CATIROC trigger will be shifted in time, matching the external trigger. The right delay to apply to the Pulse Generator signal thus has to be precisely known, and one method to

identify it is to plot the charge measured in the injected channel as a function of the delay applied on the generator signal, corresponding to the slow shaper curve.
Figure 4.16 shows the results for a 4 mV injection (40 mV with 20 dB attenuator, equivalent to 0.79 pC) in one channel. The delay is marked as a negative value because we consider the pulse to arrive later than it should have. The charge maximum is obtained for a 70 ns delay.

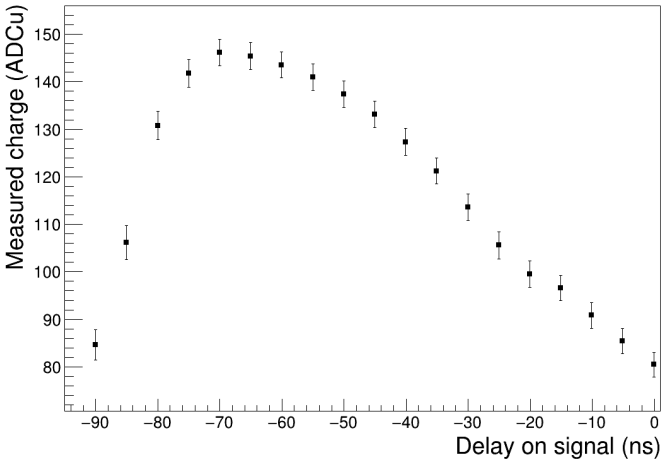

Figure 4.16: Measured charge as a function of the time delay on the pulse generator.

The measured charge using the internal trigger was measured to be 149.1 ± 2.7 ADCu and the measured charge using the external trigger and the 70 ns delay was measured to be 146.1 ± 2.8 ADCu, making the two measurements compatible. However, the injected channel will receive, almost at the same time, an internal trigger signal from the charge having exceeded the DAC trigger threshold, and a conflicting external trigger signal. One way to solve this issue is making sure that the external trigger arrives before the internal trigger, to ensure that all channels will be triggered by the same source, and increasing the width of the external trigger to include the internal trigger width as well.
In this study, for every channel of the ABC V0 board on the half equipped with SAMTEC connectors (64 channels), 3 gradually increasing charges are injected using a pulse generator. Each channel is investigated independently. For each injection (20 pC, 40 pC and 60 pC), the readout of the 128 channels is forced using the external trigger function of the board. The charge in the readout channel is then represented as a function of the charge in the injected channel, for all 3 charge injections, as shown in Figure 4.17a. The resulting graph is fitted with a first degree polynomial, since crosstalk, if observed, is expected to be linear. The slope parameter represents the induced charge proportion in the observed channel, while the intercept parameter corresponds to the pedestal value of the observed channel. In Figure 4.17a, the charges in the injected channel on the X-axis were processed in the Low Gain mode, while the charges in the observed channel on the Y-axis were processed in the High Gain mode. Due to the High Gain / Low Gain amplification ratio of 10, the slope parameter of the linear fit has to be corrected by a factor 1/10. Repeating this process for all 64 injected channels and their 127 readout channels (the injected channel itself is not investigated) yields a slope distribution, shown in Figure 4.17b.
The crosstalk induced in every channel during a charge injection in each of the 64 measured channels is shown in Figure 4.18.
To assess the reliability of the slope parameter values, one arbitrary injected channel out of the studied 64 is selected, and for each of its 127 readout channels, the intercept parameter of the first-degree polynomial fit is compared to the reference pedestal value in this channel. Figure 4.19

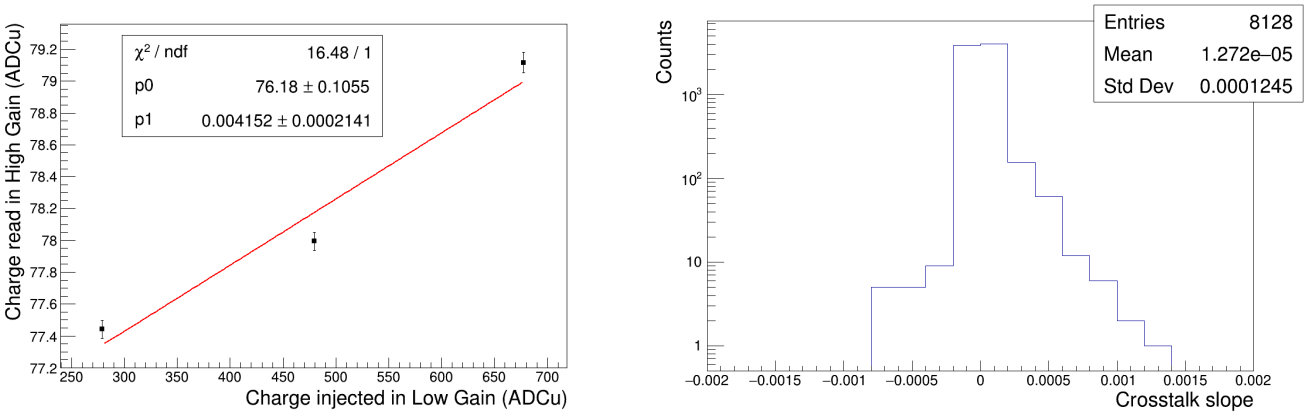

(a) (b)

Figure 4.17: (a) Mean charges in an arbitrary readout channel as a function of the mean charges in an arbitrary injected channel. The graph is then fitted and the slope parameter conserved. (b) Distribution of the slope parameter values for the 64×127 readout channels on the SAMTEC half of the ABC V0 front-end board (for each of the 64 injected channels, all channels are readout and analyzed except for the injected channel).

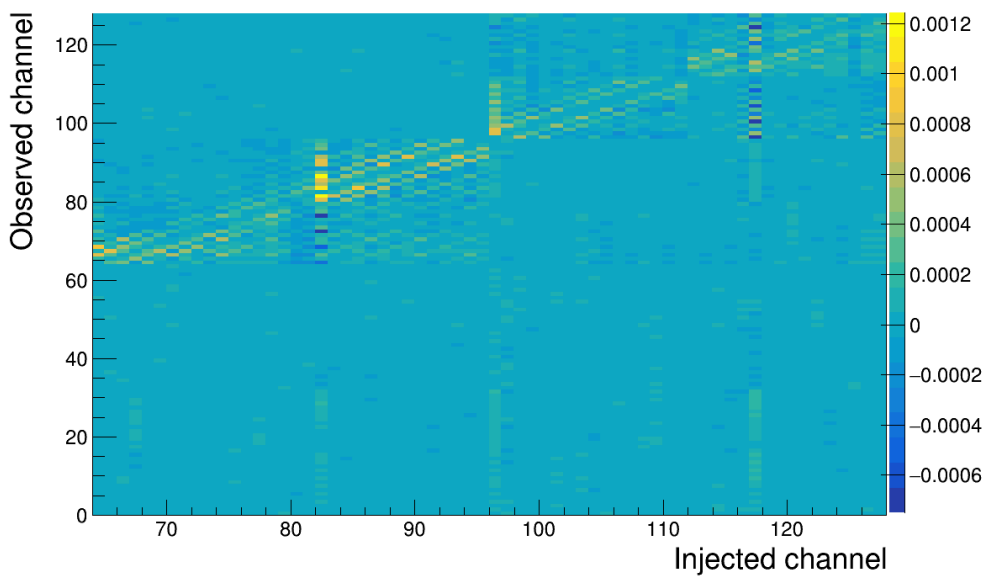

Figure 4.18: 2D distribution of the crosstalk slope parameters for channels 64 to 127 (SAMTEC connectors side). The channel in which the charge injection is performed is shown on the X-axis, while the observed channel is shown on the Y-axis.

shows the superimposition of the intercept parameters for each of the 128 channels when injecting in the reference channel (red) with the mean values per channel from a pedestal measurement made with the ABC V0 board (blue). As observed, the two graphs are perfectly compatible within their error bars, with the bottom half of Figure 4.19 showing relative differences between the two values in each channel up to a maximum of 3%, meaning that the linear fits applied in order to derive the slope parameter and quantify the crosstalk are precise and can be trusted. With this information, Figure 4.17b shows that while the crosstalk estimation can take negative values when dominated

by statistical pedestal fluctuations, the maximum absolute value of crosstalk does not exceed 1.5×10^{-3} in the SAMTEC half of the board. The SAMTEC connectors were then selected as the default connectors for the latest versions of the ABC board. Considering the worst case scenario for the physics studies, which is crosstalk inducing over 0.3 photoelectrons in adjacent channels to the one injected, the ABC board can thus accept up to ∼300 photoelectrons at once without risking going over that threshold. This should cover all physics cases, including most of the muon events.

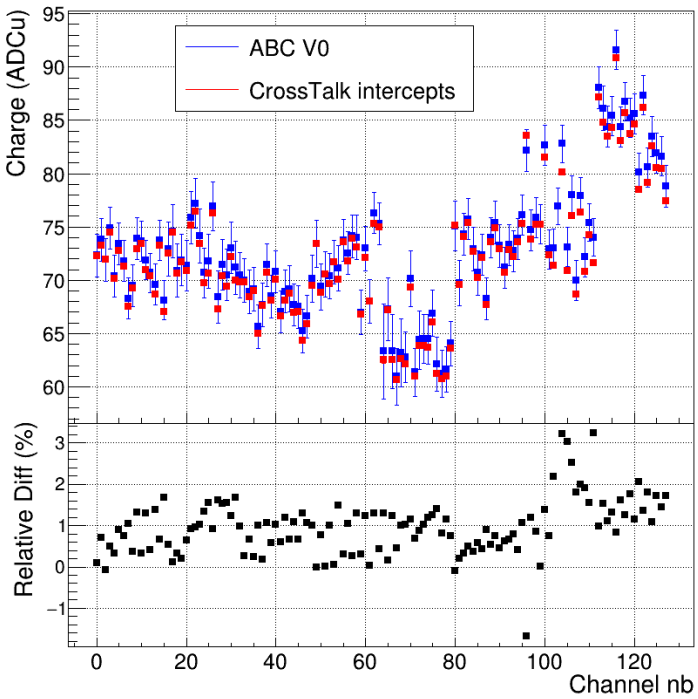

Figure 4.19: Superimposition of crosstalk fit intercept parameters with pedestal measurement on ABC V0 board. The relative difference between the two measurements is shown in the bottom half, with values within 3%.

4.3.5 S-curves

The previous sections have detailed the characterization of a number of fine performances of the ABC board, as well as the investigation of some of its characteristics. One of these characteristics is the absence of a trigger threshold for every channel of the board. One DAC threshold defines the trigger behaviour of the 16 channels of the ASIC, channels to which can be connected PMTs with different gains at nominal high voltage, and so with different positions of the SPE peak with respect to that threshold. A trigger threshold too high or too low (DAC values) can result in dark noise statistics polluting the physical events or in a loss of the SPE peak in the charge spectrum. In addition, the trigger threshold takes effect on the amplitude of the signal after the preamplifier and the fast shaper, and not on the charge equivalent of the signal. Due to amplitude fluctuations intrinsic to the nature of the signal, setting the trigger threshold for a specific charge value is challenging and susceptible to variations. A solid comprehension of the trigger mechanism is thus crucial in identifying the ideal trigger threshold to configure for each individual ASIC on the 200 ABC boards planned in the JUNO SPMT system. Rather, a compromise has to be reached for each ASIC between the value of the common configured trigger threshold and the value of the preamplifier gain for each channel. The first step in reaching this compromise is identifying

the trigger threshold DAC value required in every channel to ideally perform the discrimination between noise and SPE events. This is achieved by defining a charge value to act as a cutoff, and identifying a range of trigger threshold values which will cut a varying percentage of the slightly fluctuating signals with this given charge equivalent. In order to settle on a definitive threshold value (for a given charge equivalent in a given channel), the norm in electronics is to identifying the 50% trigger efficiency threshold.

4.3.5.1 50% trigger efficiency threshold identification

This is achieved by injecting a signal with a fixed amplitude (and so a fixed charge equivalent) with a pulse generator in the desired channel, ideally with a signal close to a 3" PMT waveform for the most realistic estimation, and by varying the DACu value of the trigger threshold and counting the number of CATIROC trigger signals in this channel in a fixed time window. This allows the identification of a threshold value beyond which the number of counted trigger signals remains constant, which corresponds to the maximum possible number of injected signals having triggered a CATIROC response and is considered the 100% trigger efficiency. The trigger efficiency for other threshold values is then defined as the ratio of the number of recorded trigger signals and the maximum number of expected trigger signals. Figure 4.20 shows the example of a signal injection at 1 kHz with an amplitude of 4.6 mV (2 PE equivalent). The trigger signals are counted over a time window of 420 ms, giving a maximum number of expected trigger signals in this time window of 420. The sudden increase in counted trigger signals as the threshold increases beyond ∼900 DACu indicates triggers on pedestal signals. Varying the DACu value of the threshold in the configuration of the ASIC results in a variation of the number of recorded trigger signals, and in the creation of a distribution shaped like an “S” and called an S-curve. This number of recorded trigger signals gradually decreases as the DACu value of the threshold increases, indicating a higher threshold. The norm in electronics is to single out the 50% trigger efficiency threshold value as being the reference value for this particular charge injection. In the example given in Figure 4.20, the 50% trigger efficiency is reached for a threshold value of around 400 DACu, for a charge injection equivalent to 2 PE. The value of the preamplifier gain greatly influences the value of the 50% trigger efficiency threshold value, as it impacts the amplification of the injected signal.

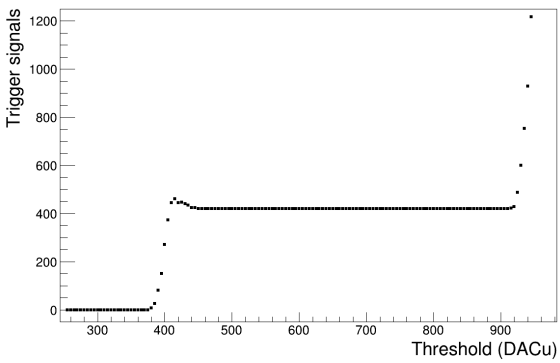

Figure 4.20: S-curve : number of trigger signals in a 420 ms time window for a 4.6 mV periodic (1 ms) signal injection as a function of the trigger threshold value. The trigger efficiency at any given threshold value is computed using the maximum number of counts, represented as the plateau. The steep rising on the right side of the plot is due to the lower threshold values no longer cutting off pedestal events.

4.3.5.2 Trigger threshold linearity

Injecting a specific charge in a channel and using the procedure described in the previous section is not the only method of identifying the 50% trigger efficiency threshold value for this charge. Should the desired charge value be too small to properly inject in the channel, for example when trying to identify thresholds for charges around 1/3 or 1/4 PE, then the method cannot be successful. However, as shown in Figure 4.21b, the trigger threshold is linear with the injected charge. By injecting several charges in the channel, and identifying the 50% trigger efficiency threshold for each charge injection, it is possible to plot the threshold DACu value as a function of the charge and apply a linear fit in order to extrapolate the 50% trigger efficiency threshold value for very small charges. In the example shown in Figure 4.21a, charges equivalent to $\frac{1}{2}$, $\frac{3}{4}$, 1 and 2 PE were injected in one of the channels of the ABC board, and their S-curves measured. Once the 50% trigger efficiency threshold value is identified for each charge, a linear fit yields a parametrization function for this channel, as shown in Figure 4.21b. This allows for the computation of the 50% trigger efficiency threshold value for any injected charge value. In this channel, this value for a $\frac{1}{3}$ PE charge was measured to be 835 DACu. This parametrization is only valid for this given channel, and for the precise preamplifier gain value of 40 configured at the time of the measurements.

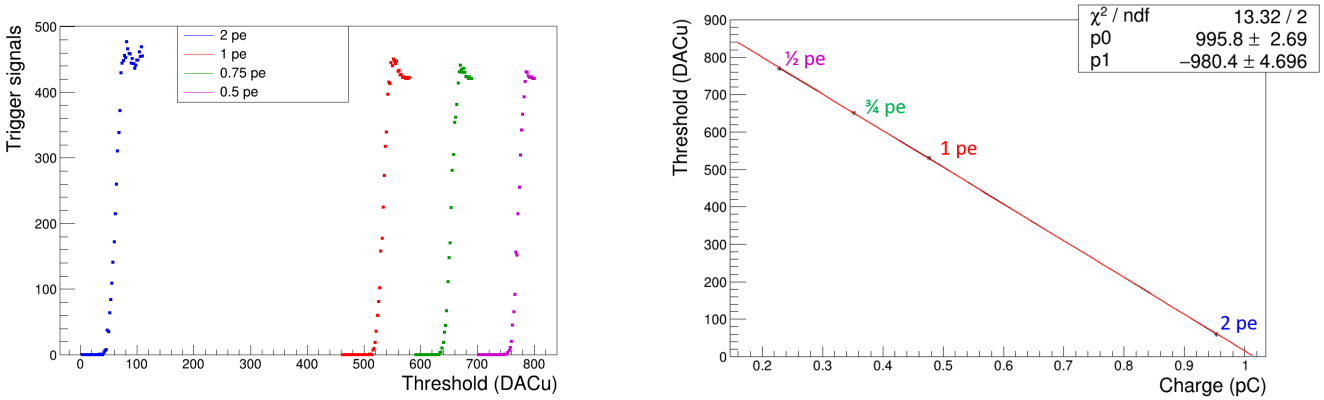

(a) (b)

Figure 4.21: (a) S-curves for multiple signal injections. (b) Linearity of the DACu trigger threshold with the injected charge, assuming a PMT gain of 3×10^6, i.e. 1 PE equivalent to 0.48 pC.

4.4 Combined tests

All the hardware components from the SPMT system have been described in the previous chapter, and have all been successfully tested individually. The main challenge for the SPMT subsystem of JUNO is the incorporation of all these components in one global readout system with satisfying performances and reliability. This is one of the motivations behind the development and commissioning of several test benches in France and China. The hardware components of these test benches will be detailed, as well as the main goals of their development.

One of the objectives of commissioning these test benches was to demonstrate that the SPMT system as a whole, with most of its components being an active part of the electronics chain, is able to properly readout a PMT signal at the single photo-electron level with an amplitude of 2 mV. Another is demonstrating that the ABC board is able to simultaneously properly readout 128 of these PMT signals. Both objectives will be achieved by connecting many PMTs to the

readout channels of the test benches and measuring their performances. This is why the two test benches were pre-commissioned in France and tested with 32 PMTs before being sent to Guangxi University to be tested with 128 PMTs. With a system able to precisely measure the performances of connected PMTs, the primary goal of having commissioned two 128-channels test benches is the mass testing of the PMT production as a follow-up to the verification of the performances done on the bare PMTs in HZC. This means after the PMTs have been potted with the final HV divider and the connector and using the proper cable length. The goals of the mass testing are to verify that the PMT is still functional, as well as measuring several key parameters such as the PMT gain, the SPE charge resolution at the PMT nominal high voltage, and the dark rate above one fourth of a photo-electron.
The following sections will present the commissioned test benches at LP2i and at Guangxi University, with a focus on the performance studies realized within the framework of this PhD : with 32 PMTs at LP2i and with 128 PMTs at LP2i. A test bench in National Taiwan University for fine measurements will also be presented.

4.4.1 V0 test benches

4.4.1.1 Description of the V0 test benches

The two test benches, named test benches A and B in following sections, are each composed of one 128-channels ABC V0 board hosting 8 CATIROC ASICs, two 64-channels HV Splitter (HVS) V0.1 boards without their HV Units, SAMTEC cables to connect the HVS board to the ABC board and one Low Voltage power supply to power the boards. The HV was supplied by external HV NIM modules. This equipment is contained in a mechanical box with a USB interface, and an example of a complete test bench is shown in Figure 4.22.

Figure 4.22: Complete assembled test bench shipped to GXU. The 2 HV Splitter boards (64 channels) are connected to the front-end ABC board (128 channels) via SAMTEC cables. The PMTs are connected to the HVS boards via MCX connectors.

It is important to note the presence of a 20 MΩ resistance on the HVS boards, which takes ∼120 V for a 6 μA PMT consumption. The schematic of the HVS boards connecting to the ABC board for 16 channels is shown in Figure 4.23. This means that ∼120 V need to be added on the HV module powering the PMTs in order to get the nominal gain of the PMTs measured at HZC (3×10^6).

When the 32 PMTs were powered in France for the first measurements, they were be powered at > 1230 V as opposed to the ∼1110 V required in HZC. The evolution of the PMT gain with the HV for 16 channels using the test benches showed that the nominal PMT gain of 3×10^6 was globally reached for the 16 PMTs for a power supply around 1230 V.

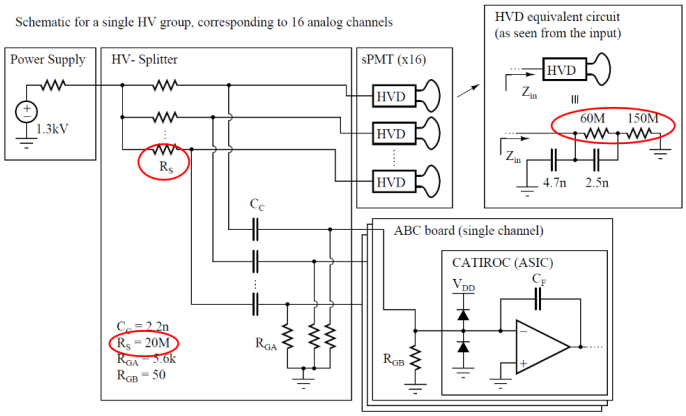

Figure 4.23: Impact of the 20 MΩ resistance on the HV Splitter boards on the required HV power supply to reach a PMT gain of 3×10^6. (a) Schematic of the the HV Splitter board for a single HV group, corresponding to 16 analog channels, highlighting the 20 MΩ resistance responsible for a larger required powering voltage than the one measured at HZC for the PMTs to reach their nominal gain.

Both test benches were fully calibrated in charge in a process described in section 4.3.2.

4.4.1.2 32 PMT performances at LP2i

At LP2i, 32 3" XP72B22 PMTs from the HZC production have been used in 2019 to validate the performances of the two test benches. Considering one of the test benches, having 32 PMTs for 128 readout channels means that each PMT can be connected and measured 4 times per test bench, and up to 8 times considering the second test bench. The goal of these measurements was to evaluate the consistency of the PMT performances whatever the channel of the ABC board, and to check the consistency with the performances measured at HZC. The group of 32 PMTs is plugged in the MCX connectors on the Splitter board, and connects to a pair of ASICs. For each test bench, the first batch of 16 PMTs was connected to and measured by ASICs 0, 3, 4 and 7, and the second batch of 16 PMTs was connected to and measured by ASICs 1, 2, 5 and 6.

Once connected to the Splitter board, the PMTs are powered by an external High Voltage Unit (not from the HV Splitter board) delivering 1230 V. The difference in HV when compared to the nominal HV required at HZC comes from a 20 MΩ resistance on the splitter board, and was described in Section 4.4.1.1.

A charge spectrum is measured in every channel connected to a PMT, and the SPE peak is fitted by a Gaussian function. Coupled with the calibration data for each channel, this allows the measurement in pC of the SPE charge and the derivation of the PMT gain. It also allows the computation of the SPE resolution. Figure 4.24 shows the charge spectrum of a PMT connected to one of the channels, with the Gaussian fit of its SPE peak. From the fit parameters, the mean charge Q_1 and the sigma σ_1 are obtained. The mean pedestal value Q_0 is also measured in every channel.

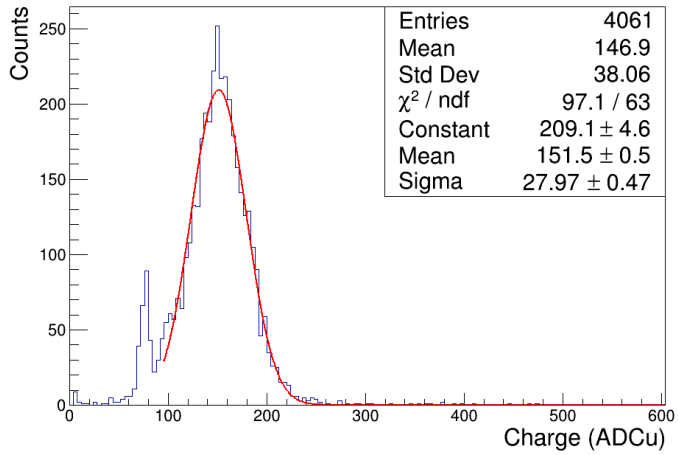

Figure 4.24: Charge spectrum and Gaussian fit for one of the PMTs connected to the ABC board. From the "Mean" and "Sigma" fit parameters, the Q_1 and σ_1 values are obtained, along with the mean pedestal value Q_0.

PMT Gain The PMT Gain G is defined as the amplification factor giving a charge value to SPE events, and is obtained with the formula :

$$G = \frac{Q_1 - Q_0}{P_1 \times 0.48} \times 3 \times 10^6 \tag{4.3}$$

where P_1 is the charge calibration slope obtained from the charge calibration performed on the two ABC V0 boards used for the combined tests. Figure 4.25 shows the 8 PMT gain measurements for both batches of 16 PMTs. All data points are compatible within error bars. The standard deviation stays within 10% of the mean PMT gain value. Two PMTs were defective in the second batch, presented in Figure 4.25b. It appears that the mean gain is below 3×10^6, meaning that the 1230 V powering voltage preliminarily used was underestimated, which is not an issue for this study aimed to demonstrate the consistency of the measurements over multiple CATIROC channels.

PMT single PE resolution The PMT resolution corresponds to the width of the charge distribution for SPE events, and is obtained with the formula :

$$RES = \frac{\sigma_1}{Q_1 - Q_0} \times 100 \tag{4.4}$$

Figure 4.26 shows the 8 SPE resolution measurements for both batches of 16 PMTs. As with the PMT gain measurements, the standard deviation stays within 12% of the mean value. The resolutions obtained with the test benches are slightly higher than the ones measured in HZC, but are still compatible with the HZC measurements within 15%, as required during the mass production of the 3" PMTs. This is most likely because the gain of the PMTs is on average lower than the nominal value, leading to a worsened SPE resolution measurement. Figure 4.27 shows that the mean values of the SPE resolutions obtained with the test benches are compatible with the HZC values within 15%.

Dark Counting Rate at 1/4 PE Figure 4.28 shows the 8 DCR measurements at $\frac{1}{4}$ PE for both batches of 16 PMTs. This study shows a larger dispersion in the data points for the 8

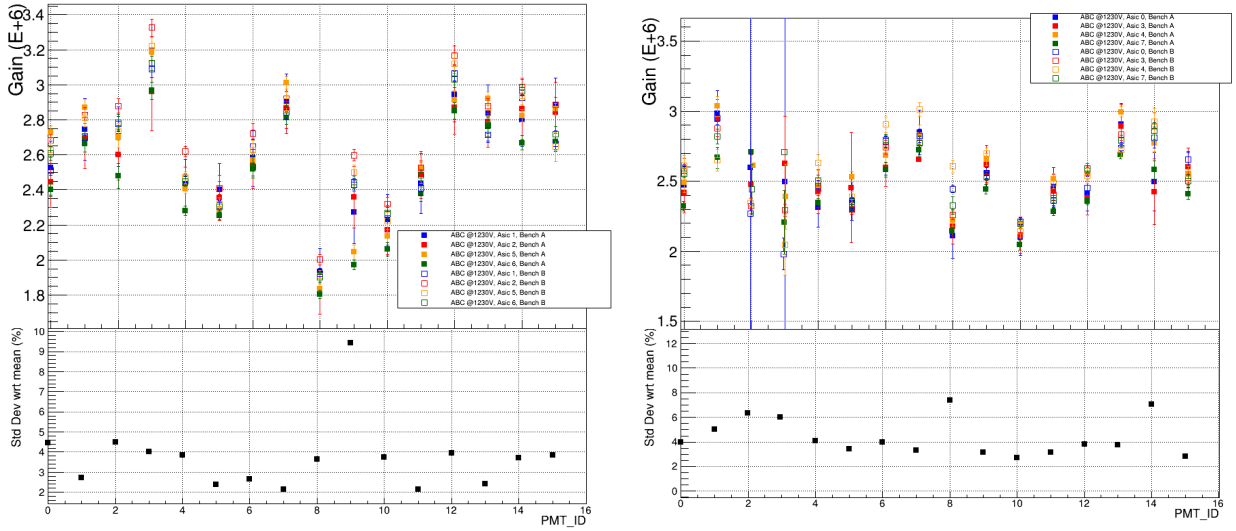

(a) (b)

Figure 4.25: Gain measurements for both sets of 16 PMTs. Top plots show the absolute values of the 8 measurements, while bottom plots show the standard deviation. (a) Gain measurements for the first batch of 16 PMTs. (b) Gain measurements for the second batch of 16 PMTs.

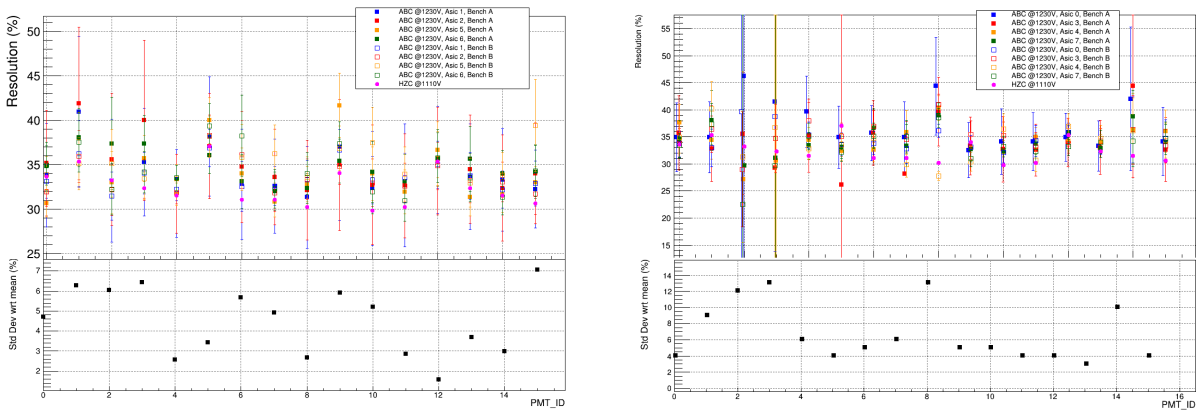

(a) (b)

Figure 4.26: SPE resolution measurements for both sets of 16 PMTs. Top plots show the absolute values of the 8 measurements, while bottom plots show the standard deviation. (a) Gain measurements for the first batch of 16 PMTs. (b) Gain measurements for the second batch of 16 PMTs.

measurements of the same PMT, meaning that the same PMT measured with different channels yielded sometimes substantially different results, with the standard deviation reaching values of up to 35% with a few exceptions beyond 70%. This can be explained as the conditions for a precise measurement of this parameter are stricter. The PMTs were not always measured at the same PMT gain as in HZC, were measured with a different electronic setup, and the measurement process at LP2i took several days, spread over several weeks, meaning that temperature differences from one measurement to another and varying rest times after PMT powering could also have had an impact of the results. Moreover, this measurement is particularly sensitive to the charge threshold, which is extremely difficult to configure identically in two different channels, let alone ASICs.

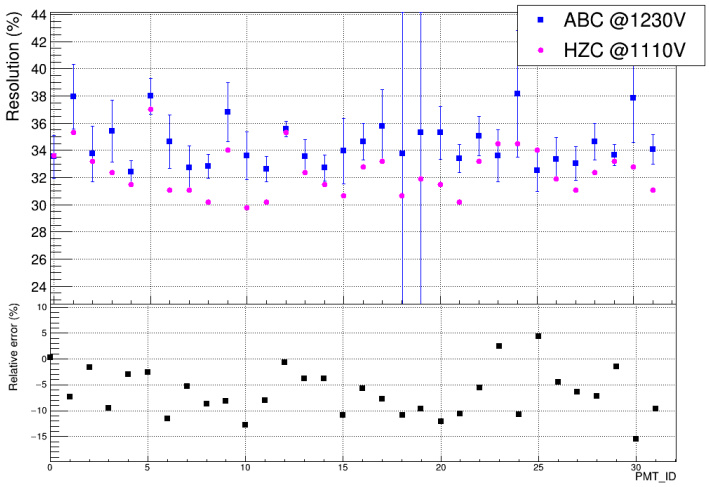

Figure 4.27: Mean SPE resolution from the 32 PMTs using the 8 measurements obtained with the test benches. Top plot shows the absolute values in %. Bottom plot shows the relative error between the two values, which is below 15%.

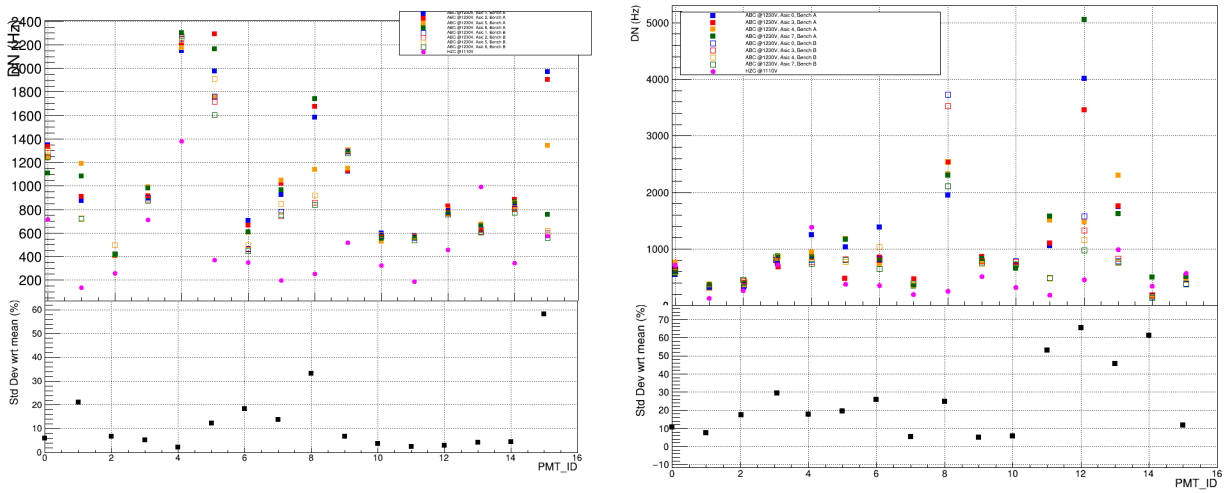

(a) (b)

Figure 4.28: Dark Counting Rate measurements at $\frac{1}{4}$ PE for both sets of 16 PMTs. Top plots show the absolute values of the 8 measurements, while bottom plots show the standard deviation. (a) DCR measurements for the first batch of 16 PMTs. (b) DCR measurements for the second batch of 16 PMTs.

4.4.1.3 SPMT mass testing at GXU

As described in section 4.4, the primary goal of having commissioned two 128-channels test benches at LP2i is the mass testing in Guangxi University (GXU) of the PMT production after potting and cabling, in order to estimate if this operation had an substantial impact on the PMT performances before delivery to the JUNO site. This enterprise falls under the responsibility of the Chinese side of the collaboration, with the measured key parameters being the PMT gain, the SPE charge resolution at the PMT nominal high voltage, and the dark rate above one fourth of a photo-electron. In GXU , a room was arranged to house a fixed PMT testing station starting from January 2020. 128 3" PMTs which were rejected from HZC's production were sent to GXU to

allow for the validation of the performances of the test benches at their full capacity. A dark room was built, able to contain many cases of PMTs, as shown in Figure 4.29a, and their communication to the outside of the room, where the two test benches (ABC V0 boards) were placed after having been sent from LP2i, is carried out by a patch panel with 16 light-tight holes equivalent to the lid of the underwater box where the UWB connectors are plugged.

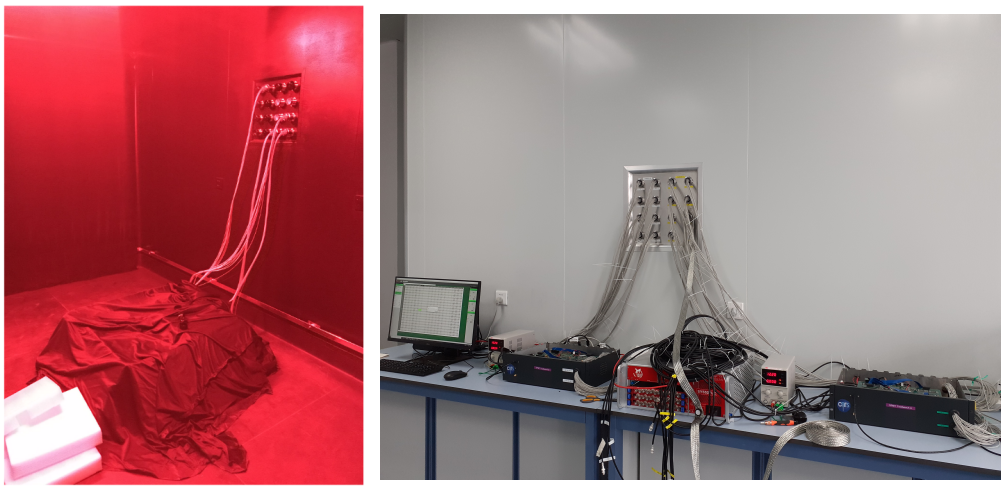

(a) (b)

Figure 4.29: (a) 128 PMTs in a dark room in GXU. (b) Overview of the testing station with a patch panel allowing 16 groups of 16 PMTs (up to 256 PMTs in total) to be connected to the two V0 test stations (black box shown in Figure 4.22).

To fully connect to a test bench, 8 connectors are necessary (A to H) to conduct the 128 PMT cables to the 2 HVS boards. A global view of the dedicated JUNO 3" PMT testing station is shown in Figure 4.29b. As with the 32 PMTs in France, the 128 PMTs available here are also swapped over different channels to measure the consistency of the PMT performances whatever the channel of the ABC board. Due to difficulties in data acquisition with the V0 version of the ABC board and an earlier version of the current test firmware (section 4.2.2), the simultaneous data acquisition of 128 PMT signals is instead replaced with the data acquisition of 16 channels, ASIC by ASIC, while signals from the other ASICS are masked. The PMTs are thus tested sequentially. Since the beginning of the mass testing operation, and at the time of writing this thesis, 8256 SPMTs have been tested (∼32% of the production) with ∼97% having passed the acceptance tests. Their performances are monitored, and a few results are illustrated in the following paragraphs.

High Voltage for PMT nominal gain As presented in section 4.4.1.1, the SPMTs tested in the test benches at GXU have to be powered with a higher HV value than during their testing in HZC, because of the 20 MΩ resistance in the Splitter board. Figure 4.30 shows, in blue, the HV required for every channel to come close to the nominal PMT gain (3×10^6), as well as the nominal HV measured for these PMTs at HZC in red. The required value can be up to ∼200 V higher than the nominal HZC value. The 20 MΩ resistance on the HVS board can only explain ∼80-∼120 V of this additional requirement. As mentioned in section 2.5.3, a few thousands of PMTs from the early production are being re-tested in HZC to verify their nominal HV, due to an observed bias in the HV stability.

PMT SPE resolution As presented in section 4.4.1.2, the SPE resolution is measured for all tested PMTs. Figure 4.31 shows the results for 128 PMTs among the 7000 tested, with the

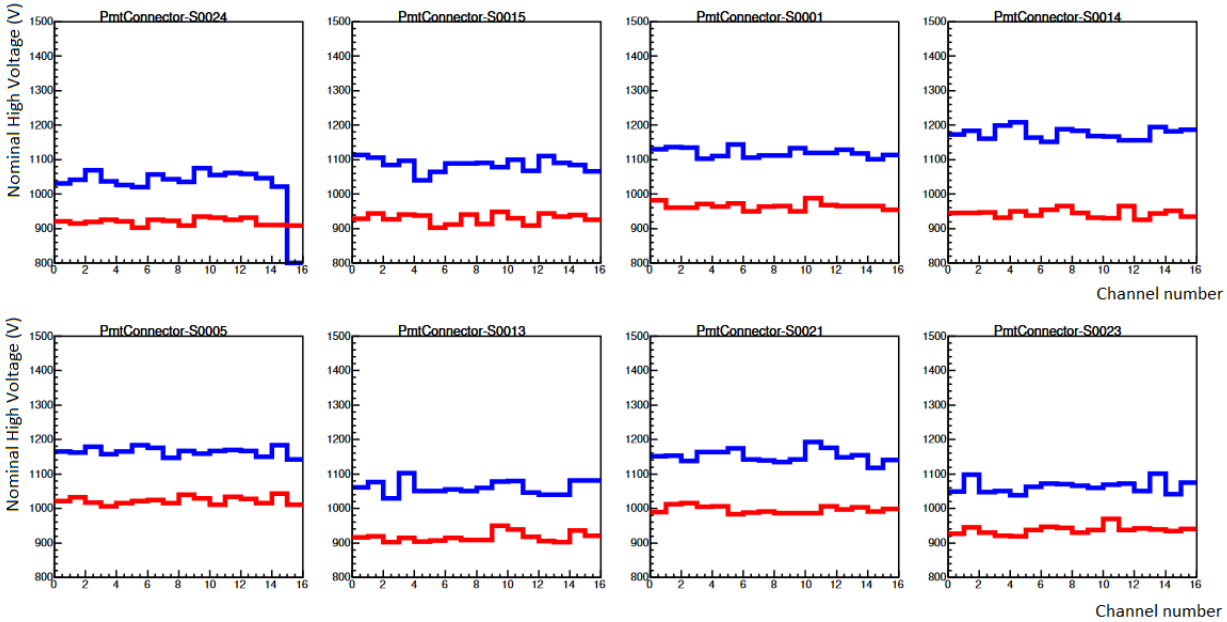

Figure 4.30: In blue, PMT High Voltage required for PMT nominal gain (3×10^6), measured for 128 PMTs in GXU. In red, nominal High Voltage measured for these PMTs at HZC. Significant differences can be observed, partly explained by a 20 MΩ resistance on the HVS board.

mean resolution measured in HZC (33.17%) represented as the dashed blue line and the upper requirement of the JUNO collaboration of 45% represented as the dashed red line. The measured resolutions are close to 33%, and all PMTs in this example have passed the acceptance criteria.

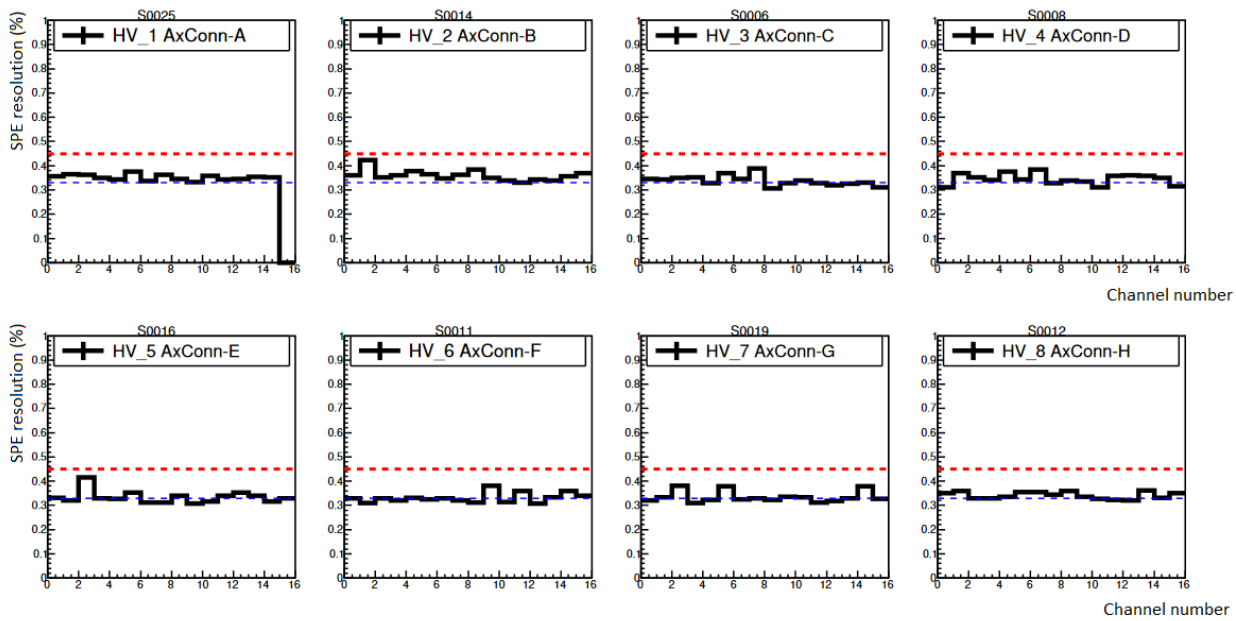

Figure 4.31: PMT single PE resolution measured for 128 PMTs in GXU. The dashed blue line represents the mean SPE resolution measured in HZC of 33%, while the dashed red line represents the acceptance criteria defined during the mass production of the SPMTs.

4.4.2 16-channels NTU test bench for fine measurements

In NTU, a test bench was developed using an ABC V0 printed circuit board (PCB) equipped with two CATIROC ASICs, one of which was calibrated in charge, in order to perform fine measurements of PMT performances on a fraction of the SPMT production having been tested at GXU. Several 3-inch PMTs from the latest HZC production are stored in a dark room in the physics department of NTU, and are kept in black tubes. They can be illuminated by an LED through optical fibers connected to these tubes, to perform these fine measurements. Figure 4.32a shows the dark room at NTU containing the PMTs kept in black tubes, while Figure 4.32b shows the electronics setup of this test bench.

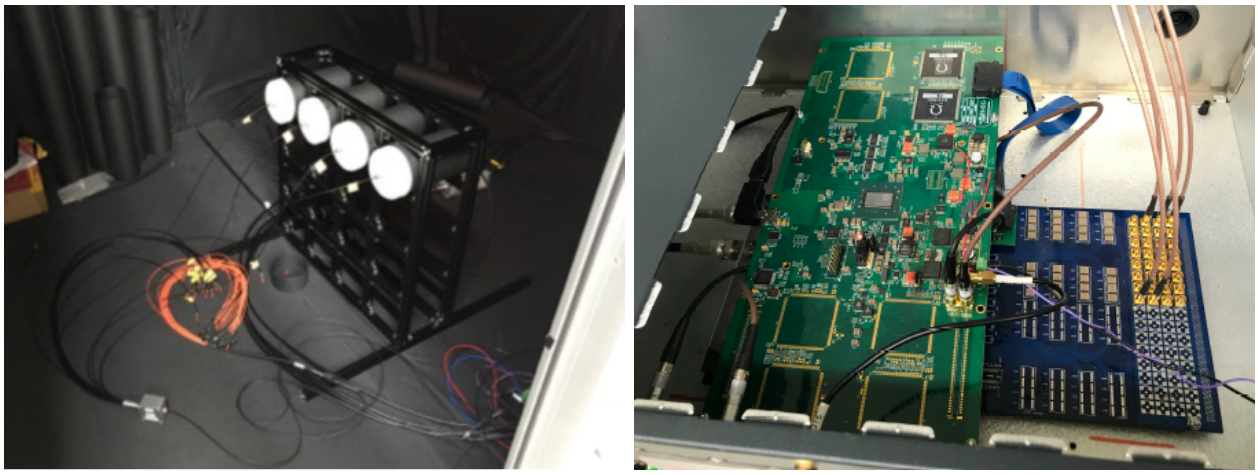

(a) (b)

Figure 4.32: (a) PMTs in dark room in NTU. (b) Electronics of the test station, with one HVS board and an ABC V0 board populated with only two ASICS.

A schematic view of the test bench is presented in Figure 4.33. The LED generates a signal which forces the readout of the 16 channels of the ASIC by using the External Trigger mode, and the charge is also read by a QDC in addition to the CATIROC measurement. With an LED illumination, the objectives for this test bench for the second half of 2021 are :

- To test the PMT linearity in the HG and LG modes.
- To test the PMT stability over a long period of time. As these tests will be performed on a small fraction of the SPMT production, longer studies can be conducted.
- To measure the pre- and after-pulses of the tested PMTs and verify that the charge of these pulses does not exceed 5% and 15%, respectively, of the charge of the signal after HV divider, potting, cable and connector.
- Depending on the jitter of the LED, the TTS of the PMTs could also be checked.

4.4.3 128 PMT performances at LP2i

Following in the footsteps on the combined test-bench employing 32 PMTs, which was developed in France and then sent to China for the mass testing of the SPMTs, a more complete test bench employing 128 SPMTs for a full coverage of all ABC channels was also developed in France at the end of my PhD.

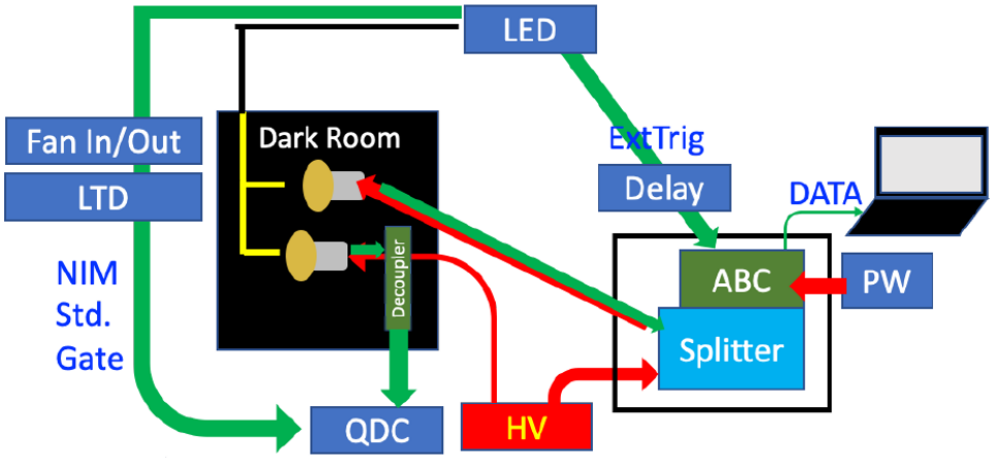

Figure 4.33: NTU LED test bench schematics.

4.4.3.1 Experimental setup

This test bench combines most of the final-state versions of all components of the SPMT electronic system. In a dark room, 128 JUNO SPMTs, shown in Figure 4.34a, are plugged in the MCX connectors on two HV Splitter (HVS) V0.3 boards via the connectors on the underwater box lid. The HVS boards then redirect the signal to a pre-production board (ABC V1.2), while a GCU V1.0 board pilots the HV Units on the HVS and powers the system. The data readout can be performed via USB (test mode as presented in section 4.2.2) or via the GCU (JUNO physics mode). The test-bench is placed within a Faraday cage for EMI shielding, as illustrated in Figure 4.34b.

(a) (b)

Figure 4.34: (a) All SPMTs in the dark room at LP2i, used for combined tests with 128 simultaneous PMT signals. (b) Combined test-bench before enclosure in the Faraday cage. The main components are one ABC V1.2 pre-production board, two HVS in the middle and one GCU board on the back.

4.4.3.2 Measurements and PMT performances

Pedestal measurements In section 4.3.1, pedestal measurements were presented and discussed on the V0 and V1.2 versions of the ABC board. Building a test-bench with the latest status on each component on the SPMT electronics enables the measurement of the pedestal charge with the ABC connected to the whole system and 128 PMTs. For each batch of 16 PMTs connected to one of the 8 ASICs, the HV can be switched ON and OFF from the USB interface, and pedestal values can be measured. Figure 4.35a shows the mean pedestal values in each channel, for the cases HV ON and HV OFF, with the pedestal mean position being shifted by up to 3 ADCu between the two cases, as shown in the bottom half of the figure. Figure 4.35b, shows the pedestal RMS values for the cases HV ON and HV OFF. Despite an increase in the pedestal RMS when the HV is switched on of up to 1.8 ADCU, as shown in the bottom half of the figure, the pedestal RMS values are still lower than 4 ADCu, and so the impact on the charge spread of the full electronics system is negligible before the charge resolution of the PMT. The stability of the pedestal mean position over a long period (months) with HV ON is under investigation but seems satisfactory.

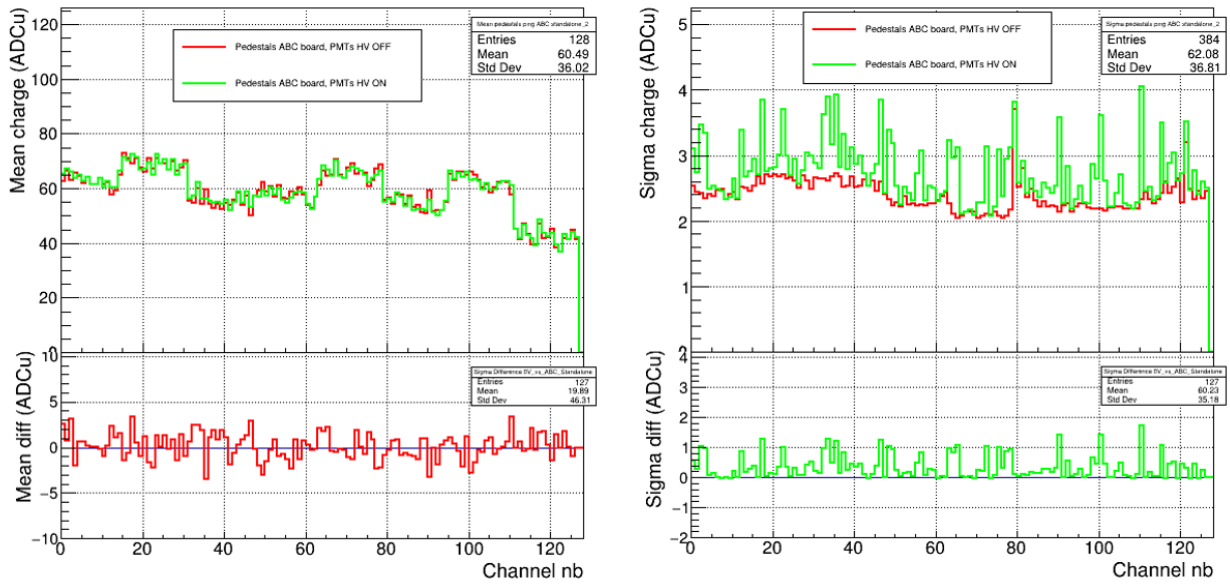

(a) (b)

Figure 4.35: Pedestal charge measurements on all 128 channels. (a) Mean pedestal values (top half) and absolute difference between the cases HV ON and HV OFF (bottom half). (b) RMS of the pedestal charge distribution in each channel (top half) and absolute difference between the cases HV ON and HV OFF (bottom half).

Charge calibration According to the procedure described in section 4.3.2, the 128 channels of the test bench were calibrated in charge, giving a pC-to-ADCu equivalence. From the linear fits of the calibration, the slope and intercept parameters are derived, stored, and used to study PMT performances.

Optimization of trigger threshold In order to measure the PMT performances, the SPE peak has to be well-defined in all channels. This implies cutting off the pedestal measurements, which requires the identification of the optimal trigger threshold according to the method described in section 4.3.5.1. The ideal trigger threshold to cut off the pedestals was identified for each of the

128 channels, and the S-curves for the channels connected to one of the ASICs are shown as an example in Figure 4.36. In this case, the minimum threshold required in order to cut off the pedestal is located around 906 DACu.

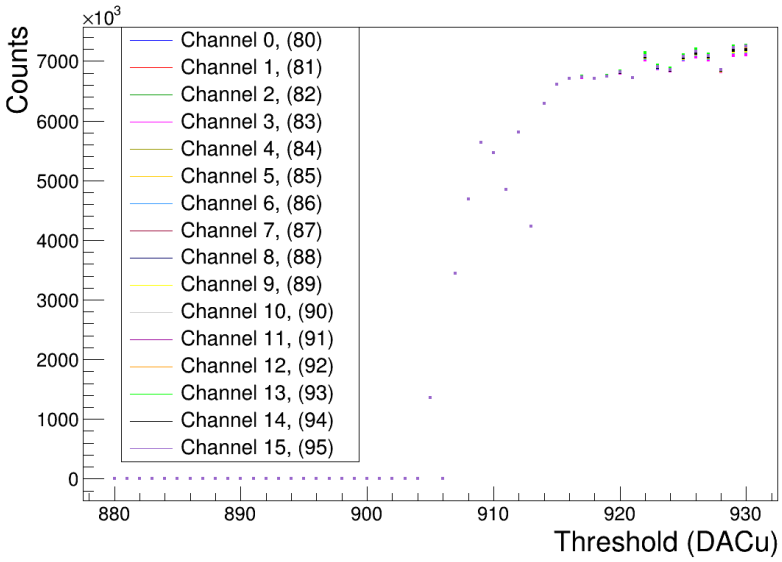

Figure 4.36: S-curves for the 16 channels of one ASIC of the 128-channels test bench (ASIC 5 in this case). The absolute channel number is shown in parentheses in the legend.

PMT Gain curve, nominal HV After the trigger threshold in each channel has been optimized, the HV powering each batch of 16 PMTs was varied from 1100 V to 1350 V and the PMT Gain curves were plotted as a function of the PMT HV to determine the nominal HV for a Gain $G = 3 \times 10^6$ for all channels. Figure 4.37 shows these Gain curves for each of the 128 channels, grouped by ASIC. Differences in the Gain curves can be observed among the channels of a same ASIC. This is partly due to the fact the HZC PMTs were not well-grouped in batches of PMTs with similar Gain at the nominal HV.
Despite these shifts in nominal HV between PMTs of the same batch, the PMT performance study conducted on the 128 SPMTs yielded very positive results, as will be illustrated in Figure 4.40a. Figure 4.38 furthermore shows a good correlation between the measured nominal HV and the HZC nominal HV, with a ΔHV of about 100 V compared to HZC nominal values, due to the HVS board and cable lengths.

Charge spectra With 128 PMTs that can be connected to the same ABC board, it is crucial to verify that the charge spectrum from any channel corresponds to expectations from the JUNO collaboration. Figure 4.39 shows the charge spectra obtained with 128 JUNO SPMTs powered at their nominal HV (derived from the previous measurements), for a simultaneous data acquisition. Calibration data was used to express the charge in pC and align the SPE peaks of each charge spectrum. The ability to operate 128 PMTs in a dark rate mode with good data quality was an extremely important milestone of the SPMT electronics system.

PMT performances In order to test the capacity of the ABC board to handle physical events in the JUNO detector, 128 PMT signals are connected to the ABC channels, with random triggers due to their DCR. From the charge spectrum in each channel and the information about the

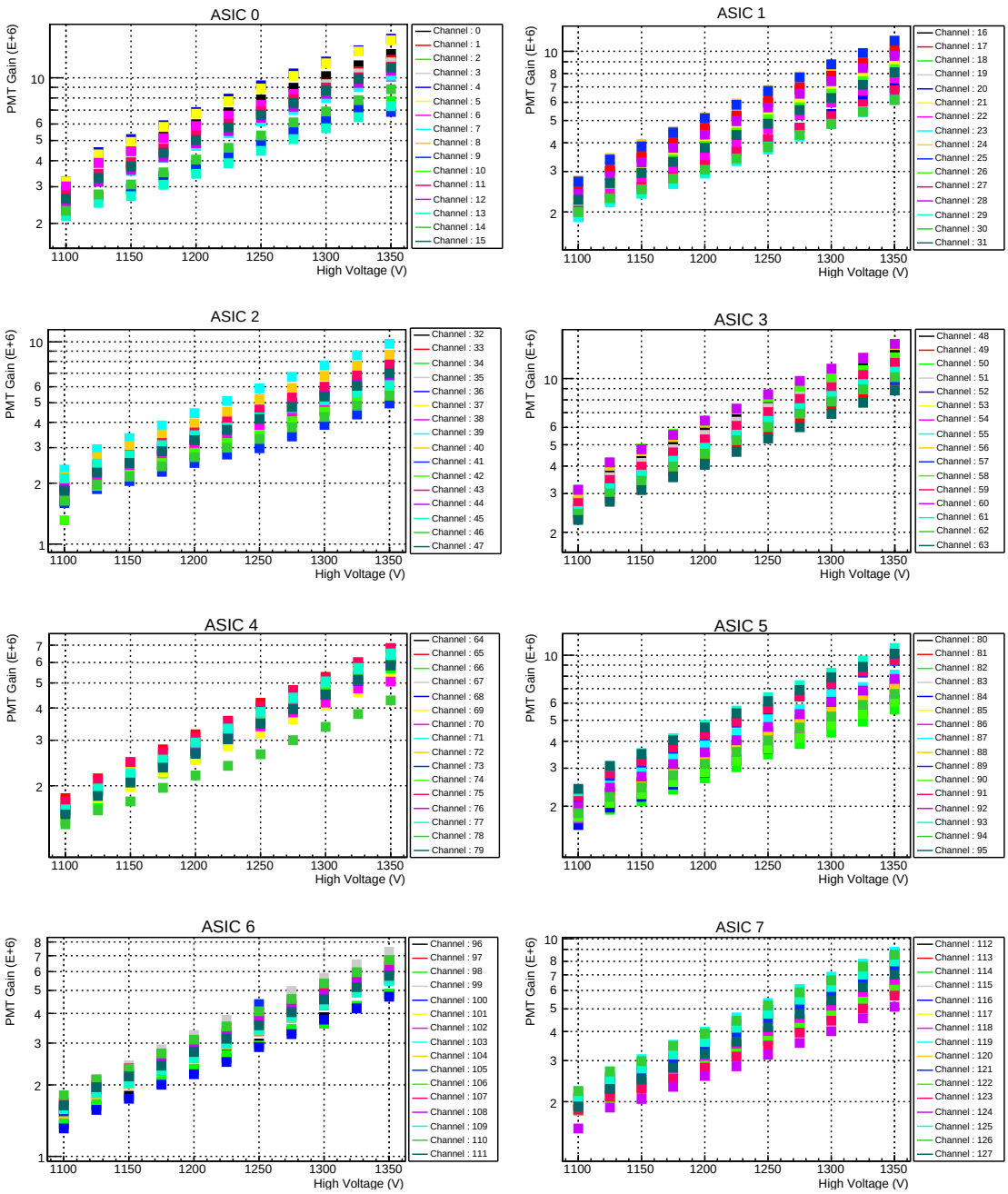

Figure 4.37: PMT Gain curves as a function of the HV, for all 128 channels. The nominal Gain 3×10^6 is typically reached in the 1100 V-1250 V range.

mean value and standard deviation (Gaussian fit) of the charge distribution, the Gain and charge resolution of the PMTs can be computed and compared to expectations. The DCR of the PMTs can also be measured and verified.

Figure 4.40a shows the Gain of the PMTs at their nominal HV for each of the 128 channels. The Gain values are distributed around the nominal Gain value of 3×10^6, which confirms the good identification of the nominal High Voltage for each PMT presented in Figure 4.37. Figure 4.40b shows the measured PMT Dark Rate, with values below 1 kHz for each tested PMT (for reminder, the JUNO requirement is <1.8 kHz).

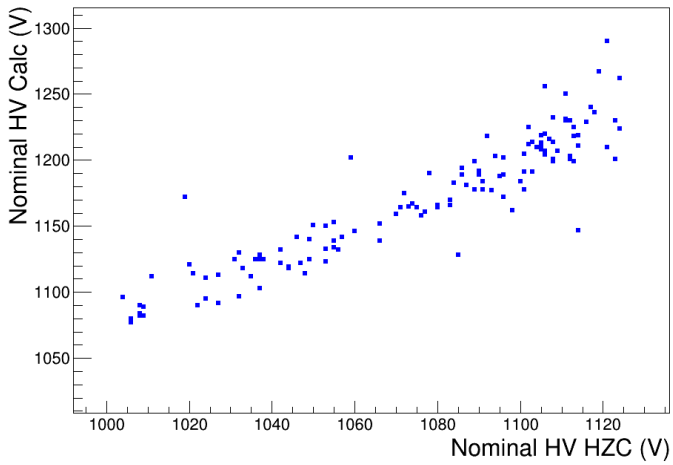

Figure 4.38: Measured nominal HV for Gain $G = 3 \times 10^6$ for all channels and comparison with HZC values of each considered PMT.

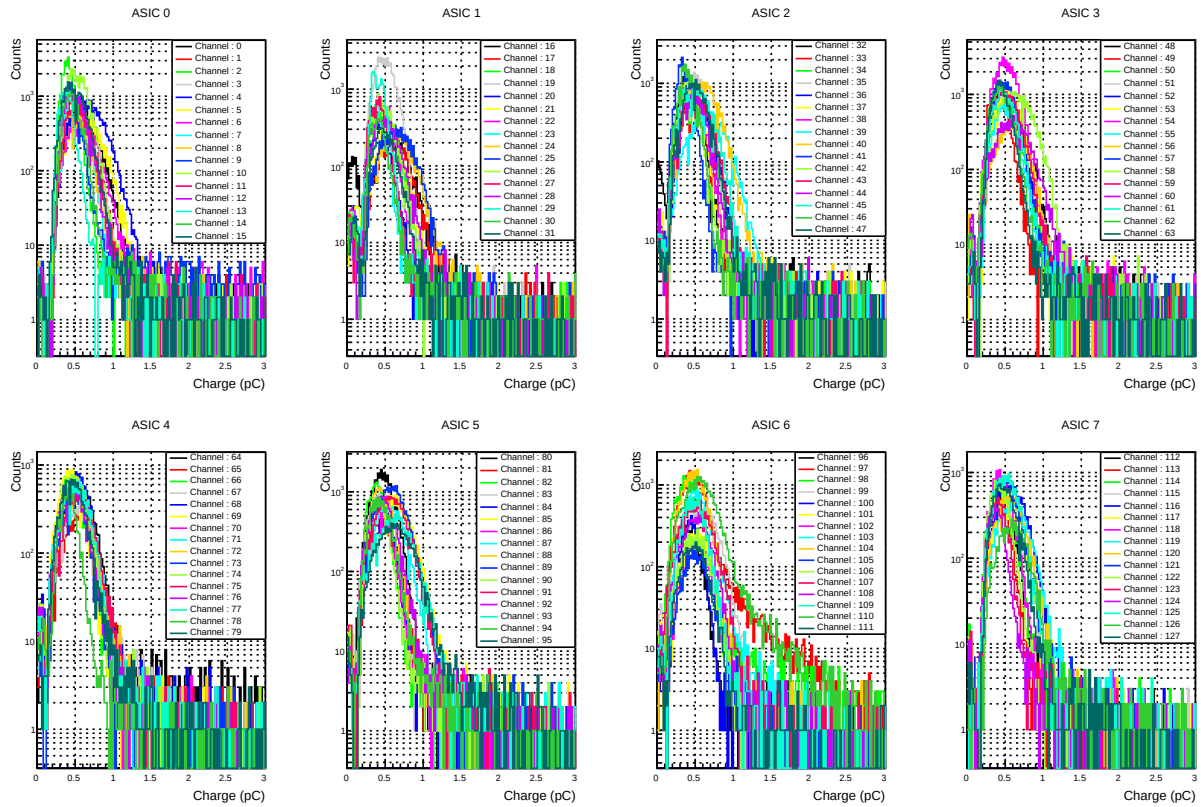

Figure 4.39: Charge spectra obtained during the final combined tests performed at LP2i for 128 3" PMTs in a dark room powered at their nominal HV per group of 16 PMTs. The charge spectra in pC are obtained after applying the calibration factor from ADCu to pC for each channel.

The SPE charge resolutions of the PMTs are shown in Figure 4.41, with a mean value of the PMT charge resolution of ∼31%, well respecting the requirement set by the JUNO collaboration of $< 40\%$.

With the simultaneous data acquisition of 128 PMT signals on a single ABC board and a good

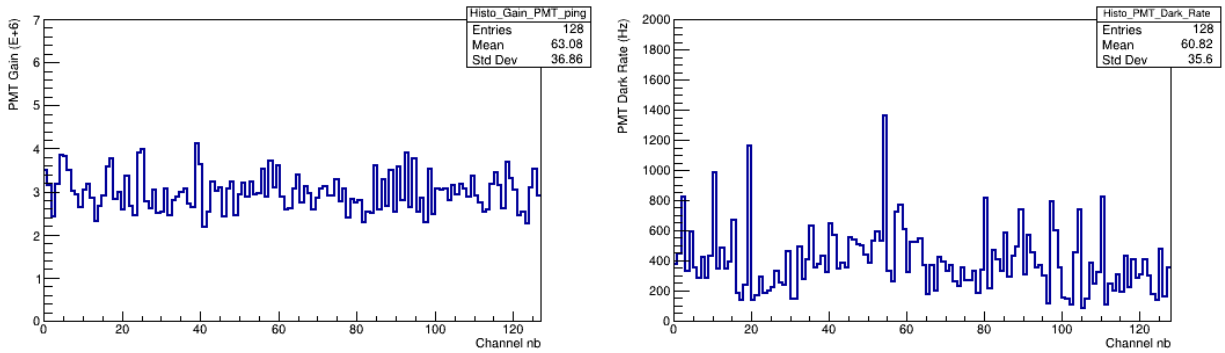

(a) (b)

Figure 4.40: (a) PMT Gain for all 128 PMTs. The proximity to the nominal Gain of 3×10^6 indicates a well-identified HV value for each PMT batch. (b) PMT Dark Rate for all 128 PMTs. The JUNO requirement of <1.8 kHz is well respected.

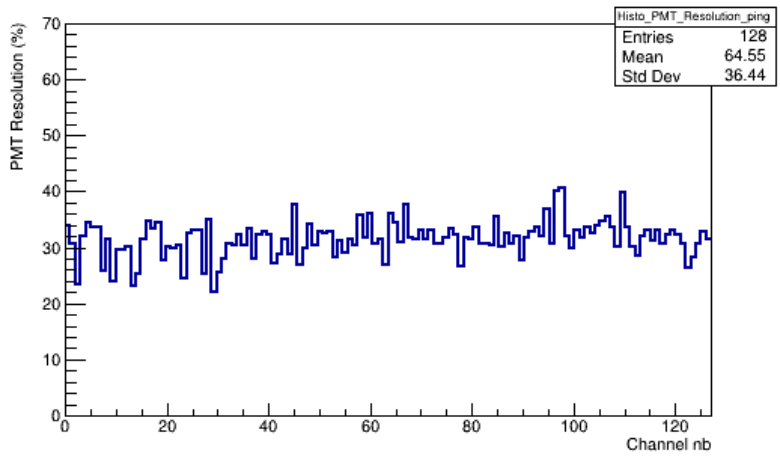

Figure 4.41: SPE charge resolution for all 128 SPMTs. SPE resolutions lower than 40% are required from the JUNO collaboration.

quality of measured PMT performances, the 128-channels test bench developed at LP2i allowed for the achievement of several important milestones for the SPMT system. This test bench is scheduled to be used for the testing of the 220 ABC V1.2 boards, which will be produced and delivered to LP2i in the fall of 2021 before integration with the rest of the electronics in China.

4.5 PMT signal and processing

4.5.1 PE collection and PMT waveform

As evidenced in section 4.4, when comparing PMT performances to validate the status of the test benches, the CATIROC ASICs will process PMT signals. Such signals are being formed by the collection of photoelectrons emitted from the photocathode of the PMTs. As illustrated in Figure 4.42a, the photoelectrons emission process, caused by the incident photons, takes place in the photocathode. A chain of electrodes, called dynodes, amplifies the flow of electrons (when an electron strikes the surface of a dynode, a certain number of secondary electrons are emitted) and

this resulting flow of electrons is collected by an anode, causing the formation of a current pulse. The amplification of the flow of electrons is caused by the voltage between the photocathode, dynodes and anode, which accelerates the electrons and causes their avalanche multiplication. After going through the PMT base and the HV divider, this current is then processed by the electronics of the system. The waveform of the PMT can also be observed on an oscilloscope by transforming the current into a tension by use of a resistor. An example of an average SPE waveform, obtained with a 3-inch PMT in the typical case of a SPE collection, is shown in Figure 4.42b. This gives a PMT signal with a typical amplitude of about 2 mV, making it very delicate to manipulate and analyse. Consecutive photons arriving on the photo-cathode of a PMT will result in consecutive flows of electrons being collected by the anode and, depending on the time window of arrival of these photons, can result in overlapping current pulses and can contribute to the same PMT waveform.

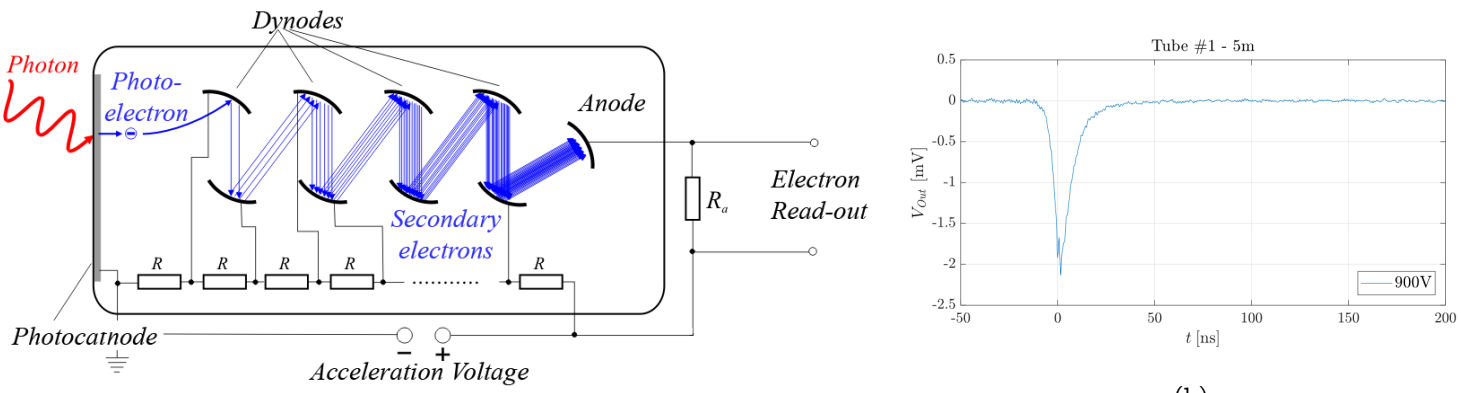

(a) (b)

Figure 4.42: (a) Photomultiplier schematics. (b) Illustrative average 3-inch PMT SPE waveform.

While the Number of collected PhotoElectrons (NPE) naturally has an impact on the collected charge and the amplitude and overall shape of the signal, PMT signals will also slightly vary for repeated instances of the same event type, leading to different charges even in the case of the same NPE collected. The distribution of these charges for a given NPE is called the charge resolution, and Figure 4.43 shows the SPE charge resolution measured in HZC for all 26,000 SPMTs. The mean value of this distribution (33.17%) can be taken as the SPE resolution for any of the SPMTs.

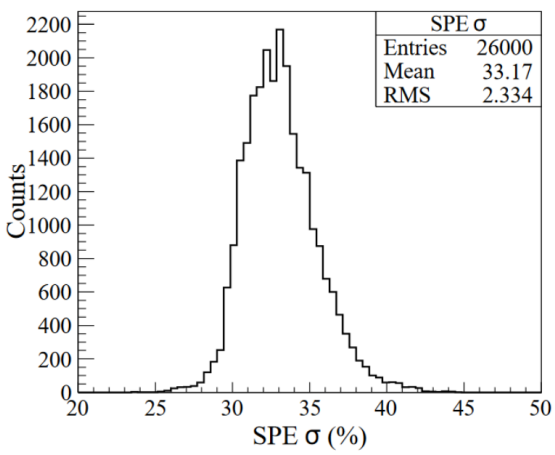

Figure 4.43: Distribution of the SPE resolutions (written as σ) for 26,000 HZC XP72B22 SPMTs.

As previously mentioned, two photons arriving on the photocathode of a PMT in a short time window can contribute to the same waveform and result in a single PMT signal. In order to verify how consecutive events are processed by the entire SPMT electronics, as well as study the charge linearity in the Low Gain mode using real events from a scintillator and study the time and charge correlation of PMT events, an experimental setup was designed at LP2i. It consisted in a spectrometer [130] using a radioactive source of ^{90}Sr and offering a monoenergetic electron beam, ranging from 0.4 to 1.8 MeV with an energy resolution (FWHM) of (1.0 $\pm$ 0.2)% at 1 MeV and a linearity better than 2%, which was aimed at a thin (2 cm) plastic scintillator with a light yield of $\sim$8000 photons per MeV. Two 3" HZC PMTs were placed on either side of the scintillator, and were each connected to a one-channel HV Splitter board to decouple the signals from the HV powering and the PMT response. The decoupled signals were then sent to an ABC V0 board as well as to a WaveCatcher module in order to precisely measure the induced charge. The decay time of $\sim$4 ns of the plastic scintillator ensured that about 63% of the photons were emitted within 4 ns, and about 95% within 12 ns. The two PMTs facing the plastic scintillator are shown in Figure 4.44a.

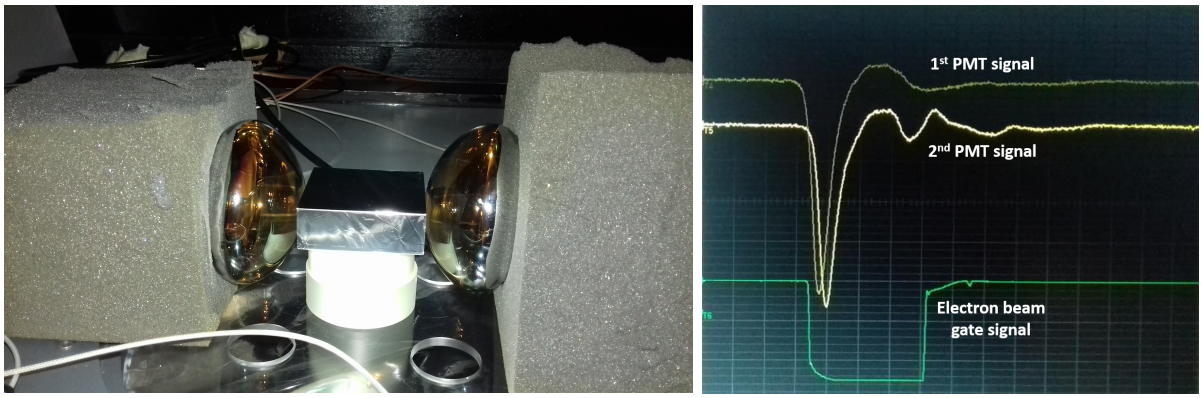

(a) (b)

Figure 4.44: (a) Two 3" PMTs facing a plastic scintillator illuminated by a monoenergetic electron beam coming from the bottom and provided by a spectrometer using a radioactive source of ^{90}Sr [130]. (b) Coincidental signals from the two PMTs facing the plastic scintillator during illumination.

The waveforms are integrated by the WaveCatcher module over a 30 ns time window to measure their charge, and can be recorded, as shown in Figure 4.45a with many waveforms overlapped using a persistence mode. Over the duration of the events, shown on the X-axis in ADCu with a 0.3125 ns/ADCu correspondence, several overshoots can be observed, leading to a ringing effect, due to adaptation issues with the single-channel HV splitter boards (not optimized). 1 MeV electrons make up the bulk of the $\sim$300 mV amplitude pulses, while signals with higher amplitudes are likely due to higher energy gammas from natural radioactivity. Most of these waveforms seem to be formed by unique pulses, despite the high light yield of the plastic scintillator, which, coupled to the rise times of the recorded waveform being typically shorter than 10 ns, as shown in Figure 4.45b, tends to confirm that most of the photons have been generated in the plastic scintillator and collected by the PMTs within a time window of $\sim$10 ns, and are contributing to a single PMT waveform.

As the two PMTs are each positioned on one side of the plastic scintillator, they are supposed to be sensitive to the same events. Comparing the charges observed by the second PMT to the charges observed by the first PMT is an effective way of verifying that the supposedly physical events have a coherent equivalent in the second measurement. Figure 4.46a shows a 2D distribution of the charges measured by the 2 PMTs for correlated events, with an event statistics peak for the first

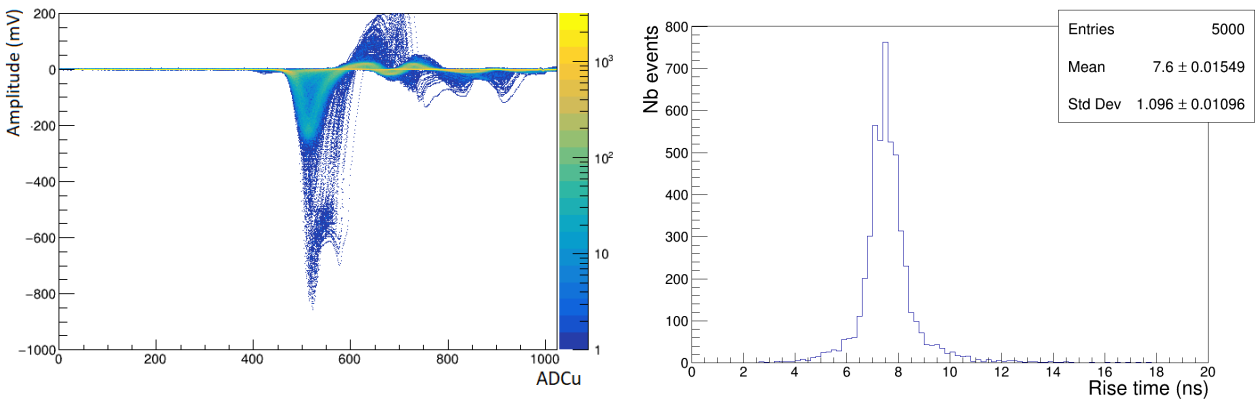

(a) (b)

Figure 4.45: (a) Overlapped PMT waveforms in persistency mode. The ADCu measurement of the event duration has a 0.3125 ns/ADCu correspondence. Most of the waveforms are only made up of a single pulse. Signals with higher amplitudes are likely due to higher energy gammas from natural radioactivity. (b) Rise time (from 10% to 90% of the waveform amplitude) distribution of the recorded waveforms.

PMT at ∼650 ADCu and this same peak for the second PMT at ∼800 ADCu. While it concludes on the coherence of the measured events, this distribution also highlights the difference in gain of the two PMTs, as there is a slight difference in the charge measurements.
The energy deposited by the electron beam was gradually increased up to 80 pC (160 PE), and while the measured charge was observed to be proportional to the deposited energy, as shown in Figure 4.46b, the recorded waveforms remained single pulses, no matter the energy. This would confirm that no matter the amount of photo-electrons collected in a short time window, they would indeed contribute to the same PMT waveform.

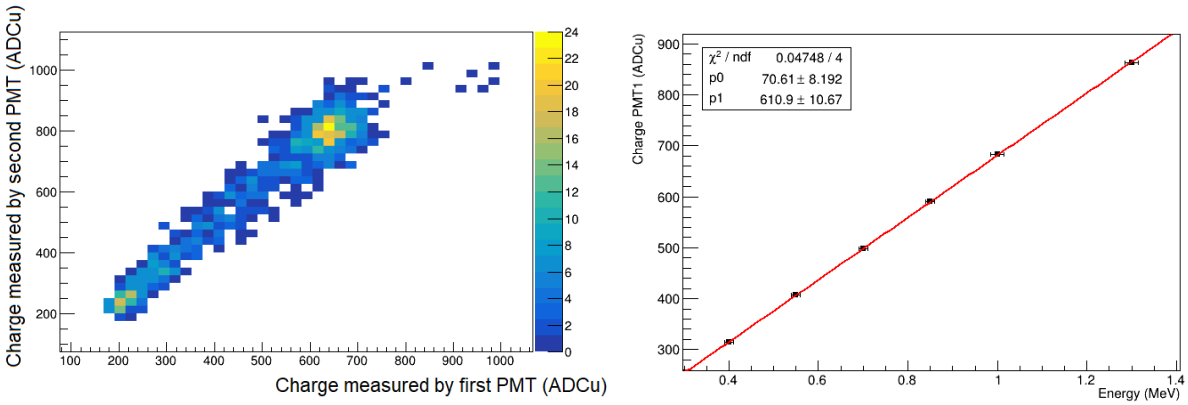

(a) (b)

Figure 4.46: (a) Charge measured by the second PMT as a function of the charge measured by the first PMT for correlated events. The position of the collected electrons confirms the coherence of the 2 measurements. (b) Charge measured by the ABC board as a function of the deposited energy, showing the good proportionality of the measurement.

Charge measurements were also performed by the WaveCatcher module in order to verify that the charge measured by the ABC board corresponds to the full expected charge. The charge as

measured by the ABC board as a function of the "reference" charge, measured by the WaveCatcher, is shown in Figure 4.47a. A good linearity can be obtained, despite a slope parameter of ∼0.92 indicating a 8% loss in the charge measurement performed by the ABC board. This loss can be explained by the treatment of wider PMT signals by the CATIROC ASICs on the ABC board. Figure 4.47b shows the charge linearity of CATIROC depending on the signal width, for different RC constants. The Y-axis contains arbitrary values, rescaled in order to obtain identical linear slopes for the three RC configurations, but a deviation from the expected charge can be observed starting at signal widths of about 20, 25 and 55 ns, respectively, for the three considered RC constants. While the Y-axis of Figure 4.47b is made up of arbitrary values, the ratio between the measured (data points) and the expected (black line) values can be taken as the fraction of charge lost due to the signal width. The width of the recorded waveforms, as can be seen in Figure 4.45a, can easily reach ∼30 ns, and for such signal widths and a RC constant of 50 used for the measurements, the fraction of lost charge can reach ∼20%. For thinner pulses, a 8% charge loss can thus be explained, especially considering the large number of PE collected (up to 160). The linearity of the charge measured by the ABC when compared to the charge measured by the WaveCatcher remains the most important parameter. In the framework of the JUNO experiment, this measured percentage of charge loss should be systematic, and calibration sources will allow for the definition of an effective charge at a given known energy. As long as the charge measurement remains linear, such a charge loss should have no impact on the charge reconstruction.

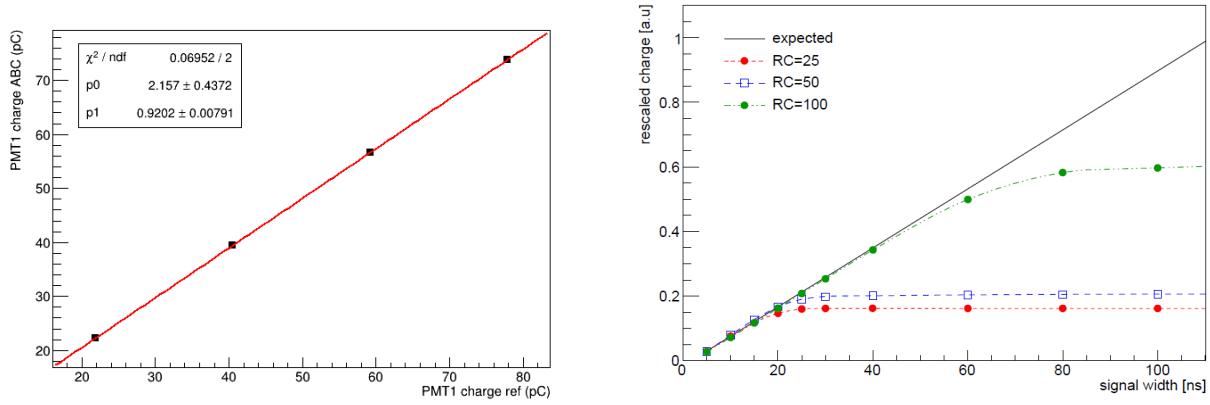

(a) (b)

Figure 4.47: (a) ABC charge as a function of the WaveCatcher charge. Linear model used to fit the data points. Excellent agreement between the 2 measurements. (b) Charge linearity as a function of the signal width for different RC constants of the slow shaper. A deviation from linearity is observed starting at about 20, 25 and 55 ns, respectively, for the three considered RC constants. [126]

4.5.2 LED test bench for PMT waveform behavior

As mentioned in section 4.4.2, several 3-inch PMTs from the latest HZC production are stored in a dark room in the physics department of NTU, are kept in black tubes, and can be illuminated by an LED through optical fibers connected to these tubes. Figure 4.33 showed a diagram of the experimental setup used in NTU to record PMT waveforms. In this setup, a XP72B22 3" HZC Photonics PMT is illuminated by a LED controlled by an external module. The LED light, of variable intensity, is carried by an optical fiber to the black tube, with a PMT - optical fiber distance of less than 10 cm. The LED module sends both the LED light and the trigger gate

to the oscilloscope simultaneously. The PMT base is a High Voltage divider from IHEP, with a single input/output cable on the PMT base. It is thus required to use a decoupling system to handle and separate the incoming high voltage powering the PMT from the PMT signal going to the oscilloscope. The nominal high voltage for this PMT was verified to be 1117 V using the PMT serial number (74548). As the PMT was powered with 1250 V, a higher PMT gain than the nominal gain of 3×10^6 is expected for the measurements. A 3 m RG/58AU Coaxial Cable ROHS TL connects the PMT output from the decoupling system to the oscilloscope to acquire the signal. Using an oscilloscope working at a 5 GHz acquisition frequency, PMT waveforms are recorded in individual text files over a 200 ns time window, leading to 1000 data points for each waveform, as well as a 0.2 ns bin width for the corresponding histogram. An example of recorded waveform is shown in Figure 4.48. In order to acquire data at different amounts of PE seen by the PMT, many LED intensities are scanned using the module, and 3000 waveforms are recorded for each of the 17 selected LED intensities.

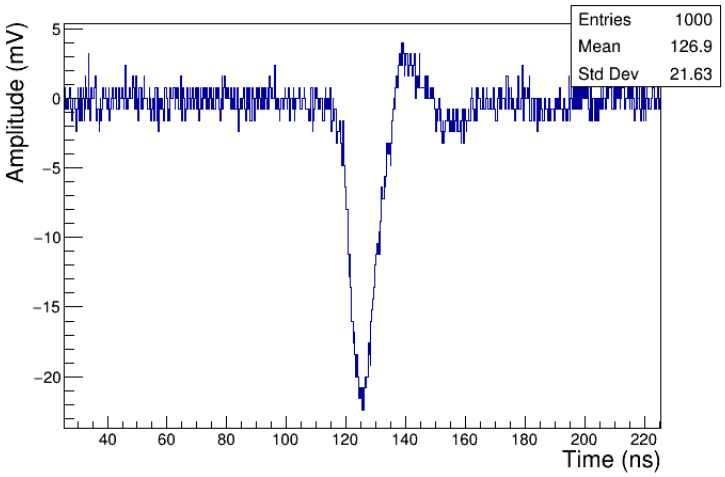

Figure 4.48: Example of a recorded waveform in a histogram.

As previously described and illustrated in Figure 4.42a, a PMT can be treated as an instrument consisting of two independent parts : a photodetector, in which the flux of photons is converted into electrons, and an amplifier (dynode system), which amplifies the initial flow of electrons. Two independent processes are therefore involved : photoconversion and electron collection, and amplification.

In the photoconversion and electron collection process, the number of photons hitting the photocathode is a Poisson distributed variable, as only a fraction of the incident photons is picked up by the PMT, while the conversion of photons into electrons (photoelectric effect) and their collection by the dynode system is a random binary process. As such, the number of observed photoelectrons can be expressed as a Poisson distribution (convolution of Poisson and binary processes) [131] :

$$P(n;\mu) = \sum_{n=0}^{\infty} \frac{\mu^n e^{-\mu}}{n!} \tag{4.5}$$

where $P(n;\mu)$ is the probability that n photoelectrons will be observed when μ is the mean number of photoelectrons collected by the first dynode.

In the amplification process, the response of a multiplicative dynode system to a single photoelectron can be approximated by a Gaussian distribution, and assuming that the amplification processes of the charges initiated by different photoelectrons are mutually independent, the charge

distribution initiated by n photoelectrons can be considered a convolution of n one-photoelectron cases [131] :

$$G_n(x) = \frac{1}{\sigma_1\sqrt{2\pi n}} e^{-\frac{(x-nQ_1)^2}{2n\sigma_1^2}} \tag{4.6}$$

where x is the variable charge, Q_1 is the average charge when one electron is collected by the first dynode (SPE case) and σ_1 is the corresponding standard deviation of the charge distribution.
The response of an ideal noiseless PMT can thus be modelled as a convolution of these two processes [131] :

$$S_{ideal}(x) = P(n;\mu) \otimes G_n(x) = \sum_{n=0}^{\infty} \frac{\mu^n e^{-\mu}}{n!} \frac{1}{\sigma_1\sqrt{2\pi n}} e^{-\frac{(x-nQ_1)^2}{2n\sigma_1^2}} \tag{4.7}$$

For a realistic PMT signal, however, various background processes have to be taken into account. Low charge processes (thermoelectron emission from the photocathode and/or the dynode system, leakage current in the PMT anode circuit, electron autoemission by electrodes, external and internal radioactivity, etc.) are involved even in the absence of a light signal and can be modelled by a Gaussian function, while some discrete processes such as photo-electrons missing the first dynode can also accompany the measured signal and can be modelled by a decreasing exponential function. The background can thus be parametrized as [131] :

$$B(x) = \frac{(1-w)}{\sigma_0\sqrt{2\pi}} e^{-\frac{x^2}{2\sigma_0^2}} + w\alpha e^{-\alpha x} \tag{4.8}$$

where σ_0 is the standard deviation of the low charge processes background distribution, w is the probability that a measured signal is accompanied by background due to discrete processes and α is the coefficient of the exponential decrease of these discrete processes.
The realistic PMT spectrum can thus be taken as the convolution of the ideal PMT signal $S_{real}(x)$ and of the background charge distribution $B(x)$: $S_{real}(x) = \int S_{ideal}(x')B(x-x')dx'$, which can be expressed as [131] :

$$S_{real}(x) = \sum_{n=0}^{\infty} \frac{\mu^n e^{-\mu}}{n!} \Bigg[(1-w)G_n(x-Q_0) + w\frac{\alpha}{2} e^{-\alpha(x-Q_n-\alpha\sigma_n^2)} \Big[erf\Big(\frac{|Q_0-Q_n-\alpha\sigma_n^2|}{\sigma_n\sqrt{2}}\Big) + sign(x-Q_n-\alpha\sigma_n^2) erf\Big(\frac{|x-Q_n-\alpha\sigma_n^2|}{\sigma_n\sqrt{2}}\Big)\Big]\Bigg] \tag{4.9}$$

where Q_0 is the pedestal charge value, Q_n is defined as $Q_0 + nQ_1$, $G_n(x)$ is defined as in Equation 4.6 but is now a convolution of the ideal PMT n-photoelectrons charge distribution with the Gaussian part of the background parametrization and has a corresponding standard deviation $\sigma_n = \sqrt{\sigma_0^2 + n\sigma_1^2}$, and $erf(x)$ is the error function.
As shown in Figures 4.49a and 4.49b, this parametrization known as the Bellamy method [131] is used to fit the charge distributions for different LED intensities, with the charge being estimated by integration of the waveforms in a 70 ns time window around the main pulse, wide enough to properly include the signal and the overshoot, ringing and settle time. In the output of the fitting process, the value Q_0 of the pedestal mean charge is already subtracted from the value Q_1 of the SPE peak mean charge. At different LED illumination regimes, low intensity in Figure 4.49a and higher intensity in Figure 4.49b, and considering a common fit method for all 17 distributions,

the values for the parameters Q_0, σ_0, Q_1 and σ_1 can be noted to be consistent. At 1250 V, the mean SPE charge is indicated to be (0.9 ± 0.1) pC, which means a linear re-scaling of the PMT gain to $(5.62 \pm 0.62) \times 10^6$. These results are presented in Table 4.1. By identifying the maximum amplitude of the waveforms and using the same fitting method, the SPE mean amplitude was estimated to be 4.5 ± 0.1 mV. If linearly re-scaled to a PMT gain of 3×10^6, the mean SPE amplitude would be 2.35 ± 0.05 mV. These values are also presented in Table 4.1.

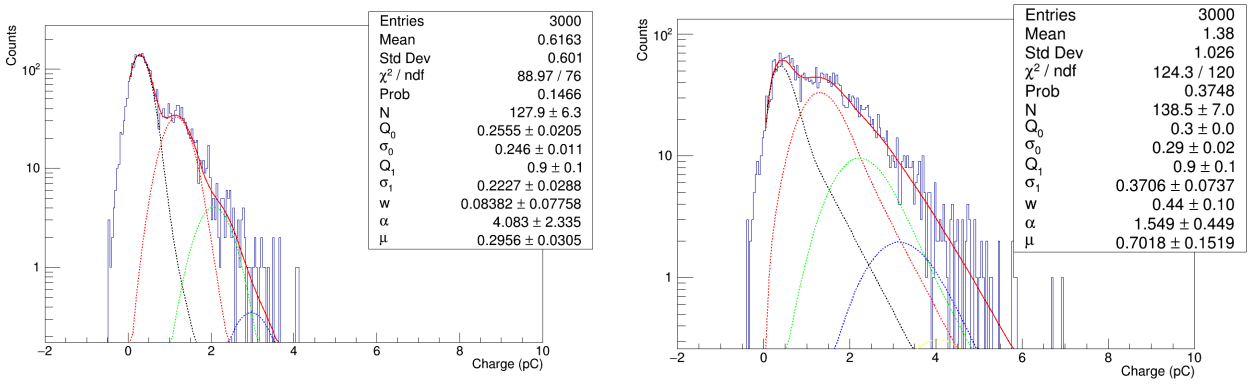

(a) (b)

Figure 4.49: (a) Bellamy fit of the charge distribution for 3000 waveforms at low LED intensity. (b) Bellamy fit of the charge distribution for 3000 waveforms at higher LED intensity.

High Voltage (V)	SPE Charge (pC)	PMT Gain ($\times 10^6$)	SPE Amplitude (mV)
1250	0.9 ± 0.1 [1]	5.62 ± 0.62 [2]	4.5 ± 0.1 [1]
Nominal HV	0.48 [3]	3 [3]	2.35 ± 0.05 [2]

[1] Measurement.
[2] Linear re-scaling.
[3] Nominal value.

Table 4.1: Investigation of the SPE charge and amplitude

These results, along with results from similar and complementary studies performed in IHEP [132] and Chile [133] are presented in Table 4.2 in a cross-checking effort to properly identify the SPE amplitude.

Investigator	Cable length (m)	Measured SPE charge (pC)	SPE amplitude at $G = 3 \times 10^6$ (mV)
NTU / LP2i	3	0.9 ± 0.1	2.35 ± 0.05
IHEP	1	0.77	2.64
IHEP	10	0.78	2.1
Chile	10	-	~ 2

Table 4.2: Cross-checking investigations of the SPE amplitude

The recorded waveforms are then fitted using a Gaussian model and a baseline function, the charge computation from such a fit ignoring the systematic undershoot observed in the recorded waveforms. Figure 4.50a shows an example of such a fitted waveform, with inverted amplitude values for an easier reading of the analysis. In terms of charge equivalents, many waveforms contribute to pedestal measurements, as there is a non-null probability that the PMT collects

0 PE, for any threshold of LED illumination. As such, an event selection is performed to select waveforms with well-defined main pulses, by requiring of the maximum amplitude of the waveform to exceed the selection threshold $Threshold_{select} = b + 5 \times RMS_b$, where b is the waveform baseline (mean amplitude computed over 40 ns) and RMS_b is the RMS of this amplitude distribution. The Gaussian fit has proven to be an effective choice for the parametrization of these waveforms, Figure 4.50b showing the charge measurement obtained by directly integrating the waveform as a function of the charge measurement obtained by integrating the Gaussian fit function. The slope parameter of the linear fit of this distribution is shown to be compatible with 1, indicating a robust match between the data and the model, despite the undershoot in the waveform.

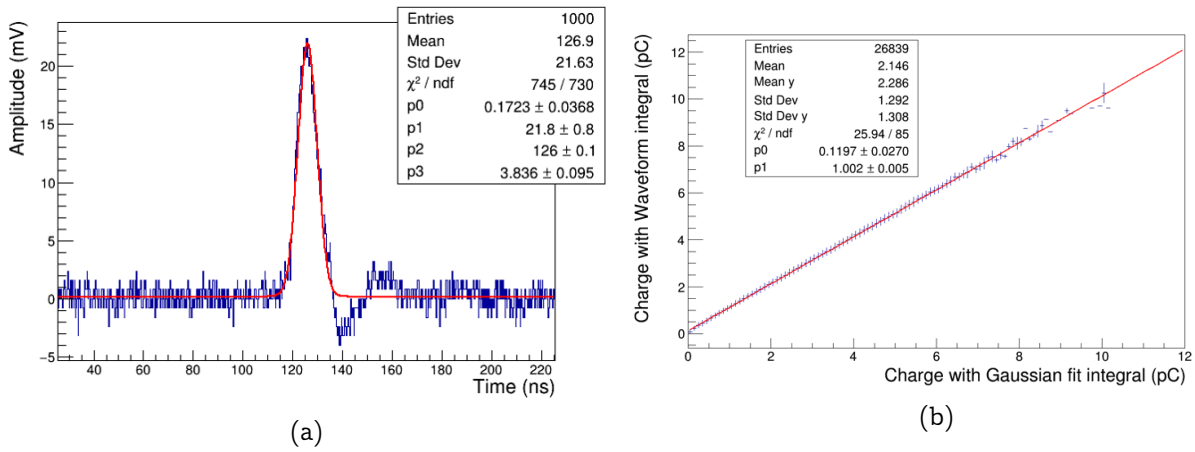

Figure 4.50: Gaussian fit of PMT waveform (a) Example of a fitted waveform. (b) Charge measured by integration of the waveform as a function of the charge measured by integrated the Gaussian fit. Fitted with linear model, the slope parameter is compatible with 1, showing that the Gaussian fit is a robust choice when compared to waveform integral.

Interesting parameters can be extracted from the waveform Gaussian fits. Figure 4.51 shows the rise time of the Gaussian fit as a function of the Gaussian charge, with a mean rise time of ∼6 ns at larger charge values and fluctuations around this mean value.

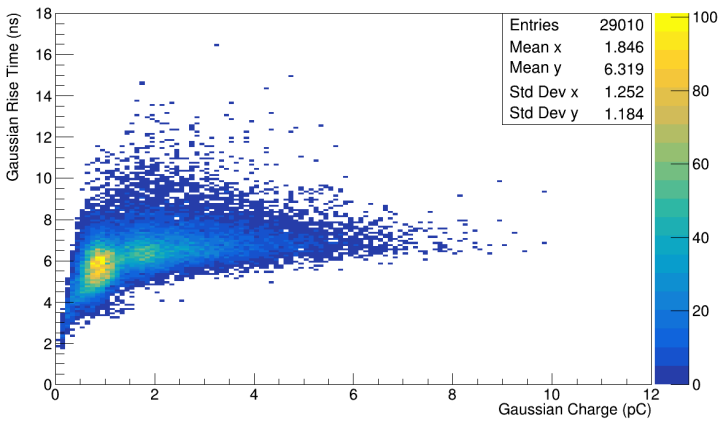

Figure 4.51: Rise time as a function of the Gaussian charge. After the peak in statistics of SPE events, the rise time quickly tends towards an almost constant value of ∼6 ns.

The amplitude of the Gaussian fit as a function of the Gaussian charge is shown in Figure 4.52a,

with a seeming linearity in its evolution. Taking larger bins on the X-axis and projecting this 2-D distribution on the Y-axis for each bin on the X-axis results in Figure 4.52b, able to be fitted with a linear model. The Y-values of the data points correspond to the mean values of the Gaussian amplitude distributions for each Gaussian charge bin, while the error bars correspond to the RMS of these distributions. A small bias can be observed on the value of the intercept parameter of the linear model, possibly due to the waveform selection having a threshold of ∼2 mV, nevertheless compatible with 0 considering the uncertainty on the parameter value. Large uncertainties on the value of the slope parameter can be observed as well, due to the spreads on the amplitude distributions for each considered charge interval in Figure 4.52a, but this function can nonetheless act as a charge-to-amplitude conversion function.

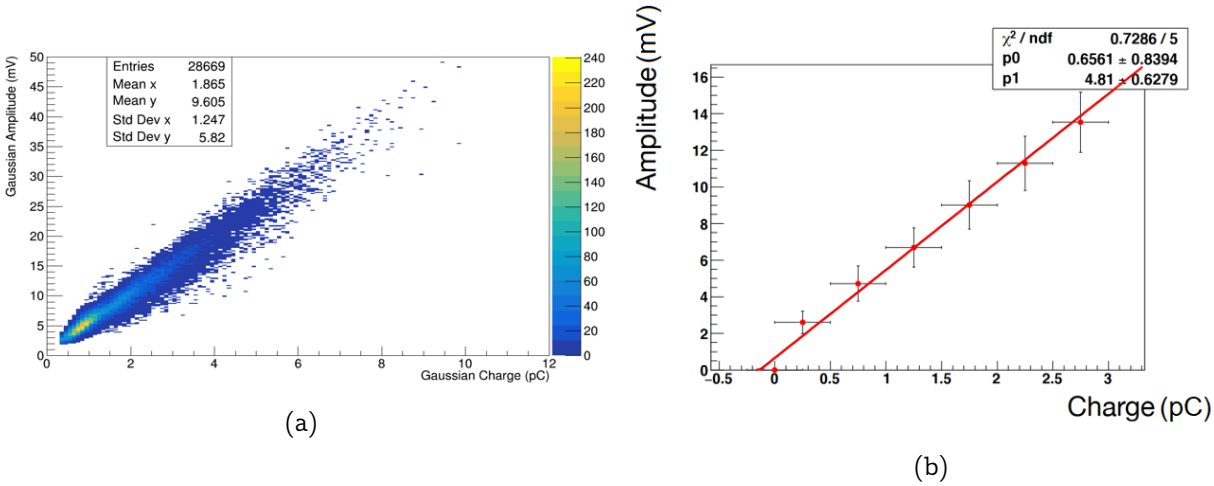

Figure 4.52: (a) 2-D distribution of the amplitude of the Gaussian fit as a function of the Gaussian charge for all considered waveforms. (b) 1-D distribution of the amplitude of the Gaussian fit as a function of the Gaussian charge for all considered waveforms. The data points are a result of the projection on the Y-axis of the 2-D distribution for each bin on the X-axis, with the mean value of each distribution as the Y-value of the data point and the RMS as the error bars. The 1-D distribution is then linearly fitted.

4.5.3 Trigger time and time walk

As was detailed in section 3.5.1, the time at which the CATIROC ASICs will trigger on PMT signals depends greatly on the amplitude of such signals. A simplified explanation would be that the time at which the fast shaper output signal exceeds the fixed trigger threshold discriminator value depends on the PMT pulse amplitude, as is illustrated in Figure 4.53. As the amplitude varies, whether it is because of a different number of photoelectrons collected or because of small variations in the PMT signal at identical NPE, the timing of the signal shifts, and as such, variations in signal amplitude can spoil the timing distribution. This phenomenon is called "time walk", and has been measured in the OMEGA laboratory in France to be ∼5 ns, at a preamplifier gain of 20, for injected signals with charge equivalents from 160 fC (1 PE at gain 10^6) to 1.6 pC (10 PEs at gain 10^6). It is the range of the possible values of trigger time. Despite many different contributions to differences in event times being registered for different PMTs, such as cable lengths, routing, these differences are constant differences and can be calibrated and taken into account during analysis. Two contributions to event time differences are not constants : PMT TTS and electronics trigger time.

Measurements of CATIROC trigger time were performed by injecting a signal from a pulse gen-

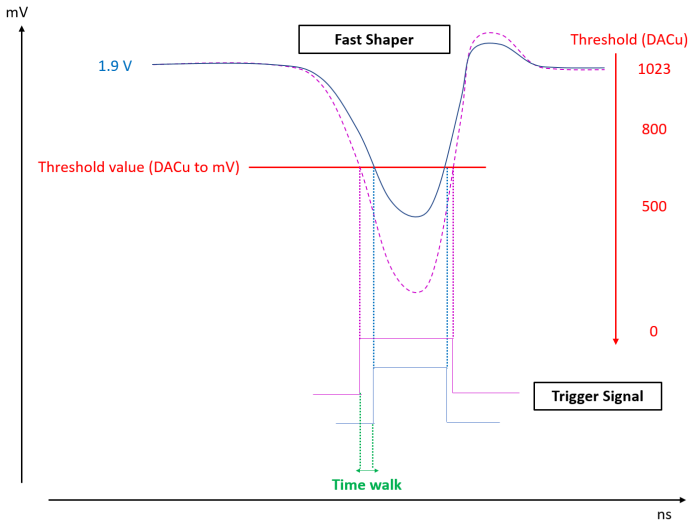

Figure 4.53: Impact of the amplitude of the signal on the trigger time of CATIROC.

erator resembling the waveforms recorded in NTU. The rise time (6 ns), fall Time (6 ns) and width (8.5 ns) have been estimated from these waveforms in order to study the trigger time with as close to a SPMT output as possible. Figure 4.54a shows a typical signal in output of the pulse generator, while Figure 4.54b shows the measurement of the trigger time Δt between the pulse generator trigger signal and the CATIROC trigger signal of the injected channel.

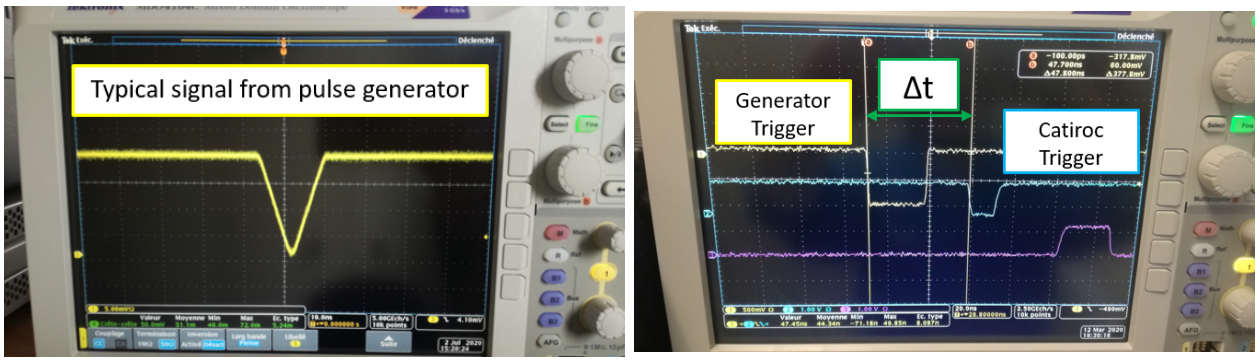

(a) (b)

Figure 4.54: Signal injection for trigger time measurements (a) Typical signal from pulse generator designed to approach PMT waveform. (b) Measurement of the trigger time Δt between pulse generator trigger signal and CATIROC trigger signal of injected channel.

The measurement procedure involved varying the signal amplitude and taking 200 measurements for each amplitude of injected signal. The Δt distribution obtained was then fitted with a Gaussian model and the mean value of the fitted model is taken as a data point to represent the trigger time as a function of the signal amplitude. Figure 4.55 shows the evolution of the trigger time with the signal amplitude for several trigger thresholds in the same channel, in order to estimate the sensibility of the trigger time to the trigger threshold DACu value. Thresholds corresponding to 1, 1/2, 1/3 and 1/4 PE were selected, after having been identified with the 50% trigger efficiency method. With a non-negligible ~1 ns difference in trigger times for close thresholds, the following

measurements for characterization will be performed at the threshold value equivalent to 1/3 PE in the corresponding channel.

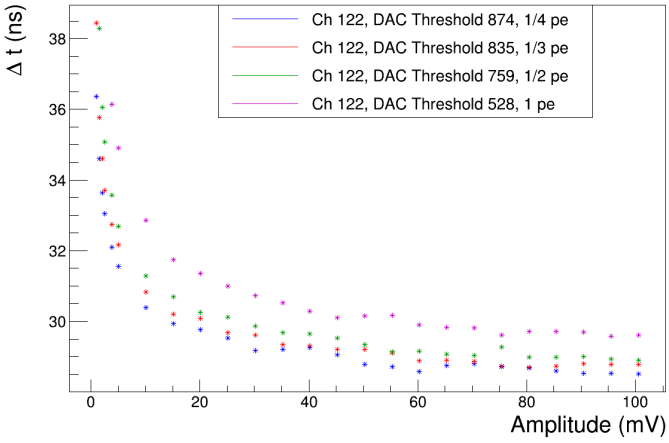

Figure 4.55: Trigger time as a function of the signal amplitude in arbitrary channel 122, for multiple trigger thresholds values.

In order to evaluate if the trigger time behaves differently with the signal amplitude in different channels, the 50% trigger efficiency threshold for 1/3 PE charge equivalent was identified in several channels according to the procedure detailed in section 4.3.5.1, and the evolution of the trigger time with the signal amplitude in each channel was compared. 2 channels (122 and 115) were selected from the same ASIC (ASIC 7), with one channel each from ASICs 6 (102), 5 (92), and 4 (72), in order to map the SAMTEC side of the ABC V0 board. Figure 4.56a shows the evolution of the trigger time with the signal amplitude in these channels, as well as a common behavior between all channels, with an apparent offset between the absolute values of the trigger times. Figure 4.56b illustrates this apparent offset by showing the difference, for each amplitude injected, of the trigger times between channels 122 and 115. The behavior of the data points can be considered as constant.

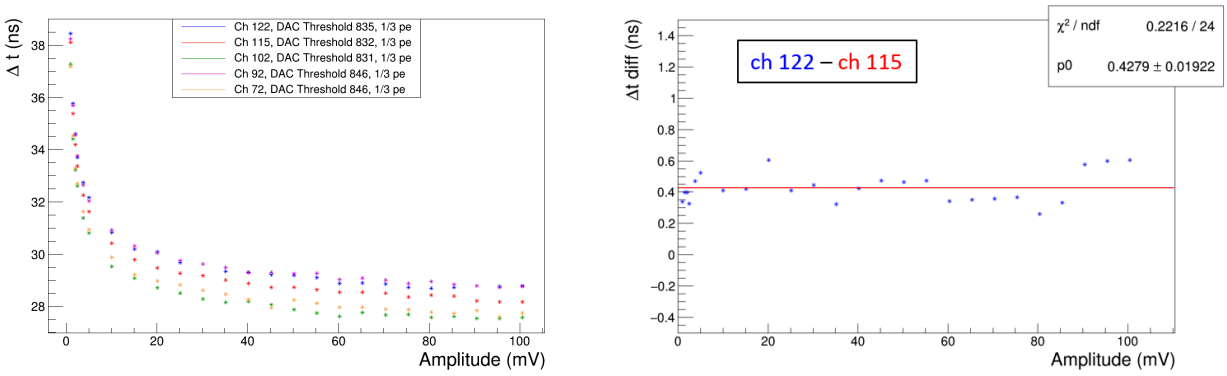

(a) (b)

Figure 4.56: Behavior of the trigger time in different channels. (a) Trigger time as a function of the signal amplitude. (b) Difference between the trigger time values in 2 different channels.

The evolution of the trigger time with the signal amplitude seems to have the same behavior in all channels, and this offset (the absolute value of which depends on the pair of channels investigated)

can be calibrated and corrected like cable lengths.
Figure 4.57a shows the evolution of the trigger time as a function of the signal amplitude in one arbitrary channel (122), with a configuration using a trigger threshold of 1/3 PE and a preamplifier gain of 40. The results are fitted with a model consisting in two decreasing exponential functions and an asymptote at large amplitudes. The fit function, expressed in Equation 4.10 is also shown in Figure 4.57a.

$$f(x) = e^{p0+p1\times x} + e^{p2+p3\times x} + p4 \tag{4.10}$$

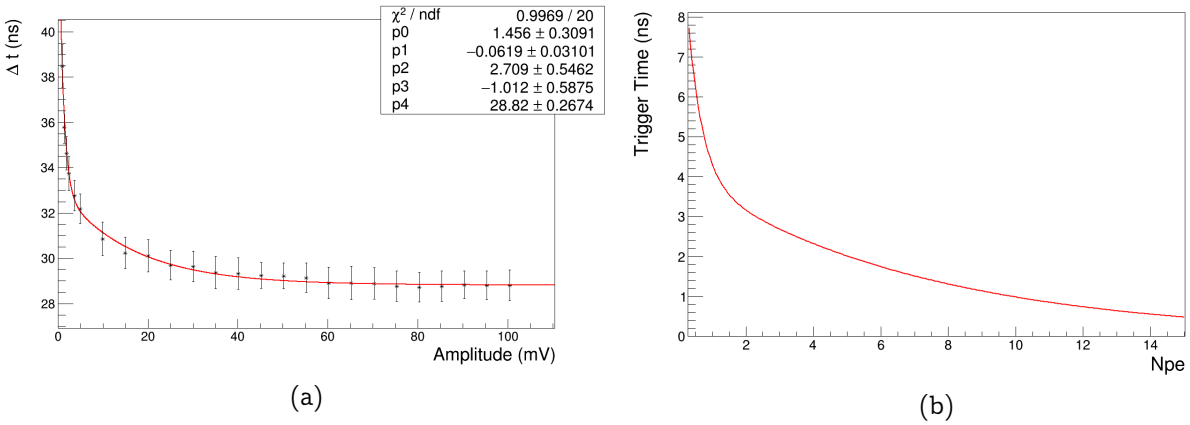

Figure 4.57: Parametrization of the trigger time as a function of the signal amplitude for a preamplifier gain of 40. (a) Direct amplitude-to-trigger time parametrization from data points. The absolute value of the trigger time is irrelevant, its behavior with the signal amplitude being the main interest. (b) Trigger time parametrization function taken as tending to 0 as the amplitude of the signal increases, and expressed as a function of the injected charge equivalent in number of photo-electrons.

As shown in Figure 4.57b, the constant parameter in Equation 4.10 can be taken to be 0. The absolute value of the trigger time is only an offset, visible in the asymptote of the function at large amplitudes. The final function gives the mean value of the trigger time for a given signal amplitude.

4.5.4 Processing consecutive PMT signals with CATIROC

4.5.4.1 CATIROC dead times

Two dead time contributions within the CATIROC ASIC have been identified [126]. The first contribution ($T_{DeadTime}$, a few μs) is due to the digitization of the charge and of the fine time, while the second contribution (~100 ns order of magnitude) is related to the trigger treatment. The dead time $T_{DeadTime}$ has been computed to reach up to 6.4 μs and 9.3 μs depending on the number of channels to readout. This is including the mitigation allowed by the use of a SCA with two layers of charge holding ("ping" and "pong" events), which implies that up to two signals can be read out without losses if they arrive within $T_{DeadTime}$ while a third signal in the same time window will be lost in the data stream. This is illustrated in Figure 4.58, with the red dots on the upper level representing the "ping" events and the red dots on the lower level representing the "pong" events. The greyed areas following the events represent the dead time, with the crossed-out

grey dot representing an event arriving after both the "ping" and "pong" levels have been filled, and so within that dead time.

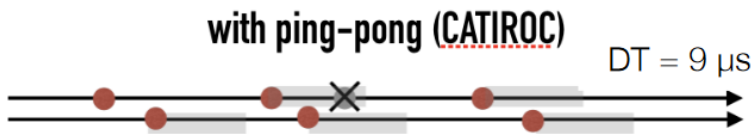

Figure 4.58: Signal digitisation dead time with ping/pong system. If 3 triggered signals arrive at less than 9.4 μs, the third one is not digitised and the measured charge will not be observed in the data stream.

This loss of events is however mitigated by the presence of a second data stream, in a system known as the Discriminator Data Stream (DDS). The output of the discriminator generating the trigger signal does not suffer dead-time due to the lack of subsequent signal digitisation. The information about the rising edge and the falling edge of this trigger signal (and so the time over threshold, which is proportional to the amplitude of the signal) is thus continuously sampled by the FPGA at a period of 2 ns, which leads to an estimation of the charge and to the preservation of the time information at the cost of a worse resolution than the time measured by CATIROC and digitized. From the previous example in Figure 4.58, a signal arriving after "ping" and "pong" are both unavailable will thus not be completely lost. While the charge information will indeed not be recorded, charges ranging from 0.3 PE to 2.5 PE can still be measured and the time information of this event will be saved in the DDS. Figure 4.59 illustrates this case, with the first two lines representing the memories of "ping" and "pong" and the third line representing the DDS. The empty circles in the DDS correspond to events that have been properly recorded in "ping" or "pong", while the red circle corresponds to an event that would not have been recorded in "ping" and of which the time information is saved in the DDS.

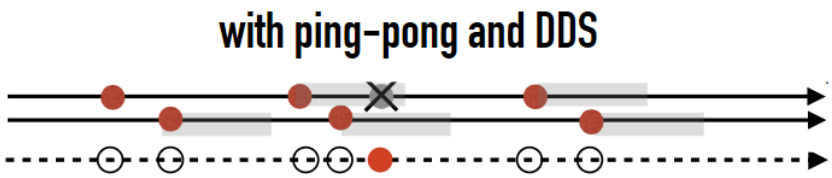

Figure 4.59: CATIROC DDS system, completing the ping/pong system. If 3 triggered signals arrive at less than 9.4 μs, the third one is not digitised and the measured charge will not be observed in the data stream, but its time information will be saved in the DDS regardless.

As described in section 3.5.1, the trigger is delayed to store the analog charge in the analog memory and is used to create the TAC ramp for time measurement. The treatment of this trigger in the analog part of the circuit introduces the second contribution of dead time, called $T_{TrigDeadTime}$. To precisely measure this dead time, a burst of two consecutive pulses is injected with a period P of 1 ms and a time separation ΔT between the two pulses varying between 15 ns and a few hundreds of ns. The obtained trigger efficiency curve is shown in Figure 4.60 [126].
A value of 1 shows the two pulses being triggered and processed as separate signals, while a value of 0 means only one trigger was detected. As is apparent in Figure 4.60, 2 pulses arriving with a ΔT larger than 90 ns will always be detected as separate signals and the charge will be measured

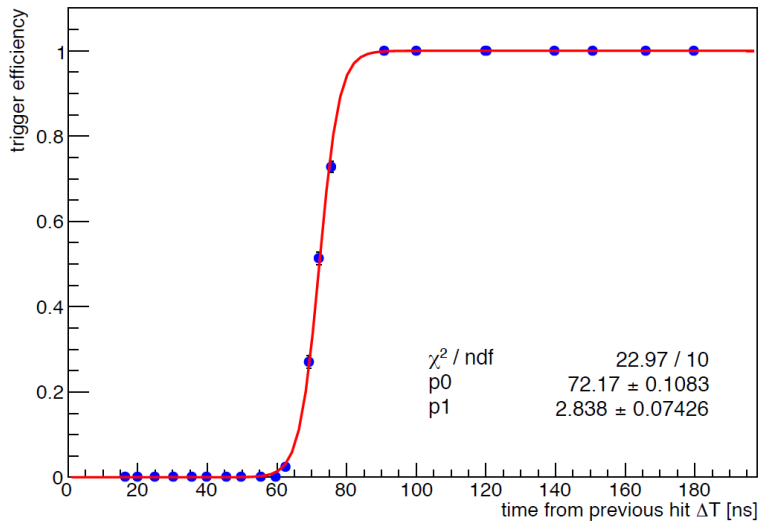

Figure 4.60: Trigger efficiency as a function of the time separation between two consecutive hits : any hit arriving within about 60 ns from the previous one will not produce an independent trigger signal and the associated charge may sum up to the previous hit. [126]

in the digital part of CATIROC. This is not always the case below 90 ns and for a $\Delta T < 60$ ns, the second pulse is not treated by the digital part of the trigger. No independent charge measurement is produced, but the charge of the second pulse sums up to the first hit depending on their relative time difference (charge acceptance).

4.5.4.2 Charge acceptance

In order to measure the charge acceptance as a function of the time separation between two consecutive pulses or signals, meaning the fraction of charge that is still measured even though the second pulse has not been triggered, a burst of two identical pulses was injected, with a period P of 1 ms and a time separation between the two pulses ΔT varying from 15 to 100 ns. q_1^* and q_2^* are defined as the charges measured by CATIROC, while q_1 and q_2 are the "true" corresponding values. In the event of the 2 signals triggered independently, $q_1 = q_2$. Depending on the time separation between the two signals, two cases have to be considered.
In the first case, $\Delta T < T_{TrigDeadTime}$, and only the first signal of each burst is triggered. The measured charge q_1^* may include a fraction of the charge of the second pulse :

$$\begin{cases} q_1^* = q_1 + \alpha(\Delta T, RC) \cdot q_2 \\ q_2^* = 0 \end{cases} \tag{4.11}$$

with $0 \leq \alpha(\Delta T, RC) \leq 1$ and α referred to as the charge acceptance. This fraction will depend on the time overlap between the two pulses as well as on the RC shape of the slow shaper, and its evolution with the time is shown in Figure 4.61a for RC values 50 and 100. The empty markers refer to injected signals with a width of 10 ns (default signal width), while the full markers refer to tests performed with a signal width of 4 ns. Two vertical separations are shown, which correspond to the slow shaper peak time (maximum of charge measurement) for both RC values.
For signal separations smaller than 15 ns, we assume the function to extrapolate up to $\alpha = 1$ for $\Delta T = 0$. All the consecutive hits arriving within $T_{SSH_{peak}}$ and $T_{TrigDeadTime}$ will not be detected,

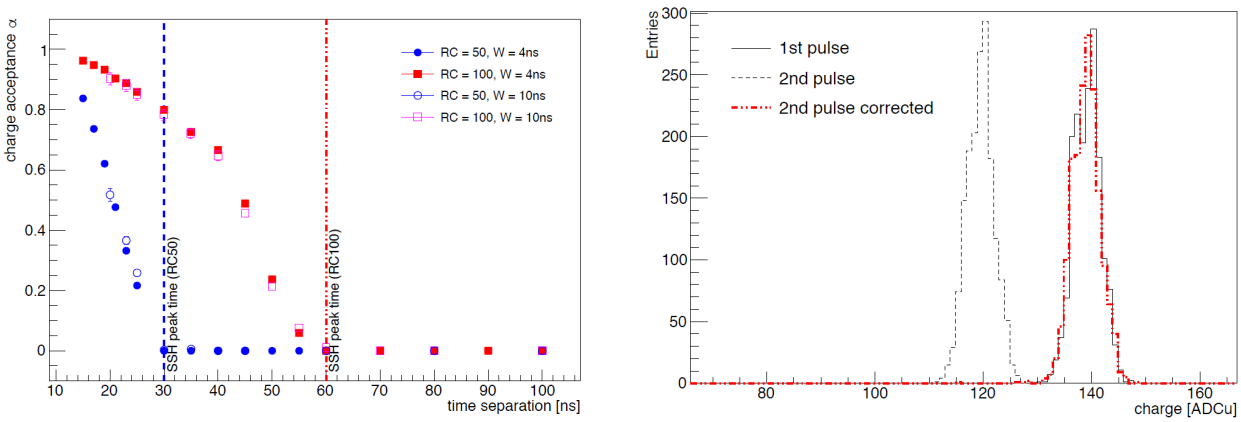

(a) (b)

Figure 4.61: (a) Charge acceptance for RC=50 (circle) and RC=100 (square) as a function of the separation time between pulses. Empty (filled) markers refer to points taken with a signal width of 10 (4) ns. The dashed lines indicate the SSH peak time for both RC values. (b) Charge distribution for first hit (solid line) and second hit (thin dotted), for $\Delta T = 100$ ns. The red dashed line shows the charge of the second hit after applying the correction for the bias introduced by the SSH undershoot. [126]

and the charge acceptance will be $\alpha = 0$.
In the second case, $\Delta T > T_{TrigDeadTime}$, and the two hits are triggered independently. However, the undershoot of the first slow shaper signal acts as an offset for the second slow shaper signal, impacting the charge measurement. This indeed induces an underestimation of the measured charge ($q_2^* < q_2$),

$$\begin{cases} q_1^* = q_1 + \alpha(\Delta T, RC) \cdot q_2 \\ q_2^* = q_2 - \kappa(\Delta T, RC) \cdot q_1 \end{cases} \tag{4.12}$$

where $\kappa(\Delta T, RC) < 0$ models the SSH signal (in ADCu) normalized to a peak amplitude equal to 1. Since the shape of the SSH normalized signal is preserved (for a given channel and RC value), it is possible, for each hit, to retrieve the "true" charges, correcting for the modeled $\kappa(\Delta T, RC)$. As illustrated in Figure 4.61b with the corrected charge distribution for a second signal delayed from the first signal by 100 ns, this correction yields very satisfying results [126].

4.6 Conclusion

After a brief exposition of the firmware and software responsible for the data acquisition, this chapter first presented a study of the standalone performances of the ABC board. Pedestal measurements were discussed, followed by a study of the excellent charge linearity of the CATIROC ASIC, an example of charge calibration for an ABC board and a study of the time resolution of the ABC board, negligible before the TTS of the PMTs. Crosstalk studies were conducted and presented, concluding that the charge measurements of the SPMT system should not result in any crosstalk, even for higher energy events such as a couple of muons. Finally, the 50% efficiency trigger identification method was detailed, with implications on the measurement of SPE signals and PMT performances.

Such studies were followed by a description of the test benches developed in France for combined tests of the SPMT electronics, along with performance studies which amount to a large portion of the work presented in this thesis. 32 PMTs were first tested simultaneously in France, with in-depth PMT performance studies performed at LP2i showing a compatibility with the reference HZC measurements within 15% as well as deviations in performances depending on the ABC board channel within 10%. The test benches were sent to GXU for the mass testing of the SPMT production. A 128-channels test bench was then developed in France to verify the simultaneous data acquisition of 128 PMT signals, reaching several important milestones for the SPMT system. 128 PMT SPE charge spectra were acquired simultaneously for the first time, and PMT performance studies showed very satisfying results well within the requirements set by the JUNO collaboration.

In the last section, the processing of a PMT signal by the ABC board, more precisely by the CATIROC ASICS, was presented. From the PE collection resulting in PMT waveforms, the behavior of such waveforms was investigated resulting in a charge-to-amplitude parametrization and an amplitude-to-trigger time parametrization when studying the response of the electronics to a PMT signal. How consecutive signals are processed by CATIROC was also presented.

This knowledge on the response of the electronics to PMT signals will be implemented in the JUNO simulation in the following chapter, with studies conducted on charge and time measurements to quantify the impact of the SPMT electronics on physical measurements.

Chapter 5

Implementation of the performances of the SPMT system in the JUNO simulation - Study of impacts on the charge and time measurements

Contents

5.1 Introduction **155**
5.2 SPMT simulation **156**
5.2.1 Electromagnetic interactions and optical properties 156
5.2.2 SPMT electronics in SNiPER 158
5.3 Impact of SPMT electronics on the reconstructed charge **162**
5.3.1 Introduction and discussion : Muon studies with trigger deadtime, charge acceptance and charge digitization deadtime 162
5.3.2 Reconstructed charge using ^{12}B events 165
5.4 Impact of SPMT electronics on the measured time **169**
5.4.1 Introduction : CATIROC trigger time spread vs PMT TTS 169
5.4.2 Vertex reconstruction with the SPMT system 171
5.4.2.1 Vertex reconstruction method 171
5.4.2.2 Toy Monte Carlo for statistical limitation with SPMTs, first results 176
5.4.2.3 Impact of the electronics on the reconstruction 178
5.5 Conclusion **181**

5.1 Introduction

Precise studies on the performances of the ABC front-end board were presented in Chapter 4, including studies on how a PMT signal is processed within the ABC board with precise parametrizations of CATIROC features such as the trigger time and time walk, the trigger deadtimes and the charge acceptance.

Such intricate knowledge of the SPMT electronics is important for the implementation in the JUNO simulation of the correct response of the SPMT system. This chapter will address this implementation as well as the impact of the response of the PMT system on physical studies involving the charge and time information of simulated events.

Section 5.2 will introduce the framework of the JUNO simulation, with section 5.2.1 presenting the simulation of the detector and section 5.2.2 focusing on the addition of the SPMT electronics

to the simulation. The impact of the SPMT electronics on the charge reconstruction will then be addressed in section 5.3. The impact of a few key CATIROC features on muon events will be investigated in section 5.3.1, and a more complete study of how the SPMT electronics affect the charge measurement will be conducted in section 5.3.2 using a continuous energy spectrum of ^{12}B events. Finally, the impact of the SPMT electronics on the measured time will be studied in section 5.4. A comparison of the CATIROC trigger time with the TTS of the SPMTs will be presented in section 5.4.1, while the development and application of a vertex reconstruction method to evaluate the impact of the SPMT electronics on the measured time will be detailed in section 5.4.2.

5.2 SPMT simulation

For its simulations and event analyses, the JUNO collaboration uses a software framework [134] based on the Software for Non-collider Physics Experiments (SNiPER) framework [135]. SNiPER was developed as a general framework to meet the requirements of both reactor electron anti-neutrino experiments and cosmic ray experiments, and is a modular framework consisting of many dynamically loadable plug-ins written in C++. The Python language is also used for the implementation of a user interface which calls these plug-ins. Additionally, the JUNO software uses the Geant4 [136–138] and the ROOT [139] libraries.
The JUNO software uses a multi-staged approach in its event treatment, which can be divided into the simulation part and the reconstruction part. Both parts use the same coordinate system, with the center of the Central Detector acting as the origin, the Cartesian Z-coordinate pointing upwards from the detector center towards the chimney and the X- and Y-coordinates arranged perpendicular to the Z-axis in arbitrary, but fixed, directions. Only the simulation part of this approach will be addressed in this section, and as the development of the JUNO software is still ongoing, properties of the simulation are expected to be modified.

5.2.1 Electromagnetic interactions and optical properties

The simulation part of the JUNO software comprises several stages, such as the physics generator and the detector simulation (DetSim), with the electronics simulation (ElecSim) stage also implemented in the case of the LPMT system. This structure is illustrated in Figure 5.1, in which the three main stages of the simulation are presented in separate blocks. The electronics simulation block is illustrated in the case of the LPMT system, while the implementation of the ElecSim stage of the simulation for the SPMT system will be addressed in the following section.
The physics generator (blue block in Figure 5.1) produces the particle list to be simulated. In addition to a simple particle gun, which allows the placement of particles with defined properties in the JUNO detector, various generators were implemented in the simulation, suited for different studies in the JUNO experiment. Such implemented generators include generators for isotope decay simulations such as the β^--decay of ^{14}C as well as generators for positron-neutron pairs resulting from an IBD reaction, following the expected JUNO spectrum.
The DetSim stage (orange block in Figure 5.1) simulates the propagation and the interactions of the generated particles inside the JUNO detector, based on the Monte Carlo (MC) simulation by the Geant4 framework [136]. To simulate this propagation and these interactions, a model of the detector and its components (all sub-systems described in Chapter 2) was implemented in detail in Geant4, and different sets of particle interactions to be simulated, called Physics Lists, can be required of Geant4 by the user. If a particle produces ionization energy, the optical photons from the scintillation and Cherenkov lights are also propagated by the simulation in the liquid scintillator (LS). Conforming with the properties of the LS described in section 2.4, the complex

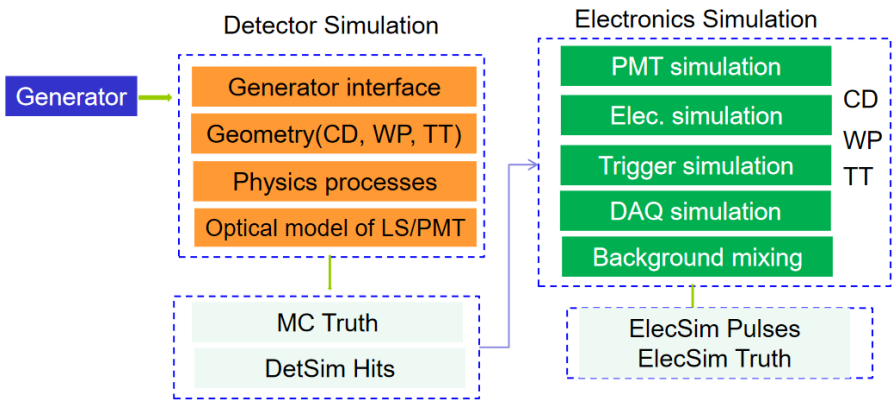

Figure 5.1: JUNO simulation software, in which the detector simulation was developed based on Geant4 within the SNiPER framework. Each of the Central Detector (CD) (which contains the LPMT and SPMT systems), Water Pool (WP) and Top Tracker (TT) systems has its own electronics simulation.

absorption and re-emission processes of optical photons are reproduced in the simulation. However, the large size of the CD and the high photon yield of the scintillator make the JUNO optical photon simulation extremely computationally challenging with regard to both processing time and memory resources. As such, optimizations to the Geant4-based optical photon simulations were implemented [140], making use of Opticks, an open source project, to integrate state-of-the-art NVIDIA GPU ray tracing to these simulations and accelerate them by factors exceeding 1500 when compared to single threaded Geant4 simulations. Simulated Cherenkov and scintillation photons from a 100 GeV muon travelling across the JUNO Central Detector are shown in Figure 5.2.

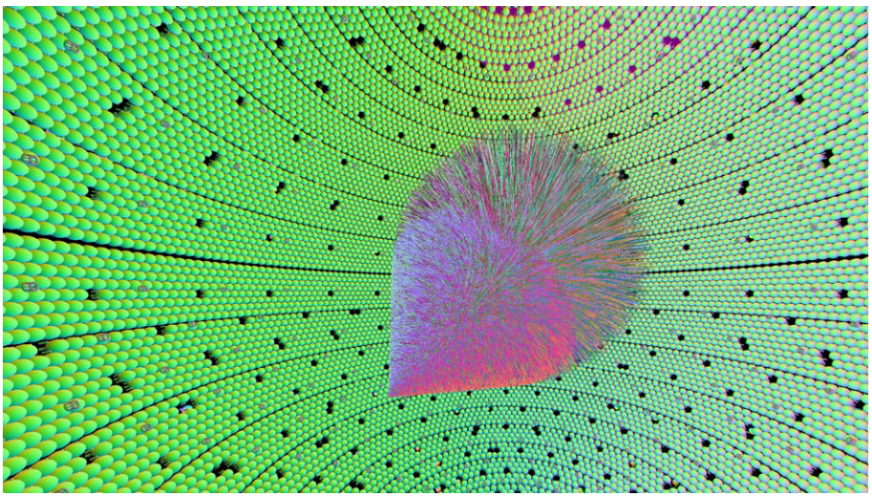

Figure 5.2: Simulated Cherenkov and scintillation photons from a 100 GeV muon travelling across the JUNO antineutrino detector viewed from inside the spherical scintillator. Primary particles are simulated by Geant4, generation "steps" of the primaries are transferred to the GPU and photons are generated, propagated and visualized all on the GPU. Photons that hit PMTs are returned back to Geant4 to be included into standard hit collections. Photon colors indicate the polarization direction. [141]

During the propagation process, if a photon reaches the photocathode of a PMT, the photoelectric effect responsible for the emission of photoelectrons is reproduced. In the case of the SPMT

system, it is reproduced according to the correct XP72B22 PMT geometry (section 2.5.3) and to the Quantum Efficiency (QE) of the SPMTs as a function of the wavelength. As the QE at 420 nm has been measured for the entire SPMT production (Figure 2.14 in section 2.5.3), these values have been implemented in the simulation at the DetSim level and each SPMT has randomly been assigned a given QE value.
The output of the DetSim stage for the SPMT system is thus a set of PMT hits which represent PEs released from the photocathode, but not amplified by the PMTs, as only the QE of the PMTs is taken into account. The full response of the SPMTs will be added at the level of ElecSim.

5.2.2 SPMT electronics in SNiPER

The several features of the electronics of the SPMT system were implemented at the ElecSim level, the purpose of which is to simulate the behavior of the PMT itself as well as the PMT readout electronics.
As described in section 2.5.3, 25600 SPMTs will be installed around the acrylic sphere in the JUNO experiment. As such, 25600 positions for the SPMTs in the simulation were optimally selected [142] out of the initially planned 36571 positions. From the 560 possible UWB positions also provided by the installation company, 200 were selected and a preliminary mapping to connect SPMTs and UWBs was developed. The SPMT positions selection was optimized in order to guarantee the uniformity of the PMT density. Considering events located at the center of the sphere, a barycenter reconstruction using an increasing number of randomly hit PMTs showed a small bias in (X,Y,Z) of $\sim$(9,6,8) mm, over a sphere of 17.7 m diameter. The chosen 25600 SPMTs positions are now implemented in the simulation and the connection SPMT/UWB is taken into account at the level of ElecSim.
In addition to the selection of the SPMT positions, the SPMT characteristics are also implemented at the level of ElecSim according to the mass production measurements presented in section 2.5.3. As shown in Figures 2.14 and 2.15, the SPE resolution (33.17% mean value) and the Dark Counting Rate (DCR) at 0.25 PE ($<$ 1.8 kHz) have been measured for the entire SPMT production whereas the TTS has only been measured for $\sim$3% of the PMTs (1.5 ns mean value). Each PMT was thus assigned a randomly drawn DCR value over the distribution, while the mean value of the TTS and of the SPE resolution are currently assigned to every SPMT. In future versions of the simulation, performances will be assigned per PMT from a database.

SPMT response simulation In order to simulate the response of the SPMTs and the merging of the collected PEs into single high-charge hits in a realistic way, all hits from the DetSim stage of the simulation are time aligned for each PMT. To account for the TTS of the PMTS, each of these PEs released from the photocathode will have their associated hit time impacted by an additional time randomly drawn over a Gaussian with a mean value of 49 ns and a σ of 1.5 ns.
As described in section 4.5.1, consecutive PEs collected by a PMT in a short time window will contribute to the same waveform and are seen as a unique signal with a higher amplitude and charge. From the mean rise time of the waveforms recorded in section 4.5.1 (Figure 4.45b), which indicated that all PEs resulting from high energy events were collected within a short time window and contributed to the same waveform, and from the waveforms widths shown in section 4.5.2 (Figure 4.51), of about 6 ns for SPE events, it is a reasonable assumption to consider a 10 ns time window to group subsequent collected PEs into a single signal with an associated number of PE corresponding to the sum of all the hits in this time window. A 10 ns-wide grouping of PEs will thus be treated in the simulation as a single event, and will be referred to as a "cluster". The hit time associated to this cluster corresponds to the hit time of the first PE in the cluster.
The charge response of the PMTs for clusters of PEs is then modelled according to a Gaussian

function. For a cluster of N collected PEs, according to PMT physics, the mean charge q_N and the resolution of the charge distribution R_N can be written as :

$$\begin{cases} q_N = N \times q_{SPE} \\ R_N = \frac{R_{SPE}}{\sqrt{N}} \end{cases} \tag{5.1}$$

where q_{SPE} is the nominal charge of SPE events and is equal to 0.48 pC at a nominal PMT gain of 3×10^6, and R_{SPE} is taken to be the mean SPE charge resolution of 33.17% assigned to each SPMT in the simulation. Depending on the generated PMT signal (N collected PEs), its equivalent charge will thus be drawn over a Gaussian distribution with parameters q_N and σ_N written as :

$$\begin{cases} q_N = N \times q_{SPE} \\ \sigma_N = \frac{R_{SPE} \times q_{SPE} \times \sqrt{N}}{100} \end{cases} \tag{5.2}$$

The signal amplitude is then directly derived from the signal charge according to the SPMT charge to amplitude parametrization described in section 4.5.2 and shown in Figure 4.52b.
The computed charges and times correspond to the input of the simulation of the CATIROC ASIC features.

CATIROC features simulation The characteristics of the CATIROC ASIC have been extensively measured [126] and have been described in section 3.5.1 and section 4.5.4. They were implemented in the simulation at the ElecSim level and are regularly updated in the light of new measurements.
For each cluster of simulated hits and its associated hit time (hit time of the first PE in the cluster), the trigger probability of CATIROC (section 4.5.4.1) is computed depending on the time difference between this cluster and the previous one. A cluster of hits will be referred to as a "signal". If a signal was previously triggered and recorded in the ~60 ns preceding the considered signal, this signal will not be triggered, and if the time difference between both signals is larger than 90 ns, both will be triggered independently. In the event of two consecutive signals recorded between 60 ns and 90 ns, the trigger probability is determined according to the function shown in Figure 4.60, and was implemented as such in the simulation. For the triggered signals, the time information is saved in the DDS, and the charge will be stored in the ping or pong capacitors depending on their availability.
If the cluster of hits is not triggered, a fraction of its charge can still be measured and added to the previous registered signal. The charge acceptance of CATIROC, described in section 4.5.4.2 and shown in Figure 4.61a, is implemented in the simulation with a parametrization for both RC values 50 and 100.
As previously mentioned, and described in section 3.5.1, the charge can only be registered when the ping or pong capacitors are available, each one having a dead-time of up to 9.4 μs. The maximum value of this charge digitization dead-time is implemented in the simulation with an initial testing of the ping/pong availability. According to the trigger rate (physical events and dark noise), the probability of having a signal in the 10 μs preceding the first signal from simulation hits is determined, and depending on this probability, the ping and pong availability is randomly estimated. If ping is determined to be unavailable, the first registered signal will occupy pong, and if neither is available, the time of the triggered signal is registered in the Discriminator Data Stream (DDS) but the charge is lost. A rate of 600 Hz is currently used to compute this probability, a bit

pessimistic when compared to the mean DCR value of the 25600 SPMTs (512.2 Hz, Figure 2.14) in order to test the worst case scenario of the SPMT electronics.
An example of the application of the CATIROC features on the clustered simulation hits, aligned in time, is presented in Figure 5.3. These hits originated from the DetSim stage and have been clustered according to the procedure described in this section. Each signal may thus correspond to a number N of clustered PEs.

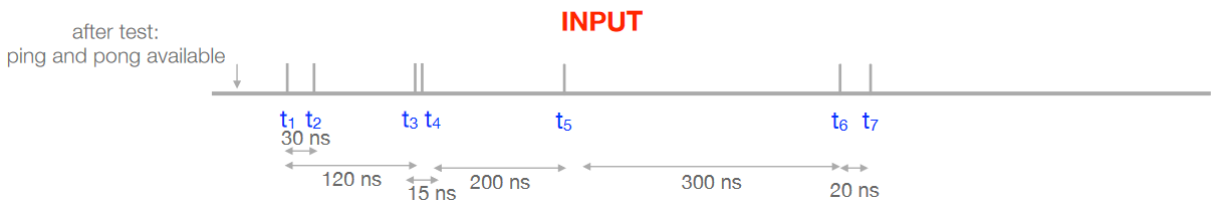

Figure 5.3: Example of the application of the CATIROC features on clustered simulation hits. Input representing the time-aligned hits clusters obtained after the DetSim stage of the simulation.

In this example :

- because it is the first signal and ping and pong are both available, $signal_1$ is triggered and t_1 is registered in the DDS.
- After a 30 ns delay from $signal_1$, $signal_2$ is not triggered and t_2 is lost i.e. not registered in the DDS, but a fraction of its charge is determined by the charge acceptance function.
- $signal_3$, after a 120 ns delay from $signal_1$, is triggered and t_3 is registered in the DDS. In parallel, the time t_1 and the charge corresponding to the charge of $signal_1$ and the charge fraction of $signal_2$ $(Q_1 + f(Q_2))$ are registered in ping. Ping then becomes unavailable for the next 9.4 μs.
- After a 15 ns delay from $signal_3$, $signal_4$ is not triggered and t_4 is lost, but a fraction of its charge is determined by the charge acceptance function.
- After a 215 ns delay from $signal_3$, $signal_5$ is triggered and t_5 is registered in the DDS. In parallel, the time t_3 and the charge corresponding to the charge of $signal_3$ and the charge fraction of $signal_4$ $(Q_3 + f(Q_4))$ are registered in pong. Pong then becomes unavailable for the next 9.4 μs.
- $signal_6$, after a 300 ns delay from $signal_5$, is triggered and t_6 is registered in the DDS. In parallel, as neither ping nor pong are available, the charge of $signal_5$ is not registered and is lost.
- After a 20 ns delay from $signal_6$, $signal_7$ is not triggered and t_7 is lost, but a fraction of its charge is determined by the charge acceptance function.
- At the next trigger occurring during the 9.4 μs since ping was occupied, as neither ping nor pong are available, the charge corresponding to the charge of $signal_6$ and the fraction of charge of $signal_7$ will be lost.

The output of the application of the CATIROC features on the clusters of simulated hits is shown in Figure 5.4. t_1 is registered in the DDS with t_1 and $Q_1 + f(Q_2)$ registered in ping, t_3 is registered

in the DDS with t_3 and $Q_3 + f(Q_4)$ registered in pong, and t_5 and t_6 are registered in the DDS.

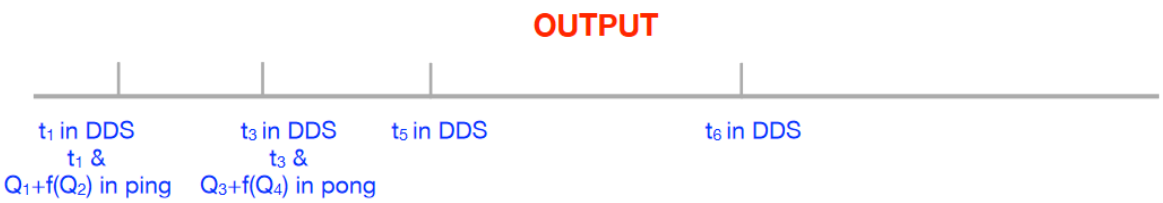

Figure 5.4: Example of the application of the CATIROC features on clustered simulation hits. Output representing the time-aligned hit clusters after the ElecSim stage of the simulation. [143]

If a signal is triggered in CATIROC, an offset on the time measurement is added by the ASIC due to its trigger time, as described in section 3.5.1 and section 4.5.3, which represents the time difference between the physical signal and the CATIROC-triggered signal. Depending on the trigger threshold that will be set for the ASIC, on the preamplifier gain in the triggered channel, and on the signal amplitude, this offset will vary and the timing of the event will be modified before being registered in the DDS. The evolution of the trigger time with the amplitude of the signal was parametrized in Figure 4.57 for a trigger of threshold corresponding to 1/3rd of a PE and a preamplifier gain of 40, which was the configuration for the mass-testing of the PMTs. For a parametrization at preamplifier gain 20, which will be close to the configuration used in the final state of the JUNO experiment, the time walk (section 4.5.3) will be smaller. The worst case of time walk is thus currently implemented in the simulation. For a low impact of the time walk on the physical measurements (charge, time), its impact will be considered negligible at lower preamplifier gain values.
The offset increases at lower charges and a spread of about 1 ns on the time value can be observed when performing repeated measurements. Given that the charge attributed to a hit cluster has a random component due to the resolution of the PMT, the amplitude of the PMT signal for a given type of event is also random and varies. This is one of the two spreads on the trigger time measurement that is taken into account in the simulation :

- The first spread is this natural spread on the charge due to the PMT resolution which has repercussions on the amplitude of the signal and on the estimation of the trigger time.
- The second spread has to be manually added based on the error bars of the data points used for the parametrization of the trigger time shown in Figure 4.57. It accounts for the jitter on the CATIROC trigger, and is added by drawing a random value on a Gaussian distribution. This distribution has the output of the trigger time parametrization function as the Mean parameter and the error bars on the data points as the σ parameter.

Overview Figure 5.5 presents a diagram illustrating the current status of the implementation of the electronics response of the SPMT system in the JUNO simulation software. While three blocks are presented, the first two make up the core of the SPMT ElecSim stage of the simulation. The PMT simulation block operates on the direct output of the DetSim stage of the simulation, which consists of the PEs released from the photocathode of the PMTs, and adds the PMT characteristics of DCR, TTS and SPE charge resolution measured for the SPMT production. Based on the hit times of the simulation hits, which are impacted by the TTS of the PMTs and to which are added the hits originating from the dark current, clusters of hits within 10 ns are created and processed as single, higher-energy signals, for which a charge and an amplitude are determined depending on the number of PEs contained in the cluster. The features of the CATIROC ASIC are then taken into account, with a trigger probability determined from the time difference between two

consecutive events. If an event is not triggered, a fraction of its charge is determined and added to the charge of the previous hit. In the case of a triggered event, the hit time associated to this event is corrected with the CATIROC trigger time depending on the amplitude of the signal, before it is registered in the DDS. Depending on the ping/pong availability at the time of trigger, estimated with the time difference (9.4 μs) with the previous ping/pong event, the charge can be either lost or measured and the ping/pong status is updated.

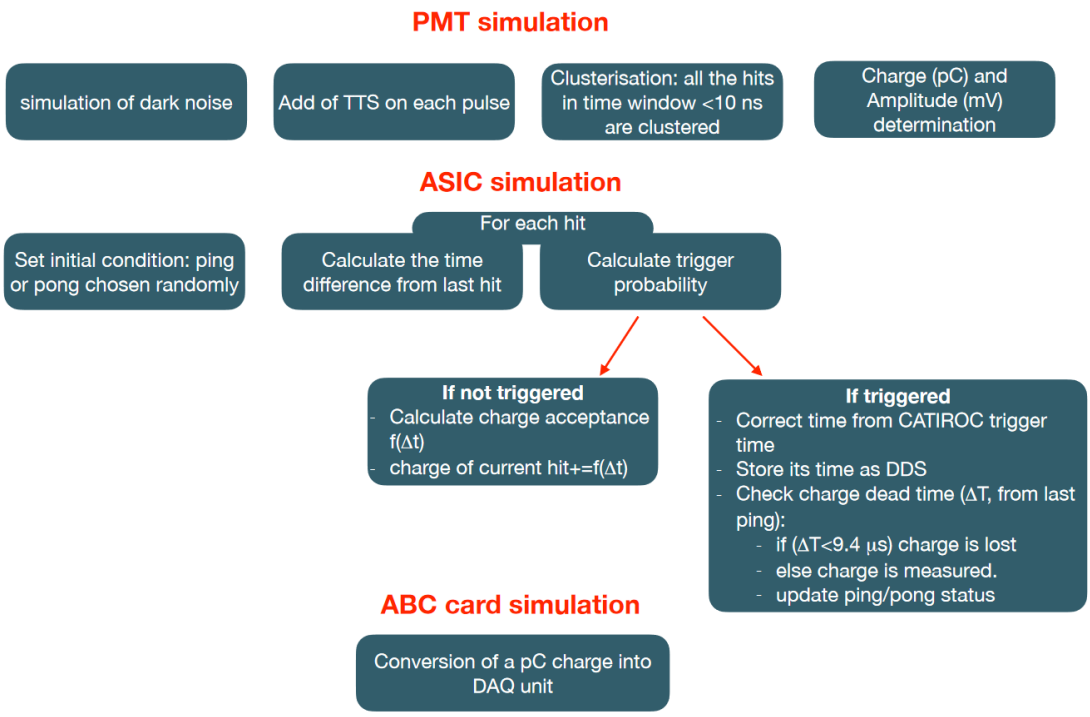

Figure 5.5: Summary of the SPMT simulation status. [143]

Finally, to reproduce the CATIROC output of an ADCu value in the simulation, a pC charge into ADC unit conversion is performed, with a reference measurement in one channel generalized to all channels. Neither spreads nor uncertainties are currently put on these calibration values. This output format is designed to represent the output of the data acquisition system in JUNO.

5.3 Impact of SPMT electronics on the reconstructed charge

As detailed in section 5.2.2, the electronics of the SPMT system have been implemented in the JUNO simulation software. The several subsequent layers of the SPMT electronics, such as the PMT response or the CATIROC features, were implemented, and their impact on the charge reconstructed by the SPMT system will be investigated in this section.

5.3.1 Introduction and discussion : Muon studies with trigger deadtime, charge acceptance and charge digitization deadtime

A first study was conducted to estimate the loss of simulation hits induced by the deadtime and charge acceptance features of the CATIROC ASIC. To this end, muon events from the JUNO simulation are considered, as they will lead to a large deposited energy in the LS and to a large number of collected PEs by the SPMTs. Furthermore, muon events are particularly important as the muon-induced ^{9}Li/^{8}He background is one of the main backgrounds for IBD events in the JUNO

experiment. The decay of such a long-lived ^{9}Li isotope (τ=257 ms) is illustrated in Figure 5.6a, which mimics the IBD signature of prompt and delayed signals, also illustrated. For the reduction of this background, a cylindrical veto volume is applied around the muon track to avoid vetoing the whole detector. It is thus critical to properly reconstruct the entry and exit points of the muon, in order to properly reconstruct its track.

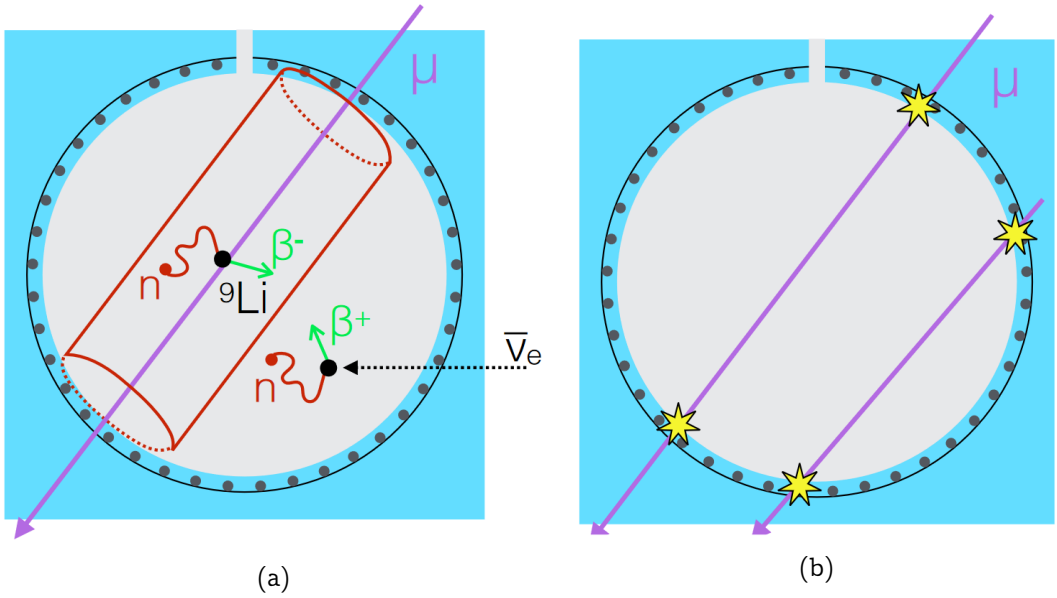

Figure 5.6: (a) Decay process of muon-induced ^{9}Li in the CD, which mimics the IBD signature. A cylindrical veto volume is applied around the muon track to reduce this background. (b) Example of a muon bundle composed of two muons with respective entry and exit points about 5 to 6 m apart.

In the event of muon bundles with respective entry and exit points potentially located near one another, as illustrated in Figure 5.6b, preliminary studies using the charge information have shown that the SPMT system can help better reconstruct muons bundles as the LPMT system is expected to be partially blinded during such events. This was illustrated in Figure 5.7, in which the (X,Y) location of collected PEs during a muon bundle event is shown for the LPMT system, for the LPMT system saturated at ~4000 PEs and for the SPMT system. Two entry points are clearly visible using the LPMT system, but degraded into one larger high-statistics zone for the saturated LPMT system. The SPMT system, however, is also able to properly identify the two separate entry points, resulting in a significantly improved muon bundle reconstruction using the SPMT system.

With the objective of comparing the charge derived from simulation hits (DetSim level) with the charge after the electronics have been added (ElecSim level), the important aspects of the electronics to take into account are the PMT response and the CATIROC features of trigger deadtime, charge acceptance and charge digitization deadtime, described in section 5.2.2. The CATIROC trigger time does not need to be taken into account, as it will only impact the time associated with each event after the event has been determined to be triggered or not or to have a fraction of its charge added to a previously triggered event. For the PMT response in this study, only the TTS is taken into account to add a spread on the arrival times of the hits from the DetSim level. In the following discussions, the number of collected PEs by each SPMT at the DetSim level and the number of registered PEs after the electronics have been taken into account will be referred to, respectively, as the charge before and after the CATIROC response.

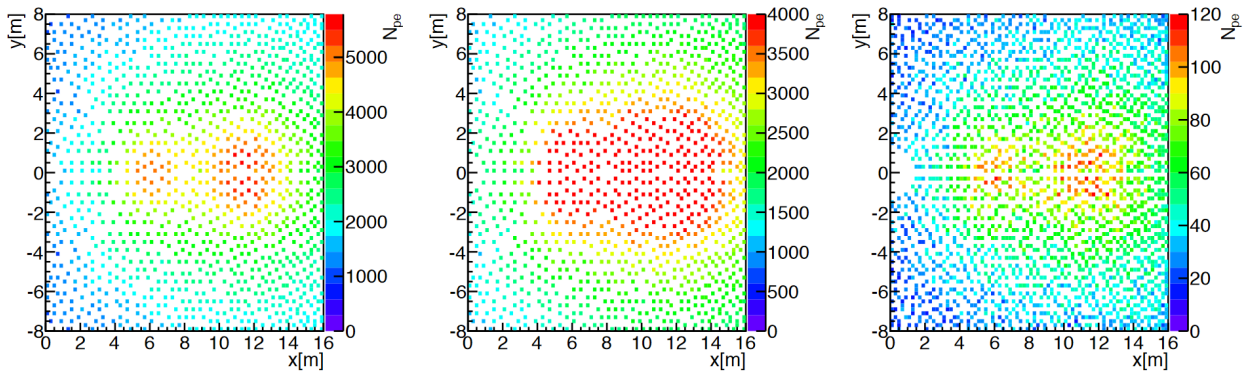

Figure 5.7: (X,Y) location of the entry points of a 2-muons muon bundle. (a) Shown for the LPMT system. (b) Shown for the LPMT system saturated at ∼4000 PEs. (c) Shown for the SPMT system.

The 2D distribution of the charge after the CATIROC response as a function of the charge before the CATIROC response is shown in Figure 5.8a for a single-muon event having travelled ∼35 m in the LS. Each entry corresponds to a SPMT having collected at least 2 PEs at the DetSim level, for the response of CATIROC to have a potential impact, with some SPMTs having collected up to ∼50 PEs. A substantial charge loss can be observed, with a maximum charge after the response of CATIROC of ∼30 PEs and a rather wide spread in the number of registered PEs at a fixed collected N_{PE} at the DetSim level. Figure 5.8b shows a similar 2D distribution constructed with 100 single-muon events having travelled varying distances in the LS and thus having deposited varying amounts of energy in the target. The same 2D shape as in Figure 5.8a can be observed, with ∼40 PEs as the seeming maximum registered charge after the CATIROC response for single-muon events.

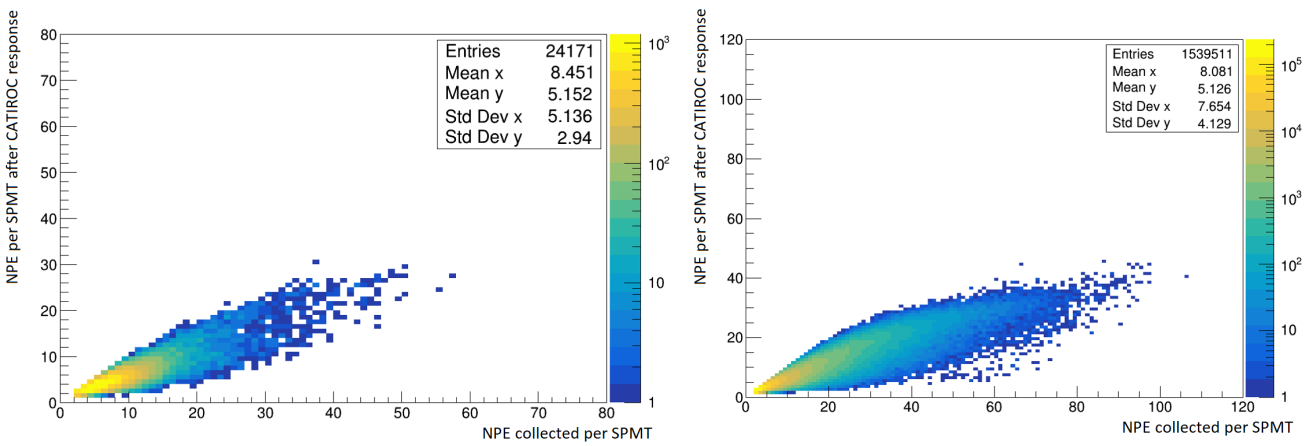

(a) (b)

Figure 5.8: Number of registered PEs per SPMT after the CATIROC response has been applied as a function of the collected number of PEs per SPMT at the DetSim level. (a) For one single-muon event having travelled ∼35 m in the LS. (b) For 100 single-muon events having travelled varying distances in the LS.

For very-high-energy events, there seems to be a substantial impact of the CATIROC features on the reconstructed charge, with charge losses increasing with the number of collected PEs on

a given PMT. These charge losses can reach ∼30% for SPMTs having collected around 5 PEs, and up to 30% to 45% for SPMTs having collected around 20 PEs. For single-muon events, this maximum registered charge after the CATIROC response has been taken into account of ∼20 pC (∼40 PEs maximally registered and a SPE charge of 0.48 pC at a nominal PMT gain of 3×10^6) will be measured in the low-gain mode of CATIROC. As the CATIROC low-gain range for this preamplifier value goes up to 70 pC, single-muon events can thus be measured without any charge measurement saturation of the SPMT system, due to the CATIROC response inducing an internal saturation in the number of registered PEs which could be corrected and allow for an identification, within some uncertainties, of the original charge of the observed event. Muon bundles of up to 3 muons could theoretically be measured as well, with additional studies required for confirmation. The SPMT system should thus be able to configure the gain of the preamplifier of each CATIROC channel to optimize SPE studies while still allowing for muon studies.

Important charge losses have been observed for very-high-energy events seen by the SPMT system, going up to 45% for SPMTs having collected 20 PEs and above. Rather paradoxically, these charge losses due to the response of the electronics of the SPMT system actually enable a non-saturated charge measurement. The charge measurement for muon events will not be corrected, as their charge information is not crucial. For muon track reconstruction, the barycenter of the fired SPMTs is likely not impacted by the charge loss due to the electronics, and, as the SPMTs do not saturate, the entry points of the muon bundle will be reconstructed more precisely. Moreover, the SPMT system will mainly operate in the photon-counting mode (section 3.1), and so the impact of the SPMT electronics on the reconstructed charge is expected to be negligible in this mode. The impact of the different contributions to the SPMT electronics (PMT response, CATIROC features) should however be investigated.

5.3.2 Reconstructed charge using ^{12}B events

To investigate the impact of the SPMT electronics on the reconstructed charge, ^{12}B decay events were fully simulated in SNiPER in order to produce a continuous energy spectrum in the MeV energy region and test the different steps of the charge digitization process on the charge reconstruction precision.

As described in section 2.9.4, the decays of light unstable isotopes produced by the cosmic-ray muon spallation process in the liquid scintillator are a source of background for the detection of solar neutrinos in JUNO, and as such, are present in rather large quantities in the detector. ^{12}B is one of such cosmogenic isotopes, with a decay energy end-point of 13.4 MeV and a mean lifetime τ of 29.1 ms. About 2300 ^{12}B nuclei per day are expected to be produced and detected in the JUNO LS [100]. This isotope is interesting for the collaboration as no calibration source scheduled to be used during the calibration process (section 2.6) will reach such energies. Simulating a continuous spectrum of ^{12}B events to study the impact of the SPMT electronics on the charge reconstruction is therefore interesting, as these events can be representative of physics events in the JUNO experiment. Furthermore, testing the response of the electronics requires events of high enough energies to yield greater multiplicities in the number of collected PEs per SPMT, for the impact of the CATIROC features, which apply mainly to consecutive events recorded by a given PMT, to be made apparent.

A first batch of uniformly simulated ^{12}B events was produced, taking into account the charge resolution aspect of the PMT response as well as the trigger threshold aspect of the CATIROC features. As described in section 5.2.2, the charge resolution of the PMTs will assign a random charge (pC) to a cluster of collected PEs, following a Gaussian distribution with a mean of 0.48 pC and a standard deviation (σ) of ∼33% for SPE events, scaling according to PMT physics with the number N of collected PEs. For these ^{12}B events, the charge resolution aspect of the PMT

response will instead assign a random number of collected PEs to each hit from the DetSim level of the simulation (each hit corresponds to one PE released from the photocathode). The 10 ns clusterization process is not yet taken into account. For CATIROC features, a trigger threshold corresponding to 1/3rd of PE is taken into account. Any DetSim hit with a randomly assigned $N_{PE} < 1/3$rd will be considered as not triggered.
The true number of collected PEs per PMT and the reconstructed number of PEs per PMT, after the previously detailed steps of the electronics have been taken into account, are shown for these ^{12}B events in Figure 5.9a. The vast majority of PMTs only collected 1 PE at the DetSim level, with about ~3% of PMTs having collected 2 PEs and a negligible fraction of PMTs having collected more. As expected, the reconstructed number of PEs per PMT is smeared due to the PMT charge resolution, with the true number of collected PEs per PMT as a discrete distribution and the reconstructed number of PEs per PMT as a continuous distribution with a lower mean value. While some hits are lost due to the threshold effect, the PMT charge resolution is mainly responsible for the lower numbers of reconstructed PEs when compared to the true number of collected PEs. The total number of PEs per event is shown in black in Figure 5.9b for all ^{12}B events, while the reconstructed number of PEs is shown in red. The counted number of hits, in blue, corresponds to the number of fired SPMTs. Figure 5.9b represents the β spectrum of ^{12}B in photoelectrons, with the end-point of the spectrum at ~540 PEs corresponding to the expected 40 PEs per MeV collected by the SPMT system at end-point ^{12}B energies of ~13.4 MeV.

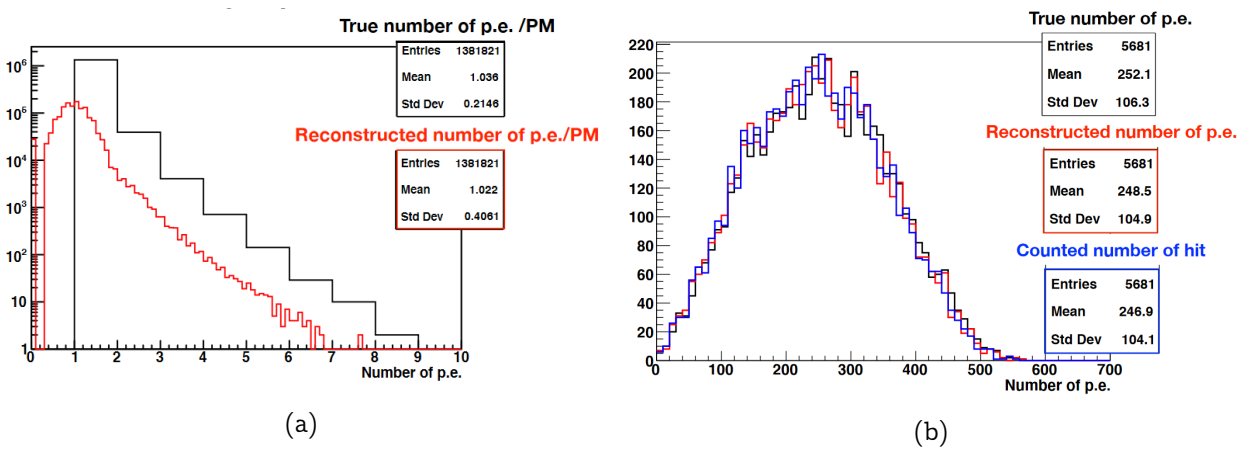

Figure 5.9: (a) Number of PEs collected (black) and reconstructed (red) per PMT, for all ^{12}B events. (b) True (black), reconstructed (red) and counted (blue) number of PE per event, all SPMTs considered.

The impact of the electronics on the charge reconstruction are evaluated by computing the relative difference $\frac{\Delta N}{N} = \frac{|N_{true} - N_{reco}|}{N_{true}}$ between the true and reconstructed number of PEs for each bin of Figure 5.9b. The results for the {PMT charge resolution, CATIROC trigger threshold} aspects of the electronics are shown in Figure 5.10a. An intrinsic smearing on the charge reconstruction of about 2% for a signal of 300 PEs is observed due to the PMT charge resolution and CATIROC trigger threshold aspects of the electronics. While statistical errors are not shown, the low statistics for low numbers of PEs per event lead to relatively large uncertainties for the [5-10]% $\frac{\Delta N}{N}$ values given for the [0-100] range of N_{PE} per event.
On these same uniformly simulated ^{12}B events, the 10 ns clusterization process described in section 5.2.2 was then additionally taken into account, with an non-negligible fraction of the consecutive hits from the DetSim level having a time difference of less than 10 ns. For these events, the charge resolution aspect of the PMT response will assign a random number of collected PEs to each cluster of hits from the DetSim level of the simulation, each cluster now potentially con-

taining a number N of PEs. The impact of the electronics on the charge reconstruction for the {10 ns clusterization, PMT charge resolution, CATIROC trigger threshold} aspects of the electronics is shown in Figure 5.10b, with barely any noticeable differences from the {PMT charge resolution, CATIROC trigger threshold} case. This would point towards the PMT charge resolution being the dominant factor in the impact of the electronics on the reconstructed charge.
The remaining CATIROC features, as well as dark noise events depending on the DCR value assigned to the considered PMT, were then added to the simulated ^{12}B events. In addition to the CATIROC trigger threshold, the CATIROC features of trigger deadtime, charge acceptance and charge digitization deadtime are therefore now taken into account as well, with the charge acceptance impacting the N_{PE} instead of the charge measured in pC. The impact of the electronics on the charge reconstruction for the {DN events, 10 ns clusterization, PMT charge resolution, CATIROC trigger threshold, CATIROC features} aspects of the electronics is shown in black in Figure 5.10c, with roughly no impact on the charge reconstruction when compared to the previous cases. The dead times of the CATIROC ASIC thus seem to have little impact on the charge reconstruction in the MeV region.
Finally, with the same configuration as the previous batch of ^{12}B events, the spread of the PMT charge acceptance was varied from ∼33% to 3% for SPE events, in order to investigate the pull of this parameter on the impact of the electronics on the charge reconstruction. The $\frac{\Delta N}{N}$ values as a function of the true number of collected PEs are shown in blue in Figure 5.10c. Changing the value of the PMT charge resolution from 33% to 3% for SPE events has a drastic impact when compared with other features from the electronics being added or modified, with the intrinsic error on the charge reconstruction reduced by about 30%. The PMT charge resolution can thus be identified as the electronics feature with the most weight when considering the impact on the charge reconstruction.

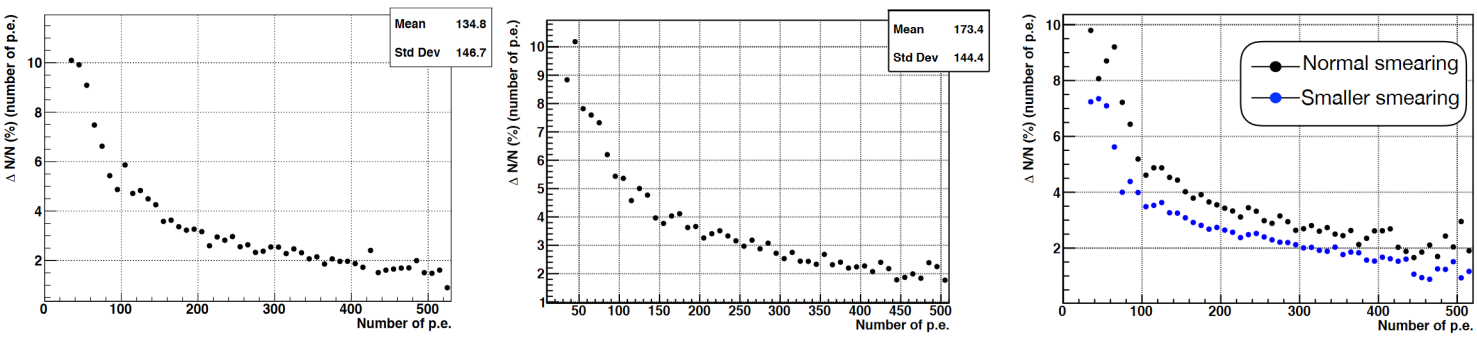

(a) (b) (c)

Figure 5.10: Relative difference between the reconstructed N_{PE} and the true N_{PE} per event, as a function of the true collected N_{PE}. (a) In the {PMT charge resolution, CATIROC trigger threshold} electronics configuration. (b) In the {10 ns clusterization, PMT charge resolution, CATIROC trigger threshold} electronics configuration. (c) In black, in the {DN events, 10 ns clusterization, PMT charge resolution, CATIROC trigger threshold, CATIROC features} electronics configuration. In blue, in the same electronics configuration with the PMT charge resolution decreased from ∼33% to 3% for SPE events.

In order to investigate the dependency on the vertex position of the impact of the electronics on the charge reconstruction, final batches of ^{12}B events were produced in a [0-6] m radius "internal" sphere, a [6-12] m radius "central" hollow sphere and a [12-17.7] m radius "external" hollow sphere. For these events, the {DN events, 10 ns clusterization, PMT charge resolution, CATIROC trigger threshold, CATIROC features} electronics configuration was taken into account. The true

number of collected PEs per PMT and the reconstructed number of PEs per PMT are shown for the ^{12}B events in these spheres in Figure 5.11, with the mean number of collected PEs and the collected PE multiplicity on a given PMT increasing as the distance-to-center of the ^{12}B events increases.

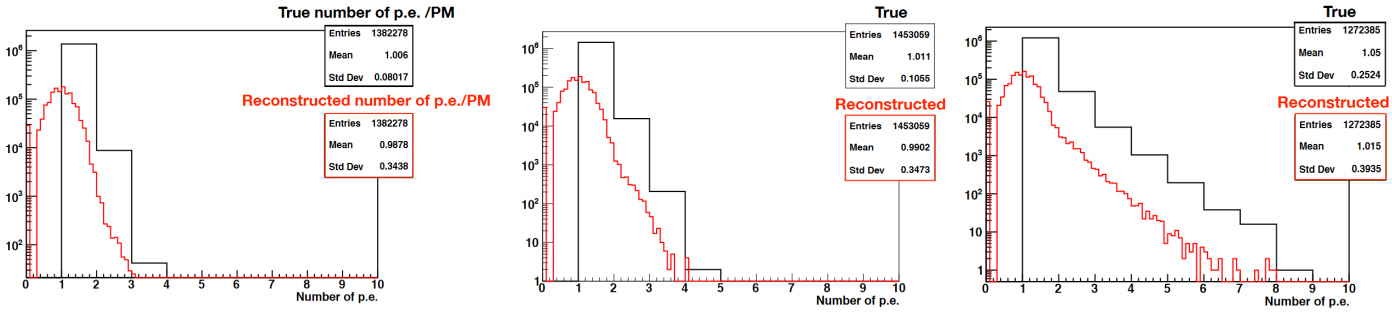

(a) (b) (c)

Figure 5.11: Number of PEs collected (black) and reconstructed (red) per PMT, for all ^{12}B events. (a) In the [0-6] m radius "internal" sphere. (b) In the [6-12] m radius "central" hollow sphere. (c) In the [12-17.7] m radius "external" hollow sphere.

The impact of the electronics on the charge reconstruction in these three configurations, represented by the $\frac{\Delta N}{N}$ values as a function of the true number of collected PEs, is shown in Figure 5.12. As can be observed, the charge reconstruction has a very weak dependence on the position of the ^{12}B vertices. As such, despite the inhomogeneous response of the CD in terms of collected PEs, a simple calibration of the charge reconstruction can suffice, without accounting for event position and mapping the detector.

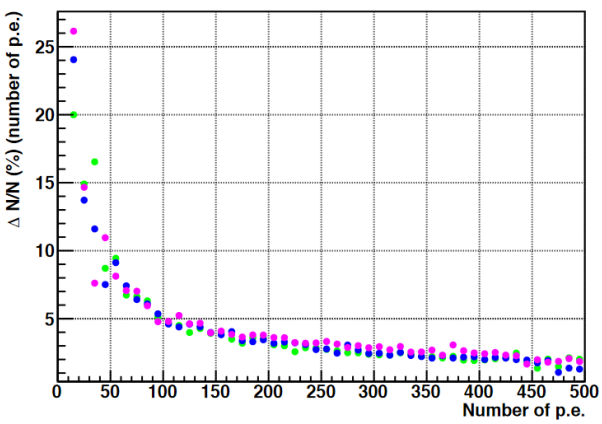

Figure 5.12: Relative difference between the reconstructed and the true N_{PE} per event, as a function of the N_{PE}, when considering all electronic features. Three areas in the target have been tested, with the ^{12}B events uniformly simulated in these areas. In a [0-6] m radius "internal" sphere (green), in a [6-12] m radius "central" hollow sphere (blue) and in a [12-17.7] m radius "external" hollow sphere (purple). The charge reconstruction shows very little dependency on the position of the ^{12}B vertices.

5.4 Impact of SPMT electronics on the measured time

Having studied the impact of the SPMT system electronics on the reconstructed charge in section 5.3, this section will now present the impact of the SPMT electronics on the measured time.

5.4.1 Introduction : CATIROC trigger time spread vs PMT TTS

The SPMT electronics will have an impact on two aspects of the measured time : the absolute value of the measurement, which is irrelevant as time delays will be calibrated and taken into account, and the resolution of the time measurement, which can be more problematic for reconstruction studies. Two steps of the SPMT electronics can be expected to be the main sources of impact on this time resolution : the Time Transit Spread (TTS) of the PMTs (section 2.5.3, Figure 2.14), and the CATIROC trigger time (section 4.5.3, Figure 4.57b).
To investigate the impact of each on the measured time resolution, 7 MeV electrons were generated uniformly over the full volume of the spherical central detector. The TTS of the PMTs and the CATIROC trigger time can be activated and taken into account independently. For 7 MeV electrons, most of the PMTs have only collected one PE ($> 98\%$), with only $\sim$2% of the PMTs having collected two or more PEs. Moreover, only $\sim$56% of PMTs having collected 2 PEs have done so within 10 ns and thus result in a 2 PE signal.
For each triggered signal, its associated CATIROC trigger time can be used to build the time distribution induced by the CATIROC features and measure its spread (no PMT TTS taken into account). This is illustrated in Figure 5.13, which shows the distributions of the CATIROC trigger times for 1 PE and 2 PE events. The two distributions have been rescaled to the same number of entries for visual clarification. As was shown in Figure 4.57b, the trigger time offset increases at lower numbers of collected PEs and lower signal amplitudes, which can be be observed in Figure 5.13 with a mean value of the time distribution for SPE signals of 4.56 ns and a mean value of the time distribution for 2 PE signals of 3.24 ns. As was detailed in section 5.2.2, two spreads are added on the trigger time impacting the hit time from the DetSim level of the simulation : a first spread due to the PMT charge resolution which has repercussions on the amplitude of the signal and on the estimation of the trigger time, and a second spread based on the error bars of the measurements used for the parametrization of the trigger time as a function of the amplitude. The first spread depends on the amplitude of the signal, as a variation in amplitude at lower amplitudes will result in a larger variation of trigger time than at higher signal amplitudes. This is also illustrated in Figure 5.13, in which the width of the SPE trigger time distribution of 1.16 ns is larger than the width of the 2 PE trigger time distribution of 0.75 ns.
The distribution of the TTS for the measured PMTs is shown in Figure 2.15, and the mean spread is 1.56 ns. This non-negligible spread is taken into account by permanently assigning a random TTS to each PMT, and, for each triggered signal, a Transit Time (TT) of 49 ns, randomly shifted by the TTS assigned to the PMT, is added to the simulation hit time on top of the CATIROC trigger time.
Figure 5.14 shows three time distributions for the SPE signals of the 7 MeV electrons. In blue is the distribution of the TT (49 ns) affected by the TTS of each individual contributing PMT. The standard deviation of this distribution is 1.57 ns, which is the mean TTS value. In red is the distribution of the CATIROC trigger time added to SPE signals, to which the TT has been added. The mean value of this distribution corresponds to the mean CATIROC trigger time (4.5 ns) added to the TT, and the standard deviation is only due to the spread on the CATIROC trigger time ($\sim$1.2 ns). In magenta is the distribution of the CATIROC trigger time associated to 1 PE events, to which the TT has been added as well as the spread due to the TTS of the PMTs. The mean value is identical, but the standard deviation of the distribution has increased, due to

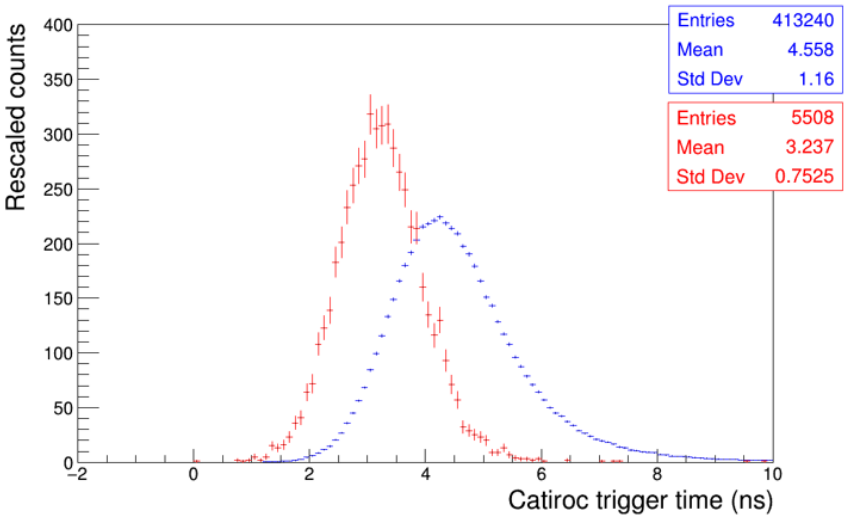

Figure 5.13: Rescaled distributions (to the same number of entries) of the CATIROC trigger times associated to 1 PE and 2 PE events (respectively the blue and red distributions).

another contribution to the spread on the time measurement. The total spread corresponds to the quadratic sum of the TTS and the CATIROC trigger time spread. It is straightforward to conclude that the deviation on the CATIROC trigger time has a smaller impact on the width of the total time distribution, since it adds 0.4 ns to the global width (∼25% of the TTS contribution).

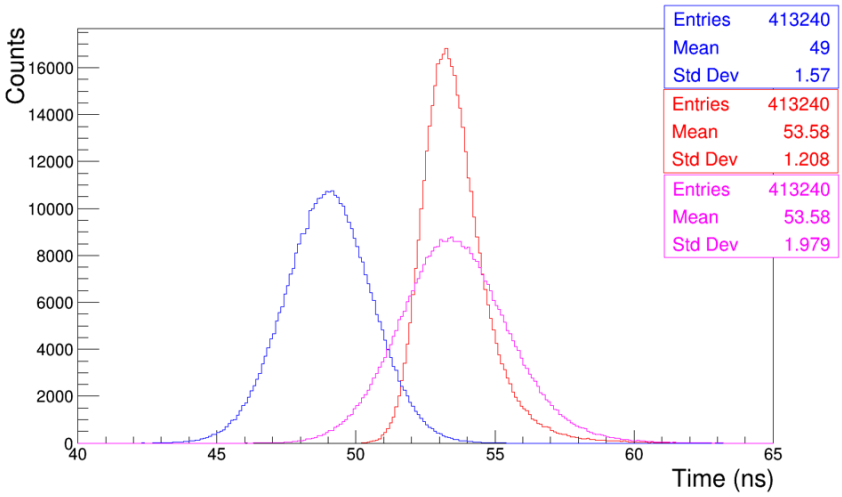

Figure 5.14: Contributions to global time spread for SPE events. In blue is the distribution of the TT affected by TTS. In red is TT and CATIROC trigger, and the width is due to the spread on the trigger time estimation. In magenta is the TT and CATIROC trigger, affected by TTS. The deviation on the CATIROC trigger time has a smaller impact on the width of the total time distribution, as it adds 0.4 ns to the global width (∼25% of TTS contribution).

A more precise and complete study should be conducted in order to try and quantify the impact of the SPMT system electronics on the time information of the collected PEs for recorded physical events. The following section will investigate the impact of the time measurement on a physical observable: the vertex of simulated events.

5.4.2 Vertex reconstruction with the SPMT system

The time information in the SPMT system is important for the correlation of the PEs collected by the different fired SPMTs in order to define a recorded physical event (sufficient number of PEs in a given time window consistent with LS decay time), as well as for offline event position reconstructions. The impact of the SPMT system electronics on the measured time will thus be investigated in this section by comparing the results of a vertex reconstruction method applied to simulated events for different aspects of the SPMT electronics taken into account. In a vertex reconstruction exercise, the LPMT system will be the main contribution to the precision of the reconstruction. The standalone performance of the SPMT system will nevertheless be studied in order to isolate the impact of the electronics. For the SPMT electronics to be more impactful on the collected PEs and thus more easily measurable and quantified, high-energy events in the central detector are required, which will result in a high level of illumination of the SPMT system with a non-negligible fraction of the fired SPMTs having collected more than one PE. As such, 20 MeV positron events were fully simulated in SNiPER, and their positions reconstructed with the following analysis method.

5.4.2.1 Vertex reconstruction method

In the liquid scintillator sphere, positron annihilation with electrons happens at an interaction vertex which is considered as the true position of the positron event. This interaction isotropically emits a number of photons increasing with the energy of the positron, which travel in the liquid scintillator until they reach the acrylic sphere, which acts as the LS/WP interface, and are refracted before traveling through the water pool to reach the PMTs. This phenomenon is illustrated in Figure 5.15 in the case of an arbitrary positron event, with the positron interaction vertex represented as the red dot A in the LS sphere and the real trajectories of several emitted photons as the red lines and arrows connecting the vertex to the fired SPMTs.

Once they hit the SPMTs, the photons have a chance to induce a photoelectric effect in the photocathode, resulting in the production of a photoelectron. As described in section 5.2.1, this part of the simulation is performed at the DetSim level, with the output for each positron event being a set of PMT hits which represent PEs released from the photocathode, associated to an arrival time and the (X,Y,Z) coordinates of the PMT having produced that PE. The PMTs used in the simulation are the 25600 SPMTs selected as described in section 5.2.2. In Figure 5.15, arrival times t_i are shown as being attributed to each fired SPMT.

The output of the DetSim level of the electronics is the input of the ElecSim level, which reproduces the PMT response as well the response of the CATIROC ASIC. The output of the ElecSim level is clusters of hits from the DetSim level, each cluster now considered as a signal, with an associated charge and time stamp, as well as the coordinates of the PMT having collected that signal.

For each positron event, all signals and their associated PMT coordinates are used to compute a barycenter as a first approximation of the vertex position. The charge and time information of the hit clusters are not taken into account. In Figure 5.15, the reconstructed barycenter is illustrated as the green B point in the LS sphere.

Having identified this barycenter as a potential position of the vertex that is relatively close to the true position from the simulation, the objective is then to hypothesize nearby positions in the LS sphere as the true vertex position and estimate which hypothesis is the most probable.

This is performed by using the TMinuit class of the ROOT library [139] to scan a $3\times3\times3$ m^3 (black cube in Figure 5.15) cubic grid in (X,Y,Z) around the barycenter position with a 10 mm step. Each tested position is taken as the position from which all photons having produced hits on the fired SPMTs (DetSim level) were emitted. In Figure 5.15, one of the tested positions is illustrated as the blue point C. For each hit cluster of the simulation output (ElecSim level), a

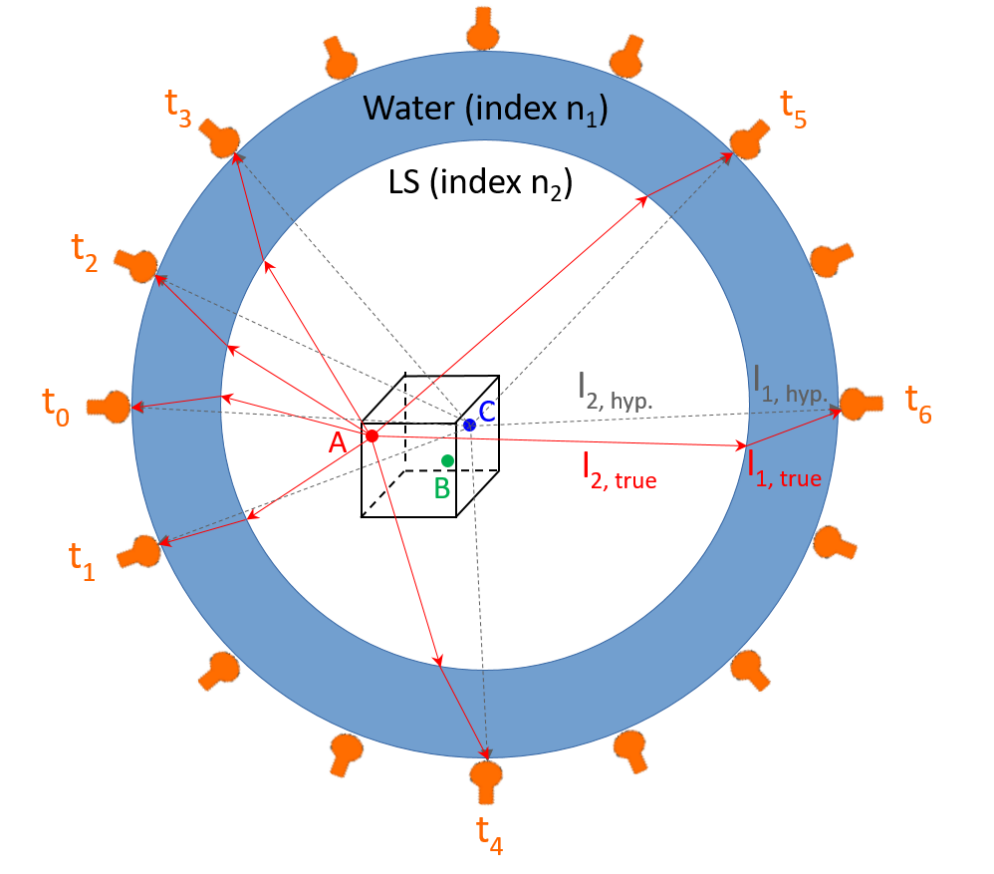

Figure 5.15: Schematic view of the vertex reconstruction process in the JUNO detector. A cross-section view of the acrylic sphere containing the LS (white circle) and of the water pool (blue circle) is represented, with a sample of SPMTs observing the central detector. The true vertex A of the event is shown as the red point from which all optical photons are emitted and propagate towards the SPMTs. Their propagation, taking refraction processes into account, is shown as the red lines and arrows. Arrival times t_i are attributed to every fired SPMT in this example, in order of arrival. The distances $l_{1,true}$ and $l_{2,true}$, respectively travelled in the water and in the liquid scintillator from the true vertex position, are represented for one photon propagation. The reconstructed barycenter from the fired SPMTs is shown as the green point B, around which a $3\times3\times3$ m^3 cubic grid is scanned to test potential vertex positions. One of such tested positions is the blue point C, from which straight lines to the fired SPMTs, represented as the grey dotted lines and arrows, are taken as the hypothesized propagations of the optical photons. The distances $l_{1,hyp.}$ and $l_{2,hyp.}$, respectively travelled in the water and in the liquid scintillator from the hypothesized vertex position, are represented for one photon propagation.

residual time is defined as :

$$t_{res} = t - ToF \tag{5.3}$$

where t is the hit time of the first PE in the cluster and ToF is the time of flight of the first optical photon, corresponding to the expected propagation time of the photon from the event vertex to the PMT. Each residual time is then corrected from the first residual time $t_{res,0}$ to form a time distribution which will be compared to a reference time distribution to test the likelihood of the position hypothesis.

Ideally, computing the time of flight of the photons should account for the large difference between the refractive index of the liquid scintillator ($n = 1.49$) and the refractive index of water ($n = 1.33$), responsible for the processes of refraction and total reflection. Figure 5.16 illustrates the optical model that accounts for the process of refraction. The event vertex is represented as the point A, the fired SPMT as the point B, and the point C represents the position on the acrylic sphere, at the interface between liquid scintillator and water, where refraction occurs. The PMT distance to the acrylic sphere is not to-scale, to allow for a better visualization of the involved geometrical optics. l_1 represents the distance travelled by the optical photon in the water pool of refractive index n_1, while l_2 represents the distance travelled by the optical photon in the liquid scintillator of refractive index n_2. Using geometrical optics, the time of flight of the photons can thus be written as :

$$ToF = \frac{(n_1 l_1 + n_2 l_2)}{c} \tag{5.4}$$

where c is the speed of light in vacuum.

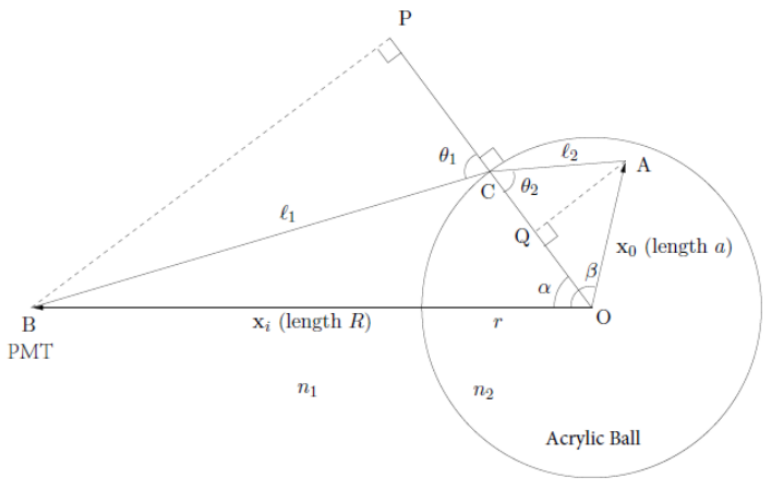

Figure 5.16: Optical model used to calculate the optical path of a photon from a given vertex to a specific PMT. A is the event vertex, O is the center of the detector, B is the PMT's photocathode and C is the point at the LS/WP interface where the photon is refracted. [144]

The distances l_1 and l_2 both depend on the α and β angles, which correspond respectively to the angle between the center O of the sphere, the refraction position C on the acrylic and the PMT position B, and to the angle between the vertex position A (one of the positions tested by Minuit), the center O of the sphere and the PMT position B. The β angle is known, and the relationship between α and β [144] can be written as :

$$1 + \left[\frac{r}{a} csc(\beta - \alpha) - cot(\beta - \alpha)\right]^2 = \left(\frac{n_2}{n_1}\right)^2 \left[1 + \left(cot(\alpha) - \frac{r}{R} csc(\alpha)\right)^2\right] \tag{5.5}$$

Isolating α in this equation, in order to compute l_1 and l_2, is particularly complex, and α is estimated by varying its value and identifying the α value for which the time of flight of the photon is minimal. Such a process however implies significantly longer computation times. As a result, considering the optical path of the photon as a straight line between the event vertex and the fired PMT is an acceptable approximation of the involved geometrical optics for large detectors in which the difference in the travelled distance due to refraction is often negligible before the distance travelled in the LS from the event vertex to the acrylic interface. In a straight

line scenario, the intersection point between the [vertex,PMT] ray and the acrylic sphere can be computed, defining the distances l_1 and l_2 travelled in each medium, and the time of flight is computed as in Equation 5.4.
The refraction process is illustrated in Figure 5.15 for the true propagation of the optical photons (red lines and arrows), with the distances $l_{1,true}$ and $l_{2,true}$, respectively travelled in the water and in the liquid scintillator from the true vertex position, represented for one photon propagation. The straight line approximation of the optical photons propagation is represented as the grey dotted lines and arrows pointing from the hypothesized vertex position C (blue point) to the fired SPMTs. The distances $l_{1,hyp.}$ and $l_{2,hyp.}$, respectively travelled in the water and in the liquid scintillator from the hypothesized vertex position, are also represented for one photon propagation.
Computing the residual time t_{res} for each hit cluster and correcting it from the first residual time $t_{res,0}$, the resulting time distribution is then compared to a reference time distribution to test the likelihood of the vertex position hypothesis. This reference distribution was constructed using the residual times from 3 MeV electron events uniformly simulated in the detector, as such events are similar to the events that will be observed in the JUNO experiment with the ^{60}Co calibration sources (section 2.6.2). Using these 3 MeV electron events to construct the reference time distribution can be considered a "realistic" take on this vertex reconstruction study. This distribution, corresponding to $f(t_{res})$, is called a probability density function (PDF) and is shown in Figure 5.17 for all electron events observed by both the LPMT and the SPMT systems.

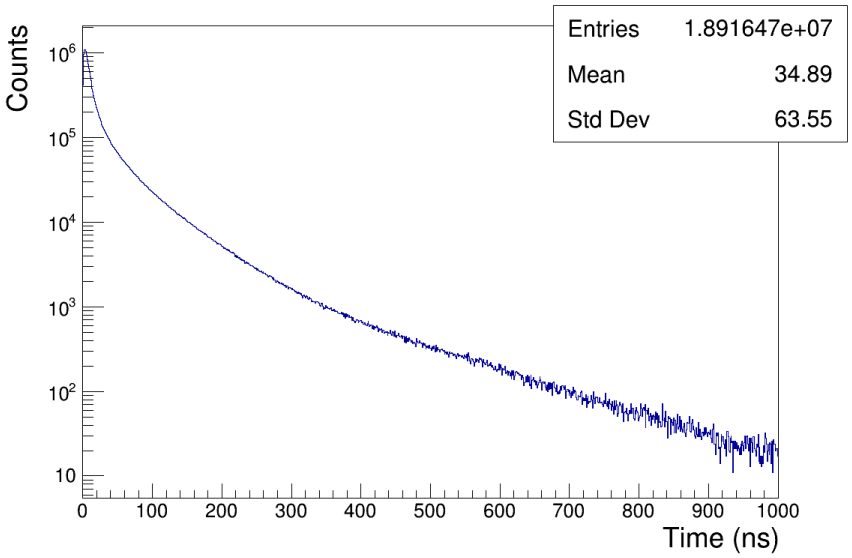

Figure 5.17: Reference PDF constructed from the residual times of 3 MeV electron events uniformly simulated, with no smearing on the time information.

As described in section 2.6, the total number of collected PEs by the LPMT and SPMT systems and the arrival times of these PEs on the fired PMTs are position-dependent in JUNO, due to PMT solid angles, optical attenuation effects, reflections at material interfaces, or shadowing due to opaque materials. Depending on the position of the electron events in the ~23000 m^3 detector volume, the distributions of the residual times are thus expected to show some differences, which will impact the vertex reconstruction of simulated events. During the calibration phase of the detector, the ^{60}Co calibration sources will be moved at different positions in the detector to calibrate the intrinsic position non-uniformity, which will allow for the construction of several different reference PDFs to be used for a finer vertex reconstruction. Five different PDFs were thus constructed from the 3 MeV uniform electron events, each PDF constructed using events

with vertices contained within radii intervals (radius R computed from the center of the sphere) making up five equivalent volumes in the detector sphere :

- Volume 1 : 0 m $\leq R <$ ~10.5 m
- Volume 2 : ~10.5 m $\leq R <$ ~13 m
- Volume 3 : ~13 m $\leq R <$ ~15 m
- Volume 4 : ~15 m $\leq R <$ ~16.5 m
- Volume 5 : ~16.5 m $\leq R <$ ~17.7 m

The PDFs for each different volume are shown in Figures 5.18a and 5.18b, with Figure 5.18b focusing on the [0,100] ns range to better highlight the small differences in the PDFs. For the vertex reconstruction of the simulated 20 MeV positron events, the reference PDF to compare to the constructed residual time distribution is selected depending on the position of the reconstructed barycenter and its distance to the center of the sphere, and thus to the detector volume interval it belongs to.

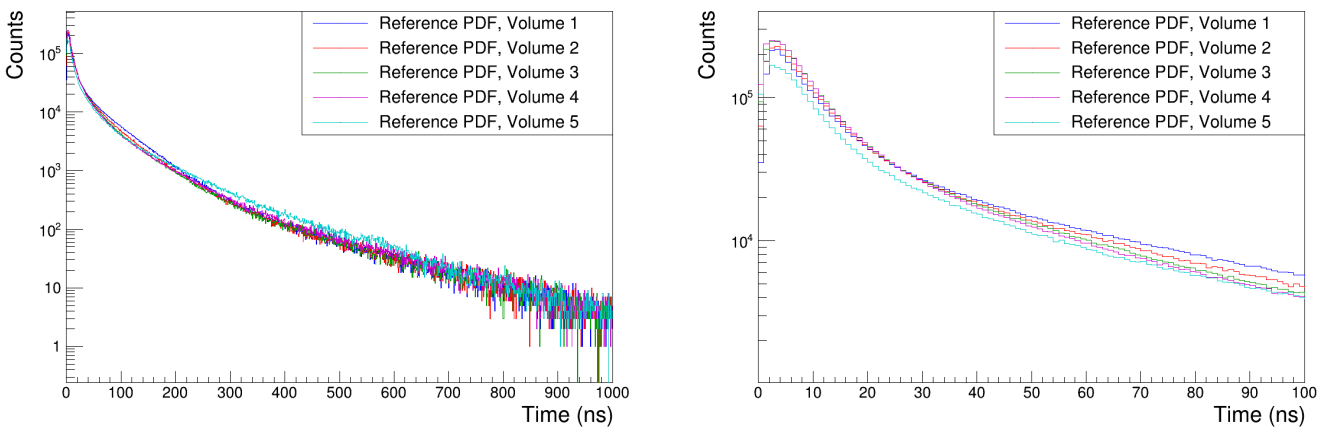

(a) (b)

Figure 5.18: Volume-dependent reference PDFs constructed from the residual times of 3 MeV e^- events uniformly simulated. (a) Over the full [0,1000] ns range. (b) Over a [0,100] ns range.

The considered reference PDF is then scaled to the number of entries of the residual time distribution constructed for the considered positron event and corresponding to the tested position in the LS, and the comparison between the two distributions is performed using a χ^2 function over a range of 100 ns, defined as :

$$\chi^2 = \sum_{i=1}^{N} \left[Ref_i - Data_i + Data_i \times log\left(\frac{Data_i}{Ref_i}\right)\right] \tag{5.6}$$

where i represents the bins of the compared distributions, N is the number of the maximum bin over which the χ^2 is computed, Ref_i is the bin content of the ith bin of the reference PDF and $Data_i$ is the bin content of the ith bin of the considered residual time distribution.
Due to occurrences of positions being identified by Minuit as the best reconstructed position despite their associated time distributions being substantially different from the reference PDF, an additional constraint on the time distributions was added by requiring of Minuit to minimize the function $f = \chi^2 + RMS_{Data}$. Minimizing the Root Mean Square (RMS) allows for the exclusion of very wide time distributions or distributions with several peaks.

5.4.2.2 Toy Monte Carlo for statistical limitation with SPMTs, first results

In the vertex reconstruction method described in section 5.4.2.1, a first approximation of the vertex position is performed using a barycenter computed from the (X,Y,Z) coordinates of the fired SPMTs with the number of collected PEs by each SPMT as the weight on these coordinates. The distance of such a barycenter to the true position of the events is intrinsically limited by the number of fired SPMTs, which has repercussions on the performances of the vertex reconstruction method as the barycenter acts as the starting point for the TMinuit scan of the $3\times3\times3$ m^3 cubic grid.

An estimation of the intrinsic limit of the SPMT system for barycenter reconstruction was performed by computing the mean distance of the barycenter to the true position of the events in a streamlined simulation environment, referred to as a very simple "Toy Monte Carlo". In this computational scenario, a 17.7 m sphere is considered for the central detector, surrounded by 25600 SPMTs, the (X,Y,Z) coordinates of which are all known and match the 25600 SPMT positions optimally selected (section 5.2.2). Assuming physical events simulated at the center of the detector, an increasing number of randomly hit PMTs are selected and used to compute a barycenter, and the distance of this barycenter to the true position of the event (center of the sphere) is recorded. For each number of randomly hit PMTs, the process is repeated many times to select different PMTs, compute a different barycenter and obtain a distribution of the barycenter distances to the center of the sphere. The mean value of this distribution is then plotted against the number of randomly hit PMTs, with the RMS of the distribution as the Y error bars. Figure 5.19a illustrates this process up to 1500 randomly hit PMTs. Considering that a fired PMT corresponds to one collected PE and that ~40 PEs are collected by the SPMT system for every MeV of deposited energy in the target, the energy equivalent of the number of fired PMTs, as seen by the SPMT system, is shown as the top X-axis in Figure 5.19a.

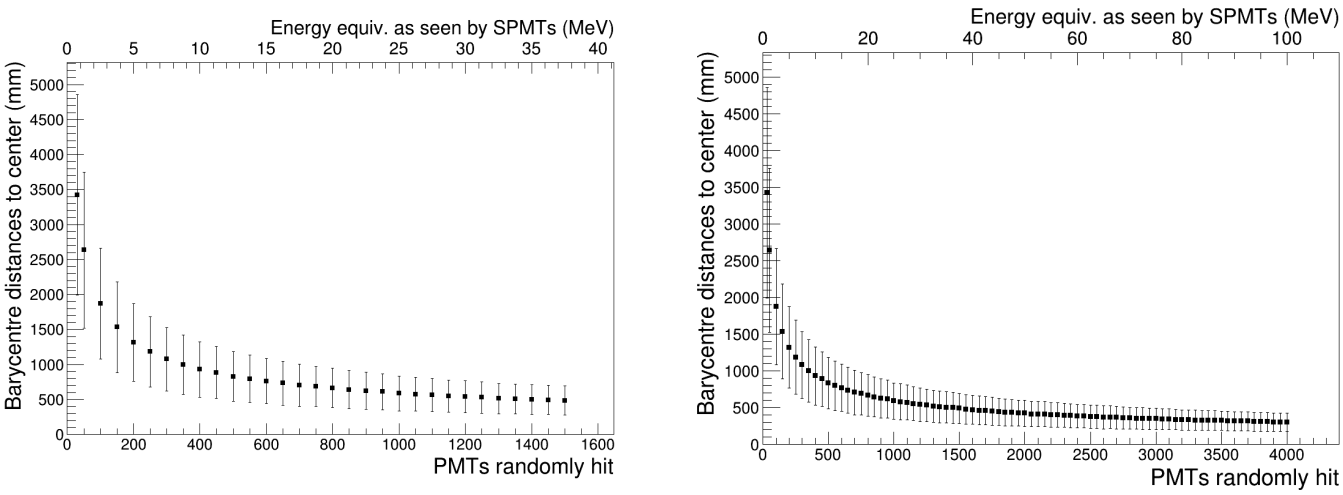

(a) (b)

Figure 5.19: Toy Monte Carlo used to illustrate the distance between the reconstructed barycenter using N randomly selected SPMTs and the center of the sphere. (a) From 0 to 1500 randomly hit PMTs. (b) From 0 to 4000 randomly hit PMTs.

For 1 MeV events, about 40 collected PEs and fired SPMTs are expected for the SPMT system, leading to an expected mean barycenter distance to the true position of the events lower than ~3 m. For the LPMT system, about 1350 collected PEs and fired LPMTs are expected, leading to an expected mean barycenter distance to the true position of the events of ~0.6 m. The difference in reconstruction precision is substantial, but the seemingly exponential decrease of

the barycenter distance to center with the number of randomly hit PMTs indicates that the reconstruction difference between the SPMT and LPMT systems will shrink with the energy of the simulated events. For 3 MeV events, about 120 collected PEs and fired SPMTs are expected for the SPMT system, leading to an expected mean barycenter distance to the true position of the events lower than ∼1.7 m. For the LPMT system, about 4000 collected PEs and fired LPMTs are expected, which leads, as shown in Figure 5.19b, to an expected mean barycenter distance to the true position of the events of ∼0.35 m.

From such computed barycenters, a more in-depth analysis using the method described in section 5.4.2.1 will improve the vertex reconstruction, but as the starting point of the analysis can be distant from the true position, the intrinsic limitation of the vertex reconstruction method lies in the precision of the barycenter reconstruction. As described in the beginning of section 5.4.2, 20 MeV positron events were simulated in SNiPER. For such events simulated without considering the SPMT electronics, hits from the DetSim level of the simulation are used as the input of the vertex reconstruction method. For these 20 MeV positron events simulated at the center of the detector, Figures 5.20a and 5.20b respectively show the vertex reconstruction results using the LPMT and SPMT systems. In each figure, the distribution of the barycenter distances to the true position of the events is shown in blue while the distribution of the distances of the best TMinuit vertex estimations to the true position of the events is shown in red.

For 20 MeV events, about 27000 collected PEs are expected for the LPMT system. With a maximum number of 18000 fired LPMTs, this leads to an expected mean barycenter distance to the true position of the events of ∼0.14 m (from the Toy Monte Carlo). In Figure 5.20a, the mean value of the barycenter distances to the true position of the events of 14.2 cm confirms the reliability of the Toy Monte Carlo. For the SPMT system, about 800 collected PEs and fired SPMTs are expected, leading to an expected mean barycenter distance to the true position of the events of lower than ∼70 cm ((from the Toy Monte Carlo)), which is confirmed by the mean value of the barycenter distances to the true position of the events in Figure 5.20b of 67.2 cm. A substantial improvement is then achieved with the vertex reconstruction method, with a mean distance between the reconstructed vertex and the true position of the event of 36.6 cm.

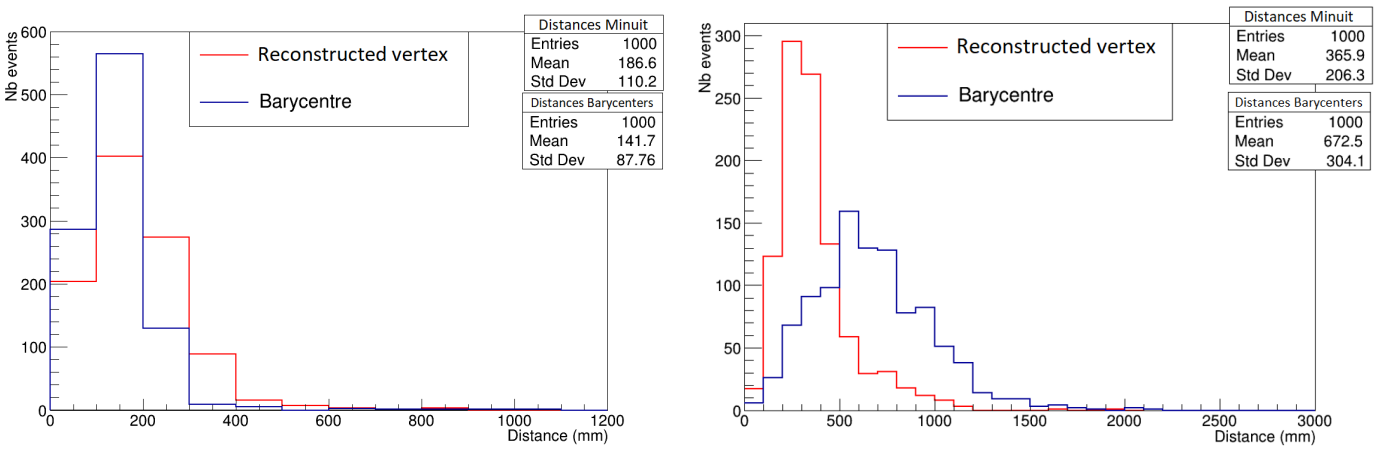

(a) (b)

Figure 5.20: Distances from the true positions of the 20 MeV positrons simulated at the center of the target for the computed barycenters (blue) and reconstructed vertices (red). (a) Using the LPMT system. (b) Using the SPMT system.

Trying to reconstruct the vertex position using the SPMT system does not perform as well as with the LPMT system, due to the much lower statistics of collected PEs (see Figure 3.1 in

Chapter 3). However, for high-energy events producing large numbers of PEs, the SPMT system can perform decently and has merits on its own. The purpose of section 5.4.2 is not to optimize a vertex reconstruction for the SPMT system, but rather to evaluate the performances that can be achieved with the standalone SPMT system using a simple reconstruction method that uses little information and that can be used on the very first recorded data. Taking the SPMT system on its own is also essential to study the impact of the SPMT electronics on the measured time, as information from the LPMT system would dominate the reconstruction process and make it impossible to observe the impact of the different aspects of the SPMT electronics.
In order to investigate the dependence of the vertex reconstruction method on the distance-to-center of the events, 20 MeV positron events were also simulated at 6, 10, 12 and 15 m along the X-axis from the center of the sphere. For a reconstruction process using the standalone SPMT system, the distributions of the distances of the best TMinuit vertex estimations to the true position of the events, for each distance-to-center of the simulated events, are shown in Figure 5.21. An expected degradation with the distance-to-center is observed.

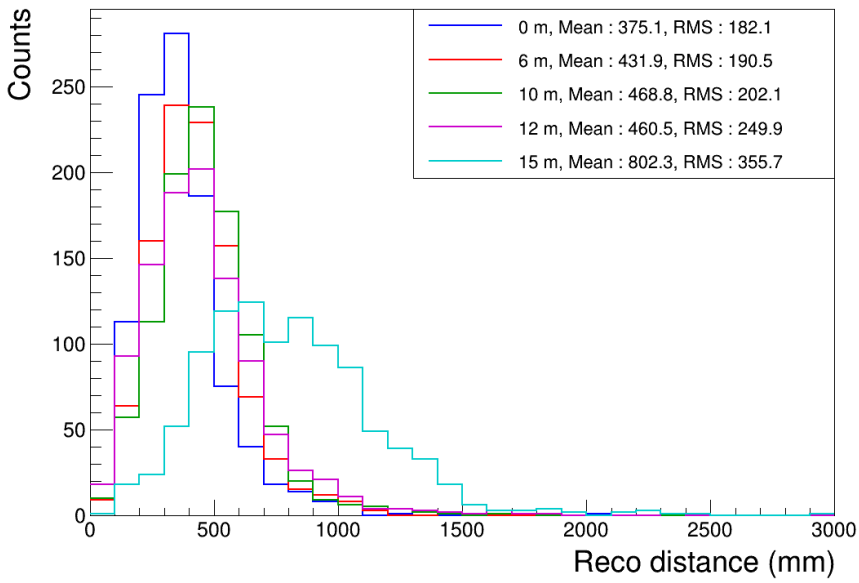

Figure 5.21: Distances between the reconstructed vertex and the true position of each of the 20 MeV positron events, simulated at different positions in the central detector.

5.4.2.3 Impact of the electronics on the reconstruction

In order to investigate the impact of the SPMT electronics on the measured time and the vertex reconstruction, several aspects of the SPMT electronics were sequentially taken into account during the simulation process, for each of the previously mentioned positions of the simulated 20 MeV positron events (0, 6, 10, 12 and 15 m from the center of sphere). The investigated electronics configurations are defined as follows :

- Configuration 1 : only the hits from the DetSim level of the simulation are taken into account, with each hit corresponding to one PE released from the photocathode of the fired PMT. In this configuration, no SPMT electronics are taken into account, to serve as the reference for an undegraded reconstruction.

- Configuration 2 : the response of the PMT is taken into account. This includes the TTS of the PMTs (1.5 ns, Figure 2.15), as well as the 10 ns clusterization process of the DetSim hits described in section 5.2.2.

- Configuration 3 : configuration 2 + the CATIROC features of trigger deadtime, charge acceptance and charge digitization deadtime (section 4.5.4), which are added and taken into account.

- Configuration 4 : configuration 3 + the CATIROC trigger time and its evolution with the amplitude of the PMT signal (Time Walk, section 4.5.3), which are added and taken into account. While the TTS of the PMTs impacts the hit times of the hits from the DetSim level before the clusterization process, the CATIROC trigger time impacts the time associated with the hit cluster if the signal was triggered. Having a configuration with the trigger time being added will allow for comparisons between the impact of the TTS and of the Time Walk on the vertex reconstruction.

The electronics taken into account in each configuration are summed up in Table 5.1.

Configuration 1	Configuration 2	Configuration 3	Configuration 4
DetSim hits	DetSim hits	DetSim hits	DetSim hits
-	PMT TTS	PMT TTS	PMT TTS
-	Hit clusterization	Hit clusterization	Hit clusterization
-	-	CATIROC features	CATIROC features
-	-	-	CATIROC trigger time

Table 5.1: Electronics taken into account in the JUNO simulation of 20 MeV positron events.

For each electronics configuration, the distributions of the distances of the best TMinuit vertex estimations to the true position of the events are respectively shown in Figures 5.22a and 5.22b for 20 MeV positrons generated at 0 m and 15 m from the center of the sphere.

In Figure 5.22a, for positron events at 0 m, a significant difference in the reconstruction distance can be observed between the first and second configurations, with respective mean values of 37.5 cm and 44.8 cm and respective RMS values of 18.2 cm and 24.2 cm. While Configuration 2 adds the TTS of the PMTs and the clusterization process to the hits from the DetSim level (Configuration 1), the number of SPMTs having collected more than one PE and thus being affected by the clusterization process is negligible for events simulated at the center of the detector. The degradation in the reconstruction process from Configuration 1 to Configuration 2 is thus overwhelmingly due to the TTS of the PMTs. In comparison, Configuration 3 barely shows any difference from Configuration 2, and Configuration 4 only slightly degrades the reconstruction process when compared to Configuration 3 (47.9 cm vs 44.6 cm mean values, 25.5 cm vs 24.4 cm RMS values). The Time Walk thus has a lower impact on the vertex reconstruction process than the TTS of the PMTs.

For positron events simulated at 15 m, Figure 5.22b shows similar impacts of the different electronics configurations, with a much larger degradation of the reconstruction process due to Configuration 2, from a mean value of 80.2 cm to a mean value of 155.3 cm, when compared to the positron events simulated at the center of the sphere. Similarly, Configurations 3 and 4 barely induce any degradation in the reconstruction process. For events simulated at 15 m from the

center of the sphere, the large reconstruction distances when the electronics are taken into account indicate that the reconstruction algorithm is not well-suited for such events. Optics processes such as total internal reflection should probably be accounted for, and comparisons to differently built PDFs could be considered. Using a neural network over computing a likelihood is also a popular analysis method for reconstruction algorithms aiming to properly reconstruct events on the edge of sizeable detectors. However, despite the reconstruction process identifying positions located up to ∼3 m away from the true event position as the most likely vertex, the impact of adding the TTS of the PMTs on the reconstruction is still very much visible, especially when compared to the other electronics configurations. In that regard, the conclusions on the dominance of the PMT response on the degradation of the vertex reconstruction are identical as for the 0 m positron events.

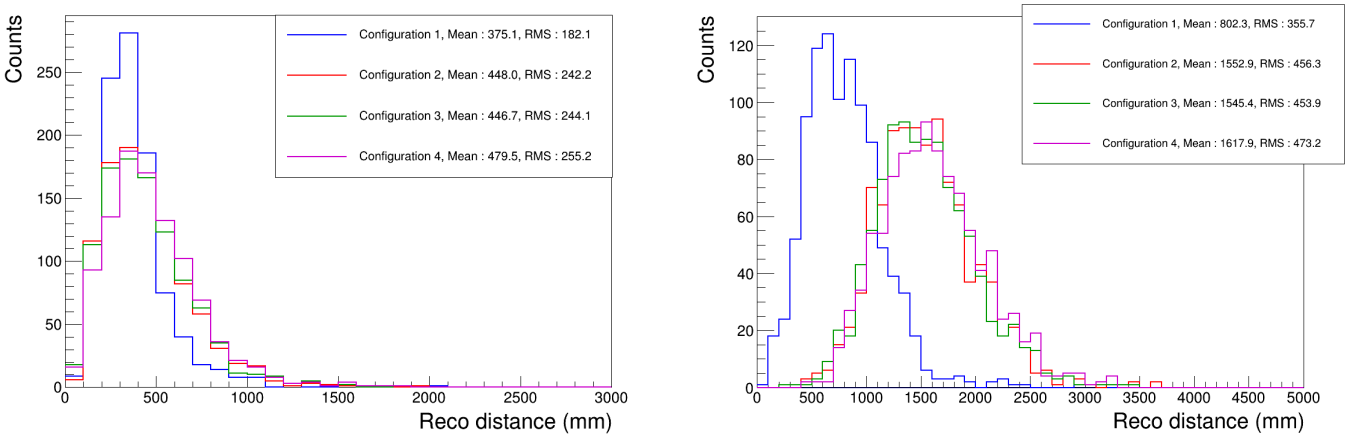

(a) (b)

Figure 5.22: Distances between the reconstructed vertex and the true position of each of the 20 MeV positron events, for all electronics configurations investigated. (a) For positron events at 0 m from the center of sphere. (b) For positron events at 15 m from the center of sphere.

For each given distance-to-center of the simulated events, the mean and RMS values from the reconstruction distances distributions for each electronics configuration can be used to plot the mean reconstruction distance as a function of the distance-to-center of the events, with the RMS value as the Y error bars. Shown in Figure 5.23 for each electronics configuration, these graphs highlight the same behaviour as observed in Figures 5.22a and 5.22b for individual distances-to-center. Configuration 2, corresponding to the introduction of the PMT TTS and of the clusterization process, induces a significant degradation of the reconstruction process when compared to the other configurations. This effect is notably important for events simulated at 12 m. With the reconstruction algorithm yielding better results than for events at 15 m, the conclusions on the PMT TTS dominance are more reliable. As was shown in section 5.4.1, the TTS of the PMTs dominates the degradation of the time measurement, and this study confirms that it also dominates the degradation of reconstruction processes using this time information. The impact of the features of the CATIROC ASIC and of the ABC board on physics studies using time information are thus negligible before the TTS values of the PMT instrumentation.

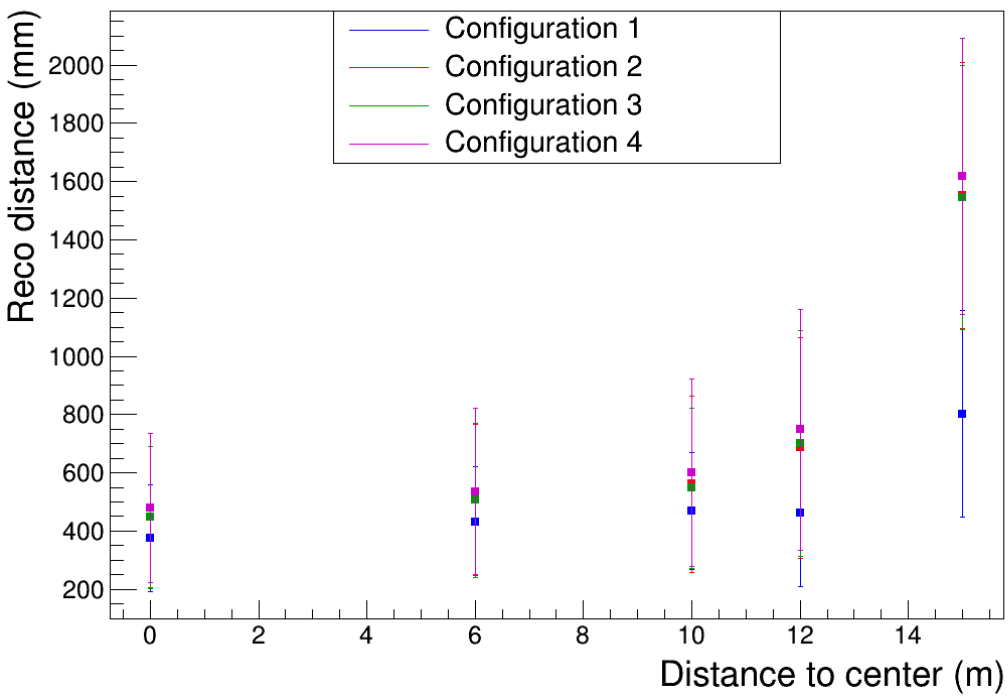

Figure 5.23: Reconstruction distance as a function of the distance-to-center of the simulated events, for each electronics configuration.

5.5 Conclusion

In this chapter, the electronics of the SPMT system were added to the JUNO simulation, and the impact of the SPMT electronics on physics studies conducted with simulation events was investigated. The impact of a few key CATIROC features on the charge reconstruction of muon events showed that despite important charge losses having been observed for very-high-energy events seen by the SPMT system, going up to 45% for SPMTs having collected 20 PEs and above, the impact of the SPMT electronics on the reconstructed charge is expected to be negligible in the photocounting mode. In the case of muon events, reconstructing the charge, and so the energy of the muons, is not the objective. The charge barycenter is only very slightly impacted by the charge saturation of the SPMT system, which is important for efficient muon tracking. Using a continuous energy spectrum of ^{12}B events further highlighted that the charge resolution of the PMT is the dominating factor in the charge measurement uncertainty. The impact of the SPMT electronics on the measured time was also studied, with a comparison of the CATIROC trigger time with the TTS of the SPMTs showing that the TTS of the PMTs is the dominating factor in the time measurement spread, contributing at ~80% while the CATIROC trigger time contributes at only ~20%. This was confirmed by the use of a vertex reconstruction method applied to 20 MeV positron events to evaluate the impact of the SPMT electronics on the measured time, which highlighted that the PMT features introduce the worst degradation of the vertex reconstruction when compared to the rest of the SPMT electronics. For events at the center of the sphere, taking into account the PMT features contributes to ~70% of the degradation while adding the electronics only contributes to ~30%.

Conclusion and Prospects

JUNO is a multi-purpose neutrino experiment currently under construction with the objective of determining the neutrino mass ordering (MO). This is planned to be achieved by detecting reactor anti-neutrinos from two nuclear power plants, with the site location optimized to have the best sensitivity for mass ordering determination. For the measurement of the oscillation parameters at the desired precision and in order to have a competitive input on the neutrino MO, it is crucial to achieve a $3\%/\sqrt{E(\mathrm{MeV})}$ energy resolution in JUNO. This will be mainly achieved through the strict requirements on the liquid scintillator (transparency and light yield), and with an unprecedented PMT coverage made up of 18000 LPMTs and 25600 SPMTs.

The work presented in this thesis was conducted on the SPMT system of the JUNO experiment. This system was designed to serve as a complementary array of photodetectors to the LPMT system, as its 3-inch PMTs will observe the same events as the LPMTs and will thus have the potential to cross-check LPMT measurements.
The SPMT system is made-up of many components, from the SPMTs themselves to the UWB containing the electronics of the system, with an entire chapter of the manuscript dedicated to the description of all the components of the system. In this manuscript, the focus was put on the electronics of the SPMT system, in its development phase at the start of the thesis, and particularly on the CATIROC ASICS and on the ABC front-end board developed at LP2i. The development of the SPMT electronics was indeed a focal point of this thesis, requiring a sizeable investment in the hardware aspect of the electronics in addition to long-lasting performance studies to guarantee that the system is working properly and meeting the requirements. Studies on the standalone performances of the ABC board were conducted, with pedestal widths of $\sim$2.2 ADCu (about 0.024 pC in the configuration used for the measurements) implying a lower than 2% contribution of the pedestal width on the charge measurement uncertainty and concluding that a spread would not be induced on the charge measurement that would have as much of an impact as the charge resolution of the PMTs. The charge linearity of the electronics was investigated, with excellent results showing deviations of the model from the data points below 0.05% in the High Gain mode, and several operations of charge calibration of ABC boards were conducted. As with the pedestal width and the charge resolution of the PMTs, the time resolution of the ABC board was measured and was evaluated as being negligible before the TTS of the PMTs, at $\sim$0.25 ns before the 1.56 ns of the TTS. Crosstalk studies were conducted, and concluded that the ABC board can accept up to $\sim$300 photoelectrons at once without risking falsely triggering channels, which should cover all physics cases including most of the muon events.

A milestone of the SPMT system was the development of test benches for combined tests of the SPMT electronics. 32 channels were made available at first in France, before the test benches were sent to China to prepare for the mass testing of the SPMT production. To this date, $\sim$7000 PMTs, about 1/3 of the production, have been tested and accepted for SPE charge measurement and charge resolution. 128 channels were then made available in France, a key milestone to be reached,

allowing for the simultaneous data acquisition of 128 random PMT signals from dark currents at 100-1000 Hz, without any impact on the quality of the recovered data. Characterizing the behavior of the SPMT electronics to one or several PMT signals was also an important part of my work. Recording waveforms and analysing them allowed for a charge-to-amplitude parametrization as well as an amplitude-to-CATIROC trigger time parametrization, thus understanding the behavior of the electronics when confronted with PMT signals of varying amplitudes.

The second part of the work presented in this thesis is the implementation of the fine responses of the SPMT electronics in the JUNO simulation, as well as the investigation of the impact of these electronic components on the physical measurements of charge and time. A first study regarding charge measurements was conducted using muon events, which led to the conclusion that the charge acceptance of the CATIROC ASICs prevents a saturation effect present in the LPMT system and responsible for blinding the system in the event of muon bundles, effectively worsening the track reconstruction processes. In an energy range closer to IBD events, with ^{12}B decay events, any degradation on the charge reconstruction is dominated by the PMT SPE charge resolution, rather than affected by the electronics of the SPMT system. Similar observations were made with time measurements. Comparing the CATIROC trigger time to the PMT TTS results in a one-sided domination of the time spread by the PMT TTS, with an 80% contribution. For further investigations, a vertex reconstruction method using only the 3-inch PMT system was developed. With no objective of being perfectly optimized, and knowing that a vertex reconstruction using the LPMT system would be miles ahead in terms of performance, this method nevertheless allowed for the study of the relative impact of adding each feature of the SPMT electronics on the degradation of the vertex reconstruction. For 20 MeV positron events simulated at the center of the detector, a mean reconstruction distance of 37.5 cm was achieved for raw simulated events, while taking into account the PMT features degraded this reconstruction to a mean value of 44.58 cm and taking into account all other electronics further degraded this reconstruction to only 47.9 cm, showing that taking into account the PMT features contributes to $\sim$70% of the degradation while adding the electronics only contributes to $\sim$30%.

The electronics of the SPMT system, namely the CATIROC ASICs and the ABC board, are thus very well-performing components of the electronic chain, especially when compared to the main component of the SPMT system, the PMTs themselves. They add little to no noise or spread on the charge and time measurements, and have shown a capacity for event recording even in the case of very high luminosity events.

What has been implemented in the simulation will allow for finer studies to be conducted and for analysis methods including the electronics to be developed until the beginning of the data-taking of the experiment. This data-taking will begin around 2023, and for a period a time, JUNO will be one of the only experiments able to study IBD events in such large quantities. After the Mass Ordering determination phase of the JUNO experiment will conclude, the purity of the LS, as well as the excellent energy resolution, will be a determining factor in the ability of JUNO to begin a phase of searches for double beta decay after 2030, with the opportunity to put constraints on the effective neutrino mass of about 5-10 meV.

Bibliography

[1] J. Chadwick. "Intensitätsverteilung im magnetischen Spectrum der β-Strahlen von radium B + C". In: *Verhandl. Dtsc. Phys. Ges.* 16 (1914), p. 383.

[2] J. Chadwick. "The existence of a neutron". In: *Proceedings of the Royal Society of London. Series A, Containing Papers of a Mathematical and Physical Character* 136.830 (1932), pp. 692–708. DOI: 10.1098/rspa.1932.0112.

[3] H. Bethe and R. Peierls. "The "Neutrino"". In: *Nature* 133 (1934), p. 532. DOI: 10.1038/133532a0.

[4] C. L. Cowan, F. Reines, F. B. Harrison, H. W. Kruse, and A. D. McGuire. "Detection of the Free Neutrino: a Confirmation". In: *Science* 124.3212 (1956), pp. 103–104. DOI: 10.1126/science.124.3212.103.

[5] C. D. Anderson and S. H. Neddermeyer. "Cloud Chamber Observations of Cosmic Rays at 4300 Meters Elevation and Near Sea-Level". In: *Phys. Rev.* 50 (4 Aug. 1936), pp. 263–271. DOI: 10.1103/PhysRev.50.263.

[6] G. Danby, J.-M. Gaillard, K. Goulianos, L. M. Lederman, N. Mistry, M. Schwartz, et al. "Observation of High-Energy Neutrino Reactions and the Existence of Two Kinds of Neutrinos". In: *Phys. Rev. Lett.* 9 (1 July 1962), pp. 36–44. DOI: 10.1103/PhysRevLett.9.36.

[7] K. Kodama, N. Ushida, C. Andreopoulos, N. Saoulidou, G. Tzanakos, P. Yager, et al. "Observation of tau neutrino interactions". In: *Physics Letters B* 504.3 (Apr. 2001), pp. 218–224. DOI: 10.1016/s0370-2693(01)00307-0.

[8] K. Nakamura and al. "Review of Particle Physics". In: *Journal of Physics G: Nuclear and Particle Physics* 37.7A (July 2010), p. 075021. DOI: 10.1088/0954-3899/37/7a/075021.

[9] M. Tanabashi, K. Hagiwara, K. Hikasa, K. Nakamura, Y. Sumino, F. Takahashi, et al. "Review of Particle Physics". In: *Phys. Rev. D* 98 (3 Aug. 2018), p. 030001. DOI: 10.1103/PhysRevD.98.030001.

[10] M. Tanabashi and al. "Review of Particle Physics". In: *Physical Review D* 98.3 (Aug. 2018). DOI: 10.1103/PhysRevD.98.030001.

[11] J. Engle, R. Pereira, and C. Rovelli. "Loop-Quantum-Gravity Vertex Amplitude". In: *Phys. Rev. Lett.* 99 (16 Oct. 2007), p. 161301. DOI: 10.1103/PhysRevLett.99.161301.

[12] S. Glashow. "Partial Symmetries of Weak Interactions". In: *Nucl. Phys.* 22 (1961), pp. 579–588. DOI: 10.1016/0029-5582(61)90469-2.

[13] A. Salam. "Weak and Electromagnetic Interactions". In: *Conf. Proc. C* 680519 (1968), pp. 367–377. DOI: 10.1142/9789812795915_0034.

[14] S. Weinberg. "A Model of Leptons". In: *Phys. Rev. Lett.* 19 (21 Nov. 1967), pp. 1264–1266. DOI: 10.1103/PhysRevLett.19.1264.

[15] G. Aad and al. "Observation of a new particle in the search for the Standard Model Higgs boson with the ATLAS detector at the LHC". In: *Physics Letters B* 716.1 (2012), pp. 1–29. DOI: https://doi.org/10.1016/j.physletb.2012.08.020.

[16] F. Englert and R. Brout. "Broken Symmetry and the Mass of Gauge Vector Mesons". In: *Phys. Rev. Lett.* 13 (9 Aug. 1964), pp. 321–323. DOI: 10.1103/PhysRevLett.13.321.

[17] G. S. Guralnik, C. R. Hagen, and T. W. B. Kibble. "Global Conservation Laws and Massless Particles". In: *Phys. Rev. Lett.* 13 (20 Nov. 1964), pp. 585–587. DOI: 10.1103/PhysRevLett.13.585.

[18] P. W. Higgs. "Broken Symmetries and the Masses of Gauge Bosons". In: *Phys. Rev. Lett.* 13 (16 Oct. 1964), pp. 508–509. DOI: 10.1103/PhysRevLett.13.508.

[19] T. D. Lee and C. N. Yang. "Question of Parity Conservation in Weak Interactions". In: *Phys. Rev.* 106 (6 June 1957), pp. 1371–1371. DOI: 10.1103/PhysRev.106.1371.

[20] C. S. Wu, E. Ambler, R. W. Hayward, D. D. Hoppes, and R. P. Hudson. "Experimental Test of Parity Conservation in Beta Decay". In: *Phys. Rev.* 105 (4 Feb. 1957), pp. 1413–1415. DOI: 10.1103/PhysRev.105.1413.

[21] E. Majorana. "Teoria simmetrica dell'elettrone e del positrone". In: *Il Nuovo Cimento* 14 (1937). DOI: 10.1007/BF02961314.

[22] T. Yanagida. "Horizontal Symmetry and Masses of Neutrinos". In: *Progress of Theoretical Physics* 64.3 (Sept. 1980), pp. 1103–1105. DOI: 10.1143/PTP.64.1103.

[23] M. Fukugita and T. Yanagida. "Barygenesis without grand unification". In: *Physics Letters B* 174.1 (1986), pp. 45–47. DOI: https://doi.org/10.1016/0370-2693(86)91126-3.

[24] E. Aprile et al. "Observation of two-neutrino double electron capture in ^{124}Xe with XENON1T". In: *Nature* 568.7753 (Apr. 2019), pp. 532–535. DOI: 10.1038/s41586-019-1124-4.

[25] M. Goeppert-Mayer. "Double Beta-Disintegration". In: *Phys. Rev.* 48 (6 Sept. 1935), pp. 512–516. DOI: 10.1103/PhysRev.48.512.

[26] T. Kirsten, O. A. Schaeffer, E. Norton, and R. W. Stoenner. "Experimental Evidence for the Double-Beta Decay of Te^{130}". In: *Phys. Rev. Lett.* 20 (23 June 1968), pp. 1300–1303. DOI: 10.1103/PhysRevLett.20.1300.

[27] J. Schechter and J. W. F. Valle. "Neutrinoless double-β decay in SU(2)×U(1) theories". In: *Phys. Rev. D* 25 (11 June 1982), pp. 2951–2954. DOI: 10.1103/PhysRevD.25.2951.

[28] X. Qian and P. Vogel. "Neutrino mass hierarchy". In: *Progress in Particle and Nuclear Physics* 83 (July 2015), pp. 1–30. DOI: 10.1016/j.ppnp.2015.05.002.

[29] J. N. Bahcall and M. H. Pinsonneault. "What Do We (Not) Know Theoretically about Solar Neutrino Fluxes?" In: *Physical Review Letters* 92.12 (Mar. 2004). DOI: 10.1103/physrevlett.92.121301.

[30] Y. Fukuda, T. Hayakawa, K. Inoue, K. Ishihara, H. Ishino, S. Joukou, et al. "Solar Neutrino Data Covering Solar Cycle 22". In: *Phys. Rev. Lett.* 77 (9 Aug. 1996), pp. 1683–1686. DOI: 10.1103/PhysRevLett.77.1683.

[31] Y. Ashie, J. Hosaka, and al. "Evidence for an Oscillatory Signature in Atmospheric Neutrino Oscillations". In: *Phys. Rev. Lett.* 93 (10 Sept. 2004), p. 101801. DOI: 10.1103/PhysRevLett.93.101801.

[32] S. Fukuda, Y. Fukuda, M. Ishitsuka, Y. Itow, T. Kajita, J. Kameda, et al. "Solar ^8B and hep Neutrino Measurements from 1258 Days of Super-Kamiokande Data". In: *Phys. Rev. Lett.* 86 (25 June 2001), pp. 5651–5655. DOI: 10.1103/PhysRevLett.86.5651.

[33] J. Abdurashitov, T. Bowles, B. Cleveland, S. Elliott, V. Gavrin, S. Girin, et al. "Measurement of the solar neutrino capture rate in Sage". In: *Nuclear Physics B - Proceedings Supplements* 118 (2003). Proceedings of the XXth International Conference on Neutrino Physics and Astrophysics, pp. 39–46. DOI: https://doi.org/10.1016/S0920-5632(03)01302-1.

[34] W. Hampel et al. "GALLEX solar neutrino observations: Results for GALLEX IV". In: *Phys. Lett. B* 447 (1999), pp. 127–133. DOI: 10.1016/S0370-2693(98)01579-2.

[35] B. Aharmim and al. "Low-energy-threshold analysis of the Phase I and Phase II data sets of the Sudbury Neutrino Observatory". In: *Phys. Rev. C* 81 (5 May 2010), p. 055504. DOI: 10.1103/PhysRevC.81.055504.

[36] S. N. Ahmed, A. E. Anthony, E. W. Beier, A. Bellerive, S. D. Biller, J. Boger, et al. "Measurement of the Total Active ^{8}B Solar Neutrino Flux at the Sudbury Neutrino Observatory with Enhanced Neutral Current Sensitivity". In: *Physical Review Letters* 92.18 (May 2004). DOI: 10.1103/physrevlett.92.181301.

[37] P. Abreu and al. "Measurement of the Proton-Air Cross Section at $\sqrt{s} = 57\ TeV$ with the Pierre Auger Observatory". In: *Phys. Rev. Lett.* 109 (6 Aug. 2012), p. 062002. DOI: 10.1103/PhysRevLett.109.062002.

[38] B. Pontecorvo. "Inverse beta processes and nonconservation of lepton charge". In: *Sov. Phys. JETP* 7 (1958), pp. 172–173.

[39] Z. Maki, M. Nakagawa, and S. Sakata. "Remarks on the unified model of elementary particles". In: *Prog. Theor. Phys.* 28 (1962), pp. 870–880. DOI: 10.1143/PTP.28.870.

[40] N. Cabibbo. "Unitary Symmetry and Leptonic Decays". In: *Phys. Rev. Lett.* 10 (12 June 1963), pp. 531–533. DOI: 10.1103/PhysRevLett.10.531.

[41] M. Kobayashi and T. Maskawa. "CP Violation in the Renormalizable Theory of Weak Interaction". In: *Prog. Theor. Phys.* 49 (1973), pp. 652–657. DOI: 10.1143/PTP.49.652.

[42] S. P. Mikheyev and A. Y. Smirnov. "Resonant amplification of ν oscillations in matter and solar-neutrino spectroscopy". In: *Il Nuovo Cimento C* 9 (1986). DOI: 10.1007/BF02508049.

[43] L. Wolfenstein. "Neutrino oscillations in matter". In: *Phys. Rev. D* 17 (9 May 1978), pp. 2369–2374. DOI: 10.1103/PhysRevD.17.2369.

[44] I. Esteban, M. Gonzalez-Garcia, M. Maltoni, T. Schwetz, and A. Zhou. "The fate of hints: updated global analysis of three-flavor neutrino oscillations". In: *Journal of High Energy Physics* 2020.9 (Sept. 2020). DOI: 10.1007/jhep09(2020)178.

[45] I. Esteban, M. Gonzalez-Garcia, M. Maltoni, T. Schwetz, and A. Zhou. *NuFIT.org, Three-neutrino fit : parameter ranges.* http://www.nu-fit.org/?q=node/228. 2020.

[46] W. Buchmüller, R. Peccei, and T. Yanagida. "LEPTOGENESIS AS THE ORIGIN OF MATTER". In: *Annual Review of Nuclear and Particle Science* 55.1 (Dec. 2005), pp. 311–355. DOI: 10.1146/annurev.nucl.55.090704.151558.

[47] H. Duan, G. M. Fuller, and Y.-Z. Qian. "Collective Neutrino Oscillations". In: *Annual Review of Nuclear and Particle Science* 60.1 (2010), pp. 569–594. DOI: 10.1146/annurev.nucl.012809.104524.

[48] B. Dasgupta, A. Dighe, G. G. Raffelt, and A. Y. Smirnov. "Multiple Spectral Splits of Supernova Neutrinos". In: *Phys. Rev. Lett.* 103 (5 July 2009), p. 051105. DOI: 10.1103/PhysRevLett.103.051105.

[49] P. D. Serpico, S. Chakraborty, T. Fischer, L. Hüdepohl, H.-T. Janka, and A. Mirizzi. "Probing the neutrino mass hierarchy with the rise time of a supernova burst". In: *Phys. Rev. D* 85 (8 Apr. 2012), p. 085031. DOI: 10.1103/PhysRevD.85.085031.

[50] A. H. for the NOνA collaboration. *New Oscillation Results from the NOνA Experiment.* July 2020.

[51] P. D. for the T2K collaboration. *Latest Neutrino Oscillation Results from T2K.* July 2020.

[52] H.-K. Proto-Collaboration, : K. Abe, K. Abe, H. Aihara, A. Aimi, et al. *Hyper-Kamiokande Design Report.* 2018.

[53] S. Adrián-Martínez, M. Ageron, F. Aharonian, S. Aiello, A. Albert, F. Ameli, et al. "Letter of intent for KM3NeT 2.0". In: *Journal of Physics G: Nuclear and Particle Physics* 43.8 (June 2016), p. 084001. DOI: 10.1088/0954-3899/43/8/084001.

[54] S. Aiello, A. Albert, S. A. Garre, Z. Aly, A. Ambrosone, F. Ameli, et al. *Determining the Neutrino Mass Ordering and Oscillation Parameters with KM3NeT/ORCA*. 2021.

[55] R. Acciarri, M. A. Acero, M. Adamowski, C. Adams, P. Adamson, S. Adhikari, et al. *Long-Baseline Neutrino Facility (LBNF) and Deep Underground Neutrino Experiment (DUNE) Conceptual Design Report Volume 1: The LBNF and DUNE Projects*. 2016.

[56] D. Collaboration, R. Acciarri, M. A. Acero, M. Adamowski, C. Adams, P. Adamson, et al. *Long-Baseline Neutrino Facility (LBNF) and Deep Underground Neutrino Experiment (DUNE) Conceptual Design Report Volume 2: The Physics Program for DUNE at LBNF*. 2016.

[57] J. Strait, E. McCluskey, T. Lundin, J. Willhite, T. Hamernik, V. Papadimitriou, et al. *Long-Baseline Neutrino Facility (LBNF) and Deep Underground Neutrino Experiment (DUNE) Conceptual Design Report Volume 3: Long-Baseline Neutrino Facility for DUNE June 24, 2015*. 2016.

[58] D. Collaboration, B. Abi, R. Acciarri, M. A. Acero, G. Adamov, D. Adams, et al. *Long-baseline neutrino oscillation physics potential of the DUNE experiment*. 2020.

[59] F. An, G. An, Q. An, V. Antonelli, E. Baussan, J. Beacom, et al. "Neutrino physics with JUNO". In: *Journal of Physics G: Nuclear and Particle Physics* 43.3 (Feb. 2016), p. 030401. DOI: 10.1088/0954-3899/43/3/030401.

[60] D. Adey, F. P. An, A. B. Balantekin, H. R. Band, M. Bishai, S. Blyth, et al. "Measurement of the Electron Antineutrino Oscillation with 1958 Days of Operation at Daya Bay". In: *Physical Review Letters* 121.24 (Dec. 2018). DOI: 10.1103/physrevlett.121.241805.

[61] G. Bak, J. H. Choi, H. I. Jang, J. S. Jang, S. H. Jeon, K. K. Joo, et al. "Measurement of Reactor Antineutrino Oscillation Amplitude and Frequency at RENO". In: *Physical Review Letters* 121.20 (Nov. 2018). DOI: 10.1103/physrevlett.121.201801.

[62] T. D. C. Collaboration. "Double Chooz θ_{13} measurement via total neutron capture detection". In: *Nature Physics* 16.5 (Apr. 2020), pp. 558–564. DOI: 10.1038/s41567-020-0831-y.

[63] Y.-F. Li, J. Cao, Y. Wang, and L. Zhan. "Unambiguous determination of the neutrino mass hierarchy using reactor neutrinos". In: *Phys. Rev. D* 88 (1 July 2013), p. 013008. DOI: 10.1103/PhysRevD.88.013008.

[64] L. Zhan, Y. Wang, J. Cao, and L. Wen. "Experimental requirements to determine the neutrino mass hierarchy using reactor neutrinos". In: *Phys. Rev. D* 79 (7 Apr. 2009), p. 073007. DOI: 10.1103/PhysRevD.79.073007.

[65] J. Liu, B. Cai, R. Carr, D. Dwyer, W. Gu, G. Li, et al. "Automated calibration system for a high-precision measurement of neutrino mixing angle θ_{13} with the Daya Bay antineutrino detectors". In: *Nuclear Instruments and Methods in Physics Research Section A: Accelerators, Spectrometers, Detectors and Associated Equipment* 750 (2014), pp. 19–37. DOI: https://doi.org/10.1016/j.nima.2014.02.049.

[66] D. Bay, J. collaborations, : A. Abusleme, T. Adam, S. Ahmad, et al. *Optimization of the JUNO liquid scintillator composition using a Daya Bay antineutrino detector*. 2020.

[67] P. Lombardi, M. Montuschi, A. Formozov, A. Brigatti, S. Parmeggiano, R. Pompilio, et al. "Distillation and stripping pilot plants for the JUNO neutrino detector: Design, operations and reliability". In: *Nuclear Instruments and Methods in Physics Research Section A: Accelerators, Spectrometers, Detectors and Associated Equipment* 925 (2019), pp. 6–17. DOI: https://doi.org/10.1016/j.nima.2019.01.071.

[68] J. Collaboration, A. Abusleme, T. Adam, S. Ahmad, R. Ahmed, S. Aiello, et al. *The Design and Sensitivity of JUNO's scintillator radiopurity pre-detector OSIRIS*. 2021.

[69] L. Wen, M. He, Y. Wang, J. Cao, S. Liu, Y. Heng, et al. "A quantitative approach to select PMTs for large detectors". In: *Nuclear Instruments and Methods in Physics Research Section A: Accelerators, Spectrometers, Detectors and Associated Equipment* 947 (Dec. 2019), p. 162766. DOI: 10.1016/j.nima.2019.162766.

[70] N. Anfimov. "Large photocathode 20-inch PMT testing methods for the JUNO experiment". In: *Journal of Instrumentation* 12.06 (June 2017), pp. C06017–C06017. DOI: 10.1088/1748-0221/12/06/c06017.

[71] T. Adam, F. An, G. An, Q. An, N. Anfimov, V. Antonelli, et al. *JUNO Conceptual Design Report.* 2015.

[72] S. group. *CDR of SPMT System for JUNO Experiment.* https://juno.ihep.ac.cn/cgi-bin/Dev_DocDB/ShowDocument?docid=3498. 2019.

[73] Y. Zhang, J. Hui, J. Liu, M. Xiao, T. Zhang, F. Zhang, et al. "Cable loop calibration system for Jiangmen Underground Neutrino Observatory". In: *Nuclear Instruments and Methods in Physics Research Section A: Accelerators, Spectrometers, Detectors and Associated Equipment* 988 (Feb. 2021), p. 164867. DOI: 10.1016/j.nima.2020.164867.

[74] Y. Zhang, J. Liu, M. Xiao, F. Zhang, and T. Zhang. "Laser calibration system in JUNO". In: *Journal of Instrumentation* 14.01 (Jan. 2019), P01009–P01009. DOI: 10.1088/1748-0221/14/01/p01009.

[75] K. Hirata, T. Kajita, M. Koshiba, M. Nakahata, Y. Oyama, N. Sato, et al. "Observation of a neutrino burst from the supernova SN1987A". In: *Phys. Rev. Lett.* 58 (14 Apr. 1987), pp. 1490–1493. DOI: 10.1103/PhysRevLett.58.1490.

[76] R. M. Bionta, G. Blewitt, C. B. Bratton, D. Casper, A. Ciocio, R. Claus, et al. "Observation of a neutrino burst in coincidence with supernova 1987A in the Large Magellanic Cloud". In: *Phys. Rev. Lett.* 58 (14 Apr. 1987), pp. 1494–1496. DOI: 10.1103/PhysRevLett.58.1494.

[77] E. Alexeyev, L. Alexeyeva, I. Krivosheina, and V. Volchenko. "Detection of the neutrino signal from SN 1987A in the LMC using the INR Baksan underground scintillation telescope". In: *Physics Letters B* 205.2 (1988), pp. 209–214. DOI: https://doi.org/10.1016/0370-2693(88)91651-6.

[78] S. A. Colgate and R. H. White. "The Hydrodynamic Behavior of Supernovae Explosions". In: *Astrophys. J.* 143 (Mar. 1966), p. 626. DOI: 10.1086/148549.

[79] H. A. Bethe. "Supernova mechanisms". In: *Rev. Mod. Phys.* 62 (4 Oct. 1990), pp. 801–866. DOI: 10.1103/RevModPhys.62.801.

[80] S. E. Woosley, A. Heger, and T. A. Weaver. "The evolution and explosion of massive stars". In: *Rev. Mod. Phys.* 74 (4 Nov. 2002), pp. 1015–1071. DOI: 10.1103/RevModPhys.74.1015.

[81] H. JANKA, K. LANGANKE, A. MAREK, G. MARTINEZPINEDO, and B. MULLER. "Theory of core-collapse supernovae". In: *Physics Reports* 442.1-6 (Apr. 2007), pp. 38–74. DOI: 10.1016/j.physrep.2007.02.002.

[82] H.-T. Janka. "Neutrino-Driven Explosions". In: *Handbook of Supernovae* (2017), pp. 1095–1150. DOI: 10.1007/978-3-319-21846-5_109.

[83] C. Kato, M. D. Azari, S. Yamada, K. Takahashi, H. Umeda, T. Yoshida, et al. *Pre-supernova neutrino emissions from ONe cores in the progenitors of core-collapse supernovae: are they distinguishable from those of Fe cores?* 2015.

[84] T. Yoshida, K. Takahashi, H. Umeda, and K. Ishidoshiro. "Presupernova neutrino events relating to the final evolution of massive stars". In: *Physical Review D* 93.12 (June 2016). DOI: 10.1103/physrevd.93.123012.

[85] J.-S. Lu, Y.-F. Li, and S. Zhou. "Getting the most from the detection of Galactic supernova neutrinos in future large liquid-scintillator detectors". In: *Physical Review D* 94.2 (July 2016). DOI: 10.1103/physrevd.94.023006.

[86] J. F. Beacom, W. M. Farr, and P. Vogel. "Detection of supernova neutrinos by neutrino-proton elastic scattering". In: *Physical Review D* 66.3 (Aug. 2002). DOI: 10.1103/physrevd.66.033001.

[87] H.-L. Li, Y.-F. Li, M. Wang, L.-J. Wen, and S. Zhou. "Towards a complete reconstruction of supernova neutrino spectra in future large liquid-scintillator detectors". In: *Physical Review D* 97.6 (Mar. 2018). DOI: 10.1103/physrevd.97.063014.

[88] H.-L. Li, X. Huang, Y.-F. Li, L.-J. Wen, and S. Zhou. "Model-independent approach to the reconstruction of multiflavor supernova neutrino energy spectra". In: *Physical Review D* 99.12 (June 2019). DOI: 10.1103/physrevd.99.123009.

[89] K. Rozwadowska, F. Vissani, and E. Cappellaro. "On the rate of core collapse supernovae in the milky way". In: *New Astronomy* 83 (Feb. 2021), p. 101498. DOI: 10.1016/j.newast.2020.101498.

[90] J.-S. Lu, J. Cao, Y.-F. Li, and S. Zhou. "Constraining absolute neutrino masses via detection of galactic supernova neutrinos at JUNO". In: *Journal of Cosmology and Astroparticle Physics* 2015.05 (May 2015), pp. 044–044. DOI: 10.1088/1475-7516/2015/05/044.

[91] A. Gando, Y. Gando, K. Ichimura, H. Ikeda, K. Inoue, Y. Kibe, et al. "SEARCH FOR EXTRATERRESTRIAL ANTINEUTRINO SOURCES WITH THE KamLAND DETECTOR". In: *The Astrophysical Journal* 745.2 (Jan. 2012), p. 193. DOI: 10.1088/0004-637x/745/2/193.

[92] R. Möllenberg, F. von Feilitzsch, D. Hellgartner, L. Oberauer, M. Tippmann, V. Zimmer, et al. "Detecting the diffuse supernova neutrino background with LENA". In: *Physical Review D* 91.3 (Feb. 2015). DOI: 10.1103/physrevd.91.032005.

[93] M. Sisti. "Physics prospects of the JUNO experiment". In: *J. Phys. Conf. Ser.* 1468.1 (2020). Ed. by M. Nakahata, p. 012150. DOI: 10.1088/1742-6596/1468/1/012150.

[94] M. Agostini, K. Altenmüller, S. Appel, V. Atroshchenko, Z. Bagdasarian, D. Basilico, et al. "Comprehensive measurement of *pp*-chain solar neutrinos". In: *Nature* 562.7728 (2018), pp. 505–510. DOI: 10.1038/s41586-018-0624-y.

[95] M. Agostini, K. Altenmüller, S. Appel, V. Atroshchenko, Z. Bagdasarian, D. Basilico, et al. *First Direct Experimental Evidence of CNO neutrinos*. 2020.

[96] K. Collaboration, K. Abe, Y. Haga, Y. Hayato, M. Ikeda, K. Iyogi, et al. *Solar Neutrino Measurements in Super-Kamiokande-IV*. 2016.

[97] Y. Nakajima. *Recent results and future prospects from Super- Kamiokande*. June 2020. DOI: 10.5281/zenodo.3959640.

[98] M. Maltoni and A. Yu. Smirnov. "Solar neutrinos and neutrino physics". In: *The European Physical Journal A* 52.4 (Apr. 2016). DOI: 10.1140/epja/i2016-16087-0.

[99] A. Serenelli, C. Peña-Garay, and W. C. Haxton. "Using the standard solar model to constrain solar composition and nuclear reactionSfactors". In: *Physical Review D* 87.4 (Feb. 2013). DOI: 10.1103/physrevd.87.043001.

[100] A. Abusleme, T. Adam, S. Ahmad, S. Aiello, M. Akram, N. Ali, et al. "Feasibility and physics potential of detecting 8B solar neutrinos at JUNO". In: *Chinese Physics C* 45.2 (Jan. 2021), p. 023004. DOI: 10.1088/1674-1137/abd92a.

[101] T. Suzuki, A. B. Balantekin, and T. Kajino. "Neutrino capture on13C". In: *Physical Review C* 86.1 (July 2012). DOI: 10.1103/physrevc.86.015502.

[102] T. Suzuki, A. B. Balantekin, T. Kajino, and S. Chiba. "Neutrino-13C cross sections at supernova neutrino energies". In: *Journal of Physics G: Nuclear and Particle Physics* 46.7 (May 2019), p. 075103. DOI: 10.1088/1361-6471/ab1c11.

[103] H. Watanabe. *Geoneutrino measurement with KamLAND*. Oct. 2019.

[104] M. Agostini, K. Altenmüller, S. Appel, V. Atroshchenko, Z. Bagdasarian, D. Basilico, et al. "Comprehensive geoneutrino analysis with Borexino". In: *Physical Review D* 101.1 (Jan. 2020). DOI: 10.1103/physrevd.101.012009.

[105] J. M. Herndon. "Feasibility of a Nuclear Fission Reactor at the Center of the Earth as the Energy Source for the Geomagnetic Field". In: *Journal of geomagnetism and geoelectricity* 45.5 (1993), pp. 423–437. DOI: 10.5636/jgg.45.423.

[106] J. M. Herndon. "Substructure of the inner core of the Earth". In: *Proceedings of the National Academy of Sciences* 93.2 (1996), pp. 646–648. DOI: 10.1073/pnas.93.2.646.

[107] V. D. Rusov, V. N. Pavlovich, V. N. Vaschenko, V. A. Tarasov, T. N. Zelentsova, V. N. Bolshakov, et al. "Geoantineutrino spectrum and slow nuclear burning on the boundary of the liquid and solid phases of the Earth's core". In: *Journal of Geophysical Research: Solid Earth* 112.B9 (2007). DOI: https://doi.org/10.1029/2005JB004212.

[108] W. V. Westrenen and R. D. Meijer. "The feasibility and implications of nuclear georeactors in Earth's core-mantle boundary region : research article". In: *South African Journal of Science* 104.3 (2008), pp. 111–118. DOI: 10.10520/EJC96784.

[109] R. Han, Y.-F. Li, L. Zhan, W. F. McDonough, J. Cao, and L. Ludhova. "Potential of geoneutrino measurements at JUNO". In: *Chinese Physics C* 40.3 (Mar. 2016), p. 033003. DOI: 10.1088/1674-1137/40/3/033003.

[110] V. Strati, M. Baldoncini, I. Callegari, F. Mantovani, W. McDonough, B. Ricci, et al. "Expected geoneutrino signal at JUNO". In: *Progress in Earth and Planetary Science* (Dec. 2015). DOI: 10.1186/s40645-015-0037-6.

[111] R. Gao, Z. Li, R. Han, A. Wang, Y. Li, Y. Xi, et al. "JULOC: A local 3-D high-resolution crustal model in South China for forecasting geoneutrino measurements at JUNO". In: *Physics of the Earth and Planetary Interiors* 299 (2020), p. 106409. DOI: https://doi.org/10.1016/j.pepi.2019.106409.

[112] X.-F. Zheng, Z. Yao, J.-H. Liang, and J. Zheng. "The Role Played and Opportunities Provided by IGP DMC of China National Seismic Network in Wenchuan Earthquake Disaster Relief and Researches". In: *Bulletin of The Seismological Society of America - BULL SEISMOL SOC AMER* 100 (Oct. 2010), pp. 2866–2872. DOI: 10.1785/0120090257.

[113] Y. Huang, V. Chubakov, F. Mantovani, R. L. Rudnick, and W. F. McDonough. "A reference Earth model for the heat-producing elements and associated geoneutrino flux". In: *Geochemistry, Geophysics, Geosystems* 14.6 (2013), pp. 2003–2029. DOI: https://doi.org/10.1002/ggge.20129.

[114] L. Wolfenstein. "Neutrino oscillations in matter". In: *Phys. Rev. D* 17 (9 May 1978), pp. 2369–2374. DOI: 10.1103/PhysRevD.17.2369.

[115] M. Blennow and T. Schwetz. "Determination of the neutrino mass ordering by combining PINGU and Daya Bay II". In: *Journal of High Energy Physics* 2013.9 (Sept. 2013). DOI: 10.1007/jhep09(2013)089.

[116] M. Aartsen, M. Ackermann, J. Adams, J. Aguilar, M. Ahlers, M. Ahrens, et al. "Combined sensitivity to the neutrino mass ordering with JUNO, the IceCube Upgrade, and PINGU". In: *Physical Review D* 101.3 (Feb. 2020). DOI: 10.1103/physrevd.101.032006.

[117] A. D. Sakharov. "Violation ofCPin variance,Casymmetry, and baryon asymmetry of the universe". In: *Soviet Physics Uspekhi* 34.5 (May 1991), pp. 392–393. DOI: 10.1070/pu1991v034n05abeh002497.

[118] H. Georgi and S. L. Glashow. "Unity of All Elementary-Particle Forces". In: *Phys. Rev. Lett.* 32 (8 Feb. 1974), pp. 438–441. DOI: 10.1103/PhysRevLett.32.438.

[119] P. Nath and P. Fileviez Pérez. "Proton stability in grand unified theories, in strings and in branes". In: *Physics Reports* 441.5-6 (Apr. 2007), pp. 191–317. DOI: 10.1016/j.physrep.2007.02.010.

[120] T. M. Undagoitia, F. von Feilitzsch, M. Göger-Neff, C. Grieb, K. A. Hochmuth, L. Oberauer, et al. "Search for the proton decay $p \to K^+ + \overline{\nu}$ in the large liquid scintillator low energy neutrino astronomy detector LENA". In: *Physical Review D* 72.7 (Oct. 2005). DOI: 10.1103/physrevd.72.075014.

[121] K. Asakura, A. Gando, Y. Gando, T. Hachiya, S. Hayashida, H. Ikeda, et al. "Search for the proton decay mode $p \to \overline{\nu}K^+$ with KamLAND". In: *Phys. Rev. D* 92 (5 Sept. 2015), p. 052006. DOI: 10.1103/PhysRevD.92.052006.

[122] G. J. Feldman and R. D. Cousins. "Unified approach to the classical statistical analysis of small signals". In: *Physical Review D* 57.7 (Apr. 1998), pp. 3873–3889. DOI: 10.1103/physrevd.57.3873.

[123] J. collaboration, A. Abusleme, T. Adam, S. Ahmad, R. Ahmed, S. Aiello, et al. *Calibration Strategy of the JUNO Experiment*. 2021.

[124] C. Genster, M. Schever, L. Ludhova, M. Soiron, A. Stahl, and C. Wiebusch. "Muon reconstruction with a geometrical model in JUNO". In: *Journal of Instrumentation* 13.03 (Mar. 2018), T03003–T03003. DOI: 10.1088/1748-0221/13/03/t03003.

[125] S. Conforti. *Datasheet CATIROC*. 2016. DOI: datasheet_CATIROC_2016_09_V4.

[126] S. Conforti, M. Settimo, C. Santos, C. Bordereau, A. Cabrera, S. Callier, et al. "CATIROC: an integrated chip for neutrino experiments using photomultiplier tubes". In: *Journal of Instrumentation* 16.05 (May 2021), P05010. DOI: 10.1088/1748-0221/16/05/p05010.

[127] C. C. et al. "Mass production and characterization of 3-inch PMTs for the JUNO experiment". In: *Nuclear Instruments and Methods in Physics Research Section A: Accelerators, Spectrometers, Detectors and Associated Equipment* 1005 (2021), p. 165347. DOI: https://doi.org/10.1016/j.nima.2021.165347.

[128] J. collaboration, A. Abusleme, T. Adam, S. Ahmad, R. Ahmed, S. Aiello, et al. *Radioactivity control strategy for the JUNO detector*. 2021.

[129] D. Breton, E. Delagnes, J. Maalmi, and P. Rusquart. "The WaveCatcher family of SCA-based 12-bit 3.2-GS/s fast digitizers". In: *2014 19th IEEE-NPSS Real Time Conference*. 2014, pp. 1–8. DOI: 10.1109/RTC.2014.7097545.

[130] C. Marquet, C. Cerna, E. Chauveau, H. Chiron, G. Claverie, L. Daudin, et al. "High energy resolution electron beam spectrometer in the MeV range". In: *Journal of Instrumentation* 10.09 (Sept. 2015), P09008–P09008. DOI: 10.1088/1748-0221/10/09/p09008.

[131] E. Bellamy, G. Bellettini, J. Budagov, F. Cervelli, I. Chirikov-Zorin, M. Incagli, et al. "Absolute calibration and monitoring of a spectrometric channel using a photomultiplier". In: *Nuclear Instruments and Methods in Physics Research Section A: Accelerators, Spectrometers, Detectors and Associated Equipment* 339.3 (1994), pp. 468–476. DOI: https://doi.org/10.1016/0168-9002(94)90183-X.

[132] D. Wu. *3-inch PMT (SPMT) Signal Test*.

[133] P. Walker. *sPMT (PUC/UCI Group) - Small-PMT gain measurements*.

[134] T. Lin, J. Zou, W. Li, Z. Deng, X. Fang, G. Cao, et al. "The Application of SNiPER to the JUNO Simulation". In: *Journal of Physics: Conference Series* 898 (Oct. 2017), p. 042029. DOI: 10.1088/1742-6596/898/4/042029.

[135] J. H. Zou, X. T. Huang, W. D. Li, T. Lin, T. Li, K. Zhang, et al. "SNiPER: an offline software framework for non-collider physics experiments". In: *Journal of Physics: Conference Series* 664.7 (Dec. 2015), p. 072053. DOI: 10.1088/1742-6596/664/7/072053.

[136] S. Agostinelli, J. Allison, K. Amako, J. Apostolakis, H. Araujo, P. Arce, et al. "Geant4—a simulation toolkit". In: *Nuclear Instruments and Methods in Physics Research Section A: Accelerators, Spectrometers, Detectors and Associated Equipment* 506.3 (2003), pp. 250–303. DOI: https://doi.org/10.1016/S0168-9002(03)01368-8.

[137] J. Allison, K. Amako, J. Apostolakis, H. Araujo, P. Arce Dubois, M. Asai, et al. "Geant4 developments and applications". In: *IEEE Transactions on Nuclear Science* 53.1 (2006), pp. 270–278. DOI: 10.1109/TNS.2006.869826.

[138] J. Allison, K. Amako, J. Apostolakis, P. Arce, M. Asai, T. Aso, et al. "Recent developments in Geant4". In: *Nuclear Instruments and Methods in Physics Research Section A: Accelerators, Spectrometers, Detectors and Associated Equipment* 835 (2016), pp. 186–225. DOI: https://doi.org/10.1016/j.nima.2016.06.125.

[139] R. Brun and F. Rademakers. "ROOT — An object oriented data analysis framework". In: *Nuclear Instruments and Methods in Physics Research Section A: Accelerators, Spectrometers, Detectors and Associated Equipment* 389.1 (1997). New Computing Techniques in Physics Research V, pp. 81–86. DOI: https://doi.org/10.1016/S0168-9002(97)00048-X.

[140] S. Blyth. "Meeting the challenge of JUNO simulation with Opticks: GPU optical photon acceleration via NVIDIA® OptiX TM". In: *EPJ Web of Conferences* 245 (Jan. 2020), p. 11003. DOI: 10.1051/epjconf/202024511003.

[141] B. S. C. "Opticks : GPU Optical Photon Simulation for Particle Physics using NVIDIA® OptiX™". In: *Journal of Physics: Conference Series* 898 (Oct. 2017), p. 042001. DOI: 10.1088/1742-6596/898/4/042001.

[142] J. Xu and Y. Malyshkin. *Note of 3-inch PMT system cable map*. May 2019.

[143] C. Jollet. *SPMT Simulation*. Jan. 2021.

[144] Q. Liu, M. He, X. Ding, W. Li, and H. Peng. "A vertex reconstruction algorithm in the central detector of JUNO". In: *Journal of Instrumentation* 13.09 (Sept. 2018), T09005–T09005. DOI: 10.1088/1748-0221/13/09/t09005.